



Universiteit  
Leiden  
The Netherlands

## **Image guided surgery: clinical validation of lesion identification technologies and exploration of nerve sparing approaches**

KleinJan, G.H.

### **Citation**

KleinJan, G. H. (2018, March 8). *Image guided surgery: clinical validation of lesion identification technologies and exploration of nerve sparing approaches*. Retrieved from <https://hdl.handle.net/1887/61007>

Version: Not Applicable (or Unknown)

License: [Licence agreement concerning inclusion of doctoral thesis in the Institutional Repository of the University of Leiden](#)

Downloaded from: <https://hdl.handle.net/1887/61007>

**Note:** To cite this publication please use the final published version (if applicable).

Cover Page



Universiteit Leiden



The following handle holds various files of this Leiden University dissertation:

<http://hdl.handle.net/1887/61007>

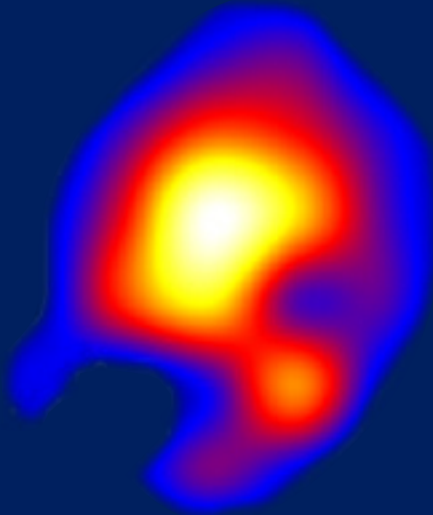
**Author:** KleinJan, G.H.

**Title:** Image guided surgery: clinical validation of lesion identification technologies and exploration of nerve sparing approaches

**Issue Date:** 2018-03-08

# IMAGE GUIDED SURGERY:

CLINICAL VALIDATION OF LESION  
IDENTIFICATION TECHNOLOGIES AND  
EXPLORATION OF  
NERVE SPARING APPROACHES



Gijsbert Hendrik KleinJan



E

**Image guided surgery:  
clinical validation of lesion identification technologies and  
exploration of nerve sparing approaches**

**Gijsbert Hendrik KleinJan**

Cover design	Bob Salentijn (B & S Grafisch Bureau)
Design and lay out	Bob Salentijn (B & S Grafisch Bureau)
Printed by	Gildeprint

The research described in this thesis was carried out at the Leiden University Medical University (Leiden) and the Netherlands Cancer Institute – Antoni van Leeuwenhoek Hospital (Amsterdam)

The studies in this thesis were financially supported by a This work was supported by ERC starting grant (2012-306890) and partially supported by the Dutch Cancer Society translational research award (PGF 2009–4344), and an NWO-STW-VIDI (STW BGT11272).

Financial support from Hamamatsu Photonics K.K., SurgicEye GmbH, KARL STORZ Endoscopie Nederland B.V., ZEISS, EuroTec B.V. and Astellas Pharma B.V. for the printing of this thesis is gratefully acknowledged.

**Image guided surgery:  
clinical validation of lesion identification technologies  
and exploration of nerve sparing approaches**

**PROEFSCHRIFT**

ter verkrijging van de graad van Doctor  
aan de Universiteit Leiden,  
op gezag van Rector Magnificus prof.mr. C.J.J.M. Stolker,  
volgens besluit van het College voor Promoties  
te verdedigen op 8 maart 2018  
klokke 16:15 uur

door

**Gijsbert Hendrik KleinJan**

geboren te Apeldoorn  
in 1985

Promotor: Prof. dr. M.A. van Buchem

Co-promotores: Dr. F.W.B. van Leeuwen  
Dr. R.A. Valdes Olmos

Leden

Promotie commissie: Prof. dr. H.J. Tanke  
Prof. dr. A.J.M. Balm  
Prof. dr. M.A. de Jong  
Dr. A.R. van Erkel  
Dr. H.G. van der Poel

## TABLE OF CONTENTS

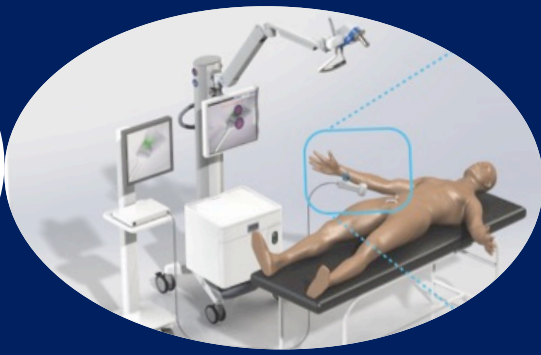
Chapter 1.	General introduction and outline of this thesis	8
<b>PART ONE: CLINICAL EVALUATION OF HYBRID SURGICAL GUIDANCE DURING SENTINEL LYMPH NODE PROCEDURES</b>		
Chapter 2.	Multimodal imaging in radioguided surgery	16
Chapter 3.	The best of both worlds: A hybrid approach for optimal pre- and intraoperative identification of sentinel lymph nodes	42
Chapter 4.	Optimisation of fluorescence guidance during robot-assisted laparoscopic sentinel node biopsy for prostate cancer	76
Chapter 5.	Multimodal hybrid imaging agents for sentinel node mapping as a means to (re)connect nuclear medicine to advances made in robot-assisted surgery	96
Chapter 6.	Fluorescence guided surgery and tracer-dose: fact or fiction?	116
<b>PART TWO: NEW SURGICAL MODALITIES</b>		
Chapter 7.	Hybrid surgical guidance: Does hardware integration of gamma- and fluorescence- imaging modalities make sense?	142
Chapter 8.	Toward (hybrid) navigation of a fluorescence camera in an open surgery setting	158
Chapter 9.	Extending the use of hand-held gamma camera technologies to generate intraoperative freehandSPECT images suitable for surgical navigation; a feasibility study in head-and-neck melanoma patients undergoing sentinel node biopsy	176
<b>PART THREE: NERVE SPARING SURGERY</b>		
Chapter 10.	A prediction model that relates intraoperative fascia preservation to erectile dysfunction in patients that underwent nerve-sparing prostatectomy	196
Chapter 11.	Diffusion-weighted-preparation (D-prep) MRI as a future extension of SPECT/CT based surgical planning for sentinel node procedures in the head and neck area?	220
Chapter 12.	Fluorescent lectins for local <i>in vivo</i> visualization of peripheral nerves	242

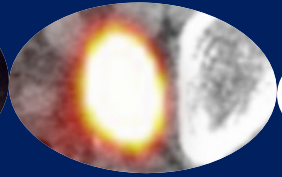
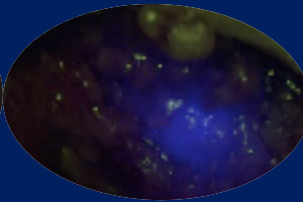
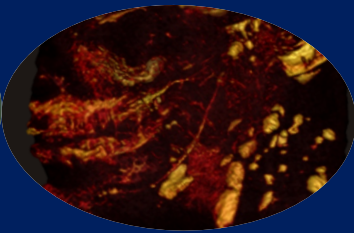
## OUTLOOK

Chapter 13.	Future perspectives	266
	Summary	268
	Samenvatting	274
	Resume	282
	Publication list	283
	Dankwoord	286



# Chapter 1





1

## General introduction and outline of this thesis

2

3

4

5

6

7

8

9

10

11

12

13

# **IMAGE GUIDED SURGERY: CLINICAL VALIDATION OF LESION IDENTIFICATION TECHNOLOGIES AND EXPLORATION OF NERVE SPARING APPROACHES**

## **GENERAL INTRODUCTION**

Surgery is considered the golden standard to treat the primary tumour and regional spread of many different cancer types. In addition to the pathological evaluation of surgical margins, the evaluation of lymph nodes is needed to stage the metastatic dissemination of the disease [1,2]. Both these aspects are critical in accomplishing radical excision and are, as such, providing true prognosis. However, the quest for complete cure should be in balance with the desire for minimally invasive surgery [3–5]. Hereby it can be assumed that surgical side effects may negatively influence the patient's quality of life.

Advanced image guided surgery technologies can be used to improve the surgical resection and to minimize the invasive nature of the procedure [6]. In this thesis both these technologies are discussed. Hereby we focussed on the locoregional assessment of the lymphatic tumour spread via sentinel lymph node procedures [7–11]. In addition technologies that support nerve-sparing surgery have been pursued. To realize these ambitious goals, a combination of imaging modalities has been used, ranging from fluorescence to nuclear imaging and hybrid combinations of the same.

## OUTLINE OF THIS THESIS

In **part one** the hybrid surgical guidance concept for sentinel lymph node (SN) resection using the hybrid tracers ICG-<sup>99m</sup>Tc-nanocolloid is discussed. In **chapter 2** the potential of hybrid tracers in radioguided surgery is discussed. The study described in **chapter 3** underlines the potential of hybrid tracers discussing the summarizing of the use of a hybrid SN tracer in 501 procedures performed in varying malignancies. Here SNs were identified based on the hybrid combination of gamma tracing and fluorescence. Hereby the fluorescence emission of the hybrid tracer allowed highly sensitive intraoperative identification of the exact same nodes as those defined using preoperative SPECT/CT. **Chapter 4** describes how technical improvements to the sensitivity and visualization-settings help increase the clinical usability of a fluorescence laparoscope during pelvic surgery. In **chapter 5** the hybrid surgical guidance procedure and laparoscopic fluorescence detection has been fully integrated in a robot-assisted setting. These two chapters indicate that both fluorescence camera optimization and integration of the technology in surgical routine help to provide added benefit.

**Chapter 6** evaluates the relation between hybrid tracer dose and the ability to obtain fluorescence guidance. This relation was studied both during open and laparoscopic procedures and in vivo and ex vivo fluorescence guidance was benchmarked against visibility on SPECT/CT.

**Part two** describes new surgical modalities that can be used during the hybrid surgical concept. Since a hybrid tracer was used to integrate pre- and intraoperative imaging findings using nuclear and fluorescence signatures, an attempt was also made to create hybrid analogues of the intraoperative hardware. In **Chapter 7** the first-in-human evaluation of physically integrating radio- and fluorescence modalities is reported on. Two hybrid detection modalities were created whereby one combined fluorescence- with gamma-imaging, while the other one combined fluorescence-imaging with acoustic gamma tracing. **Chapter 8** presents a different type of hardware integration, namely the geometrical tracking of a fluorescence camera in a SPECT-based navigation set-up for open surgery. Alternatively, in **chapter 9**, surgical navigation based on intraoperative freehandSPECT in combination with a handheld gamma camera is described. Here the intraoperative radioguidance provides a surgical roadmap for fluorescence guidance.

**Part three** of this thesis describes technologies that help advance nerve sparing surgery. In **chapter 10** the direct relation between intraoperative fascia preservation and postoperative erectile function was determined in a large cohort of prostate cancer patients. Based on the findings a nomogram was developed to predict the functional outcome after robot-assisted prostatectomy. In an attempt to visualize nerves prior to surgery the use of a magnetic resonance based imaging technique was pursued in the head and neck area (**Chapter 11**). With so-called D-Prep MRI it was possible to accurately visualize the anatomical variation in nerve distributions. At the same time, the technology assisted in the more accurate visualization of lymph nodes and their distribution. Alternatively, fluorescence imaging was used to pursue intraoperative detection of peripheral-nerves. To this end in **chapter 12**, lectin-based fluorescence tracers were evaluated for their nerve staining capacities following local administration.

In **chapter 13** a summary of both parts is provided and suggestions for future research directions have been given.

## REFERENCES

1. Kang YJ, Abalajon MJ, Jang WS, Kwon JK, Yoon CY, Lee JY, et al. Association of Anterior and Lateral Extraprostatic Extensions with Base-Positive Resection Margins in Prostate Cancer. Sung S-Y, editor. *PLoS One*. 2016;11(7):e0158922.
2. Kates M, Sopko NA, Han M, Partin AW, Epstein JI. Importance of Reporting the Gleason Score at the Positive Surgical Margin Site: Analysis of 4,082 Consecutive Radical Prostatectomy Cases. *J Urol*. 2016;195(2):337–42.
3. Micali S, Pini G, Teber D, Sighinolfi MC, De Stefani S, Bianchi G, et al. New trends in minimally invasive urological surgery. What is beyond the robot? *World J Urol*. 2013;31(3):505–13.
4. Rassweiler J, Rassweiler M-C, Koenig H, Frede T, Michel M-S, Alken P, et al. The past, present and future of minimally invasive therapy in urology: A review and speculative outlook. *Minim Invasive Ther Allied Technol*. 2013 Aug;22(4):200–9.
5. van den Berg NS, van Leeuwen FWB, van der Poel HG. Fluorescence guidance in urologic surgery. *Curr Opin Urol*. 2012;22(2):109–20.
6. Greco F, Cadeddu JA, Gill IS, Kaouk JH, Remzi M, Thompson RH, et al. Current perspectives in the use of molecular imaging to target surgical treatments for genitourinary cancers. *Eur Urol*. 2014;65(5):947–64.
7. Wit EMK, Acar C, Grivas N, Yuan C, Horenblas S, Liedberg F, et al. Sentinel Node Procedure in Prostate Cancer: A Systematic Review to Assess Diagnostic Accuracy. *Eur Urol*. 2017;71(4):596-605.
8. Leijte JAP, Kroon BK, Valdés Olmos RA, Nieweg OE, Horenblas S. Reliability and safety of current dynamic sentinel node biopsy for penile carcinoma. *Eur Urol*. 2007;52(1):170–7.
9. de Rosa N, Lyman GH, Silbermins D, Valsecchi ME, Pruitt SK, Tyler DM, et al. Sentinel node biopsy for head and neck melanoma: a systematic review. *Otolaryngol Head Neck Surg*. 2011;145(3):375–82.
10. Paleri V, Rees G, Arullendran P, Shoaib T, Krishnan S. Sentinel node biopsy in squamous cell cancer of the oral cavity and oral pharynx: a diagnostic meta-analysis. *Head Neck*. 2005;27(9):739–47.
11. Van der Zee AGJ, Oonk MH, De Hullu JA, Ansink AC, Vergote I, Verheijen RH, et al. Sentinel node dissection is safe in the treatment of early-stage vulvar cancer. *J Clin Oncol*. 2008;26(6):884–9.

# Part one

1

2

3

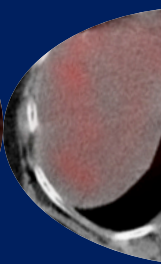
4

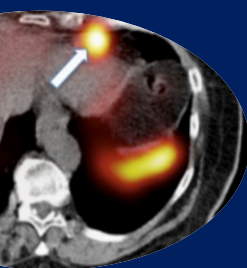
5

6

**Clinical evaluation of  
hybrid surgical guidance  
during sentinel lymph  
node procedures**

# Chapter 2





2

## Multimodal imaging in radioguided surgery

*G. H. KleinJan*

*A. Bunschoten*

*O. R. Brouwer*

*N. S. van den Berg*

*R. A. Valdés Olmos*

*F. W. B. van Leeuwen*

*Clin Transl Imaging (2013) 1:433–444*

## ABSTRACT

Radioguided surgery (RGS) utilizes radiolabeled tracers that accumulate in the lesion of interest following local or systemic administration. RGS is an expanding surgical guidance technology, but unfortunately most currently available radiotracers are unable to provide intraoperative optical information regarding the location of the lesion. In 2011, a new hybrid tracer (both radioactive and fluorescent) was introduced for sentinel lymph node detection. This hybrid tracer (indocyanine green-<sup>99m</sup>Tc-nanocolloid) has helped to generate a hybrid surgical guidance concept that builds on traditional RGS. Based on its radioactive signature a hybrid tracer is able to preserve the “traditional” role for RGS. Furthermore, as an additional tool in the operating room, a hybrid tracer provides optical information via fluorescence guidance.

This review discusses the most common RGS approaches. Different clinically used radioactive tracers and their potential hybrid derivatives are also discussed. Furthermore, the various imaging devices designed for radioactivity-based detection are reviewed in the context of generating hybrid-imaging modalities.

## INTRODUCTION

The goal of radioguided surgery (RGS) is to take advantage of local accumulation of a preoperatively injected radioactive tracer to achieve effective intraoperative localization of a lesion of interest. RGS, allows more complete resections, reducing the need for reoperations (Figure 1). Both gamma- and beta-emitting radioisotopes can be used for RGS, e.g., fluorine-18 ( $^{18}\text{F}$ ), gallium-67 ( $^{67}\text{Ga}$ ), technetium-99m ( $^{99\text{m}}\text{Tc}$ ), indium-111 ( $^{111}\text{In}$ ) and iodine-125 or iodine-131 ( $^{125}\text{I}$ ,  $^{131}\text{I}$ ) [1]. With the radiation penetrating deeply through tissue, the influence of tissue attenuation on the detection sensitivity is limited. This beneficial feature also allows the radioactive signal to be used for the acquisition of preoperative (3D) images by means of, for example, single photon emission computed tomography (SPECT) or positron emission tomography (PET). The value of SPECT or PET data further improves when these modalities are supplemented with anatomical detail provided by computed tomography (CT) or magnetic resonance imaging (MRI). To this end, SPECT/CT and PET/CT were introduced, followed more recently by PET/MRI.

The information provided by these combined modalities, depicting the radioactive target lesion(s) within the patient's body, constitutes a useful roadmap for surgeons. While the radioactive signal allows the surgeon to sensitively locate the area of interest prior to incision, during the operation itself, the limited spatial resolution of the current nuclear modalities may impair resection accuracy. It must be noted that while good spatial resolution can be obtained with SPECT in the preoperative setting (0.25 mm), this resolution cannot be obtained intraoperatively with the currently available modalities [1, 2]. Furthermore, 'signal bleeding' can make it difficult to accurately locate the origin of the radioactive signal during surgery. To compensate for these limitations, there is an increasing need, alongside RGS, for approaches that provide high-resolution (optical) information.

Optical information plays a key role in real-time assessment and surgical decision-making. For example, it allows movement of anatomical structures to be monitored by the surgeon, while dyes can be used to mark an area of interest. The surgical identification of lymph vessels and lymph nodes using vital blue dye (e.g., patent or methylene blue) during radioguided sentinel lymph node (SLN) biopsy is perhaps the best known example of the clinical application of dyes [3, 4]. The use of Cerenkov-emitting PET tracers and/or (near-infrared) fluorescent dyes [e.g., fluorescein, indocyanine green (ICG) or 5-aminolevulinic acid] can further improve the optical detection of lesions [5, 6]. Since the tissue penetration

of a fluorescent dye is dependent on the excitation and emission wavelength of the dye, an increased penetration depth can be achieved by applying near-infrared dyes; ICG, for example, allows optical detection of lesions embedded in up to 1 cm of tissue. Clearly, the tissue penetration of these optical signals remains limited in comparison to the penetration depth of the above-mentioned radioactive tracers, rendering the nuclear approach indispensable for 3D localization. Preclinical validation was recently followed by the clinical introduction of multimodal (hybrid) tracers that contain both a radioactive and a fluorescent moiety [7, 8], and the potential of these hybrid tracers to enhance conventional RGS technologies with the beneficial properties of optical guidance has already been demonstrated [9, 10]. This review discusses the most common RGS approaches.

Different clinically used radioactive tracers and their potential hybrid derivatives are also discussed. Furthermore, the various imaging devices designed for radioactivity-based detection are reviewed in the context of generating hybrid-imaging modalities.

## FIGURES

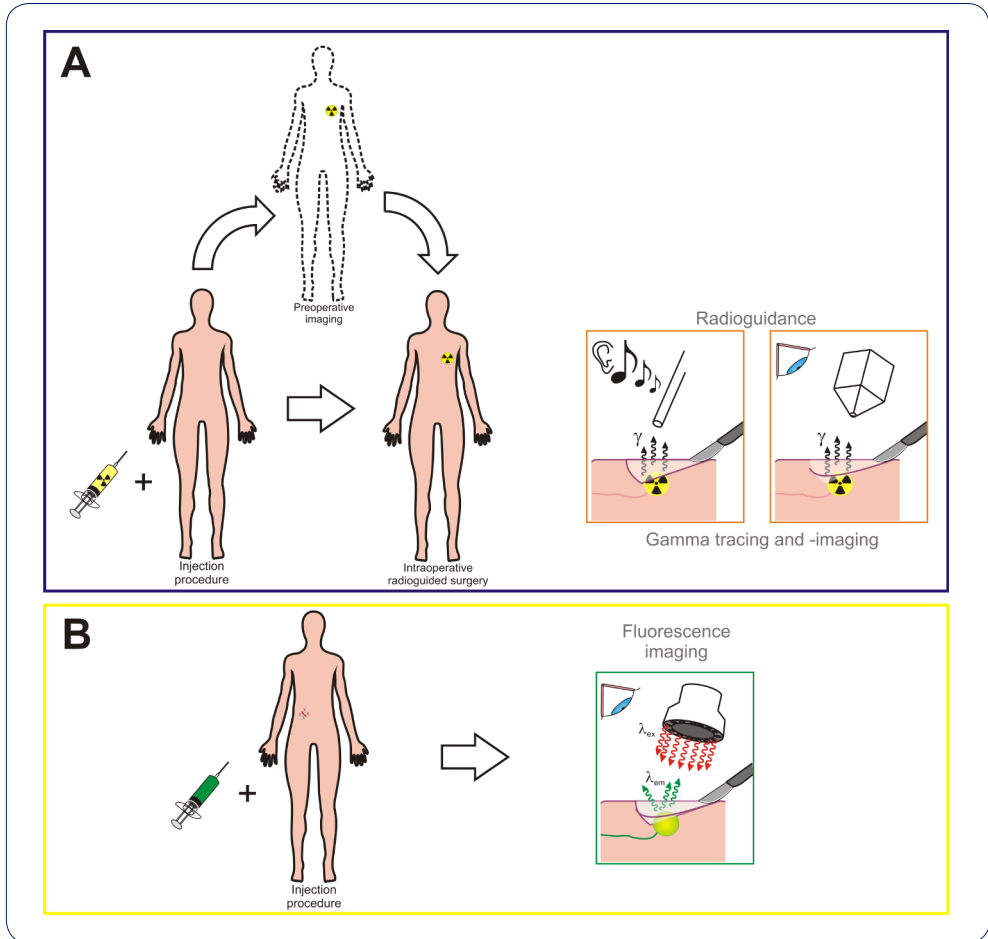


**Figure 1. Schematic** overview of the addition of optical guidance to the conventional radioguided surgery approach.

**A** Radioguided surgery approach. Following radiotracer injection, preoperative imaging can be performed to localize the lesion of interest. Intraoperatively, the lesion of interest can then be approached/ localized with a gamma/PET probe and/ or via gamma imaging using a portable gamma camera.

**B** With the injection of a fluorescent tracer, e.g., incorporated in a hybrid tracer, intraoperative fluorescence imaging allows visualization of the lesion of interest.

## RADIOGUIDED SURGERY TECHNIQUES

### RADIOGUIDED SURGERY TECHNIQUES BASED ON INTRAVENOUS RADIOTRACER ADMINISTRATION

#### **Radioguided intraoperative margin evaluation (RIME)**

In RIME, radioactivity is used to check whether the resection margins are negative. Depending on the tumor targeting capabilities of the radiolabeled tracer, accumulation in the tumor, or on its surface, can, during the operation, be detected with a gamma-ray detection probe (hereafter referred to as gamma probe). The acoustic readout of the gamma probe helps to detect the extent of the tumor, and therefore allows more complete surgical removal [11]. If any residual activity is encountered in the resection area, this tissue can then also be excised. Radio-immuno-guided surgery (RIGS) is a technique applied in tumor localization. It involves the intravenous injection of radiolabeled monoclonal antibodies, or antibody fragments, that target antigens expressed on tumor cells or in the tumor stroma. These radiotracers can be used for both diagnostic imaging and, in a similar way, in RIME, for surgical localization of tumors [12]. For example, carcinoembryonic antigen-specific monoclonal antibody (anti-CEA MoAB) can be used to locate specific tumors, e.g., rectal cancer [13].

### RADIOGUIDED SURGERY TECHNIQUES BASED ON LOCAL INJECTION OF A RADIOTRACER

#### **Sentinel lymph node biopsy**

The most commonly applied RGS procedure is SLN biopsy [1]. This approach involves local injection of a radiotracer, whose accumulation is used to detect occult lymph node (micro-) metastases at an early stage by means of selective identification, and biopsy of the lymph node(s) directly draining from the primary tumor (the SLN) [4].

The SLN approach was introduced by Morton et al. [3] and became the clinical standard for the staging of clinically lymph node-negative patients. Later, lymphoscintigraphy following a radiocolloid injection was combined with the use of optical blue dye for SLN identification [14]. Most commonly applied for breast cancer and melanoma, this technique has been found to be valuable for lymphatic staging in a variety of cancers [1].

#### **Radioguided seed localization (RSL)**

Radioguided seed localization with a radioactive  $^{125}\text{I}$ -seed has been introduced as an alternative to the wire-guided localization (WGL) technology. The  $^{125}\text{I}$ -seed is placed in the

tumor center stereotactically or under ultrasound (US) guidance. During surgery, the seed can be localized with a dual-isotope gamma probe, without interfering with, for example,  $^{99m}\text{Tc}$ -based SLN biopsy.

Radioguided seed localization is also useful in the neoadjuvant setting. Because of the long half-life of the  $^{125}\text{I}$ -seed (59 days), it can be placed prior to the start of the neoadjuvant chemotherapy while remaining traceable after completion of the chemotherapy regimen [15]. Migration of the seed is rare and high rates of radical excision have been reported both in primary surgery and after neoadjuvant chemotherapy [15, 16].

### **Radioguided occult lesion localization (ROLL)**

Radioguided occult lesion localization, similar to RSL, also provides an alternative to WGL. With this technique, injection of  $^{99m}\text{Tc}$ -labeled radiocolloid into the tumor is followed by a local excision, guided by the gamma probe. In the neoadjuvant setting, a twist marker is inserted into the tumor before the start of neoadjuvant chemotherapy. After the chemotherapy and prior to surgery, the  $^{99m}\text{Tc}$  is inserted next to the marker. High rates of radical resections have been reported with ROLL [17].  $^{99m}\text{Tc}$  has a short half life (6 h) and, for this reason, its application in the neoadjuvant setting requires, for ROLL, two interventions before surgery (i.e., insertion of the marker and injection of the radiocolloid); for RSL, on the other hand, only insertion of the  $^{125}\text{I}$  seed is required [18]. An advantage of ROLL over RSL is that ROLL can be directly combined with SLN biopsy, resulting in so-called sentinel node occult lesion localization (SNOLL) [19, 20].

### **Radioguided ultrasound-guided lymph node localization (RULL)**

In RULL, radiocolloid injection is followed by conventional preoperative SLN mapping. This is then combined with US examination of the SLNs to ascertain whether there are metastases present. The positive lymph nodes are marked and then surgically excised. RULL constitutes a possible refinement of the “traditional” SLN biopsy procedure [21].

## RADIOTRACERS

### RADIOTRACERS FOR INTRAVENOUS ADMINISTRATION

#### Antibodies

In RIGS, the overexpression of specific biomarkers on tumor cells (or in their stroma) is used to identify areas of disease. Targeting is accomplished using radiolabeled monoclonal antibodies or antibody fragments [12]. In colorectal cancer patients, targeting with anti-TAG-72 antibodies was used to detect residual tumor tissue; a poorer survival outcome was found in patients with residual hot spots residual hot spots after resection [22]. This finding suggests that the technique may help optimize radical surgery. Povoski et al. [23] recently applied RIGS in the resection of renal cell carcinoma; the imaging and detection approach used by these authors was based on  $^{124}\text{I}$ -cG250 ( $^{124}\text{I}$ -girentuximab), which targets carbonic anhydrase IX.

In addition to complete antibodies,  $^{111}\text{In}$ -labeled antibody fragments of trastuzumab have also been used in human epidermal growth factor 2-positive carcinoma of the breast [24]. Unfortunately, in a pilot study of six patients this tracer did not aid in intraoperative tumor localization; the main reason for the detection failure was believed to be the low dose of activity administered (74 MBq).

Although antibodies have a high affinity and specificity for their target antigen, a disadvantage of applying antibodies for RGS is their long circulation time. To obtain sufficient tumor to-background ratios, the unbound antibodies must be allowed to clear [13]. With antibody fragments, this unbound antibody clearance should be faster, making it possible to reduce the time elapsing between injection and surgery.

#### $^{123}\text{I}$ -iodide and $^{131}\text{I}$ -iodide

The standard therapy for thyroid cancer is complete thyroidectomy followed by  $^{131}\text{I}$ -iodide ablation therapy. The two most important radionuclides for localization of thyroid tissue are  $^{123}\text{I}$ -iodide and  $^{131}\text{I}$ -iodide. When performing a complete thyroidectomy, tracing the radioactive iodine may be used to confirm complete resection; iodine is taken up by thyroid tissue and, on the basis of the radioactive signal, can be used to locate residual thyroid tissue after resection [25]. However, a study by Tunca et al. [26] concluded that the RGS approach was not superior to conventional complete thyroidectomy (Figure 2).

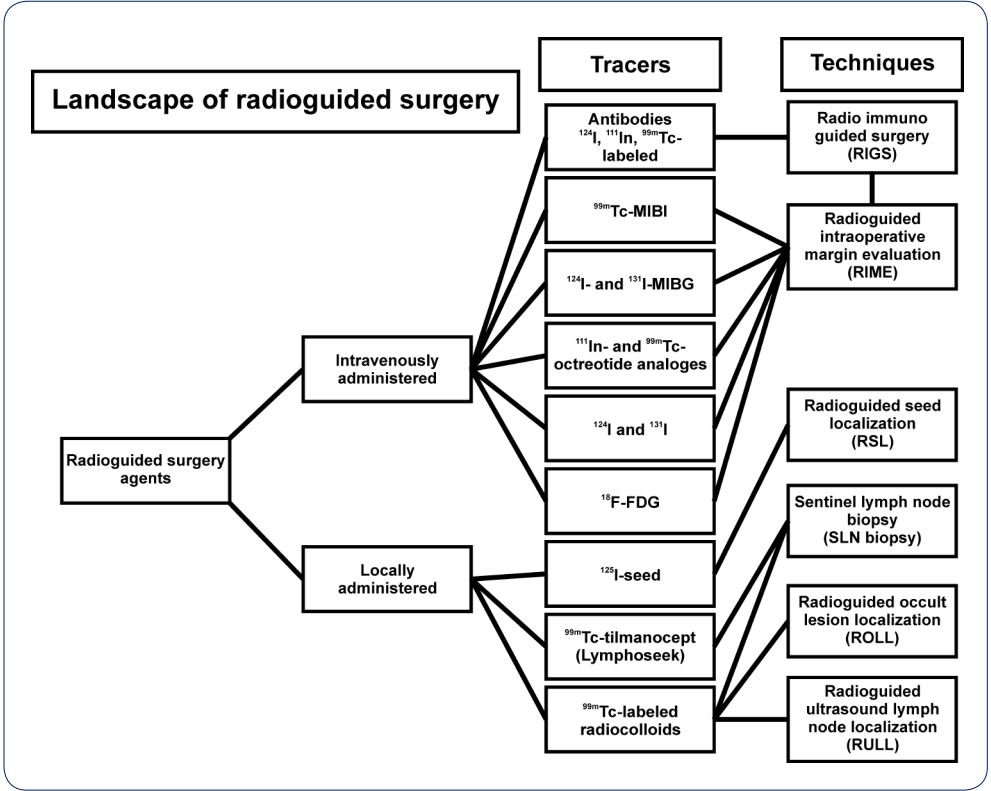


Figure 2. The landscape of radioguided surgery.

<sup>124</sup>I iodine-124, <sup>125</sup>I iodine-125, <sup>131</sup>I iodine-131, <sup>111</sup>In indium-111, <sup>99m</sup>Tc technetium-99m, <sup>18</sup>F-FDG fluorine-18-fluorodeoxyglucose, MIBG meta-iodobenzylguanidine

### **<sup>99m</sup>Tc-sestamibi (<sup>99m</sup>Tc-MIBI)**

Parathyroidectomy with bilateral lymphatic neck dissection is the standard procedure for primary hyperparathyroidism patients [27]. This procedure has very high success rates, but a single residual adenoma can lead to recurrent hyperparathyroidism. Due to its retention in mitochondria, <sup>99m</sup>Tc-MIBI can be used for preoperative parathyroid identification using scintigraphy and SPECT/CT imaging (Figure 3) [28]. During surgery, a gamma probe can then be used to localize the <sup>99m</sup>Tc-MIBI accumulated in adenomas. Similarly, <sup>99m</sup>Tc-MIBI can also be used for recurrent parathyroid adenomas [29].

<sup>99m</sup>Tc-MIBI has also been used for RGS in iodine negative recurrent differentiated and medullary thyroid cancer [30]. This agent allowed gamma probe localization and subsequent resection of thyroid tissue that had not shown uptake of <sup>123</sup>I-iodide or <sup>131</sup>I-iodide.

<sup>99m</sup>Tc-MIBI scintigraphy can also be used for the detection of breast carcinoma. Its use in a clinical study assessing the RIME technique in breast cancer patients showed a 82.6 % success rate, with a mean tumor free margin of 4.8 mm [11].

### **Meta-iodobenzylguanidine (MIBG)**

<sup>123</sup>I- and <sup>131</sup>I-MIBG (Adreview®) can be used for the detection/treatment of neuroendocrine tumors (NETs). MIBG mimics the structure of noradrenaline and, therefore, targets the noradrenaline transporter. A systematic review by van Hulsteijn et al. [31] discussed the application of MIBG for the intraoperative detection and resection of NETs. They concluded that in specific cases, like small non-palpable tumors or tumors located in adhesive scar tissue, MIBG can be useful for intraoperative detection.

However, in some instances somatostatin analogs like <sup>111</sup>In-pentetreotide may have higher sensitivity than MIBG labeled with iodine for targeting NETs [31]. <sup>111</sup>In- and <sup>99m</sup>Tc-octreotate analogs <sup>111</sup>In-diethylenetriamine penta-acetic (DTPA)-octreotide (Octreoscan®), <sup>99m</sup>Tc-depreotide (Neotect®) and <sup>111</sup>In-pentetreotide can be used for the detection of tumors overexpressing the somatostatin receptor [e.g. NETs, (non) small cell lung cancer] (Figure 4) [32–34]. The highly specific uptake of these compounds in the tumor tissue allowed radioguidance towards the tumor. For example, complete resection of ACTH-secreting bronchial carcinoids was achieved with RGS after injection of <sup>111</sup>In-pentetreotide [34]. With this tracer, even millimeter-sized tumor nodules and lymph node metastases could be resected. A big advantage of these receptor-targeted peptides is their good biodistribution and rapid unbound tracer clearance, which results in a good tumor-to-background ratio in a relatively short time (1–24h). However, their short *in vivo* half-life does impose strict timing of injection, preoperative imaging, surgical planning and the RGS procedure.

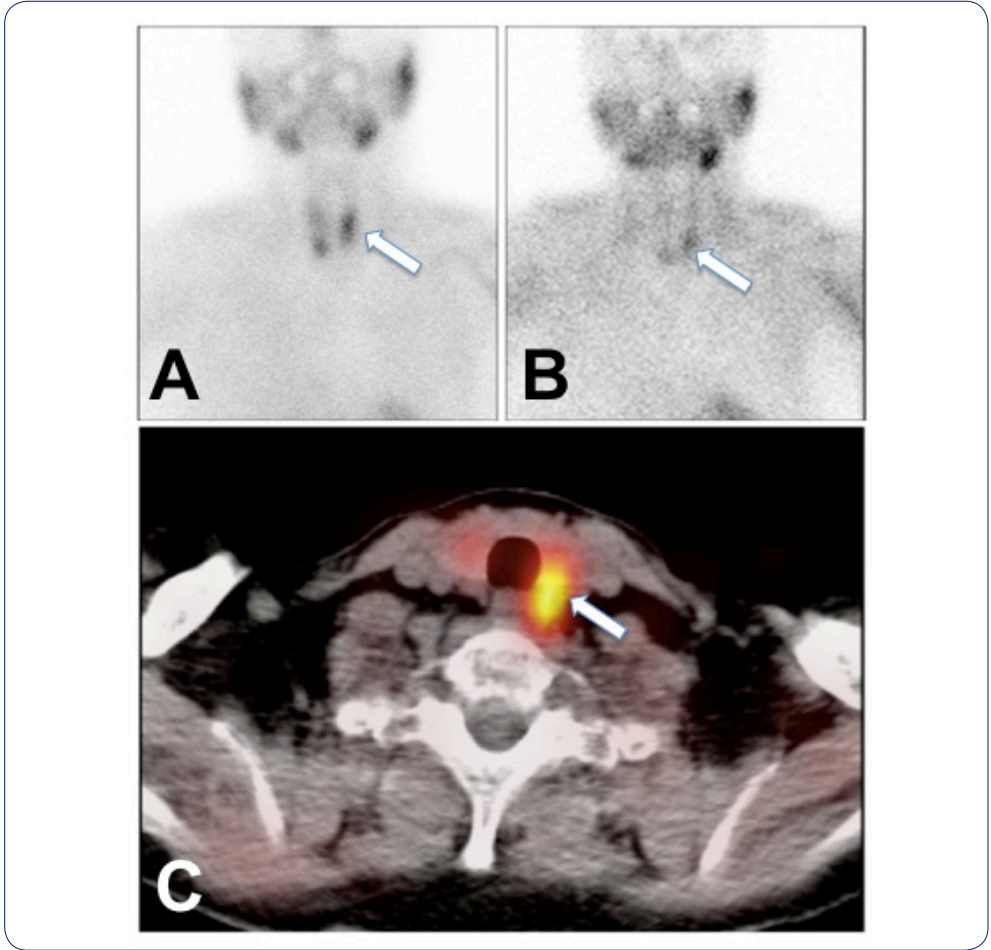


**Figure 3. <sup>99m</sup>Tc-MIBI for parathyroid adenoma localization.**

**A** <sup>99m</sup>Tc- MIBI scintigram showing heterogenous thyroid uptake on the early image with **B** retention of the tracer in the left lobe on the 3 h postinjection image. **C** SPECT/CT clarifies the abnormal uptake seen in the dorsal area of the left thyroid lobe. During radioguided surgery a parathyroid adenoma was resected

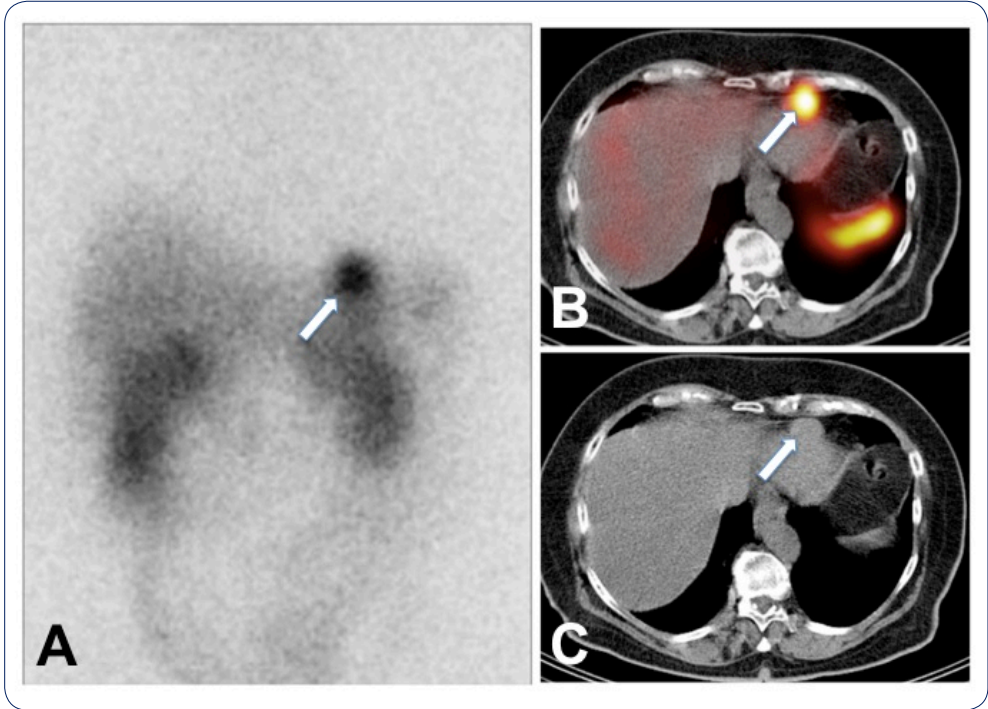


**Figure 4.**  $^{111}\text{In}$ -DTPA octreotide for carcinoid tumor localization.

**A** Following an intravenous injection of  $^{111}\text{In}$ -DTPA octreotide, accumulation in the left side of the liver was seen on the scintigram (arrow).

**B** Fused SPECT/CT and **c** CT image showing radiotracer uptake in a prehepatic lymph node.

### **<sup>18</sup>F-FDG**

Generally, malignant tumors have an accelerated glucose metabolism, which results in higher uptake of the PET tracer <sup>18</sup>F-FDG. Due to the high signal-to-background ratios obtained, <sup>18</sup>F-FDG is considered valuable for imaging tumor diffusion throughout the body in a variety of malignancies [35]. The ability to detect different types of malignancies makes this tracer a possible generic tracer for RGS-based tumor resection [36].

## **RADIOTRACERS FOR LOCAL ADMINISTRATION**

### **Radiocolloids**

The most frequently used radiotracers for RGS, especially for SLN biopsy, are <sup>99m</sup>Tc-sulfur colloid, <sup>99m</sup>Tc-colloidal human albumin (<sup>99m</sup>Tc-nanocolloid), <sup>99m</sup>Tc antimony trisulfide colloid, and <sup>99m</sup>Tc-tin colloid [1, 37]. <sup>99m</sup>Tc-labeled radio colloids have been applied mainly in SLN biopsy and ROLL/SNOLL procedures [4, 17]. Particle sizes and the amount/volume of radiocolloid injected influence the lymphatic flow and the overflow of these tracers into higher echelon nodes; accumulation of all these SLN tracers is based on uptake in the macrophages [38]. Recently, a PET derivative was introduced in the form of 89-zirconium (<sup>89</sup>Zr)-labeled nanocolloid [39].

### **Tilmanocept (Lymphoseek®)**

<sup>99m</sup>Tc-tilmanocept was introduced as an alternative to the above-mentioned radiocolloids [40, 41]. <sup>99m</sup>Tc-tilmanocept is smaller than most radiocolloids (mean molecular diameter of 7 vs. 10–600 nm); it is based on a dextran backbone substituted with multiple mannose subunits and chelates to allow radiolabeling with <sup>99m</sup>Tc [42]. It has been suggested that <sup>99m</sup>Tc-tilmanocept accumulates in the SLNs by binding to mannose receptors on reticulo-endocytes [43].

## INTRODUCTION OF (FLUORESCENT) DYE GUIDANCE TO EXTEND RADIOGUIDED SURGERY

Radioguided surgery is an excellent technique for the preoperative localization of a lesion of interest. However, as mentioned above, in the intraoperative setting the limited spatial resolution of this modality is suboptimal for precise (last millimeter) localization. For this part of the resection, an additional tool based on real-time and high-resolution imaging (e.g., fluorescence) can be of great benefit.

Blue dye is commonly used to visualize the lymph vessels and the SLN during the surgical procedure. Motomura et al. [44] were the first to describe the use of the near infrared dye ICG for SLN biopsy in breast cancer; ICG was used in a manner similar to blue dye. Thereafter, many different research groups adapted this fluorescence-based approach with ICG for SLN biopsy in different types of cancer, e.g., in melanoma and breast cancer [45, 46]. Fluorescent dyes have a higher tissue penetration compared to conventional blue dye, but unfortunately, the tissue penetration remains limited to approximately 1 cm [46]. This limitation can be overcome by combining ICG with the high tissue penetration of radioactive agents [9, 47, 48].

### Hybrid-imaging agents

In 2011, we introduced the clinical application of a hybrid radiolabeled colloid (ICG non-covalently bound to  $^{99m}\text{Tc}$ -nanocolloid) in prostate cancer patients [49]. With a single injection of this hybrid tracer, we were able to visualize the SLNs both preoperatively, using lymphoscintigraphy and SPECT/CT, and intraoperatively via fluorescence imaging (Figure 5). The same hybrid tracer has now been used for SLN biopsy in various types of malignancies, e.g., melanoma and penile cancer [10, 47, 50]. This success should encourage further extension of the hybrid approach to surgical areas where there is room for improvement of the RGS technique.

To provide a hybrid derivative for the detection of parathyroid disease, methylene blue has been iodinated with  $^{123}\text{I}$  [51]. However, in a clinical study, this tracer was not found to be effective enough to replace the standard tracer  $^{99m}\text{Tc}$ -MIBI [52]. Methylene blue labeled with  $^{125}\text{I}$  has instead been evaluated for SLN biopsy in a clinical trial in breast cancer [10]. The solution of  $^{125}\text{I}$ -methylene blue are injected locally in or around the tumor, after which it was transported by the lymphatic system to the SLN. With a hand-held gamma camera, the gamma rays were detected and the blue signature of methylene blue was used to optically identify the SLN. Rapid lymphatic drainage of the hybrid tracer is a possible downside of this approach.

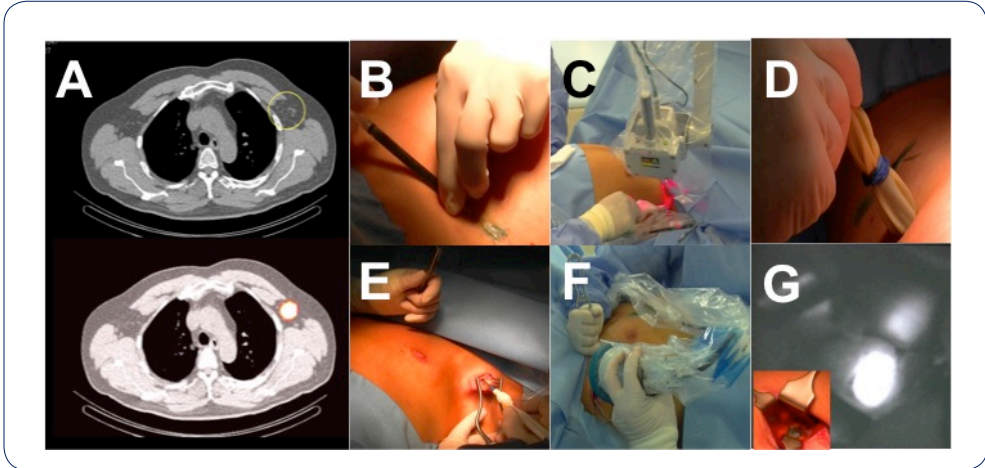


**Figure 5. Multimodal surgical guidance towards the sentinel lymph node.**

- A** Following ICG- $^{99m}\text{Tc}$ -nanocolloid injection, preoperative lymphoscintigraphy and SPECT/CT imaging are performed to locate the SLN (circle).
- B** Prior to the start of the operation patent blue dye is injected.
- C** Prior to incision, an image with gamma camera is obtained to confirm the localization of the SLN.
- D** Pre-incision gamma tracing with the gamma probe allows localization of the SLN.
- E** Incision.
- F** Camera used to detect the fluorescent signal in the SLN. **G** Fluorescence signal detected in the SLN. SLN sentinel lymph node.

In the preclinical setting, a great number of hybrid alternatives to existing RGS tracers are currently being developed and evaluated (Table 1). For example,  $^{99m}\text{Tc}$ -tilmanocept has been covalently labeled with Cy7 for fluorescence imaging. In a mouse model it was shown that the popliteal SLN could be visualized with fluorescence imaging following a footpad injection with Cy7- $^{99m}\text{Tc}$ -tilmanocept [53]. Multimodal marker seeds have been shown to allow hybrid RSL towards a mouse prostate [54]. Here, the  $^{99m}\text{Tc}$  signature allowed preoperative SPECT imaging, whereas intraoperative fluorescence detection provided optical information about the exact location of the seed [54].

### Targeted hybrid-imaging agents

Research efforts are currently focusing on the development of targeted hybrid tracers allowing accurate tumor identification. Despite these efforts, which have been reviewed by Kuil et al. [8] and Azhdarinia et al. [55], to date no such tracers have been clinically implemented. Hybrid-labeled derivatives of the clinically applied octreotide have been extensively evaluated

preclinically, yielding fluorescent and radioactively labeled imaging agents with high affinity for the somatostatin receptor [8, 56]. Alongside these hybrid counterparts of clinically used peptide-based tracers, several other interesting hybrid tracers are being developed, based, for example, on tumor targeting peptides targeting the chemokine receptor 4 and the gastric releasing peptide receptor [8]. A hybrid tracer targeting the prostate-specific membrane antigen (PSMA), which is frequently overexpressed in prostate cancer, was recently developed by Banerjee et al. [57] by combining the near-infrared dye CW800 and  $^{111}\text{In}$ -1,4,7,10-tetraazacyclododecane-1,4,7,10-tetracarboxylic acid (DOTA) with a PSMA-inhibitor.

Multiple hybrid tracers have been generated for avb3- integrin, which is overexpressed by activated endothelial cells during angiogenesis. These hybrid tracers contain a Cy5- or Cy7-derivative as fluorescent dye and a DTPA, deferoxamine or DOTA chelate to introduce  $^{111}\text{In}$ ,  $^{64}\text{Cu}$  or  $^{68}\text{Ga}$ , respectively [8]. Liu et al. [58] recently introduced a tracer that combines the fluorescent dye BODIPY, containing  $^{18}\text{F}$ , with the cyclic arginine–glycine–aspartate (RGD) peptide targeting the avb3-integrin for combined PET and optical imaging.

In addition, various hybrid-labeled antibodies have been tested in mouse models [59–62].  $^{64}\text{Cu}$ -1,4,7-triazacyclononane-1,4,7-triacetic acid (NOTA)-bevacizumab-800CW was applied to detect human glioblastoma tumors by both nuclear and optical imaging [63]. The anti-CD105 antibody TRC105 was labeled with  $^{64}\text{Cu}$  or  $^{89}\text{Zr}$  for PET imaging and 800CW for intraoperative optical fluorescence-based detection in a mouse model of breast cancer-derived lung metastases [64]. Recently, Cohen et al. [65] described a protocol for the labeling of monoclonal antibodies with 800CW and  $^{89}\text{Zr}$  for hybrid imaging. Although not yet used for clinical studies these antibody-based hybrid tracers seem promising for future applications.

## **MODALITIES USED DURING HYBRID-RADIOGUIDED SURGERY**

Different modalities can be used for the intraoperative localization of the preoperatively injected radiotracers. Devices to locate both gamma- and positron-emitting radioisotopes, as well as devices that can excite fluorescent dyes and collect their emission light, are discussed below. Ideally, the introduction of a hybrid approach also drives the development of hybrid-imaging devices.

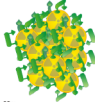
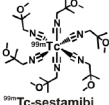
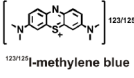
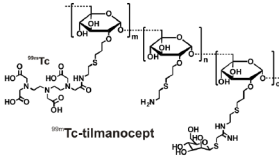
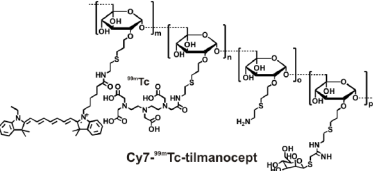
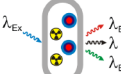
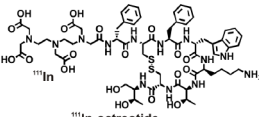
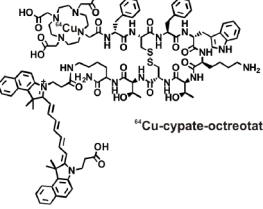
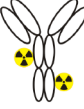
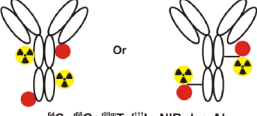
Radiotracers for RGS	Hybrid tracers for combined RGS / Fluorescence guided surgery	Hybrid tracers in clinical use	Ref
 <p><sup>99m</sup>Tc-nanocolloid</p>	 <p><sup>99m</sup>Tc-nanocolloid</p>	Yes	49
 <p><sup>99m</sup>Tc-sestamibi</p>	 <p>[<sup>123I/125I</sup>] <sup>123I/125I</sup>-methylene blue</p>	Yes	10, 51
 <p><sup>99m</sup>Tc-tilmanocept</p>	 <p>Cy7-<sup>99m</sup>Tc-tilmanocept</p>	No (Preclinical)	53
 <p><sup>125I</sup> marker seed</p>	 <p>Hybrid marker seed</p>	No (Preclinical)	54
 <p><sup>111</sup>In-octreotide</p>	 <p><sup>64</sup>Cu-cypate-octreotate</p>	No (Preclinical)	56
 <p><sup>64</sup>Cu/<sup>67</sup>Ga/<sup>99m</sup>Tc/<sup>111</sup>In-Ab</p>	 <p>Or <sup>64</sup>Cu/<sup>67</sup>Ga/<sup>99m</sup>Tc/<sup>111</sup>In-NIR-dye-Ab</p>	No (Preclinical)	59-62
 <p><sup>123I</sup>-MIBG</p>	Not available	Not applicable	-
 <p><sup>18</sup>F-FDG</p>	Not available	Not applicable	-

Table 1. Currently used radiotracers and preclinically and clinically used hybrid-imaging agents

### **PET detection probes**

Positron emission tomography detection probes are capable of detecting the 511-KeV gamma rays that are emitted by the annihilation of a positron–electron pair. Unfortunately, the collimators and shielding used for detection make these probes less convenient during surgery; 511-keV gamma rays are highly penetrating [36, 66, 67]. Another PET tracer-detection method is direct detection of the  $\beta$ -particles (positrons). These particles have limited soft tissue penetration (max. 2.4 mm) [68]. As a result, direct positron detection is easily hindered by overlying/ surrounding tissue, similarly to what happens with the use of fluorescent dyes [6]. On the other hand, this property may provide increased resolution, making it possible to distinguish between tumor tissue and healthy tissue [66].

Cerenkov luminescence emitted by  $\beta$ -emitters can also potentially be used for intraoperative optical detection and might be an alternative to hybrid agents with a fluorescent dye [69]. That said, Chin et al. [6] concluded that with the current imaging modalities, the fluorescent signature of a hybrid tracer is superior to Cerenkov luminescence.

### **Gamma probes**

Gamma probes can be used to locate different isotopes with low, medium and high energies. The technical features and capabilities of common gamma probes have been reviewed by Zanzonico and Heller [66, 70]. In these reviews they also discuss the capabilities of the gamma probes.

With gamma probes, it is sometimes difficult to locate areas of interest near the injection site, because the signal can be masked by background ‘signal bleeding’ [71]. As hybrid radioactive and fluorescent imaging agents emerge, a possible future development would be a gamma probe that is also capable of (acoustic) fluorescence detection.

Hybrid-imaging devices can be obtained either by modifying existing RGS devices or fluorescence cameras or by developing new imaging devices. Although it is not yet available for fluorescence imaging, there does exist a system that allows acoustic gamma tracing and acoustic blue dye tracing (Euro-rad, Strasbourg, France). A gamma probe that can also detect fluorescence could be used to determine margins intraoperatively, overcoming the limited tissue penetration of near-infrared dyes.

### **Gamma cameras**

While a gamma probe provides an acoustic signal when it detects gamma rays, a gamma camera allows the generation of 2D visual images of the location of the radioactive signal [36]. Compared to gamma probes, mobile gamma cameras show improved imaging

resolution [66]. Several hand-held and mobile gamma cameras are described in a review by Tsuchimochi and Hayama [36]. The main advantage of a mobile gamma camera is that it allows reproduction, in the operating room, of preoperatively acquired images. Moreover, by generating pre-incision and post-excision images, a comparison can be made to determine whether there is any residual activity at the excision site, which should also be removed.

A disadvantage of gamma cameras is the delay in visualization of hot spots, which results in long acquisition times in the presence of a weak radioactive signal in the lesion of interest. Moreover, since the current systems do not provide 'white light' options to visualize the surgical field, there is a lack of anatomical information of the area of interest. Furthermore, the current gamma camera systems do not usually provide depth information.

A promising development for gamma cameras may therefore be their integration with optical cameras to provide visualization of radioactive hot spots within the corresponding anatomical context. Blake et al. [72] published data relating to the application of a prototype mini-gamma camera integrated with an optical camera: the first results in patients injected with  $^{99m}\text{Tc}$ -hydroxymethylene diphosphate for a standard bone scan showed accumulation of the activity in the thumb.

A next step may be the integration of fluorescence cameras. In combination with the right hybrid tracer, devices of this kind would be capable of hybrid surgical guidance using a single modality.

### **Intraoperative navigation devices**

The simplest example of navigation uses a mobile gamma camera that allows dual-isotope detection, as shown by Vermeeren et al. [73] during laparoscopic SLN biopsy in prostate cancer. After a  $^{125}\text{I}$ -seed had been attached to the tip of a laparoscopic gamma probe, its location could be detected on screen together with the signal coming from  $^{99m}\text{Tc}$  in the SLN. By moving the gamma probe towards the SLN, the signal from the  $^{125}\text{I}$ -seed could be followed on the gamma probe, providing on-screen 2D navigation to the SLN [74].

The introduction of freehand SPECT technology has made it possible for surgeons to intraoperatively acquire a SPECT scan of a region of interest. By tracking both the gamma probe and a positioning system fixed on the patient's body, this technique allows intraoperative 3D mixed reality-based navigation of the gamma probe to the lesion of interest, e.g., during SLN biopsy for breast cancer [75]. As well as allowing real-time acquisition of SPECT scans in the operating room, the system can also load preoperatively acquired SPECT/CT data. It has been shown that this approach can also be used to navigate tools other than the gamma probe, e.g., a fluorescence laparoscope, towards radioactive hotspots [76]. Fluorescence

imaging allows errors within the 1-cm range (due to organ movement or deformation for example) to be compensated for [76].

With the exception of a navigation system that uses virtual reality to visualize the radioactive hot spots in the anatomical context, the current RGS techniques do not provide anatomical information [77]. An additional tool that combines the beneficial properties of both modalities would be of great value in this field of surgery.

## **CONCLUSION**

The applications of RGS are continuously expanding as new receptor-targeted imaging agents and intraoperative tools emerge. Since radio- and fluorescence-based surgical guidance modalities each have their own beneficial properties, the development of hybrid approaches, which combine advantageous features of both techniques, holds great promise for the further refinement of RGS.

## REFERENCES

1. Pivoski SP, Neff RL, Mojzisek CM, O'Malley DM, Hinkle GH, Hall NC, Murrey D, Knopp MV, Martin EW (2009) A comprehensive overview of radioguided surgery using gamma detection probe technology. *World J Surg Oncol* 7:11
2. Goorden MC, Van der Have F, Kreuger R, Ramakers RM, Vastenhout B, Burbach JPH, Booij J, Molthoff CFM, Beekman FJ (2013) VECTor: a preclinical imaging system for simultaneous submillimeter SPECT and PET. *J Nucl Med* 54:306–312
3. Morton DL, Wen DR, Wong JH, Economou JS, Cagle LA, Storm FK, Foshag LJ, Cochran AJ (1992) Technical details of intraoperative lymphatic mapping for early stage melanoma. *Arch Surg* 127:392–399
4. Nieweg OE, Tanis PJ, Kroon BB (2001) The definition of a sentinel node. *Ann Surg Oncol* 8:538–541
5. Van den Berg NS, Van Leeuwen FWB, Van der Poel HG (2012) Fluorescence guidance in urologic surgery. *Curr Opin Urol* 22:109–120
6. Chin PTK, Welling MM, Meskers SCJ, Valdes Olmos RA, Tanke H, Van Leeuwen FWB (2013) Optical imaging as an expansion of nuclear medicine: Cerenkov-based luminescence vs. fluorescence-based luminescence. *Eur J Nucl Med Mol Imaging* 40:1283–1291
7. Buckle T, Van Leeuwen AC, Chin PTK, Janssen H, Muller SH, Jonkers J, Van Leeuwen FWB (2010) A self-assembled multimodal complex for combined pre- and intraoperative imaging of the sentinel lymph node. *Nanotechnology* 3(21):355101
8. Kuil J, Velders AH, Van Leeuwen FWB (2010) Multimodal tumor-targeting peptides functionalized with both a radio- and a fluorescent label. *Bioconjug Chem* 21:1709–1719
9. Brouwer OR, Buckle T, Vermeeren L, Klop WMC, Balm AJM, Van der Poel HG, Van Rhijn BW, Horenblas S, Nieweg OE, Van Leeuwen FWB, Valde's Olmos RA (2012) Comparing the hybrid fluorescent-radioactive tracer indocyanine green-99mTc-nanocolloid with 99mTc-nanocolloid for sentinel node identification: a validation study using lymphoscintigraphy and SPECT/CT. *J Nucl Med* 53:1034–1040
10. Harkrider WW, Diebold AE, Maloney T, Espenan G, Wang YZ, Stafford SJ, Camp A, Frey D, Chappuis C, Woltering EA (2013) An extended phase II trial of iodine-125 methylene blue for sentinel lymph node identification in women with breast cancer. *J Am Coll Surg* 216:599–605 (discussion 605–606)
11. Duarte GM, Cabello C, Torresan RZ, Alvarenga M, Telles GHC, Bianchessi ST, Caserta N, Segala SR, de Lima MCL, Etchebehere ECSC, Camargo EE (2007) Radioguided intraoperative margins evaluation (RIME): preliminary results of a new technique to aid breast cancer resection. *Eur J Surg Oncol* 33:1150–1157
12. Mery CM, Shafi BM, Binyamin G (2006) Molecular imaging and radioimmunoguided surgery. *Semin Pediatr Surg* 15:259–266
13. Arnold M, Schneebaum S, Martin E (1996) Radioimmunoguided surgery in the treatment and evaluation of rectal cancer patients. *Cancer Control* 3:42–45
14. Uren RF, Howman-Giles RB, Shaw HM, Thompson JF, McCarthy WH (1993) Lymphoscintigraphy in high-risk melanoma of the trunk: predicting draining node groups, defining lymphatic channels and locating the sentinel node. *J Nucl Med* 34:1435–1440
15. Van Riet YEA, Maaskant AJG, Creemers GJ, van Warmerdam LJC, Jansen FH, van de Velde CJH, Rutten HJT, Nieuwenhuijzen GAP (2010) Identification of residual breast tumour localization after neo-adjuvant chemotherapy using a radioactive 125 iodine seed. *Eur J Surg Oncol* 36:164–169
16. Alderliesten T, Loo CE, Pengel KE, Rutgers EJT, Gilhuijs KGA, Vrancken Peeters MJ (2011) Radioactive seed localization of breast lesions: an adequate localization method without seed migration. *Breast J* 17:594–601
17. Donker M, Straver ME, Rutgers EJTh, Valde's Olmos RA, Loo CE, Sonke GS, Wesseling J, Vrancken Peeters MJ (2012) Radioguided occult lesion localisation (ROLL) in breast-conserving surgery after neoadjuvant chemotherapy. *Eur J Surg Oncol* 38:1218–1224
18. Donker M, Drukker CA, Valde's Olmos RA, Rutgers EJTh, Loo CE, Sonke GS, Wesseling J, Alderliesten T, Vrancken Peeters MJ (2013) Guiding breast-conserving surgery in patients after neoadjuvant systemic therapy for breast cancer: a comparison of radioactive seed localization with the ROLL technique. *Ann Surg Oncol* 20:2569–2575
19. Thind CR, Tan S, Desmond S, Harris O, Ramesh HSJ, Chagla L, Ray A, Audisio R (2011) SNOLL: sentinel node and occult (impalpable) lesion localization in breast cancer. *Clin Radiol* 66:833–839
20. Ahmed M, Douek M (2013) ROLL versus RSL: toss of a coin? *Breast Cancer Res Treat* 140:213–217

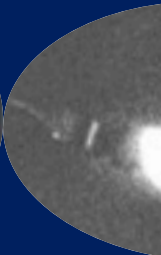
21. Roach M III, Alberini JL, Pecking AP, Testori A, Verrecchia F, Soteldo J, Ganswindt U, Joyal JL, Babich JW, Witte RS, Unger E, Gottlieb R (2011) Diagnostic and therapeutic imaging for cancer: therapeutic considerations and future directions. *J Surg Oncol* 103:587–601
22. Sun D, Bloomston M, Hinkle G, Al-Saif OH, Hall NC, Povoski SP, Arnold MW, Martin EW Jr (2007) Radioimmunoguided surgery (RIGS), PET/CT image-guided surgery, and fluorescence image-guided surgery: past, present, and future. *J Surg Oncol* 15(96):297–308
23. Povoski SP, Hall NC, Murrey DA Jr, Sharp DS, Hitchcock CL, Mojzisk CM, Bahnson EE, Knopp MV, Martin EW Jr, Bahnson RR (2013) Multimodal imaging and detection strategy with 124I-labeled chimeric monoclonal antibody cG250 for accurate localization and confirmation of extent of disease during laparoscopic and open surgical resection of clear cell renal cell carcinoma. *Surg Innov* 20:59–69
24. Scollard DA, Chan C, Holloway CM, Reilly RM (2011) A kit to prepare 111In-DTPA-trastuzumab (Herceptin) Fab fragments injection under GMP conditions for imaging or radioimmunoguided surgery of HER2-positive breast cancer. *Nucl Med Biol* 38:129–136
25. Francis CL, Nalley C, Fan C, Bodenner D, Stack BC Jr (2012) 18F-fluorodeoxyglucose and 131I radioguided surgical management of thyroid cancer. *Otolaryngol Head Neck Surg* 146:26–32
26. Tunca F, Giles Y, Terzioglu T, Mudun A, Adalet I, Salmasioglu A, Tezelman S (2008) Does intraoperative radioguided surgery influence the complication rates and completeness of completion thyroidectomy? *Am J Surg* 196:40–46
27. Ikeda Y, Takayama J, Takami H (2010) Minimally invasive radioguided parathyroidectomy for hyperparathyroidism. *Ann Nucl Med* 24:233–240
28. Hetrakul N, Civelek AC, Stagg CA, Udelsman R (2001) In vitro accumulation of technetium-99m-sestamibi in human parathyroid mitochondria. *Surgery* 130:1011–1018
29. Norman JG, Jaffray CE, Chheda H (2000) The false-positive parathyroid sestamibi: a real or perceived problem and a case for radioguided parathyroidectomy. *Ann Surg* 231:31–37
30. Negele T, Meisetschläger G, Brückner T, Scheidhauer K, Schwaiger M, Vogelsang H (2006) Radio-guided surgery for persistent differentiated papillary thyroid cancer: case presentations and review of the literature. *Langenbecks Arch Surg* 391:178–186
31. van Hulsteijn LT, Corssmit EP, van der Hiel B, Smit JW, Stokkel MP (2012) Is there a role for radioguided surgery with iodine-labeled metaiodobenzylguanidine in resection of neuroendocrine tumors? *Clin Nucl Med* 37:1083–1088
32. Wang YZ, Diebold A, Woltering E, King H, Boudreaux JP, Anthony LB, Campeau R (2011) Radioguided exploration facilitates surgical cytoreduction of neuroendocrine tumors. *J Gastrointest Surg* 16:635–640
33. Keskin O, Yalcin S (2013) A review of the use of somatostatin analogs in oncology. *Oncol Targets Ther* 6:471–483
34. Porziella V, Cesario A, Lococo F, Cafarotti S, Margaritora S, D'Errico G, Granone P (2011) The radioguided 111In-pentetreotide surgery in the management of ACTH-secreting bronchial carcinoid. *Eur Rev Med Pharmacol Sci* 15:587–591
35. Pinilla I, Rodríguez-Vigil B, Gómez-León N (2008) Integrated FDG PET/CT: utility and applications in clinical oncology. *Clin Med Oncol* 2:181–198
36. Tsuchimochi M, Hayama K (2013) Intraoperative gamma cameras for radioguided surgery: technical characteristics, performance parameters, and clinical applications. *Phys Med* 29:126–138
37. Wilhelm AJ, Mijnhout GS, Franssen EJ (1999) Radiopharmaceuticals in sentinel lymph-node detection—an overview. *Eur J Nucl Med* 26(4 Suppl):S36–S42
38. Uren RF, Howman-Giles R, Thompson JF (2003) Patterns of lymphatic drainage from the skin in patients with melanoma. *J Nucl Med* 44:570–582
39. Heuveling DA, van Schie A, Vugts DJ, Hendrikse NH, Yaqub M, Hoekstra OS, Karagozoglu KH, Leemans CR, van Dongen GA, de Bree R (2013) Pilot study on the feasibility of PET/CT lymphoscintigraphy with 89Zr-nanocolloidal albumin for sentinel node identification in oral cancer patients. *J Nucl Med* 54:585–589
40. Wallace AM, Han LK, Povoski SP, Deck K, Schneebaum S, Hall NC, Hoh CK, Limmer KK, Krontiras H, Frazier TG, Cox C, Avisar E, Faries M, King DW, Christman L, Vera DR (2013) Comparative evaluation of [99mTc]-tilmanocept for sentinel lymph node mapping in breast cancer patients: results of two phase 3 trials. *Ann Surg Oncol* 20:2590–2599
41. Sondak VK, King DW, Zager JS, Schneebaum S, Kim J, Leong SP, Faries MB, Averbook BJ, Martinez SR, Puleo CA, Messina JL, Christman L, Wallace AM (2013) Combined analysis of phase III trials evaluating [99mTc]-tilmanocept and vital blue dye for identification of sentinel lymph nodes in clinically nodeneegative cutaneous melanoma. *Ann Surg Oncol* 20:680–688

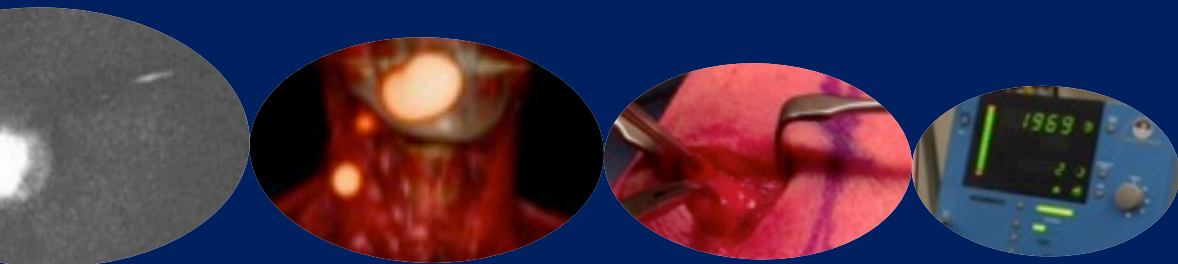
42. Vera DR, Wallace AM, Hoh CK, Mattrey RF (2001) A synthetic macromolecule for sentinel node detection: 99mTc-DTPA-mannosyl-dextran. *J Nucl Med* 42:951–959
43. Tokin CA, Cope FO, Metz WL, Blue MS, Potter BM, Abbruzzese BC, Hartman RD, Joy MT, King DW, Christman LA, Vera DR, Wallace AM (2012) The efficacy of Tlmanocept in sentinel lymph node mapping and identification in breast cancer patients: a comparative review and meta-analysis of the 99mTc-labeled nanocolloid human serum albumin standard of care. *Clin Exp Metastasis* 29:681–686
44. Motomura K, Inaji H, Komoike Y, Kasugai T, Noguchi S, Koyama H (1999) Sentinel node biopsy guided by indocyanine green dye in breast cancer patients. *Jpn J Clin Oncol* 29:604–607
45. Schaafsma BE, Mieog JS, Hutteman M, van der Vorst JR, Kuppen PJ, Lo'wik CW, Frangioni JV, van de Velde CJ, Vahrmeijer AL (2011) The clinical use of indocyanine green as a near infrared fluorescent contrast agent for image-guided oncologic surgery. *J Surg Oncol* 104:323–332
46. Polom K, Murawa D, Rho YS, Nowaczyk P, Hunerbein M, Murawa P (2011) Current trends and emerging future of indocyanine green usage in surgery and oncology: a literature review. *Cancer* 117:4812–4822
47. Brouwer OR, Klop WMC, Buckle T, Vermeeren L, van den Brekel MWM, Balm AJM, Nieweg OE, Valdés Olmos RA, van Leeuwen FWB (2012) Feasibility of sentinel node biopsy in head and neck melanoma using a hybrid radioactive and fluorescent tracer. *Ann Surg Oncol* 19:1988–1994
48. van den Berg NS, Brouwer OR, Klop WM, Karakullukcu B, Zuur CL, Tan IB, Balm AJ, van den Brekel MW, Valde's Olmos RA, van Leeuwen FW (2012) Concomitant radio- and fluorescence guided sentinel lymph node biopsy in squamous cell carcinoma of the oral cavity using ICG-99mTc-nanocolloid. *Eur J Nucl Med Mol Imaging* 39:1128–1136
49. van der Poel HG, Buckle T, Brouwer OR, Valdés Olmos RA, van Leeuwen FW (2011) Intraoperative laparoscopic fluorescence guidance to the sentinel lymph node in prostate cancer patients: clinical proof of concept of an integrated functional imaging approach using a multimodal tracer. *Eur Urol* 60:826–833
50. Schaafsma BE, Verbeek FP, Rietbergen DD, van der Hiel B, van der Vorst JR, Liefers GJ, Frangioni JV, van de Velde CJ, van Leeuwen FW, Vahrmeijer AL (2013) Clinical trial of combined radio- and fluorescence-guided sentinel lymph node biopsy in breast cancer. *Br J Surg* 100:1037–1044
51. Blower PJ, Carter NJ (1990) Rapid preparation of 123I-labelled methylene blue and toluidine blue: potential new agents for parathyroid scintigraphy. *Nucl Med Commun* 11:413–420
52. Blower PJ, Kettle AG, O'Doherty MJ, Collins RE, Coakley AJ (1992) 123I-methylene blue: an unsatisfactory parathyroid imaging agent. *Nucl Med Commun* 13:522–527
53. Emerson DK, Limmer KK, Hall DJ, Han SH, Eckelman WC, Kane CJ, Wallace AM, Vera DR (2012) A receptor-targeted fluorescent radiopharmaceutical for multipore sentinel lymph node imaging. *Radiology* 265:186–193
54. Buckle T, Chin PT, van den Berg NS, Loo CE, Koops W, Gilhuijs KG, van Leeuwen FWB (2010) Tumor bracketing and safety margin estimation using multimodal marker seeds: a proof of concept. *J Biomed Opt* 15:056021
55. Azhdarinia A, Ghosh P, Ghosh S, Wilganowski N, Sevick-Muraca EM (2012) Dual-labeling strategies for nuclear and fluorescence molecular imaging: a review and analysis. *Mol Imaging Biol* 14:261–276
56. Edwards WB, Xu B, Akers W, Cheney PP, Liang K, Rogers BE, Anderson CJ, Achilefu S (2008) Agonist-antagonist dilemma in molecular imaging: evaluation of a monomolecular multimodal imaging agent for the somatostatin receptor. *Bioconjug Chem* 19:192–200
57. Banerjee SR, Pullambhatla M, Byun Y, Nimmagadda S, Foss CA, Green G, Fox JJ, Lupold SE, Mease RC, Pomper MG (2011) Sequential SPECT and optical imaging of experimental models of prostate cancer with a dualmodality inhibitor of the prostate-specific membrane antigen. *Angew Chem Int Ed Engl* 50:9167–9170
58. Liu S, Lin TP, Li D, Leamer L, Shan H, Li Z, Gabbai FP, Conti PS (2013) Lewis acid-assisted isotopic 18F-19F exchange in BODIPY dyes: facile generation of positron emission tomography/fluorescence dual modality agents for tumor imaging. *Theranostics* 3:181–199
59. Ghosh SC, Ghosh P, Wilganowski N, Robinson H, Hall MA, Dickinson G, Pinkston KL, Harvey BR, Sevick-Muraca EM, Azhdarinia A (2013) Multimodal chelation platform for near infrared fluorescence/nuclear imaging. *J Med Chem* 56:406–416
60. Zhang Y, Hong H, Engle JW, Yang Y, Theuer CP, Barnhart TE, Cai W (2012) Positron emission tomography and optical imaging of tumor CD105 expression with a dual-labeled monoclonal antibody. *Mol Pharm* 9:645–653
61. Zhang Y, Hong H, Engle JW, Yang Y, Theuer CP, Barnhart TE, Cai W (2012) Multimodality imaging of breast cancer experimental lung metastasis with bioluminescence and a monoclonal antibody dual-labeled with 89Zr and IRDye 800CW. *Mol Pharm* 9:645–653

62. Sevick-Muraca EM (2012) Translation of near-infrared fluorescence imaging technologies: emerging clinical applications. *Annu Rev Med* 63:217–231
63. Zhang Y, Hong H, Engle JW, Yang Y, Barnhart TE, Cai W (2012) Positron emission tomography and near-infrared fluorescence imaging of vascular endothelial growth factor with dual labeled bevacizumab. *Am J Nucl Med Mol Imaging* 2:1–13
64. Zhang Y, Hong H, Nayak TR, Valdovinos HF, Myklejord DV, Theuer CP, Barnhart TE, Cai W (2013) Imaging tumor angiogenesis in breast cancer experimental lung metastasis with positron emission tomography, near-infrared fluorescence, and bioluminescence. *Angiogenesis* 16:663–674
65. Cohen R, Vugts DJ, Stigter-van Walsum M, Visser GW, van Dongen GA (2013) Inert coupling of IRDye800CW and zirconium-89 to monoclonal antibodies for single- or dual-mode fluorescence and PET imaging. *Nat Protoc* 8:1010–1018
66. Heller S, Zanzonico P (2011) Nuclear probes and intraoperative gamma cameras. *Semin Nucl Med* 41:166–181
67. Gulec SA (2007) PET probe-guided surgery. *J Surg Oncol* 96:353–357
68. Piert M, Burian M, Meisetschläger G, Stein HJ, Ziegler S, Nährig J, Picchio M, Buck A, Siewert JR, Schwaiger M (2007) Positron detection for the intraoperative localisation of cancer deposits. *Eur J Nucl Med Mol Imaging* 34:1534–1544
69. Thorek DL, Abou DS, Beattie BJ, Bartlett RM, Huang R, Zanzonico PB, Grimm J (2012) Positron lymphography: multimodal, high-resolution, dynamic mapping and resection of lymph nodes after intradermal injection of 18F-FDG. *J Nucl Med* 53:1438–1445
70. Zanzonico P, Heller S (2000) The intraoperative gamma probe: basic principles and choices available. *Semin Nucl Med* 30:33–48
71. Bricou A, Duval MA, Charon Y, Barranger E (2013) Mobile gamma cameras in breast cancer care: a review. *Eur J Surg Oncol* 39:409–416
72. Lees JE, Bassford DJ, Blake OE, Blackshaw PE, Perkins AC (2012) Hybrid camera for simultaneous imaging of gamma and optical photons. *JINST* 7:P06009
73. Vermeeren L, Meinhardt W, van der Poel HG, Valdés Olmos RA (2010) Lymphatic drainage from the treated versus untreated prostate: feasibility of sentinel node biopsy in recurrent cancer. *Eur J Nucl Med Mol Imaging* 37:2021–2026
74. Olmos RA, Vidal-Sicart S, Nieweg OE (2009) SPECT/CT and real-time intraoperative imaging: new tools for sentinel node localization and radioguided surgery? *Eur J Nucl Med Mol Imaging* 36:1–5
75. Okur A, Ahmadi SA, Bigdelou A, Wendler T, Navab N (2011) MR in OR: first analysis of AR/VR visualization in 100 intraoperative Freehand SPECT acquisitions. In: 10th IEEE international symposium on mixed and augmented reality, pp 211–218
76. Brouwer OR, Buckle T, Bunschoten A, Kuil J, Vahrmeijer AL, Wendler T, Valdés-Olmos RA, van der Poel HG, van Leeuwen FW (2012) Image navigation as a means to expand the boundaries of fluorescence-guided surgery. *Phys Med Biol* 57:3123–3136
77. Wendler T, Herrmann K, Schnelzer A, Lasser T, Traub J, Kutter O, Ehlerding A, Scheidhauer K, Schuster T, Kiechle M, Schwaiger M, Navab N, Ziegler SI, Buck AK (2010) First demonstration of 3-D lymphatic mapping in breast cancer using freehand SPECT. *Eur J Nucl Med Mol Imaging* 37:1452–1461



# Chapter 3





3

# The best of both worlds: A hybrid approach for optimal pre- and intraoperative identification of sentinel lymph nodes

*KleinJan GH  
van Werkhoven E  
van den Berg NS  
Karakullukcu MB  
Zijlmans HJMAA  
van der Hage JA  
BA van de Wiel  
T Buckle  
Klop WMC  
Horenblas S  
Valdés Olmos RA  
van der Poel HG  
van Leeuwen FWB  
Submitted for publication*

## ABSTRACT

### INTRODUCTION

Hybrid image-guided surgery technologies such as combined radio- and fluorescence-guidance are increasingly gaining interest, but their added value still needs to be proven. In order to evaluate if and how fluorescence-guidance can help realize improvements beyond the current state-of-the-art in sentinel node (SN) biopsy procedures, use of the hybrid tracer indocyanine green (ICG)-<sup>99m</sup>Tc-nanocolloid was evaluated in a large cohort of patients.

### METHODS

A heterogeneous cohort of 495 patients with different malignancies (skin malignancies, oral cavity cancer, penile cancer, prostate cancer and vulva cancer) was assessed. After injection of ICG-<sup>99m</sup>Tc-nanocolloid, SNs were preoperatively identified based on lymphoscintigraphy and SPECT/CT. Intraoperatively, SNs were pursued via gamma tracing, visual identification (blue dye) and/or near-infrared fluorescence imaging. In a prospective trial (n = 501 procedures), wherein the patients acted as their own control, use of hybrid guidance was compared to conventional radioguidance and the use of blue dye (n = 300) based on reported surgical complications, overall survival, LN recurrence free survival, and false negative rates (FNR).

### RESULTS

1327 SN-related hotspots were identified on 501 preoperative SPECT/CT scans. Intraoperatively, a total number of 1643 SNs were identified based on the combination of gamma-tracing (>98%) and fluorescence-guidance (>95%). In patients wherein blue dye was used (n= 300) fluorescence-based SN detection was superior over visual blue dye-based detection (22-78%). No adverse effects related to the use of the hybrid tracer or the fluorescence-guidance procedure were found and outcome values were not negatively influenced.

### CONCLUSION

With ICG-<sup>99m</sup>Tc-nanocolloid, the SN biopsy procedure has become more accurate and independent of the use of blue dye. With that, the procedure has become universal for different malignancies and anatomical locations.

## INTRODUCTION

Sentinel node (SN) biopsy is a routine procedure in the management of breast cancer and melanoma, where it allows for loco-regional staging of lymph nodes (LNs) [1, 2]. For the identification of SNs, targeting nanoparticles entitled radiocolloids (e.g.  $^{99m}\text{Tc}$ -nanocolloid) are considered the standard. The migration kinetics and accumulation of radiocolloids in individual lymphatic basins can be mapped in a non-invasive manner using lymphoscintigraphy and SPECT/CT [3]. For intraoperative tracing of radiocolloid containing SNs, a portable gamma camera or more common a gamma probe can be used [4].

For the surgeons convenience, however, the radioguidance approach is often strengthened by optical guidance in the form of blue dye [5]. Unfortunately, blue dye also has some short-comings, the main ones being the staining of the injection site, allergic reactions and the limited degree of nodal identification[6]. The last is a result of the lack of SNs specificity of this lymphangiographic agent and the limited sensitivity of this light-absorbance based detection method. Almost two decades ago, the fluorescent dye indocyanine green (ICG) was introduced as an alternative lymphangiographic dye[7]. At high concentrations ICG is green in color, but at low concentrations it can only be detected using dedicated near-infrared fluorescence cameras ( $\lambda = 820 \text{ nm}$ ) [8]. One of the advantages, compared to blue dye is the superior penetration depth of the fluorescence emission (up to 1cm) [9]. Nevertheless, as a result of its molecular size, ICG still shares a shortcoming with blue dye, namely an unrestricted lymphatic migratory pattern and with that a lack of specificity for SNs compared to higher echelon nodes. This same feature also induces spillages during surgical manipulations of the tissue.

In an ideal situation, the best features related to both the radioguided surgery and optical guidance procedures would be integrated, meaning SN specificity should be combined with sensitive intraoperative optical guidance. Such a best-of-both-worlds scenario could be realized following the development of the hybrid tracer, ICG- $^{99m}\text{Tc}$ -nanocolloid and its clinical translation in 2009 [10]. In various malignancies this hybrid tracer was shown to allow for: 1) non-invasive preoperative localization of the SNs, 2) intraoperative rough localization based on the gamma signal and/or using radioguidance based navigation approaches, 3) detailed intraoperative guidance based on the fluorescent signal [11-14].

Promising new surgical guidance technologies using radio- and fluorescence- imaging are gaining interest from a scientific, medical and industrial perspective. However, translation

of such technologies generally has been restricted to first-in-human trials with small patient groups and in specialized academic hospitals [9]. Internal controls and follow up of patients and outcome data for larger and more heterogeneous patient groups are essential to benchmark new technologies and assess their added value over the state-of-the-art. This study presents the validation of the ICG-<sup>99m</sup>Tc-nanocolloid based hybrid SN procedure in a relatively large (495 patients) and heterogeneous patient group (skin malignancies, oral cavity cancer, penile cancer, prostate cancer and vulva cancer) and includes both follow-up and outcome data. By relating the hybrid procedure to the traditional radioguidance and blue dye approaches, in the same patient, the added value of the new technology could be determined.

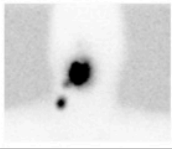
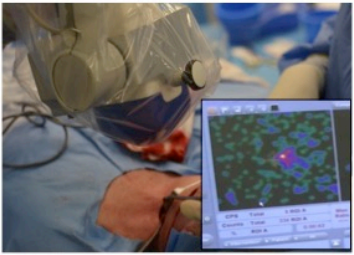
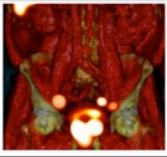
## METHODS

Between March 2010 and January 2016, 495 patients were prospectively included. Of this group 234 patients were previously included in different studies [3, 11-14]. All patients were operated at the Netherlands Cancer Institute – Antoni van Leeuwenhoek Hospital. Approval for these studies was obtained from the local institution review board approved and the trial was registered under reference NL 26699.031.09 and NL40636.031.12. The off-label use of the hybrid tracer was approved by the local pharmacy (approval received in November 2012).

### Patients

All included patients were  $\geq 18$  years of age and had a histologically proven malignancy (See Supplemental information (SI), Table S11). All patients were regional clinically node-negative (cN0) as defined by palpation and ultrasound-guided fine-needle aspiration cytology. Patients with squamous cell carcinoma (SCC) of the penis and vulva were also eligible when cN1 on the contralateral side. All patients were scheduled for SN biopsy and subsequent treatment of the primary tumor site (Figure 1 and 2).

The hybrid tracer (ICG-<sup>99m</sup>Tc-nanocolloid) was commercially obtained from (GE Healthcare, Leiderdorp, The Netherlands). Injection procedure, preoperative imaging procedure, surgical procedures and pathological examination have been reported previously and are explained in more detail in the supporting information section [3, 11-14] (Figure 1 and 2).

Indications	Lymphoscintigraphy	SPECT/CT	Intraoperative radioguidance	
			Gamma probe	Gamma camera
Open				
Melanoma (head and neck) Oral cavity				
Melanoma (leg, arm, trunk)				
Penile cancer Vulvar cancer				
Laparoscopic			Laparoscopic gamma probe	
Prostate				

**Figure 1. Radioguidance enabled by the hybrid tracer.**

The first three rows presents open surgical procedures (head and neck area, trunk and groin), while the last row presents a laparoscopic procedure (pelvis). The first two columns display examples of preoperative lymphoscintigraphy and SPECT/CT illustrating drainage to the neck, axilla, groin and pelvis. The last column gives an indication of the radioguidance technologies used intraoperatively.

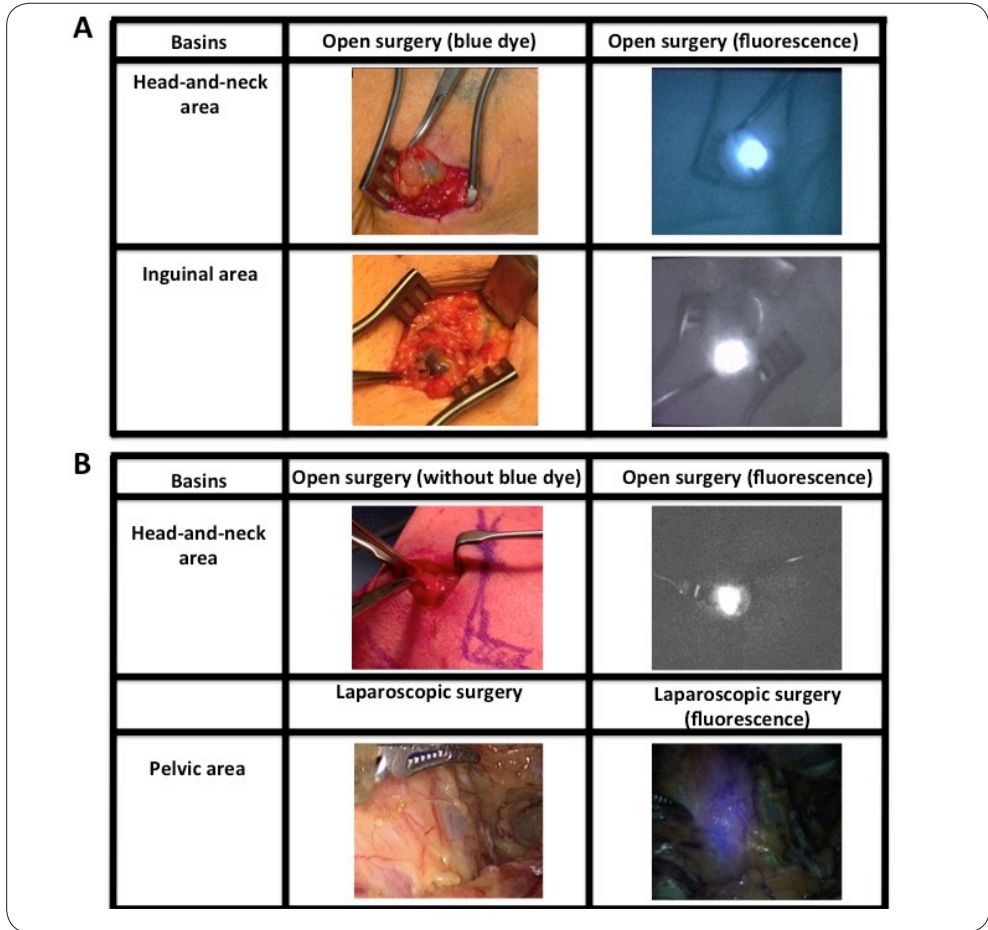


**Figure 2. Optical guidance enabled by the hybrid tracer and blue dye.**

**A)** Typical examples of procedures combining use of blue dye and the hybrid tracer ICG-<sup>99m</sup>Tc-nanocolloid in the head-and-neck region and groin.

**B)** Typical examples of procedures using only the hybrid tracer for optical guidance (head-and-neck and pelvic region).

The first column demonstrates what is seen by eye, while the second column provides insight in the signal obtained via fluorescence imaging with a (laparoscopic) near-infrared dedicated fluorescence camera.

## Follow-up

Complication rates within 90 days after surgery were reported following the Clavien-Dindo score and were scored per patient [15].

The overall survival for the total group was determined up to six years after surgery. The overall survival was also determined for different malignancies in different anatomical indications stratified by pN0 R0 and pN+ R0 (N = nodal status and R0 = resection margin negative). This was presented in Kaplan Meier curves (using R statistical software; R Development Core Team, 2008, Vienna, Austria). To yield homogenous patient groups, in the group of skin malignancies only patients with melanoma were included. In the penile cancer group only the SCC patients were included and this was also the case for the patients with tumors located on the vulva. For the prostate cancer patients we reported the biochemical recurrence rate (BCR)-free (prostate specific antigen (PSA) >0.01ng/ml) survival as indication of disease-free survival [3].

False negative patients were defined as patients with LN recurrence during follow up and negative SN in the originally explored lymph node basin and negative non-SN at time of primary surgery [16]. Patients with synchronous primary tumor recurrence and LN recurrence were excluded from this calculation. Those patients that presented with in-transit metastases on follow-up were also excluded from the FNR calculation.

To allow for comparison between the group where blue dye was used and only the hybrid tracer was used, the LN recurrences were determined on a per patient basis. For the SN penis and vulva procedures the FNR per groin was also reported. When applicable, the FNR rates were also reported without inclusion of the first fifteen procedures, which were considered as an initial learning curve with the technology.

## Statistical analysis

The intraoperative SN detection rates were calculated as percentages of SNs. Fluorescence detection was compared to blue detection and gamma detection for the overall group, and per indication. Associations of fluorescence detection in vivo and ex vivo with BMI of the patient were investigated with logistic regression, using the Huber-White method to adjust the variance-covariance matrix to correct for correlated responses from nodes clustered within the same patient (using R function `robcov` from package `rms`) [17]. The fluorescence detection in vivo and ex vivo was also correlated to the body mass index (BMI) of the patient. A 95% confidence interval (CI) was given and a p-value  $\leq 0.05$  was considered significant. Wilcoxon's rank sum tests were performed to test associations between whether primary

tumor site removal was before or after SN biopsy and SN detection rates. The same test was used to assess associations of a one- or two day protocol with the SN detection rates and the gamma counts measured by the gamma probe. A log-rank test was used to analyze the statistical differences between the Kaplan Meier curves.

## RESULTS

### **Preoperative SN mapping via nuclear imaging**

In the SI section, the preoperative-imaging findings are described. In total 1327 SN-related hotspots were identified in these images.

### **Intraoperative SN identification rates enabled by surgical guidance modalities**

The intraoperative detection rates using radioguidance, fluorescence and blue dye are summarized in Figure 3 and Table 1 and Table SI2. In total 1643 SNs specimens were surgically removed.

Of the SNs that were surgically removed, 99% could be detected using gamma tracing. Overall, using the hybrid tracers' fluorescent signature, the SNs could be optically identified in > 95% of the cases (combined in vivo and ex vivo examination in the surgical theatre). The anatomy of the basin in which the SNs were situated did not influence these find rates (Figure 2). In contrast to what has been reported for the use of "free" ICG [18], the hybrid tracer nodal dissections did not suffer from pollution of the surgical field as result of tracer leakage from the lymphatic system. For the procedures where blue dye was used, a wide variation in blue stained SNs was observed in the SNs (20-72%; n = 300; 950 SNs; Figure 3). These SN find rates were significantly poor compared to those obtained with the fluorescent signature of the hybrid tracer (p-value < 0.001). Blue dye was most helpful in the axilla 72%, but proved to be of limited value in the head-and-neck area (23%), arm and shoulder (20%). Merely 1% (9 SNs) was dissected based on blue coloration only (Table 1 and SI table 3).

Potential damage to surrounding structures withheld the surgeon from resection in 2.2% (29/1327) of the SN-related hotspots identified on SPECT/CT e.g. in the pararectal space. In these cases despite a clear gamma read-out, the inability to detect a fluorescence signal indicated the SNs were located > 0.5-1 cm deep within in the tissue. This depth estimation helped establish a benefit/risk balance on which the decision was made to abandon further dissection in these areas.

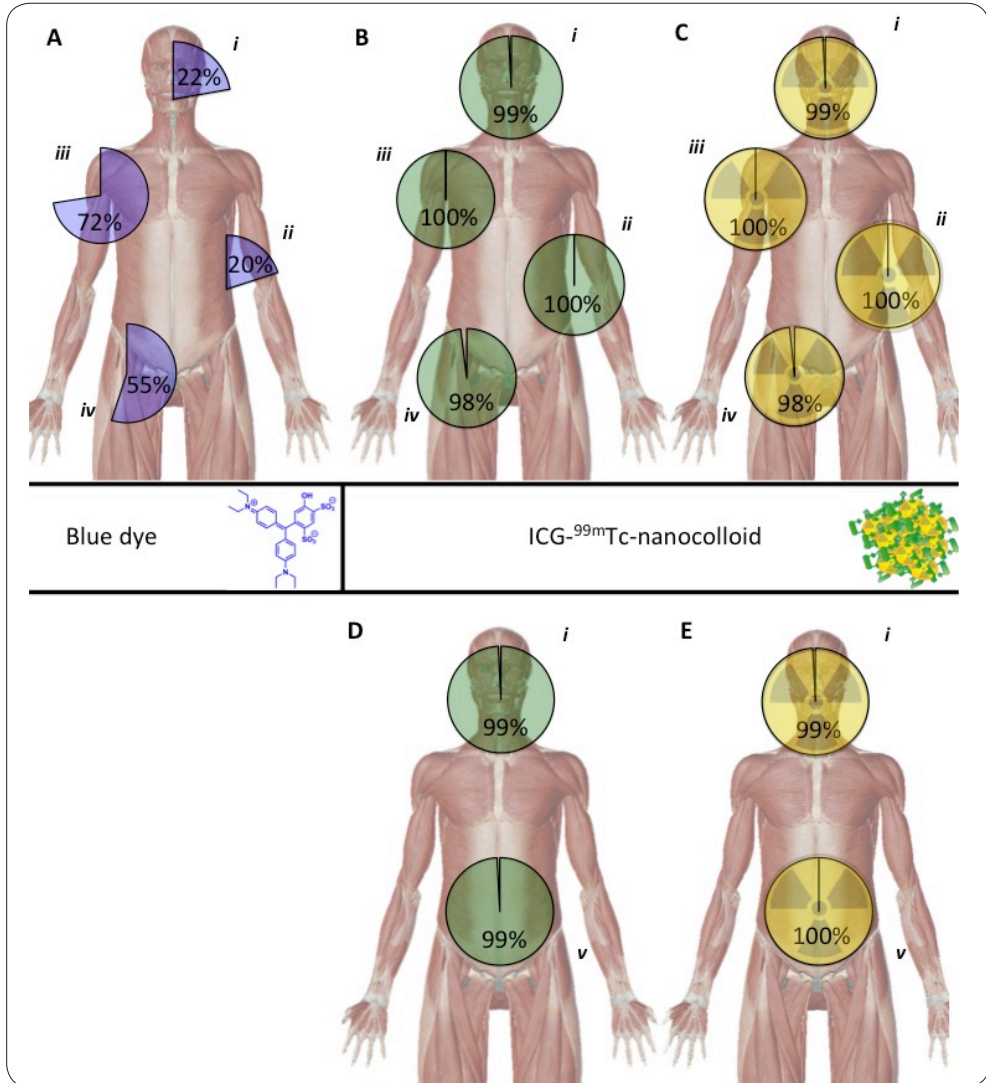


**Figure 3. Intraoperative detection rates for the different surgical guidance modalities used**

**A)** Blue dye-based SN identification percentages in patients who received blue dye subsequently to the hybrid tracer (total n= 300), **B)** Fluorescence-based SN identification percentages (total n= 501); **C)** Radioactivity-based SN identification percentages (total n= 501); **D)** and **E)** respectively depict the fluorescence-based and radioactivity based SN identification percentages in the patient groups that did not receive blue dye (total n= 201). Detection rates are provided for different regions: i) head and neck area, ii) arm and trunk, iii) axilla, iv) inguinal area and v) pelvic region.

Table 1. Fluorescence-, blue- and radioactivity-based detection rate per indication (see also Figure 3)

	Skin malignancies body		Head-and-neck skin malignancies		Oral cavity				Penis		Prostate		Vulva		Total		
	Yes	No	Yes	No	Yes	No	Yes	No	Yes	No	Yes	No	Yes	No	Yes	No	
<b>In vivo detection rates</b>																	
<b>Blue used</b>																	
- No optical identification (SNs)	3 (2%)	15 (4%)	2 (2%)	15 (4%)	-	7 (5%)	9 (2%)	28 (22%)	9 (2%)	28 (22%)	2 (3%)	64 (4%)					
- Blue only SNs	1 (1%)	-	1 (1%)	-	0	-	6 (1%)	-	6 (1%)	-	0	8 (1%)					
- Fluorescent only <sup>2</sup> SNs	37 (28%)	334 (96%)	73 (73%)	334 (96%)	3 (100%)	149 (96%)	244 (46%)	99 (78%)	244 (46%)	99 (78%)	21 (37%)	959 (66%)					
- Fluorescent <sup>3</sup> and blue SNs	88 (67%)	-	24 (24%)	-	0	-	272 (51%)	-	272 (51%)	-	34 (60%)	418 (29%)					
- Total fluorescent SNs	125 (95%)	334 (96%)	97 (97%)	334 (96%)	3 (100%)	149 (96%)	516 (97%)	99 (78%)	516 (97%)	99 (78%)	55 (96%)	1377 (95%)					
- SNs not evaluated for staining	0	25	10	25	3	36	110	0	110	0	5	194					
- Total radioactive <sup>4</sup> SNs	131 (100%)	356 (98%)	108 (100%)	356 (98%)	5 (83%)	142 (95%)	604 (98%)	82 (100%)	604 (98%)	82 (100%)	61 (98%)	1499 (98%)					
- SNs not evaluated for radioactivity	0	8	0	8	0	43	8	45	8	45	1	60					
<b>Total (in vivo and ex vivo* combined)</b>																	
<b>Blue used</b>																	
- No optical identification (SNs)	0	3 (1%)	1 (1%)	3 (1%)	0	3 (2%)	1 (0%)	1 (1%)	1 (0%)	1 (1%)	1 (2%)	14 (1%)					
- Blue only SNs	0	-	0	-	0	-	9 (1%)	-	9 (1%)	-	0	9 (1%)					
- Fluorescent <sup>3</sup> only SNs	36 (27%)	368 (99%)	81 (75%)	368 (99%)	0	184 (98%)	284 (46%)	126 (99%)	284 (46%)	126 (99%)	22 (36%)	1105 (69%)					
- Fluorescent <sup>3</sup> and blue SNs	95 (73%)	0	26 (24%)	0	5 (100%)	-	323 (52%)	-	323 (52%)	-	39 (63%)	484 (30%)					
- Total fluorescent SNs	131 (100%)	368 (99%)	107 (99%)	368 (99%)	5 (100%)	184 (98%)	607 (98%)	126 (99%)	607 (98%)	126 (99%)	61 (98%)	1589 (99%)					
- SNs not evaluated for staining	0	3	0	3	1	5	1	0	1	0	0	31					
- Total radioactive <sup>4</sup> SNs	131 (100%)	373 (100%)	239 (100%)	373 (100%)	6 (100%)	180 (98%)	625 (98%)	127 (100%)	625 (98%)	127 (100%)	57 (100%)	1612 (99%)					
- SNs not evaluated for radioactivity	0	0	0	0	0	9	6	0	6	0	0	15					

SN = sentinel node, \* = vivo validation of the fluorescence signal, because tissue attenuation, the in vivo detection of the fluorescent signal could be hampered. Ex vivo the SNs are more exposed and as such the fluorescence detection increases. <sup>2</sup>Due to the hybrid nature of the tracer the fluorescence and radioactive signatures are directly related.

The relation between pre-operative and intraoperative SN find rates, the influence of the surgical resection order (see Figure SI1) and BMI (see Figure SI2) on the surgical guidance procedure are described in the SI section, please see the SI.

### **Pathological evaluation**

From the excised 1643 SN specimens, 1938 LNs were harvested at pathology. In Table SI2 the percentage of tumor positive SNs is reported. In the supporting information section a further description of the tumor find rate (TFR) is also provided.

### **Follow-up**

The complication grade score according to Clavien-Dindo ranged from I-V in this study cohort and was highest in the group of penile cancer patients (Table SI4). In none of the 501 procedures did adverse effects occur that could be related to the use of the hybrid tracer or blue dye. There was no correlation between the removal of additional SNs and complication in the follow-up (p-value 0.478). The overall survival results are provided in the SI section (Figure SI3).

In pN0 R0 patients (n=321 (65%)), the LN recurrence-free survival varied from 93–100% for the various indications, with an average of 93% at two-year follow-up (Figure 4A, B). In the prostate cancer patients, a BCR-free survival of 90% (CI 73-100%) was found at two-year follow-up (Figure 4C). No LN recurrences occurred in patients with melanoma on the body or vulvar cancer. In the penile cancer patients, the LN recurrence-free survival rate was the lowest (77%) at five-year follow-up.

In a relatively small group of pN0 R0 patients with head-and-neck melanoma, wherein the hybrid tracer was used in combination with (n=19) or without (n=80) blue dye, we were able to study if use of blue dye had an influence on LN recurrence-free survival. The group wherein the hybrid tracer alone was used had a 97% (CI 93%-100%) LN recurrence-free survival probability, while the group with the hybrid tracer in combination with blue dye had a slightly lower LN recurrence-free survival of 94% (CI 84%-100%). Both groups were comparable for T-stage. These findings indicate that use of blue dye next to the hybrid tracer does not lead to a better prognosis (Figure 4D).

In the overall population, 10 isolated LN recurrences (2%) were reported, yielding a combined FNR of 14% (see SI-Table 4 for the FNRs of the individual procedures). Interestingly, many of the false negative (during follow up) findings occurred in the first fifteen cases, indicating a

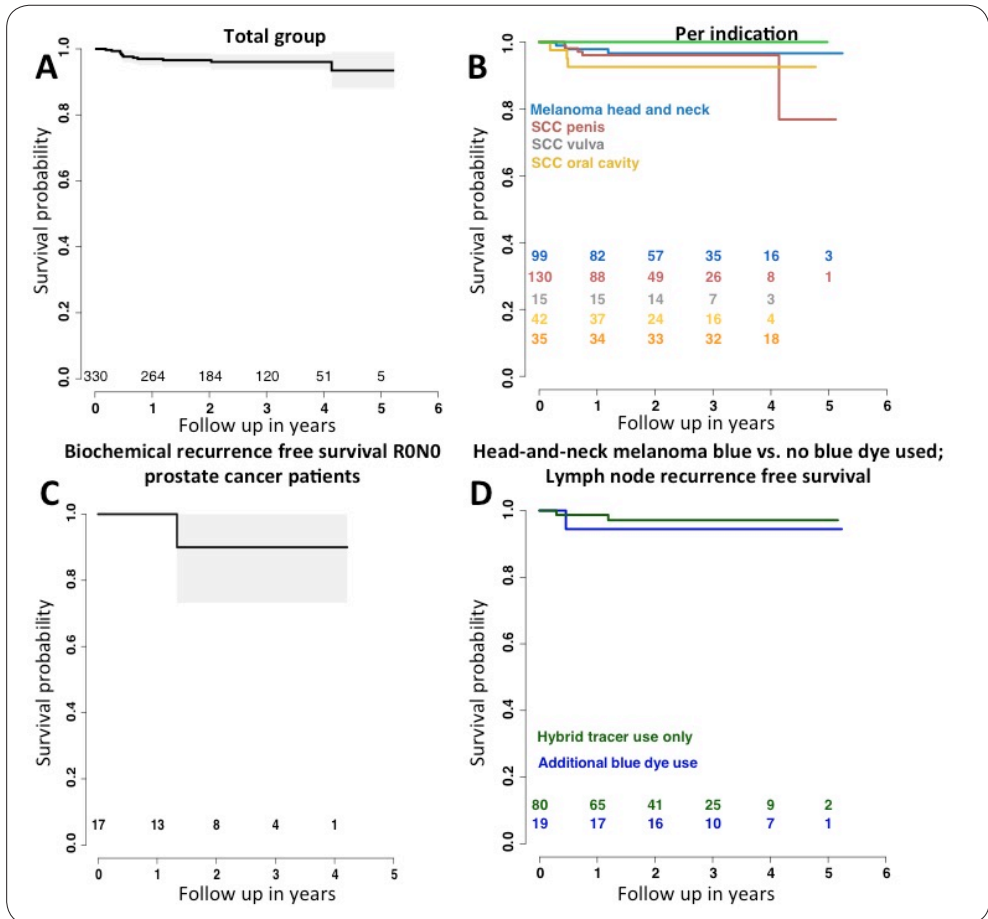


**Figure 4. Lymph node- and biochemical recurrence curves.** In A) and B) the LN recurrences curves are shown for the total group and per indication, respectively. C) Biochemical recurrence free survival of pN0 R0 prostate cancer patients. To relate outcome to the use of the hybrid tracer with or without the use of blue dye, recurrence rates are shown for the head melanoma group in figure D) LN recurrence rates for R0N0 head-and-neck melanoma patients) ( $p = 0.29$ ).

learning curve, a feature that was reported on previously [19]. After this learning curve, the combined FNR decreases to 10.3 % (Table SI4). A low FNR was found in the melanoma body group (0%) and a modest FNR (7%) in the melanoma head-and-neck group. These values are lower than the weighted literature FNRs for head-and-neck melanoma, which averaged 12.5% (range 0-34%) [20]. The FNR in oral cavity cancer (22%) was in line with the range previously reported (9-29%) [21, 22]. In the penile cancer group the FNR was 16%, which lower than the initial report of the sentinel node biopsy for penile cancer (22%) described

by Tanis et. al.[23]. The FNR rate dropped to 14% following exclusion of the re-sentinel node procedures, which indicates the sixteen repeat SN procedures in patients with local recurrence had a negative influence on the FNR (Table SI4). The 0% FNR we found for the vulvar cancer patients is in line with the report of Van der Zee et al. (2.3-3%) [24]. The FNR of the SN procedure in the prostate cancer group compared to the extended pelvic lymph node dissection (ePLND) was 11.3%, again comparable to other reports [25],

## DISCUSSION

The current longitudinal study of a 495 patient cohort indicates that the generation of a hybrid set-up that includes fluorescence guidance in an otherwise standard SN-procedure creates value for the operating surgeons while preserving the clinical outcome. The hybrid guidance provided was irrespective of the anatomical location wherein the SNs were pursued, surgical timing, the order of resection, or the surgical setting used (open or laparoscopic). With the hybrid tracer, the much-desired optical guidance becomes available at indications where use of the blue dye is neither desirable nor possible. This improvement also means that SN procedures can be performed in an uniform manner, allowing expansion of the SN procedure to non-traditional SN indications.

The availability of fluorescence imaging was considered a valuable addition during the resection, a feature that was most obvious for procedures in the head-and-neck and pelvic area. The ability to perform radioguidance and enhance it by fluorescence imaging of the exact same features improved the accuracy of SN identification, in relation to the SN-related hotspots detected by SPECT/CT. This yielded enhanced intraoperative SN find rates: 24% more nodes were identified intraoperatively [11, 14]. Unfortunately, fluorescence imaging, even in the near-infrared region of the light spectrum, suffers tremendously from tissue attenuation when compared to radioguidance technologies [9]. The difference between *in vivo* and *ex vivo* fluorescence detection rates (Table 1 and Table SI3) also underline that radioguidance remains essential for *in vivo* SN localization and that *ex vivo* validation remains critical to assess the presence of fluorescence [8]. This effect increases with an increase in BMI (see Figure SI2). Uniquely, lack of fluorescence detection could also be used by the surgeons to assess the depth and with that the change of surgical complications in delicate anatomies.

Intra-patient comparisons indicate the fluorescence signature of ICG-<sup>99m</sup>Tc-nanocolloid significantly outperforms blue dye in the optical identification of SNs (Table 1) (p-value <

0.001). One aspect we have not addressed in this patient cohort was the differentiation of SNs from higher echelon nodes via visualization of the afferent lymphatic ducts, a blue dye technique commonly performed by expert surgeons [5]. Although the fluorescence guidance modalities used in this study were able to visualize the afferent lymphatic ducts [14], as a result of the labor intensive exposure of these ducts this visualization was not relied on as routine tool. We recently reported that lymph duct visualization becomes much more straight forward with next generation fluorescence guidance modalities [26]. When such hardware improvements are integrated, use of the hybrid tracer strengthens a recent statement by Van der Ploeg et al. who suggests blue dye may potentially be omitted in SN biopsy for melanoma [27]. The LN recurrences free survival reported for a homogenous head and neck melanoma population (Figure 4 D) also indicates that use of blue dye did not positively influence outcome.

The follow up data provided for the hybrid SN procedure is positive (Figure 4 and Figure S13) and an overall FNR of 10.1% (Table S14) is acceptable, but from the current data it is not yet possible to conclude whether use of the hybrid tracer improves the oncological outcome. Given the complexity of the diagnostic SN procedure, the limited tumor find rates, and the dependence on factors that extend beyond the operating theatre e.g. tracer administration and pathological accuracy, we wonder whether expecting such improvements would even be realistic. Following the availability of the hybrid SN tracer and the optimized intraoperative imaging modalities, it seems that further refinement of the oncological outcome requires a critical look at the patient inclusion, tracer deposition, and means of pathological evaluation. In this cohort, for example, some patients were staged with a higher T-stage than those described in the guidelines of treatment of the different malignancies, which could have negatively influenced the findings (Table S11). For the tracer deposition, earlier and ongoing studies indicate that the location of tracer deposition directly relates to the lymphatic drainage and thus refinements in this area could help improve the ability to detect lymphatic metastasis [28]. The relation between the FNR and the accuracy of the surgical guidance procedure is not a direct one as the FNR is also highly dependent on the quality of the pathological accuracy, in particular when micro-metastases occur [29]. Hence advances in the pathological examination of SN specimens could also help to improve the procedure. Since all surgeons involved in the current study had previous experience with SN-procedures, and use of ICG-<sup>99m</sup>Tc-nanocolloid was appreciated as an improvement in the surgical procedure, there seems to be little value in a prospective randomized study. Scoring the surgeons experiences and randomly blinding them to different aspects in the hybrid image

guidance procedure could, however, help to provide more detailed insight into the value of the individual components in the guidance procedure. Another feature that could be studied in combination with experienced surgeons is the ability of the hybrid approach to shorten the surgical time. Combined with the limited tracer costs, the last may reduce procedural cost, which on its own would provide value.

## CONCLUSION

This study underlines that the proposed hybrid SN approach, which uses the hybrid tracer ICG-<sup>99m</sup>Tc-nanocolloid, not only provides preoperative SN mapping but also allows for superior optical surgical guidance compared to blue dye. Outcome data such as recurrence free survival and FNR underline the efficiency and general applicability of the technology.

## REFERENCES

1. Morton DL, Thompson JF, Cochran AJ, Mozzillo N, Elashoff R, Essner R, et al. Sentinel-node biopsy or nodal observation in melanoma. *N Engl J Med*. 2006; 355: 1307-17.
2. Veronesi U, Paganelli G, Viale G, Luini A, Zurrida S, Galimberti V, et al. A randomized comparison of sentinel-node biopsy with routine axillary dissection in breast cancer. *N Engl J Med*. 2003; 349: 546-53.
3. KleinJan GH, van den Berg NS, Brouwer OR, de Jong J, Acar C, Wit EM, et al. Optimisation of fluorescence guidance during robot-assisted laparoscopic sentinel node biopsy for prostate cancer. *Eur Urol*. 2014; 66: 991-8.
4. Heller S, Zanzonico P. Nuclear probes and intraoperative gamma cameras. *Semin Nucl Med*. 2011; 41: 166-81.
5. Nieweg OE, Tanis PJ, Kroon BB. The definition of a sentinel node. *Ann Surg Oncol*. 2001; 8: 538-41.
6. Chao C, Wong SL, Edwards MJ, Ross MI, Reintgen DS, Noyes RD, et al. Sentinel lymph node biopsy for head and neck melanomas. *Ann Surg Oncol*. 2003; 10: 21-6.
7. Motomura K, Inaji H, Konoike Y, Kasugai T, Noguchi S, Koyama H. Sentinel node biopsy guided by indocyanine green dye in breast cancer patients. *Jpn J Clin Oncol*. 1999; 29: 604-7.
8. KleinJan GH, Bunschoten A, van den Berg NS, Olmos RA, Klop WM, Horenblas S, et al. Fluorescence guided surgery and tracer-dose, fact or fiction? *Eur J Nucl Med Mol Imaging*. 2016; 43: 1857-67.
9. van Leeuwen FW, Hardwick JC, van Erkel AR. Luminescence-based Imaging Approaches in the Field of Interventional Molecular Imaging. *Radiology*. 2015; 276: 12-29.
10. Brouwer OR, Buckle T, Vermeeren L, Klop WM, Balm AJ, van der Poel HG, et al. Comparing the hybrid fluorescent-radioactive tracer indocyanine green-<sup>99m</sup>Tc-nanocolloid with <sup>99m</sup>Tc-nanocolloid for sentinel node identification: a validation study using lymphoscintigraphy and SPECT/CT. *J Nucl Med*. 2012; 53: 1034-40.
11. Brouwer OR, van den Berg NS, Matheron HM, van der Poel HG, van Rhijn BW, Bex A, et al. A hybrid radioactive and fluorescent tracer for sentinel node biopsy in penile carcinoma as a potential replacement for blue dye. *Eur Urol*. 2014; 65: 600-9.
12. Matheron HM, van den Berg NS, Brouwer OR, Kleinjan GH, van Driel WJ, Trum JW, et al. Multimodal surgical guidance towards the sentinel node in vulvar cancer. *Gynecol Oncol*. 2013; 131: 720-5.
13. van den Berg NS, Brouwer OR, Klop WM, Karakullukcu B, Zuur CL, Tan IB, et al. Concomitant radio- and fluorescence-guided sentinel lymph node biopsy in squamous cell carcinoma of the oral cavity using ICG-(<sup>99m</sup>Tc)-nanocolloid. *Eur J Nucl Med Mol Imaging*. 2012; 39: 1128-36.
14. van den Berg NS, Brouwer OR, Schaafsma BE, Matheron HM, Klop WM, Balm AJ, et al. Multimodal Surgical Guidance during Sentinel Node Biopsy for Melanoma: Combined Gamma Tracing and Fluorescence Imaging of the Sentinel Node through Use of the Hybrid Tracer Indocyanine Green-(<sup>99m</sup>Tc)-Nanocolloid. *Radiology*. 2015; 275: 521-9.
15. Clavien PA, Barkun J, de Oliveira ML, Vauthey JN, Dindo D, Schulick RD, et al. The Clavien-Dindo classification of surgical complications: five-year experience. *Ann Surg*. 2009; 250: 187-96.
16. Nieweg OE, Estourgie SH. What is a sentinel node and what is a false-negative sentinel node? *Ann Surg Oncol*. 2004; 11: 169S-73S.
17. FE H. Regression modeling strategies with applications to linear models, survival analysis and logistic regression: Springer International Publishing; 2001.
18. Manny TB, Patel M, Hemal AK. Fluorescence-enhanced robotic radical prostatectomy using real-time lymphangiography and tissue marking with percutaneous injection of unconjugated indocyanine green: the initial clinical experience in 50 patients. *Eur Urol*. 2014; 65: 1162-8.
19. Morton DL, Cochran AJ, Thompson JF, Elashoff R, Essner R, Glass EC, et al. Sentinel node biopsy for early-stage melanoma: accuracy and morbidity in MSLT-I, an international multicenter trial. *Ann Surg*. 2005; 242: 302-11; discussion 11-3.
20. Valsecchi ME, Silbermins D, de Rosa N, Wong SL, Lyman GH. Lymphatic mapping and sentinel lymph node biopsy in patients with melanoma: a meta-analysis. *J Clin Oncol*. 2011; 29: 1479-87.
21. Flach GB, Bloemena E, Klop WM, van Es RJ, Schepman KP, Hoekstra OS, et al. Sentinel lymph node biopsy in clinically N0 T1-T2 staged oral cancer: the Dutch multicenter trial. *Oral oncology*. 2014; 50: 1020-4.
22. Pezier T, Nixon IJ, Gurney B, Schilling C, Hussain K, Lyons AJ, et al. Sentinel lymph node biopsy for T1/T2 oral cavity squamous cell carcinoma—a prospective case series. *Ann Surg Oncol*. 2012; 19: 3528-33.

23. Tanis PJ, Lont AP, Meinhardt W, Olmos RA, Nieweg OE, Horenblas S. Dynamic sentinel node biopsy for penile cancer: reliability of a staging technique. *J Urol.* 2002; 168: 76-80.
24. Van der Zee AG, Oonk MH, De Hullu JA, Ansink AC, Vergote I, Verheijen RH, et al. Sentinel node dissection is safe in the treatment of early-stage vulvar cancer. *J Clin Oncol.* 2008; 26: 884-9.
25. Wit EMK, Acar C, Grivas N, Yuan C, Horenblas S, Liedberg F, et al. Sentinel Node Procedure in Prostate Cancer: A Systematic Review to Assess Diagnostic Accuracy. *Eur Urol.* 2017; 71: 596-605.
26. van den Berg NS, Miwa M, KleinJan GH, Sato T, Maeda Y, van Akkooi AC, et al. (Near-Infrared) Fluorescence-Guided Surgery Under Ambient Light Conditions: A Next Step to Embedment of the Technology in Clinical Routine. *Ann Surg Oncol.* 2016; 23: 2586-95.
27. van der Ploeg IM, Madu MF, van der Hage JA, Wouters MW, Klop WM, van der Hiel B, et al. Blue dye can be safely omitted in most sentinel node procedures for melanoma. *Melanoma Res.* 2016; 26: 464-8.
28. Buckle T, Brouwer OR, Valdes Olmos RA, van der Poel HG, van Leeuwen FW. Relationship between intraprostatic tracer deposits and sentinel lymph node mapping in prostate cancer patients. *J Nucl Med.* 2012; 53: 1026-33.
29. Karim RZ, Scolyer RA, Li W, Yee VS, McKinnon JG, Li LX, et al. False negative sentinel lymph node biopsies in melanoma may result from deficiencies in nuclear medicine, surgery, or pathology. *Ann Surg.* 2008; 247: 1003-10.

## SUPPLEMENTAL INFORMATION

### METHODS

#### **Injection procedure**

In the patient group with skin malignancies (melanoma, Merkel cell carcinoma (MCC) and Squamous cell carcinoma (SCC)) ICG-<sup>99m</sup>Tc-nanocolloid was intradermally injected in four depots around the primary tumor site (approximately total 90 MBq). In penile cancer, vulvar cancer and oral cavity cancer patients the hybrid tracer was peritumorally injected in three-four depots (approximately total 90 MBq). In prostate cancer patients the hybrid tracer was administered intraprostatically, four depots, into the peripheral zone of the prostate (approximately 240 MBq)[1].

#### **Preoperative imaging procedure**

Dynamic imaging (anterior and lateral) was performed to visualize the drainage of the hybrid tracer via the lymphatic vessels from the injection site in the first couple of minutes (up to ten minutes). Early lymphoscintigraphy was performed 15 minutes after injection of the hybrid tracer, this was repeated after two hours (late lymphoscintigraphy). Both 2D planar imaging sessions were performed with a dual-head camera (Symbia T, Siemens, Erlangen, Germany).

Two hours post tracer administration three-dimensional imaging was performed with SPECT and low-dose CT (40 mAs; 130 kV) (Symbia T) acquisition. After correction for scatter and tissue attenuation SPECT and CT images were fused. SPECT/CT and CT images were correlated using multiplanar reconstruction (Osirix medical imaging software; Pixmeo, Geneva, Switzerland) with volume rendering to display anatomical LN mapping.

To determine the number and anatomical location of the SN(s), the nuclear medicine physician evaluated all acquired images and pointed out the SNs based on the comprehensive use of early and late lymphoscintigraphy as well as fused SPECT/CT images. SNs were identified based on their status of being directly draining LNs for the injection/ primary tumor site [2]. The location of the lymphatic basin containing the SNs was reported to the surgical specialists and the images sent to Picture Archiving and Communication System (PACS) for display in the operating room during SN biopsy. The findings were discussed with the surgeon who performed the operation, either by the nuclear medicine physician or by the research-associate.

### **Surgical procedure**

A detailed step-by-step description of the robot-assisted laparoscopic surgical procedure for prostate cancer or the open surgery procedure for head-and-neck, vulvar and penile cancer is provided below (see figure 1 and 2). In total 501 surgical procedures were evaluated. In short and generalized: when patients were operated in a one-day protocol, the hybrid tracer was injected in the morning of the day of surgery. When patients were operated in a two-day protocol, the injection was performed in the late morning or early afternoon of the day prior to surgery. The time-interval between injection and surgery remained < 30 h (Table 1).

Depending on the indication and the surgeon's preference, the primary lesion (and thus sites of tracer deposition) could be removed before or after the SN biopsy. This procedural difference was taken into account when analyzing the data. In all patients with melanoma, vulvar and penile cancer and in a minority (15% (28/186) of patients with head-and-neck cancer (melanoma and oral cancer) (total n = 300), in the operation room, before disinfection, 1.0 mL patent blue V dye (Laboratoire Guerbet, Aulnay-Sous-Bois, France) was administered at the injection sites used for ICG-<sup>99m</sup>Tc-nanocolloid. Blue dye was never administered in patients with prostate cancer. In prostate cancer patients, besides SN biopsy an additional extended pelvic lymph node dissection was performed [1-3].

During surgery a gamma probe, a near-infrared fluorescence camera or near-infrared fluorescence laparoscope and when necessary a portable gamma camera were used to locate, guide and confirm SN removal. Before (in vivo) and after (ex vivo) resection of the SN, the individual nodes were scored for being radioactive (Y/N), fluorescent (Y/N) and/or blue (Y/N). When possible also the gamma probe counts were registered.

### **“Open” surgery**

The operations were performed by surgical specialists with experience in (radioguided) SN biopsy procedures and experience in the use of blue dye.

For tumors in the head and neck area generally SN biopsy was performed prior to removal of the primary tumor or scar; in these patients radioguided SN identification could be influenced by the radioactivity related to the injections around the primary lesion.

Before incision, a pre-incision overview image of the area harboring the SN was generated with a portable gamma camera (Sentinella, Oncovision, Valencia, Spain) in the head-and-

neck area or when SNs were expected in the vicinity of the injection site. Subsequently, a gamma probe (Neoprobe; Johnson & Johnson Medical, Hamburg, Germany), was used to guide the surgeon to the SN using its acoustic read-out.

In the group in which blue dye was used (penile cancer, melanoma, vulva), most surgeons tried to identify the blue lymphatic ducts running to the SN. When the SN was in reach of a couple of mm, a near-infrared fluorescence camera (PhotoDynamic Eye; Hamamatsu Photonics, Hamamatsu, Japan) was used to optically identify the SN harboring the hybrid tracer. To visualize the ICG signal the lights in the operation room had to be dimmed.

After the excision of the SNs the portable gamma camera and fluorescence camera were used to check for residual radio- or fluorescence-activity. When there was still activity left on the spot from where the SN was excised, this indicated that the previously removed SN had been part of a cluster of SNs. These nodes were considered additional SNs and also harvested. Before closing the SN biopsy wound, it was evaluated for palpable suspicious (non- fluorescent/blue or –radioactive) LN.

### **Robot-assisted laparoscopic surgery**

SPECT/CT images were used to identify the area of interest and recognize anatomical landmarks. After preparation of the tissue, a laparoscopic gamma probe (Europrobe, Strassbourg, France) was introduced via the assistant-portal and was used in similar fashion as in an open procedure, based on the acoustic read out SNs were located. A laparoscopic fluorescence camera was introduced via a portal to identify the fluorescence signal within the SNs [1]. After localization of the SNs, an additional ePLND and prostatectomy were performed.

### **BMI associated optical detection**

The surrounding fatty tissue could hamper the fluorescence detection within the SN. To study the probable fatty tissue influence and as such body mass index (BMI), we evaluated if fluorescence detection was associated with the BMI of the patient.

### **One-day vs. two-day protocol**

In this study we compared the detection rates of the hybrid tracer and blue dye. Because the gamma signal subject to decay of the signal, this could hinder the gamma signal detection rate. Here the detection for fluorescence and blue dye were also compared.

## Pathological evaluation

All LNs identified in the removed tissue specimens entitled SN were examined as SN by an extended pathological protocol. After formalin fixation all SNs were bisected through the central plane and paraffin embedded. Histopathological examination was performed on multiple levels using haematoxylin and eosin staining (H&E) and immunohistochemistry with partly different protocols depending on the cancer type (for further details see below). Immunohistochemistry was performed with an automated IHC system (Ventana BenchMark Ultra, Ventana Medical Systems Inc, Tucson, AZ, USA).

For melanoma the SN was cut at 6 levels with intervals of 50  $\mu\text{m}$ . Each section was stained with H&E and melanA (clone A103, Dako, Carpinteria, CA, USA). For all other cancer types the SN was cut at 3 levels with intervals of 150 $\mu\text{m}$  and each section was stained with H&E. Except for vulvar cancer all second levels were used for immunohistochemistry using the following antibodies: CAM (clone CAM5.2, Becton Dickinson, San Jose, CA, USA) for prostate cancer and MCC and pankeratin (clone AE1/3, Thermo Fisher Scientific Inc, Waltham, MA, USA) for penile and oral cancer. All three levels were used for immunohistochemistry for vulvar cancer with the pankeratin clone AE1/3.

## Sentinel node Tumor find rate ( $_{\text{SN}}\text{TFR}$ )

The tumor find rate (TFR) illustrates the rate of probability of finding a tumor-positive SN with SN biopsy. The SN tumor find rate ( $_{\text{SN}}\text{TFR}$ ) was calculated based on the two following formulas for SPECT/CT and intraoperative SN detection: positive SNs at pathological evaluation /  $\text{SN}_{\text{SPECT/CT}} * 100\% = \text{TFR}_{\text{SPECT/CT}}$  and positive SNs at pathological evaluation /  $\text{SN}_{\text{intraoperative}} * 100\% = \text{TFR}_{\text{intraoperative}}$ .

## RESULTS

### Preoperative imaging

On the early- and late lymphoscintigraphy, respectively, 826 and 1209 (31.7% increase) SN-related hotspots were identified. SPECT/CT imaging yielded another 10% increase in SN-related hotspots based on preoperative imaging (1327; Table S11; Figure S11). This increase was in line with a previous study and most prominent in the head and neck area and pelvis [4]. By placing the SN-related hot spots within their anatomical context SPECT/CT provided valuable three-dimensional (3D) guidance information, a so-called virtual map, for the operating surgeons. SPECT/CT also improved the detection of SNs residing in the proximity of the injection site.

	Skin malignancies body	Head-and-neck skin malignancies	Oral cavity	Penis	Prostate	Vulva	Total
Nr. patients	56	135	51	192	40	21	495
Nr. procedures	56	135	51	198 #	40	21	501
Re-sentinel node biopsy	0	0	0	14	0	0	14
Age (median, IQR)	52 (42-66)	61 (50-70)	61 (56-66)	67 (59-75)	64 (61-68)	70 (54-77)	64 (54-72)
BMI (median, IQR)	25 (22-28)	26 (24-29)	25 (23-28)	27 (25-29)	26 (25-27)	26 (22-28)	26 (24-28)
SCC	1 (2%)	0	51 (100%)	194 (98%)	0	19 (90%)	265 (53%)
Melanoma	54 (96%)	129 (96%)	0	1 (0.5%)	0	2 (10%)	186 (37%)
Adenocarcinoma	0	0	0	1 (0.5%)	40 (100%)	0	41 (8%)
MCC	1 (2%)	6 (4%)	0	0	0	0	7 (1%)
UC	0	0	0	1 (0.5%)	0	0	1 (0%)
Sarcoma	0	0	0	1 (0.5%)	0	0	1 (0%)
Clinical TNM							
Breslow (median, IQR)	2 (1-3)	2 (1-4)	-	2 (2-2)	-	10 (10)	2 (1-4)
cT1	5 (9%)	15 (11%)	33 (65%)	64 (32%)	10 (25%)	0	127 (25%)
cT2	26 (46%)	48 (36%)	17 (33%)	107 (54%)	30 (75%)	0	228 (46%)
cT3	14 (25%)	41 (30%)	1 (2%)	23 (12%)	0	0	79 (16%)
cT4	8 (14%)	27 (20%)	0	0	0	1 (5%)	36 (7%)
FIGO 1	0	0	0	0	0	19 (90%)	19 (4%)
NA	3 (5%)	4 (3%)	0	4 (2%)	0	1 (5%)	12 (2%)
cN0	56 (100%)	134 (99%)	51 (100%)	182 (92%)	40 (100%)	20 (95%)	483 (96%)
cN1	0	1 (1%)	0	16 (8%)	0	1 (5%)	18 (4%)
Pathological TNM							
pTx	0	0	0	8 (4%)	0	0	8 (2%)
pT1	4 (7%)	11 (8%)	32 (63%)	50 (25%)	7 (17%)	0	104 (21%)
pT2	30 (54%)	47 (35%)	18 (35%)	121 (61%)	22 (55%)	0	238 (47%)
pT3	12 (21%)	43 (32%)	0	18 (9%)	11 (28%)	0	84 (17%)
pT4	6 (11%)	26 (19%)	1 (2%)	0	0	1 (5%)	34 (7%)
NA	4 (7%)	8 (6%)	0	2 (1%)	0	1 (5%)	15 (3%)
FIGO 1	-	-	-	-	-	15 (72%)	15 (3%)
FIGO 2	-	-	-	-	-	0	0
FIGO 3	-	-	-	-	-	4 (19%)	4 (1%)
R1	1 (2%)	0	2 (4%)	24 (12%)	18 (45%)	0	45 (9%)
pN +	18 (32%)	26 (19%)	7 (14%)	42 (22%)	8 (20%)	5 (24%)	106 (21%)

**Table S11. Patient characteristics per anatomical location**

Nr. = number, IQR = interquartile range, BMI = body mass index, SCC = squamous cell carcinoma, MCC = Merkel cell carcinoma, UC= Urethral carcinoma, NA = not answered, c = clinical, p = pathological, T = tumor stage, N= nodal stage, R = resection margin, FIGO = Fédération Internationale de Gynécologie et d'Obstétrique. # Number of procedures is more compared to the included patients in penile cancer patient group, because part of these patients were treated with a re-sentinel node biopsy procedure, # 6 patients were scheduled for multiple SN procedures, 4 patients were treated with a re-sentinel node and 2 patients were treated with three sentinel node procedures. Patients with prostate cancer presented with >5% risk on LN metastases according to the Briganti nomogram.

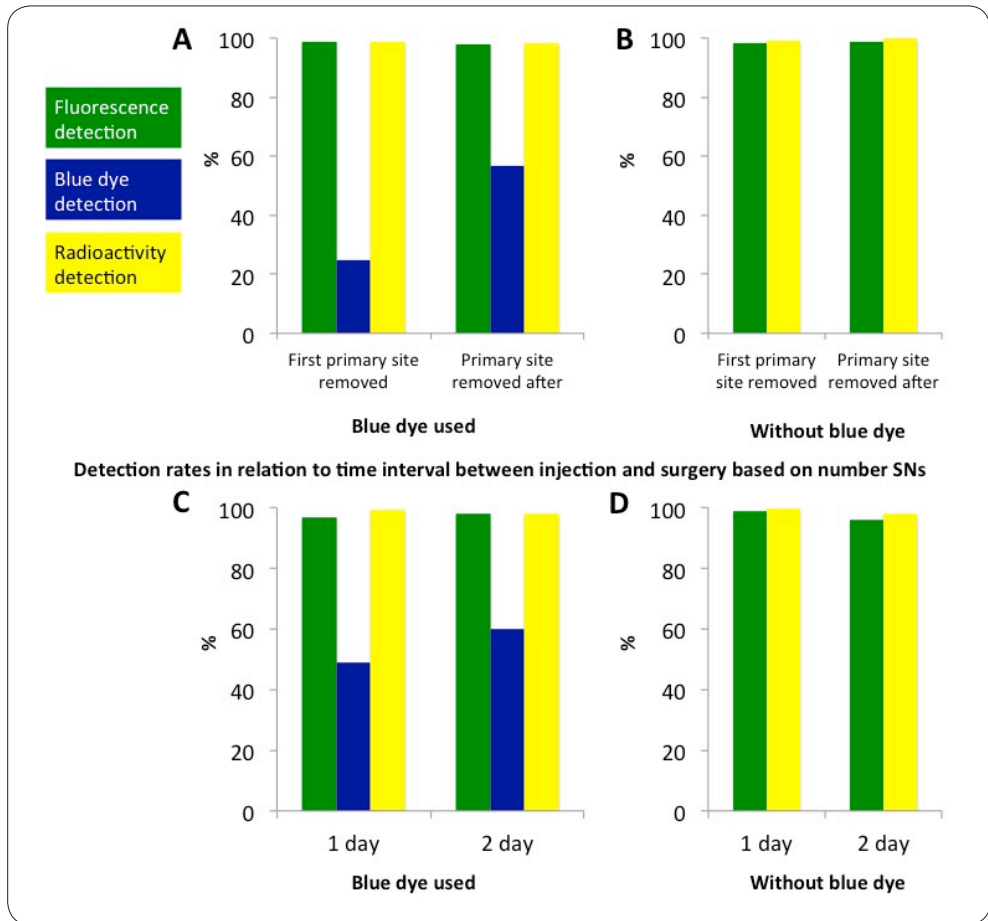


**Figure S11.** The influence of the surgical logistics on imaging findings A) and B) show the detection rates (%) in relation to the order in which the surgical procedure was performed. C) and D) show the detection rates (%) in relation to the time of hybrid tracer administration and the surgical procedure (1-day and 2-day protocol). The green bar represents the fluorescence detection, the blue bar represents the blue optical detection and the yellow bar represents the gamma detection.

### **Intraoperative SN identification vs. SPECT/CT SN identification**

Preoperative imaging with SPECT/CT suffers from its inability to accurately define clustered SNs and can thus underestimate the exact number of SNs that require resection [1-5]. This combined with the improved surgical guidance realized resulted in a discrepancy between preoperatively defined SN-hotspots and excised SN specimens (1327 SNs vs. 1643 SNs; Table SI1, SI2), which in some cases lead to prolongation of the surgical procedures. Here it is important to mention that the increased nodal resection did not negatively influence the morbidity rate when compared to earlier studies using mono-tracers [6-10]. The influence of the increased nodal resection in relation to the tumor find rate is discussed below.

As also reported earlier [6-11], prospective analysis of the CT scans indicated that SN-related hot-spots as observed on SPECT in some cases overlapped with multiple LNs. Recent findings suggest that D-prep MRI could in the future help improve delineation of individual LNs within a single hot-spot [11].

Twelve percent (194/1643) Of the SN's were superficially located and could be resected without the use of the fluorescence signature (these SNs did clearly express a fluorescent signature). In more complex anatomical locations e.g. the head-and-neck or pelvic area, fluorescence guidance was routinely applied and in some cases replaced gamma tracing as go-to guidance modality. Here the fluorescence signal provided superior spatial contrast and helped to better place the SNs within the context of other anatomic structures in the surgical field (Figure SI2). In 8 patients (1.6% of total) an SN could not be distinguished from the injection site with the gamma probe. Yet these SNs were preoperatively identified by SPECT/CT and could readily be resected using fluorescence guidance.

### **Association with body mass index detection rates**

Body mass index (BMI) negatively influenced the *in vivo* fluorescence guidance but did not influence on the radioguidance procedure (Figure SI2). The increase in detection probability for gamma tracing, which was not statistically significant *in vivo* ( $p=0.87$ ) nor *ex vivo* ( $p=0.41$ ), can be partly explained by the fact that in patients with a higher BMI surgeons automatically rely more on this technology than on the optical alternatives. More careful *ex vivo* imaging of the resected tissues yielded improved fluorescence-based identification rates, thereby indicating that this shortcoming was the result of signal attenuation caused by fatty tissues overlaying the SNs. The blue dye identification also improved following *ex vivo* tissue examination.

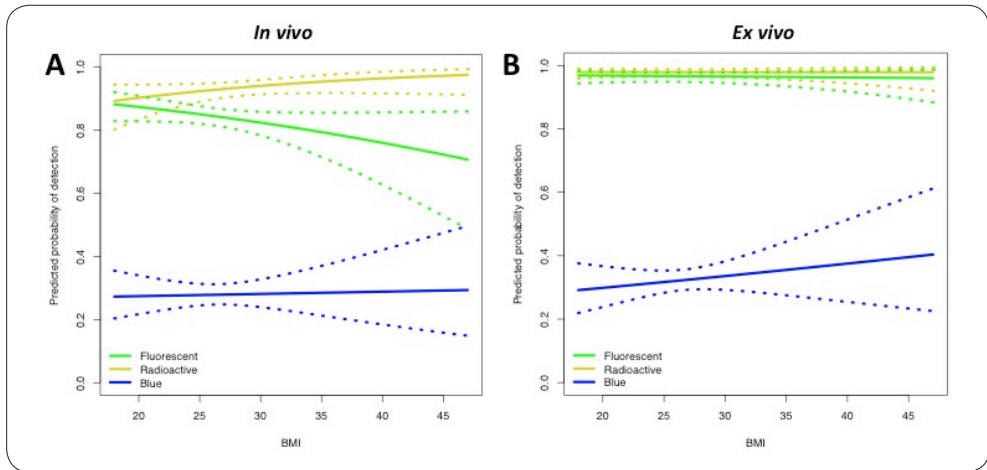


**Figure S12.** Detection curves in relation to body mass index (BMI) A) Depicts the relation between body mass index (BMI) and the *in vivo* probability of detection for the respective modalities used. B) Depicts the same feature, but here the additional *ex vivo* screening was used to extend the *in vivo* findings. The broken lines represent the 95% confidence interval.

### One-day vs. two-day protocol

In the surgical community there is debate with regard to the order wherein SN procedures are performed (primary tumor site removal followed by SN biopsy or SN biopsy followed by primary tumor site removal, or one-day vs. two-day protocol) [12]. We found that the order in which SN biopsy and primary tumor removal was performed did not influence the detection rates of the hybrid tracer (>95% based on *ex vivo* validation). It also indicates that the hybrid tracer reaches its optimal drainage pattern prior to surgery (>2h). However, there was an association between the order, and the blue dye-based SN identification rates: more blue nodes were visualized in patients wherein the SN biopsy was performed before primary tumor removal ( $p < 0.0001$ ) (Figure S11). This finding indicates that migration of lymphangiographic agents such as blue dye to the SNs still occurs during the resection process [13].

No significant differences in fluorescence- or radioactivity-based SN detection percentages between the one- and two-day protocols could be observed (Figure S11 C, D). This finding indicates that migration of lymphangiographic agents such as blue dye to the SNs still occurs during the resection process [13].

	<b>Skin malignancies body</b>	<b>Head-and-neck skin malignancies</b>	<b>Oral cavity</b>	<b>Penile cancer</b>	<b>Prostate</b>	<b>Vulva</b>	<b>Total</b>
Injected dose (MBq), median + IQR	76 (71-80)	82 (73-89)	81 (73-87)	82 (75-86)	218 (206-228)	86 (76-92)	82 (74-90)
<b>Preoperative imaging findings</b>							
Total SNs on early lymphoscintigrams	97	272	121	249	51	36	826
SNs on early lymphoscintigrams, median (IQR)	2 (1-2)	2 (1-3)	2 (2-3)	1 (0-2)	1 (0-2)	1 (1-2)	2 (1-2)
Total SNs on late lymphoscintigrams	114	318	145	494	89	49	1209
SNs on late lymphoscintigrams, median (IQR)	2 (1-3)	2 (1-3)	3 (2-4)	2 (2-3)	3 (2-4)	2 (2-3)	2 (2-3)
Total SNs SPECT/CT	117	348	156	537	119	50	1327
SNs on SPECT/CT, median (IQR)	2 (1-3)	2 (2-3)	3 (2-4)	3 (2-3)	3 (2-4)	2 (2-3)	2 (2-3)
<b>Interval between injection and surgery</b>							
Time (hr) from injection till surgery, median (IQR)	18 (5-20)	5 (5-8)	5 (4-11)	6 (5-19)	5 (4-5)	7 (4-21)	5.75 (4.57- 18.53)
Nr. 1-day protocol procedures (%)	19 (34%)	104 (78%)	38 (75%)	123 (63%)	40 (100%)	12 (57%)	336 (68%)
Nr 2-day protocol procedures (%)	37 (66%)	30 (22%)	13 (25%)	72 (37%)	0	9 (43%)	161 (32%)
<b>Post-operative pathology findings</b>							
Total SNs detected at pathology	138	583	293	691	160	73	1938
Total LNs* detected at pathology	155	656	357	891	326	89	2474
Total nr. positive SNs	24	35	10	41	16	6	132

**Table S12. Preoperative imaging findings and postoperative pathological evaluation per indication of primary tumor location**

MBq = MegaBequerel, IQR = Interquartile range, SN = sentinel node, LN = lymph node, nr. = number, \* These are all nodes found after pathological evaluation, sentinel nodes and lymph nodes together. In the penile cancer patient group and in the prostate cancer group relatively more LNs were found because an additional lymph node dissection.

### Sentinel node Tumor find rate ( $_{SN}TFR$ )

$_{SN}TFR$  rates (see supporting information) were used to place the additionally resected SNs in clinical perspective by relating the number of resected SNs to the 132 tumor positive SNs. Hereby we compensate for the fact that all the SNs identified at pathology are harvested of the surgically dissected specimens labeled as SN. This gave an  $_{SN}TFR_{intraoperative}$  of 8% (132/1643), with a 5.2-18.3% range based on the indication for SN biopsy this decreased slightly if we compensate for the SNs that were not removed 7.8% (132/1693). When the same number was related to the SN-associated hotspots preoperatively identified by SPECT/CT, the  $_{SN}TFR_{SPECT/CT}$  was 9.9 % (132/1327).

Using the  $_{SN}TFR$  values we could show that an overall increase of 19.2 % (611 SNs) resected SNs compared to those identified on SPECT/CT, only yielded a non-proportional 2.1 % drop in  $_{SN}TFR$  (Table S13). If the resection of these additional SNs had no oncologic value, i.e. the additional nodes did not contain cancer, it would be reasonable to expect this drop would have been more substantial. Hence, not resecting these additional SNs could potentially have left nodal metastasis in situ, which may have impacted the FN rates [6, 8, 10]. Since all LNs in the SN labeled pathological specimens were deemed SNs, this gave a 15% increase in SNs-rate compared to the amount of SNs identified during surgery. This increase complicated pathological analysis and was by far the highest in the head-and-neck area, where a 34% increase was presented (Table 1).

Intraoperative detection per location in vivo detection							
	Head-and-neck	Shoulder/arm	Axilla	Inguinal	Pelvic area	Other	Total
Sentinel node evaluated with blue dye							
No optical identification (SNs)	1 (1%)	0	2 (3%)	11 (2%)	-	0	14
Blue only SNs	0	0	1 (1%)	6 (1%)	-	0	7
Fluorescent only SNs	80 (76%)	4 (80%)	22 (29%)	270 (43%)	-	1 (50%)	377
Fluorescent and blue SNs	24 (23%)	1 (20%)	52 (67%)	340 (54%)	-	1 (50%)	418
Total fluorescent SNs	104 (99%)	5 (100%)	74 (96%)	610 (97%)		100 (100%)	795 (97%)
SNs not evaluated for staining	13	0	3	117	-	0	133
Radioactive SNs	117 (99%)	5 (100%)	80 (100%)	722 (97%)	-	2 (100%)	926 (98%)
SNs NA for radioactivity	0	0	0	0	0	0	0
Sentinel nodes evaluated without blue dye							
No optical identification (SNs)	22 (4%)	-	-	-	28 (22%)	-	50 (8%)
Fluorescent SNs	482 (96%)	-	-	-	99 (78%)	-	581 (92%)
SNs not evaluated for staining	61	-	-	-	0	-	61
Radioactive SNs	498 (96%)	-	-	-	82 (100%)	-	580 (97%)
SNs not evaluated for radioactivity	0	-	-	-	0	-	0
Detection per location (ex vivo and in vivo combined)							
	Head-and-neck	Shoulder/ arm	Axilla	Inguinal	Pelvic area	Other	Total
Sentinel node evaluated with blue dye							
Not stained SNs	1 (1%)	0	0	6 (1%)	-	0	7 (1%)
Blue SNs	0	0	0	9 (1%)	-	0	10 (1%)
Fluorescent SNs	90 (77%)	4 (80%)	22 (27%)	310 (43%)	-	1 (50%)	426 (46%)
Fluorescent and blue SNs	26 (22%)	1 (20%)	58 (73%)	397 (55%)	-	1 (50%)	482 (52%)
Total Fluorescent	116 (99%)	5 (100%)	80 (100%)	707 (98%)		2 (100%)	908 (98%)
SNs not evaluated for staining	0	0	0	-	-	0	0
Radioactive SNs	118 (100%)	5 (100%)	80 (100%)	726 (98%)	-	2 (100%)	931 (99%)
Sentinel nodes evaluated without blue dye							
Not stained SNs	6 (1%)	-	-	-	1 (1%)	-	7 (1%)
Fluorescent SNs	552 (99%)	-	-	-	126 (99%)	-	678 (99%)
SNs not evaluated for staining	8	-	-	-	0	-	8
Radioactive	553 (99%)	-	-	-	127 (100%)	-	680 (99%)
SNs not evaluated for radioactivity	0	-	-	-	0	-	0

Table S13. Intraoperative detection per location

Complications rate (Clavien dindo)	Melanoma body	Head and neck melanoma	Oral cavity cancer	Penile cancer	Prostate cancer	Vulva cancer	Total
Grade I	-	3 (2%)	2 (4%)	4 (2%)	1 (3%)	2 (10%)	12 (2.4%)
Grade II	-	3 (2%)	2 (4%)	21 (11%)	5 (13%)	1 (5%)	32 (6.4%)
Grade IIIa	-	-	-	6 (3%)	3 (8%)	1 (5%)	10 (2.0%)
Grade IIIb	1 (2%)	1 (1%)	1 (2%)	6 (3%)	1 (3%)	-	10 (2.0%)
Grade IVa	-	1 (1%)	-	2 (1%)	-	-	3 (0.6%)
Grade IVb	-	-	-	-	-	-	-
Grade V	-	-	-	1 (1%)	-	-	1 (0.2%)
$^{SN}TFR_{SPECT/CT}$	20.5% (24/117)	10.1% (35/348)	6.4% (10/156)	7.6% (41/537)	13.4% (16/119)	12% (6/50)	9.9% (132/1327)
$^{SN}TFR_{intraoperative}$	18.3% (24/131)	7.3% (35/482)	5.2% (10/193)	6.4% (41/640)	12.6% (16/127)	9.7% (6/62)	8.0% (132/1643)
False negative rate (FNR in %)	0%	7% (2/28)	22% (2/9)	16% (6/37) <sup>§</sup>	13 (1/8)	0%	14% (12/87)
FNR without initial n=15	0%	7% (2/28)	0%	16% (6/37)	*	#	10.1% (8/ 79)
FNR based on groins	-	-	-	15% (6/40)	-	0%	-
FNR without re-sentinel nodes	-	-	-	14% (5/36)	-	0%	-

**Table SI4. Complication rates (Clavien-Dindo), TFR, False negative rates.**

TFR = tumor find rate; FNR = false negative rate; <sup>§</sup>FNR 19% including pN1 patient; \* previous reported patients not analyzed for this study, # only 19 patients analyzed.

## Overall survival

In the Kaplan Meier curve of the total study population, with a median follow-up of 33 months, a 78% (CI 67%-90%) survival was found (Figure S13). The overall 5-year survival for the different indications ranged from 40% to 90%, dependent on the primary tumor type (Figure S13B). In all the groups of pR0 patients (n= 437 (88%)), the overall survival decreased when patients were staged pN+ after SN biopsy (Figure S13 C, D).

Despite the fact that the individual patient groups still were relatively small, from overall survival curves we can deduce that the survival for the prostate cancer patients (n = 40; these patients also received an extensive pelvic nodal dissection in addition to the SN procedure), penile cancer patients (n = 186) and the head-and-neck melanoma group (n = 128) were the lowest. For the patients with a melanoma located on the body (n = 53), and the vulva cancer patients (n =19) the survival rates were higher. Unfortunately, the evaluated groups were too small for further stratification of the tumors. Stratification did show that smaller tumors without pN+ have a longer overall survival compared to the higher T-stage tumors. These survival curves are comparable to the ones previously reported for SN procedures performed using routine radioguidance procedures.[10, 14-16] For prostate cancer patients after SN biopsy and ePLND combined with prostatectomy no literature on survival rates is available, as has been described by Wit et al.[3]

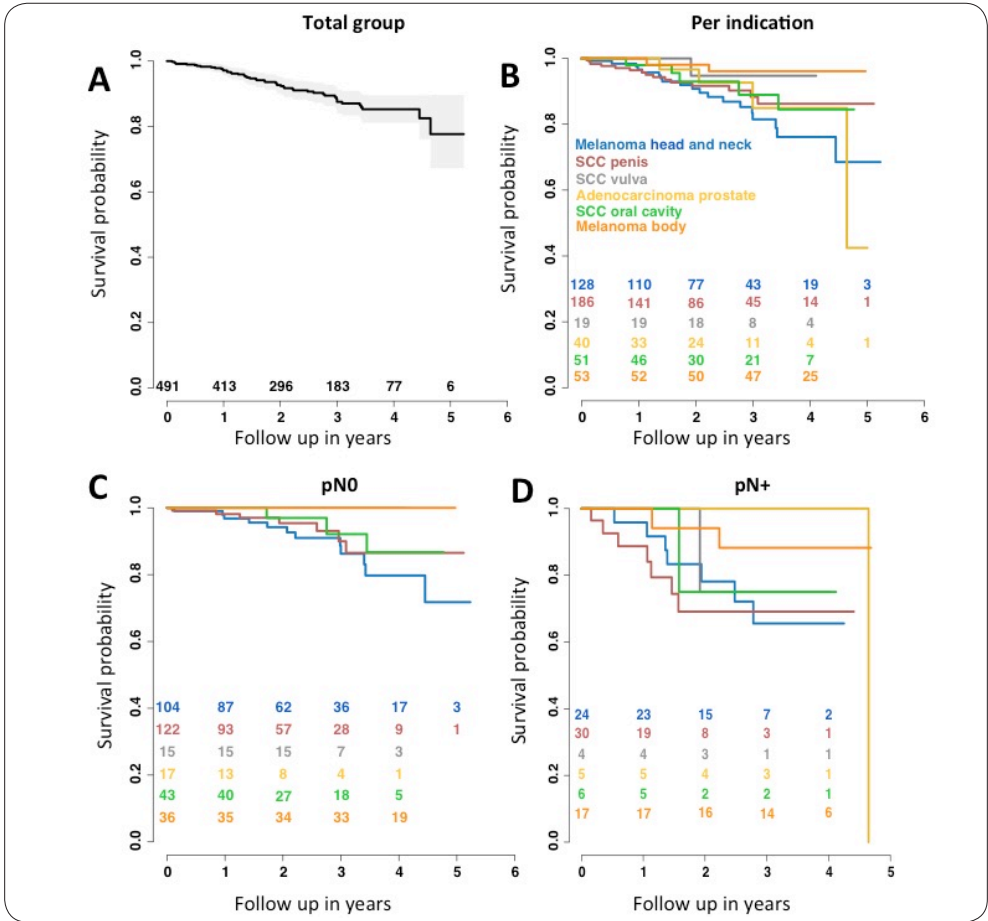


**Figure S13. Overall survival curves:**

**A)** The overall Kaplan Meier survival curve of all patients combined,

**B)** The overall survival for each individual group.

In **C)** and **D)** the survival curves are shown for the pN0 and pN+ patients, respectively.

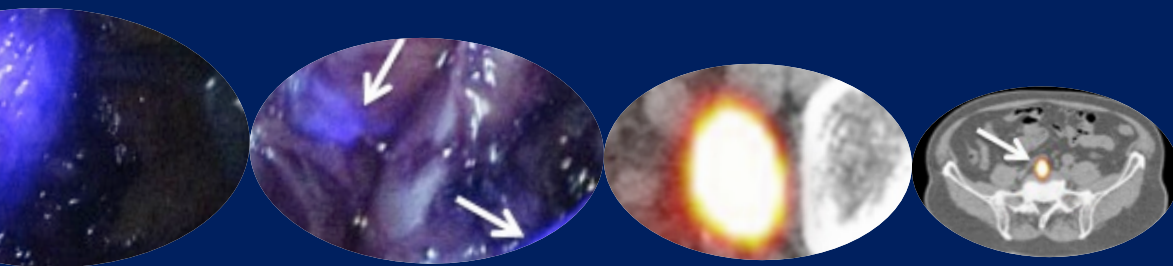
## REFERENCES

1. KleinJan, G.H., et al., Optimisation of fluorescence guidance during robot-assisted laparoscopic sentinel node biopsy for prostate cancer. *Eur Urol*, 2014. 66(6): p. 991-8.
2. Nieweg, O.E., P.J. Tanis, and B.B. Kroon, The definition of a sentinel node. *Ann Surg Oncol*, 2001. 8(6): p. 538-41.
3. Wit, E.M.K., et al., Sentinel Node Procedure in Prostate Cancer: A Systematic Review to Assess Diagnostic Accuracy. *Eur Urol*, 2017. 71(4): p. 596-605.
4. Jimenez-Heffernan, A., et al., Results of a Prospective Multicenter International Atomic Energy Agency Sentinel Node Trial on the Value of SPECT/CT Over Planar Imaging in Various Malignancies. *J Nucl Med*, 2015. 56(9): p. 1338-44.
5. van den Berg, N.S., et al., Multimodal Surgical Guidance during Sentinel Node Biopsy for Melanoma: Combined Gamma Tracing and Fluorescence Imaging of the Sentinel Node through Use of the Hybrid Tracer Indocyanine Green-(99m)Tc-Nanocolloid. *Radiology*, 2015. 275(2): p. 521-9.
6. Flach, G.B., et al., Sentinel lymph node biopsy in clinically N0 T1-T2 staged oral cancer: the Dutch multicenter trial. *Oral Oncol*, 2014. 50(10): p. 1020-4.
7. Kretschmer, L., et al., Nodal Basin Recurrence After Sentinel Lymph Node Biopsy for Melanoma: A Retrospective Multicenter Study in 2653 Patients. *Medicine (Baltimore)*, 2015. 94(36): p. e1433.
8. Pezier, T., et al., Sentinel lymph node biopsy for T1/T2 oral cavity squamous cell carcinoma--a prospective case series. *Ann Surg Oncol*, 2012. 19(11): p. 3528-33.
9. Valsecchi, M.E., et al., Lymphatic mapping and sentinel lymph node biopsy in patients with melanoma: a meta-analysis. *J Clin Oncol*, 2011. 29(11): p. 1479-87.
10. Van der Zee, A.G., et al., Sentinel node dissection is safe in the treatment of early-stage vulvar cancer. *J Clin Oncol*, 2008. 26(6): p. 884-9.
11. Buckle, T., et al., Diffusion-weighted-preparation (D-prep) MRI as a future extension of SPECT/CT based surgical planning for sentinel node procedures in the head and neck area? *Oral Oncol*, 2016. 60: p. 48-54.
12. Dimopoulos, P., et al., Dynamic sentinel lymph node biopsy for penile cancer: a comparison between 1- and 2-day protocols. *BJU Int*, 2016. 117(6): p. 890-6.
13. Manny, T.B., M. Patel, and A.K. Hemal, Fluorescence-enhanced robotic radical prostatectomy using real-time lymphangiography and tissue marking with percutaneous injection of unconjugated indocyanine green: the initial clinical experience in 50 patients. *Eur Urol*, 2014. 65(6): p. 1162-8.
14. Djajadiningrat, R.S., et al., Contemporary management of regional nodes in penile cancer-improvement of survival? *J Urol*, 2014. 191(1): p. 68-73.
15. Lee, D.Y., et al., Predictors and Survival Impact of False-Negative Sentinel Nodes in Melanoma. *Ann Surg Oncol*, 2016. 23(3): p. 1012-8.
16. Schilling, C., et al., Sentinel European Node Trial (SENT): 3-year results of sentinel node biopsy in oral cancer. *European Journal of Cancer*. 51(18): p. 2777-2784.



# Chapter 4





4

# Optimization of fluorescence guidance during robot-assisted laparoscopic sentinel node biopsy for prostate cancer

*Gijs H. KleinJan\**  
*Nynke S. van den Berg\**  
*Oscar R. Brouwer*  
*Jeroen de Jong*  
*Cenk Acar*  
*Esther M. Wit*  
*Eric Vegt*  
*Vincent van der Noort*  
*Renato A. Valdés Olmos*  
*Fijs W.B. van*  
*Leeuwen*

*Henk G. van der Poel*  
*Eur Urol. 2014;66:991-8.*

*\* Authors share first authorship.*

## ABSTRACT

### INTRODUCTION

The hybrid tracer was introduced to complement intraoperative radiotracing towards the sentinel nodes (SNs) with fluorescence guidance. In this chapter the hybrid tracer preparation, injection technique, and fluorescence imaging hardware were adjusted to optimize the *in vivo* fluorescence-based SN identification for prostate cancer.

### METHODS

Forty patients with a Briganti nomogram-based risk >5% of lymph node (LN) metastases were included. After intraprostatic tracer injection, SN mapping was performed (lymphoscintigraphy and single photon emission computed tomography with computed tomography (SPECT/CT)). In groups 1 and 2, SNs were pursued intraoperatively using a laparoscopic gamma probe followed by fluorescence imaging. In group 3, SNs were initially located via fluorescence imaging. Compared with group 1, in groups 2 and 3, a new tracer formulation was introduced that had a reduced total injected volume (2.0 mL vs. 3.2 mL) but increased particle concentration. For groups 1 and 2, the Tricam SLII with D-Light C laparoscopic fluorescence imaging system was used. In group 3, the laparoscopic fluorescence imaging system was upgraded to an Image 1 HUB HD with D-Light P system. Number and location of the preoperatively identified SNs, *in vivo* fluorescence-based SN identification rate, tumor status of SNs and LNs, postoperative complications, and biochemical recurrence (BCR) were scored.

### RESULTS

Mean fluorescence-based SN identification improved from 63.7% (group 1) to 85.2% and 93.5% for groups 2 and 3, respectively ( $p=0.012$ ). No differences in postoperative complications were found. In three pN0 patients BCR occurred during follow up.

### CONCLUSIONS

Stepwise optimization of the hybrid tracer formulation and the LFI system led to a significant improvement in fluorescence-assisted SN identification. Preoperative SPECT/CT remained essential for guiding intraoperative SN localization. Patient summary: Intraoperative fluorescence-based SN visualization can be improved by enhancing the hybrid tracer formulation and laparoscopic fluorescence imaging system.

## INTRODUCTION

Sentinel node (SN) biopsy using a radioactive tracer was introduced for prostate cancer (PCa) to minimize the extent of the pelvic lymph node (LN) dissection (PLND) while retaining diagnostic accuracy [1]. The concept behind SN biopsy is to identify the LNs that are most likely to contain metastatic cells in case migration from the primary prostate tumor has occurred, the so-called SNs. Visualization of this direct drainage pathway transcends the anatomic location of the SN. Therefore, this technique also enables the identification of potential tumor-bearing LNs outside the extended PLND (ePLND) template [2,3] that would otherwise have been missed. When performing SN biopsy in combination with an ePLND, improved lymphatic staging can be achieved; pathologists can evaluate the SNs more extensively, decreasing the possibility of sampling errors, which can result in improved diagnostic accuracy [4,5].

Since its introduction, the procedure has been subject to various refinements. In the past 15 years, the surgical technique has shifted from a mainly open procedure to a laparoscopic and later a robot-assisted procedure. For preoperative SN mapping, following the injection of a radioactive tracer, lymphoscintigrams are taken. The introduction of single photon emission computed tomography with computed tomography (SPECT/CT) resulted in improved anatomic SN localization, allowing better planning of the operation and reducing operative time [6].

To date, intraoperative SN identification is based primarily on the use of a (laparoscopic) gamma probe (LGP; radio-guided approach). The recent introduction of fluorescence imaging (FI) during surgery was shown to aid the surgeon in optical, fluorescence-based, visualization of the SNs [7,8]. Yet, the limited penetration depth of the near-infrared fluorescent dye indocyanine green (ICG; < 1.0 cm) prohibits preoperative SN mapping, meaning that during surgery meticulous scanning of, and beyond, the entire ePLND template is required [2,6]. This exploration is extensive and time-consuming and may potentially miss SNs. Hence, the use of ICG is often combined with radiocolloid-based preoperative SN mapping methods [8]. To facilitate the integrated use of preoperative imaging with fluorescence guidance, we introduced the hybrid tracer ICG-<sup>99m</sup>Tc-nanocolloid [6]. Being both radioactive and fluorescent, a single ICG-<sup>99m</sup>Tc-nanocolloid administration allows for preoperative SN mapping as well as intraoperative fluorescence guidance to these exact hotspots. In our previous studies, the hybrid nature of this tracer was shown to complement the radio-guided approach and outperformed blue dye [9,10].

Following our initial feasibility study in PCa [11], 40 additional PCa patients were included. In

these patients, we systematically evaluated whether optimization of the tracer formulation and FI hardware improvements could help increase *in vivo* fluorescence-based SN identification during robot-assisted laparoscopic procedures.

## METHODS

### Patients

Between December 2010 and July 2013, 40 patients with localized PCa and a Briganti nomogram–estimated risk >10% of LN metastases were included after informed consent was obtained. Patients were scheduled for robot-assisted radical prostatectomy (RARP) and SN biopsy followed by an ePLND. The first nine patients were included under registration of the feasibility study (N09IGF), and the patient population was completed through off-label use of the hybrid tracer.

Three groups were formed for statistical analysis. In group 1 (n = 11; December 2010 – April 2011), the previously described hybrid tracer preparation [11] and the Tricam SLII with D-Light C laparoscopic fluorescence imaging (LFI) system (KARL STORZ GmbH & Co. KG, Tuttlingen, Germany) was used. In group 2 (n = 13; April 2011 – November 2012), the particle concentration was increased, and the injected volume decreased. In group 3 (n = 16; December 2012 – July 2013), the tracer formulation was identical to that used in group 2, but an upgraded LFI system (Image 1 HUB HD with D-Light P system KARL STORZ GmbH & Co. KG) was introduced.

### Tracer preparation

Two different tracer formulations were used. In group 1, we prepared the hybrid tracer as previously described (0.4 ml in the syringe; referred to as the previously described tracer formulation) [11]. In groups 2 and 3, we used the new tracer formulation.

The new tracer formulation was prepared as follows:  $^{99m}\text{Tc}$ -nanocolloid was made by adding 2.0 ml pertechnetate (approximately 300 MBq) to a vial of nanocolloid (GE Healthcare, Eindhoven, The Netherlands). ICG- $^{99m}\text{Tc}$ -nanocolloid was then formed by adding 0.05 ml (0.25 mg) of ICG solution (5.0 mg/ml; PULSION Medical, Feldkirchen, Germany) to the vial. After *in situ* formation of ICG- $^{99m}\text{Tc}$ -nanocolloid, the tracer was subtracted from the vial and diluted with saline to a total volume of 2.0 ml in the syringe. Procedures were performed in accordance with the Dutch guidelines for good manufacturing practice and with approval of the local pharmacist.

### Tracer injection

The hybrid tracer was injected transrectally into the peripheral zone of each quadrant of the prostate under ultrasound guidance [11]. In group 1, four deposits of 0.1 ml ICG-<sup>99m</sup>Tc-nanocolloid were given. After each injection, the needle was flushed with 0.7 ml saline (total injected volume: 3.2 ml). In groups 2 and 3, patients received four deposits of 0.5 ml ICG-<sup>99m</sup>Tc-nanocolloid (total injected volume: 2.0 ml).

### Preoperative sentinel node mapping

Static planar lymphoscintigraphy was performed 15 min and 2 h after injection, followed by a SPECT and low-dose CT scan (Symbia T; Siemens Healthcare, Erlangen, Germany). SPECT and low-dose CT images were fused, and a three-dimensional (3D) SPECT/CT-based volume-rendering reconstruction was created using OsiriX medical imaging software (Pixmeo, Geneva, Switzerland). Images were analyzed by an experienced nuclear medicine physician according to previously described criteria [12].

### Surgical procedure

Operations were performed by HGvdP using the da Vinci S Surgical system (Intuitive Surgical Inc., Sunnyvale, CA, USA). Patients, first underwent SN biopsy, followed by ePLND and RARP. In the case of a one-sided SN non-visualization following preoperative imaging, an ePLND was performed on that side. The ePLND comprised all LNs in the internal, obturator, and external regions proximal of the ureter vessel crossing and distally from the pubic bone. SNs outside the ePLND template were defined as described by Meinhardt et al. [13].

Preoperatively acquired SPECT/CT images and the 3D volume-rendered image were used as a virtual roadmap for the localization of the individual SNs. Intraoperatively, in groups 1 and 2, SNs were initially pursued using an LGP (Europrobe 2; Eurorad, Eckbolsheim, France) followed by confirmatory FI. In group 3, SNs were initially localized via FI followed by *ex vivo* confirmation via gamma tracing. Real-time fluorescence images were introduced into the da Vinci S system via the TilePro function [11].

### Fluorescence imaging hardware

In this study, two generations of laparoscopic fluorescence imaging systems were used: the Tricam SLII with D-Light C system (groups 1 and 2) and the Image 1 HUB HD with D-Light P system (group 3) (both KARL STORZ GmbH & Co. KG).

### **Pathologic examination**

LNs and SNs were formalin fixed, cut at 2 mm, and paraffin embedded. LN sections were stained with haematoxylin and eosin (H&E). SNs were cut at three levels (150 nm intervals), and sections were H&E stained. In addition, on the second level, an immuno-histochemical stain was performed using a CAM5.2 antibody (catalogue number 345779; Becton Dickinson Biosciences, San Jose, CA, USA). Prostatectomy specimens were formalin fixed, paraffin embedded, and classified according to the 2009 TNM classification.

### **Follow-up**

Postoperative complications (within 90 d post surgery) were scored using the Clavien-Dindo score [14]. Patients were evaluated for biochemical recurrence (BCR; prostate-specific antigen > 0.1 ng/ml) during follow-up.

### **Statistical analysis**

For continuous variables, the mean or median and interquartile range (IQR; 25–75%) is given. For discrete variables, frequencies and percentages are reported. Study end points were as follows: intraoperative fluorescence-based SN identification rate - defined for each patient as  $([\text{number of SNs intraoperatively visualized via fluorescence imaging}] / [\text{total number of SNs seen on preoperative imaging}]) \times 100\%$  -, postoperative complications, and BCR.

A one-way analysis of variance was performed for evaluation of the number of postoperative complications in the three groups. We used the nonparametric Kruskal-Wallis test for evaluation of between-group differences in intraoperative fluorescence-based SN identification rate and the number of harvested SNs and LNs. For BCR-free survival, we performed a log-rank test comparing groups 1 and 2 with group 3. A chi-square test was performed to evaluate whether there was a difference in pN1 patients among the three groups. Statistical analysis was performed using SPSS v.20 (IBM Corp., Armonk, NY, USA). In general, viewing our 40 patients as a random sample of the entire population, our null hypothesis is that the unknown distributions of these rates in the population are the same across the three groups. A p value <0.05 was considered significant.

	<b>Total</b>	<b>Group 1</b>	<b>Group 2</b>	<b>Group 3</b>
No. patients	40	11	13	16
Age, median (IQR)	64 (60-68)	62 (59-69)	64 (61-67)	65 (60-70)
Preoperative PSA-level (ng/mL), median (IQR)	8.5 (6.4-13.9)	12.0 (8.1-17.2)	9.0 (6.9-15.5)	6.8 (5.2-9.0)
<b>Clinical T-stage</b>				
- 1c (%)	7	2	3	2
- 2a (%)	3	1	1	1
- 2b (%)	10	4	3	4
- 2c (%)	9	1	3	4
- 3a (%)	9	3	2	4
- 3b (%)	2	0	1	1
<b>Biopsy Gleason sum score</b>				
- 6 (%)	4	4	0	0
- 7 (%)	30	6	8	16
- 8 (%)	5	1	4	0
- 9 (%)	1	0	1	0
- 10 (%)	0	0	0	0
<b>Pathologic T-stage</b>				
- 2a (%)	0	0	0	0
- 2b (%)	6	2	1	3
- 2c (%)	16	3	5	8
- 3a (%)	16	5	6	5
- 3b (%)	2	1	1	0
<b>Pathologic Gleason sum score</b>				
- 6 (%)	4	0	2	2
- 7 (%)	28	9	6	14
- 8 (%)	3	1	2	0
- 9 (%)	4	0	3	0
- 10 (%)	1	1	0	0

**Table 1. Patient characteristics**

IQR = interquartile range; no. = number; PSA = prostate specific antigen.

	<b>Total (n=38<sup>a</sup>)</b>	<b>Group 1</b>	<b>Group 2</b>	<b>Group 3</b>	<b>p-value</b>
Number of intraoperatively detected SNs, per patient, median (IQR)	3 (2-4)	2 (2-3)	4 (2.5-4)	4 (2-4)	0.2 <sup>a</sup>
<b>In vivo SN identification</b>					
- Fluorescence-based SN identification rate <sup>#</sup> in vivo, per patient, mean % (mean% corrected for malfunctioning equipment)	72.9% (84.0%*)	50.9% (63.7%*)	63.8% (85.2%*)	93.5% (93.5%*)	0.005 <sup>a</sup> (0.012 <sup>a</sup> )
- Radioactivity-based SN detection in vivo, per patient, mean%	100%	100%	100%	NA	-
<b>Ex vivo SN measurements</b>					
- Fluorescence-based SN detection ex-vivo, %	96.9%	92.6%	97.7%	100.0%	-
- Radioactivity-based SN detection ex vivo, %	100.0%	100.0%	100.0%	100.0%	-
Time per combined SN, ePLND and prostatectomy procedure (h), median (IQR)	2:07 (2:00-2:12)	2:01 (1:50-2:01)	2:04 (2:00-2:14)	2:06 (2:02-2:14)	0.2 <sup>b</sup>

**Table 2. Intraoperative sentinel node identification and ex vivo measurements**

<sup>a</sup> Two patients were excluded due to non-visualization on preoperative images (one patient in group 1, and one patient in group 2).

<sup>#</sup> Intraoperative fluorescence-based SN identification rate is defined as: defined for each patient as: ((number of SNs intraoperatively visualized via fluorescence imaging) / (total number of SNs seen on preoperative imaging)) x 100%.

\* Intraoperative fluorescence-based SN identification rate after correction for non-visualization due to malfunctioning equipment.

<sup>a</sup> = Kruskal-Wallis test; <sup>b</sup> = ANOVA-test; n = number; NA = not applicable,

IQR = interquartile range; SN = sentinel node; n = number of patients.

## RESULTS

### Preoperative imaging

Patient characteristics are shown in Table 1. At least one SN was preoperatively identified in 38 of the 40 patients. Bilateral non-visualization occurred in two patients (5.0%) and unilateral non-visualization in five patients (12.5%). Lymphoscintigraphy and SPECT/CT identified a total of 119 SNs (median: 3; IQR: 0–2). Results per subgroup are specified in Supplemental Table 1. Changing the hybrid tracer formulation did not yield a significant difference in the number of preoperatively visualized SNs (Table 2). However, with the new tracer formulation, flushing was no longer necessary between placement of the different tracer deposits, thereby reducing injection time and increasing the ease of the procedure.

### Intraoperative sentinel node identification

Six of the preoperatively identified SNs could not be resected because of the risk of injury or mechanical limitations of the robot (pararectal region inside the mesorectal fascia ( $n = 3$ ), presacral region ( $n = 2$ ), and right iliac region ( $n = 1$ ; Table 3).

In 7 patients, 14 additional SNs were removed during surgery based on their fluorescent and radioactive appearance in the same region as the SNs detected with preoperative imaging. In retrospect, in six of these seven patients, LN clusters could be visualized on CT (Figure 1). Overall, 127 SNs (median: 3 per patient; IQR: 2–4; Table 2) were identified during surgery. In 16 patients (40.0%), an SN was located outside the ePLND template (Figs. 2 and 3; Table 3). The two patients who had non-visualization on preoperative imaging were excluded from the intraoperative SN detection outcome analysis. With every stepwise modification, the intraoperative fluorescence-based SN visualization rate increased (Table 2). The mean optical SN visualization percentage modestly increased from 50.9% (group 1) to 63.8% (group 2) after the tracer formulation was altered. In these two groups, in five patients (group 1: two patients; group 2: three patients), none of the SNs could be intraoperatively visualized via FI for reasons of malfunctioning equipment (damaged light cable). After excluding these patients, the *in vivo* fluorescence-based SN visualization percentage of groups 1 and 2 was found to be 63.7% and 85.2%, respectively. Following the introduction of the upgraded LFI system (group 3), the mean intraoperative visualization percentage went up to 93.5% ( $p = 0.012$ ). *Ex vivo* measurements in the operating room revealed a fluorescent signal in 123 of the 127 excised SNs.

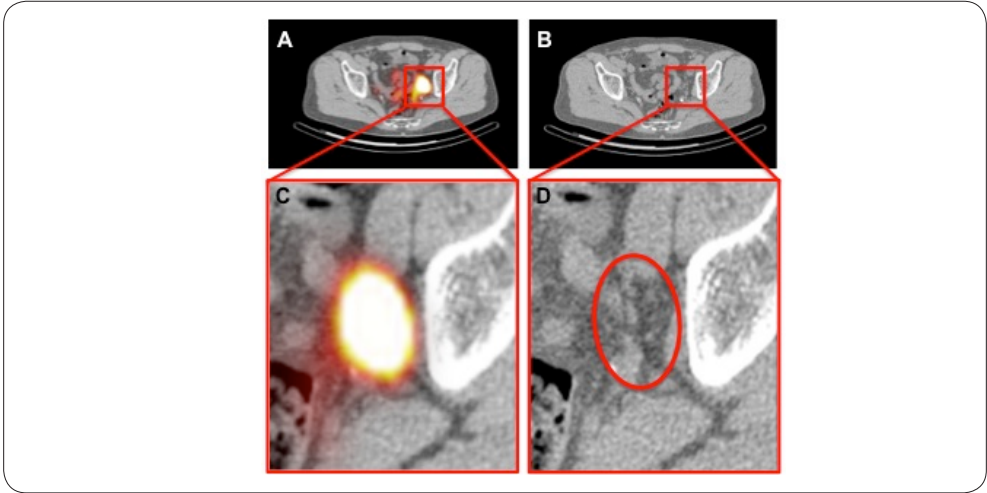


**Figure 1. Clustered lymph nodes as seen on single-photon emission computed tomography with computed tomography (SPECT/CT) imaging:**

- (A)** Fused SPECT/CT image showing the location of a single radioactive hotspot in the left obturator region;
- (B)** corresponding CT image; **(C)** zoom showing the radioactive hotspot; **(D)** multiple lymph nodes were visualized on the CT image in the area of the radioactive hotspot.

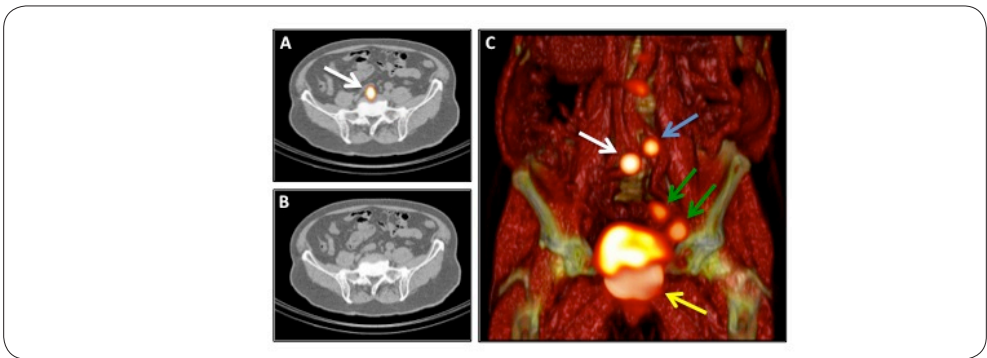


**Figure 2. Illustration of the localization of sentinel nodes (SNs) outside the extended pelvic lymph node dissection template:**

- (A)** Fused single-photon emission computed tomography with computed tomography (CT) image showing the location of a single radioactive hotspot at the aorto-caval level (white arrow);
- (B)** corresponding CT image;
- (C)** three-dimensional volume rendering showing the injection site (yellow arrow), the aorto-caval SN (white arrow), and two SNs at the external iliac and obturator region (green arrows). A higher-echelon para-aortic lymph node (blue arrow) was also visualized.

### Pathologic examination

Overall, histopathologic analysis of the excised tissues yielded 467 LNs: 160 nodes in the SN specimens and 307 additional nodes resected from the subsequent ePLND template. In 8 patients, a total of 32 tumor-positive nodes was found: 16 SNs and 16 LNs (Table 4; Supplemental Table 2). In three patients, the SN was the only tumor-positive node. In three other patients, next to a tumor-positive SN, a tumor-positive LN was also found. Strikingly, in 1 of these 3 patients, next to 2 tumor-positive SNs, we found 12 tumor-positive LNs (Supplemental Table 2). In the last two positive patients, SNs were tumor free, but a tumor-positive LN was found. In one of these two patients, the positive LN was found in the ePLND tissue (false-negative SN biopsy procedure). In the other patient, a small positive LN (3 mm) was found in the prostatectomy specimen. This particular LN was not seen on preoperative images.

On a per-patient basis, the sensitivity of the SN biopsy procedure was 75.0% (six out of eight pN1 patients correctly staged with SN biopsy), with a negative predictive value of 94.1%. On a per-tumor-positive node basis, this sensitivity is 50.0% (16 tumor-positive SNs on a total of 32 positive nodes; Table 4).

### 3.4. Follow-up

No significant differences in postoperative complications were found among the three groups ( $p = 0.9$ ; Table 5). Although follow-up was relatively short, in patients without nodal metastases (pN0), the Kaplan-Meier curve showed an improvement in BCR-free survival in group 3 ( $n = 0$ ; total follow-up: 25 months) versus men in groups 1 and 2 ( $n = 3$ ; total follow-up: 38 months;  $p = 0.2$ ; Figure 4).

### Discussion

This study demonstrates that optimization of the hybrid tracer formulation and injection technique, as well as upgrading the LFI system, improved *in vivo* fluorescence-based SN identification during RARP. Without altering the efficacy of preoperative SN mapping, the new tracer formulation increased the injected amount of ICG-<sup>99m</sup>Tc-nanocolloid particles 2.5-fold and reduced the injected volume 1.6-fold. In combination with initial LGP exploration, the *in vivo* fluorescence visualization efficiency increased by 21.5% (group 1 vs. group 2). This increase contradicts our previous findings in breast cancer patients, where a 2-fold increase in the amount of injected particles did not lead to a change in fluorescence visualization efficiency [15]. Feedback from previous studies taught us that the SN has to be exposed within millimeters of the surface to allow for *in vivo* fluorescence-based detection

	Total	Group 1	Group 2	Group 3
<b>SNs removed from ePLND template, no. (% total)</b>				
- Left obturator region	19 (15.0%)	4 (3.1%)	4 (3.1%)	11 (8.7%)
- Right obturator region	28 (22.0%)	7 (5.5%)	10 (7.9%)	11 (8.7%)
- Left external region	18 (14.2%)	6 (4.7%)	8 (6.3%)	4 (3.1%)
- Right external region	16 (12.6%)	5 (3.9%)	5 (3.9%)	6 (4.7%)
- Left internal region	9 (7.1%)	0	5 (3.9%)	4 (3.1%)
- Right internal region	7 (5.5%)	0	2 (1.6%)	5 (3.9%)
- Left common iliac trunk	10 (7.9%)	3 (2.4%)	4 (3.1%)	3 (2.4%)
- Right common iliac trunk	2 (1.6%)	0	0	2 (1.6%)
Subtotal	109 (85.8%)	25 (19.7%)	38 (29.9%)	46 (36.2%)
<b>SN removed outside ePLND template, no. (% total)</b>				
- Pararectal (mesorectal fascia) region	5 (3.9%)	1 (0.8%)	0	4 (3.1%)
- Presacral region	5 (3.9%)	1 (0.8%)	2 (1.6%)	2 (1.6%)
- Paravesical region	4 (3.1%)	0	0	4 (3.1%)
- Right umbilical ligament	1 (0.8%)	0	1 (0.8%)	0
- Left umbilical ligament	1 (0.8%)	0	1 (0.8%)	0
- Para-aortal region	2 (1.6%)	0	2 (1.6%)	0
Subtotal	18 (14.2%)	2 (1.6%)	6 (4.7%)	10 (7.9%)
Total	127 (100.0%)	27 (21.3%)	44 (34.6%)	56 (44.1%)
<b>Not removed SN, no.</b>				
- Pararectal region	3	1	1	1
- Presacral region	2	0	1	1
- Right iliac region	1	1	0	0
Total	6	2	2	2

**Table 3. Number and location of the intraoperatively identified sentinel nodes**

SN = sentinel node; ePLND = extended pelvic lymph node dissection; no. = number.

	Total	Group 1	Group 2	Group 3	p-value
No. patients pN1	8	2	3	3	0.9 <sup>b</sup>
<b>SN evaluation</b>					
- No. harvested SNs / patient, median (IQR)	4 (2.3-5.0)	3 (2.0-3.0)	4 (2.5-5.5)	4 (3.0-5.8)	0.028 <sup>a</sup>
- Total no. SNs	160	29	57	74	
- Total no. tumor-positive SNs	16	1	5	9	
<b>LN evaluation</b>					
- No. harvested LNs from ePLND/patient, median (range)	8 (4.5-11.0)	4 (4.0-10.0)	6 (4.5-12.0)	9 (7.3-11.0)	0.2 <sup>a</sup>
- Total no. LNs	307	65	95	147	
- Total no. tumor-positive LN	16	1	13	2	
<b>SN + LN evaluation</b>					
- Total no. removed nodes per patient (SN + ePLND), median (IQR)	12 (9.0-14.8)	9 (6.0-11.0)	11 (8.0-15.5)	12 (11.0-16.0)	0.026 <sup>a</sup>
- Total no. harvested SNs + LNs	467	94	152	221	

**Table 4. Pathologic node evaluation**

<sup>a</sup> = Kruskal-Wallis test; <sup>b</sup> = Chi-square test.

no. = number of patients; IQR = interquartile range; No. = number; SN = sentinel node; LN = lymph node; ePLND = extended pelvic lymph node dissection; pN1 = positive for regional lymph node metastases.

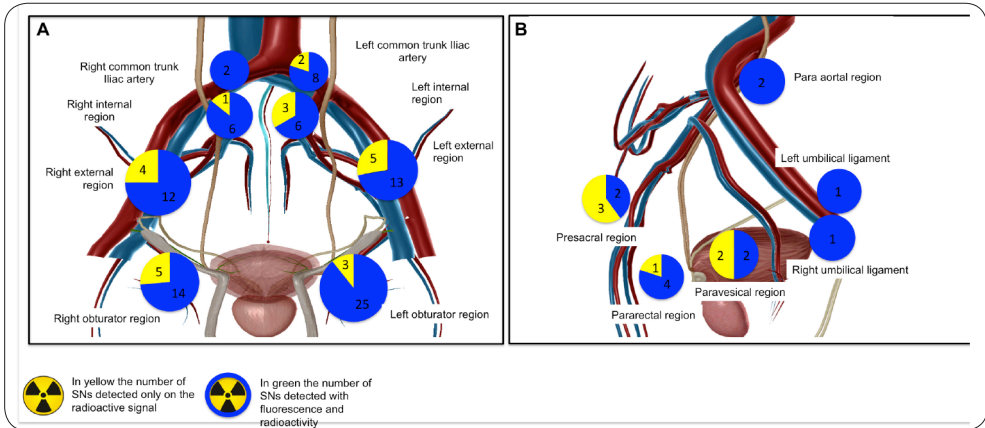


**Figure 3. Intraoperative sentinel node (SN) location.**

(A) SNs inside the extended pelvic lymph node dissection (ePLND) template;

(B) SNs outside the ePLND template. Intraoperatively, nodes were detected using radio-guidance (yellow) or radio-and fluorescence guidance (blue). The schematic images used to illustrate the location of the detected SNs were generated with Visible Body software (Argosy Publishing, Newton Upper Falls, MA, USA).

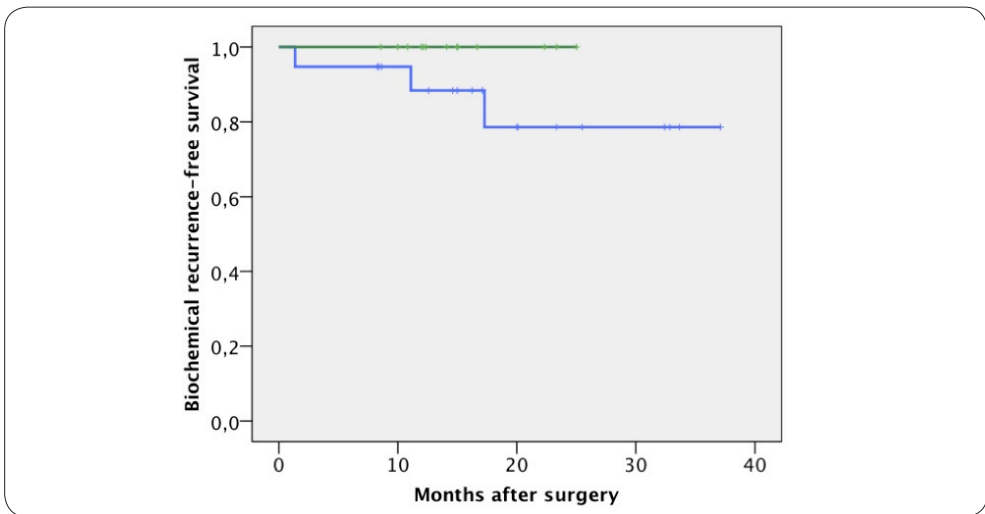


**Figure 4. Kaplan-Meier curve illustrating biochemical recurrence (BCR) in pN0 patients.**

The blue line represents groups 1 and 2, in which three BCRs were found. The orange line represents group 3.

[9,10,16]. Hence, an explanation for this finding may lie in the time taken for the now more routine surgical exploration; findings in group 1 turned out lower than the reported 85% in our feasibility study, which was based on the same approach.

After upgrading the LFI system (group 3), the mean intraoperative fluorescence-based SN visualization percentage increased to 93.5%, transforming the procedure in a potential driver to improve intraoperative localization of tumor-positive SNs, even within the standard ePLND template. This improvement may provide better nodal staging (the “Will Rogers” phenomenon) and help improve the BCR-free survival rate, as was seen in group 3 [17]. The tailored filter settings allowed visualization of the near-infrared fluorescence signal (displayed in blue) as an integral part of the patient anatomy (displayed in “normal” colored view; Figure 5). Despite a slight loss in sensitivity, this continuous exploration of the surgical field via FI proved extremely valuable for the localization of the SN. In combination with the 3D information that SPECT/CT provided, this improvement may render initial exploration with the LGP *in vivo* redundant, provided that the fluorescence-based SN identification rate equals that of its radioactive counterpart. This is attractive because fluorescence does not suffer from the shine-through phenomenon from the tracer deposits in the prostate, as is the case for the radio-guided approach [18].

Of the 16 tumor-positive SNs that were resected during the operation, one was located outside the ePLND template (6.3%). This finding underlines previous reports stating that metastatic spread may occur beyond the ePLND template [13,19]. In 5 of the 8 LN-positive patients, we found positive LNs beyond the resected SNs; in total, 16 additional tumor-positive LNs were recovered from the ePLND specimens. It must be noted that one patient accounts for 75% of these positive LNs (Supplemental Table 2). Based on our findings, we believe that SN identification via the hybrid approach (including SPECT/CT) combined with ePLND provides the best approach for nodal staging in combination with RARP.

The main limitations of the study are the small patient population, the possibility that SN identification rates may increase over time because of a learning curve, and the relatively low number of overall nodes removed. The cost-effectiveness and the independent use of intraoperative fluorescence guidance remain to be investigated; currently, an international multicenter study is being initiated to address this question. Still an important question remains to be answered: What is the best hybrid tracer injection technique? In our current, ongoing study (N12IGP), we will evaluate whether the location of hybrid tracer injection (intraprostatic vs. intratumoural) is relevant for the detection and localization of tumor-positive SNs.

	<b>Total</b>	<b>Group 1</b>	<b>Group 2</b>	<b>Group 3</b>
No. patients	40	11	13	16
Injected dose (MBq), median (IQR)	217.8 (205.3-228.7)	218.2 (205.7-236.7)	223.8 (207.8-236.7)	209.6 (203.8-222.8)
<b>Preoperative imaging results, no. per patient</b>				
- SNs on early lymphoscintigrams, median (IQR)	1 (0-2)	1 (0-2)	1 (0-2)	1 (0-2)
- SNs on late lymphoscintigrams, median (IQR)	2 (1-3)	2 (2-3)	2 (1-3)	2 (2-3)
- SNs on SPECT/CT, median (IQR)	3 (0-6)	2 (2-3)	4 (2-4)	3 (2-4)
- Higher-echelon LNs, median (IQR)	0 (0-1)	1 (0-2)	0 (0-1)	0 (0-.75)
Time from injection to surgery (h), median (IQR)	5:44 (4:15-5:07)	4:34 (4:15-5:05)	5:05 (4:14-5:35)	4:42 (4:13-5:04)

**Table SI-1. Preoperative imaging results**

MBq = Mega Becquerel; IQR = interquartile range; SN = sentinel node; LN = lymph node; n = number of patients; no. = number; SPECT/CT = single photon emission computed tomography combined with computed tomography.

<b>Patient</b>	<b>No. tumor-positive SNs</b>	<b>Location tumor-positive SNs</b>	<b>No. tumor-positive LNs from ePLND</b>	<b>Total no. tumor-positive SNs + LNs from ePLND</b>
1	0/1	-	1/3	1/4
2	1/7	Right external region	0/4	1/13
3	1/12	Right external region	1/7	2/19
4	2/2	Left internal region, Right obturator region	12/13	14/15
5	3/3	Left external region (2x), Left paravesical region	0/8	3/11
6	0/3	-	1/12	1/15
7	5/9	Left internal region (4x), Right obturator region	0/12	5/21
8	4/6	Left external region, Left obturator region, Right internal region, Right obturator region	1/13	5/19
Total	16/43		16/72	32/115

**Table SI-2. pN1 Pathological findings**

SN = sentinel node; LN = lymph node; ePLND = extended pelvic lymph node dissection.

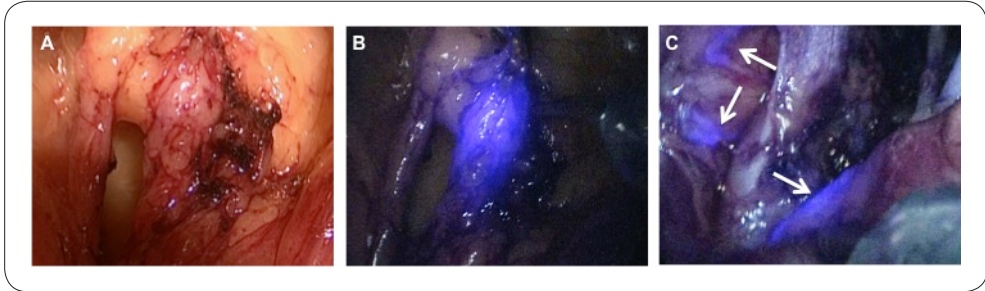


**Figure 5. Intraoperative sentinel node (SN) and lymphatic duct identification via fluorescence guidance:**

- (A)** white-light image illustrating the area that harbors the SN;
- (B)** fluorescence guidance clearly shows the contours of the SNs (the adjusted filter settings of the Image 1 HUB HD with D-Light P system (KARL STORZ GmbH & Co. KG, Tuttlingen, Germany) allows clear visualization of anatomic detail in the background);
- (C)** lymphatic ducts visualized via fluorescence imaging (white arrows).

## CONCLUSION

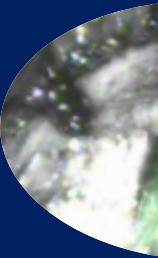
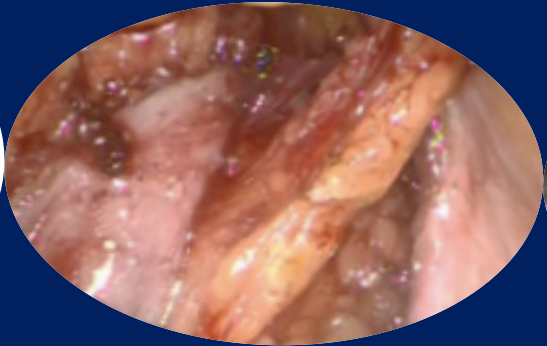
Altering the hybrid tracer formulation and injection technique and upgrading the LFI system significantly improved *in vivo* fluorescence-based SN identification. Further improvement of *in vivo* fluorescence-based SN detection, reaching rates similar to that of the conventional radio-guided approach, may make intraoperative LGP redundant. Still, SPECT/CT remains an essential tool for preoperative SN localization.

## REFERENCES

1. Wawroschek F, Vogt H, Weckermann D, Wagner T, Harzmann R. The sentinel lymph node concept in prostate cancer - first results of gamma probe-guided sentinel lymph node identification. *Eur Urol* 1999;36:595–600.
2. Van Leeuwen FWB, Hruby S. Fluorescence guidance during radical prostatectomy. *Eur Urol* 2014;65:1169–1170.
3. Rousseau C, Rousseau T, Campion L, et al. Laparoscopic sentinel lymph node versus hyperextensive pelvic dissection for staging clinically localized prostate carcinoma: a prospective study of 200 patients. *J Nucl Med* 2014;55:753–758.
4. Staník M, Capák I, Macík D, et al. Sentinel lymph node dissection combined with meticulous histology increases the detection rate of nodal metastases in prostate cancer. *Int Urol Nephrol*. In press. <http://dx.doi.org/10.1007/s11255-014-0704-3>
5. Wawroschek F, Wagner T, Hamm M, Weckermann D, Vogt H, Ma B. The influence of serial sections, immunohistochemistry, and extension of pelvic lymph node dissection on the lymph node status in clinically localized prostate cancer. *Eur Urol* 2003;43:132–137.
6. Warncke SH, Mattei A, Fuechsel FG, Brun SZ, Krause T, Studer UE. Detection rate and operating time required for probe-guided sentinel lymph node resection after injection of technetium-<sup>99m</sup> nanocolloid into the prostate with and without preoperative imaging. *Eur Urol* 2007;52:126–133.
7. Manny TB, Patel M, Hemal AK. Fluorescence-enhanced robotic radical prostatectomy using real-time lymphangiography and tissue marking with percutaneous injection of unconjugated indocyanine green: the initial clinical experience in 50 patients. *Eur Urol* 2014;65:1162–1168.
8. Jeschke S, Lusuardi L, Myatt A, Hruby S, Pirich C, Janetschek G. Visualization of the lymph node pathway in real time by laparoscopic radioisotope-and fluorescence-guided sentinel lymph node dissection in prostate cancer staging. *Urology* 2012;80:1080–1087.
9. Brouwer OR, van den Berg NS, Mathe'ron HM, et al. A hybrid radioactive and fluorescent tracer for sentinel node biopsy in penile carcinoma as a potential replacement for blue dye. *Eur Urol* 2014;65:600–609.
10. Matheron HM, van den Berg NS, Brouwer OR, et al. Multimodal surgical guidance towards the sentinel node in vulvar cancer. *Gynecol Oncol* 2013;131:720–725.
11. Van der Poel HG, Buckle T, Brouwer OR, Valde's Olmos RA, van Leeuwen FWB. Intraoperative laparoscopic fluorescence guidance to the sentinel lymph node in prostate cancer patients: clinical proof of concept of an integrated functional imaging approach using a multimodal tracer. *Eur Urol* 2011;60:826–33.
12. Nieweg OE, Tanis PJ, Kroon BB. The definition of a sentinel node. *Ann Surg Oncol* 2001;8:538–541.
13. Meinhardt W, van der Poel HG, Valde's Olmos RA, Bex A, Brouwer OR, Horenblas S. Laparoscopic sentinel lymph node biopsy for prostate cancer: the relevance of locations outside the extended dissection area. *Prostate Cancer* 2012;751753.
14. Dindo D, Demartines N, Clavien P-A. Classification of surgical complications: a new proposal with evaluation in a cohort of 6336 patients and results of a survey. *Ann Surg* 2004;240:205–213.
15. Schaafsma BE, Verbeek FPR, Rietbergen DDD, et al. Clinical trial of combined radio-and fluorescence-guided sentinel lymph node biopsy in breast cancer. *Br J Surg* 2013;100:1037–1044.
16. Brouwer OR, Klop WMC, Buckle T, et al. Feasibility of sentinel node biopsy in head and neck melanoma using a hybrid radioactive and fluorescent tracer. *Ann Surg Oncol* 2012;19:1988–1994.
17. Gofrit ON, Zorn KC, Steinberg GD, Zagaja GP, Shalhav AL. The Will Rogers phenomenon in urological oncology. *J Urol* 2008;179:28–33.
18. Fukuda M, Egawa M, Imao T, Takashima H, Yokoyama K, Namiki M. Detection of sentinel node micrometastasis by step section and immunohistochemistry in patients with prostate cancer. *J Urol* 2007;177:1313–1317.
19. Joniau S, Van den Bergh L, Lerut E, et al. Mapping of pelvic lymph node metastases in prostate cancer. *Eur Urol* 2013;63:450–458.



# Chapter 5



# Multimodal hybrid imaging agents for sentinel node mapping as a means to (re)connect nuclear medicine to advances made in robot-assisted surgery



5

*Gijs H. KleinJan  
Nynke S. van den Berg  
Jeroen de Jong  
Esther M. Wit  
Helene Thygessen  
Erik Vegt  
Henk G. van der Poel and  
Fijs W. B. van Leeuwen  
EJNMMI 2016; 43(7):1278-1287*

## ABSTRACT

### INTRODUCTION

Radical prostatectomy and complementary extended pelvic lymph node dissection (ePLND) of lymph nodes (LNs) at risk of containing metastases are increasingly being performed using high-tech robot-assisted approaches. Although this technological evolution has clear advantages, the physical nature of robotic systems limits the integrated use of routine radioguided surgery technologies. Hence, engineering effort in robotics are focused on the integration of fluorescence guidance technologies. Using the hybrid sentinel lymph node (SN) tracer indocyanine green-<sup>99m</sup>Tc-nanocolloid (radioactive and fluorescent), in this chapter, we investigated whether the robot-assisted approach affects the accuracy of fluorescence detection of SNs identified preoperatively using nuclear medicine.

### METHODS

The study included 55 patients (Briganti nomogram-based risk >5 % on LN metastases) scheduled for robot-assisted radical prostatectomy, SN biopsy and ePLND. Following indocyanine green-<sup>99m</sup>Tc-nanocolloid injection, preoperative nuclear imaging (lymphoscintigraphy and SPECT/CT) was used to locate the SN(s). The fluorescence laparoscope was used intraoperatively to identify the SN(s) with standard fluorescence settings (in 50 patients) and with customized settings (in 5 patients). The number and location of the SNs, the radioactive, fluorescence (both *in vivo* and *ex vivo*) and tumor status of the resected SNs/LNs, and postoperative complications were recorded and analyzed.

### RESULTS

Preoperative lymphoscintigraphy and SPECT/CT imaging combined identified 212 SNs (median 4 per patient). Intraoperative fluorescence imaging using standard fluorescence settings visualized 80.4% (148/184SNs; 50 patients; *ex vivo* 97.8%). This increased to 85.7% (12/14 SNs; 5 patients; *ex vivo* 100%) with customized fluorescence settings. SPECT/CT images provided guidance towards the residual SNs. *Ex vivo* all removed SNs were radioactive. SNs were tumor-positive in 25.4% of patients (14/55; false-negative rate 7%, 1/14 patients). In ten patients, the SN was the only tumor-positive LN. Surgical complications were minimal.

## CONCLUSION

Linking 3D preoperative nuclear imaging-based identification of SNs to a robot-integrated fluorescence laparoscope improved the surgeon's use of the technology and did not influence the sensitivity or morbidity of the procedure. To our surprise, however, the detection rates with the current fluorescence camera did not improve.

## INTRODUCTION

In complex anatomies, accurate preoperative mapping of sentinel nodes (SNs) using nuclear medicine (lymphoscintigraphy with or without SPECT/CT) and intraoperative radioguidance are vital for planning and performing nodal resection [1,2]. Imaging in combination with the intraoperative use of gamma probes and/or portable gamma cameras has been shown to be valuable not only in patients with melanoma, penile, vulvar and breast cancer [3–5], but also during the sampling of pelvic SNs originating from prostate cancer [6–8]. With SPECT/CT it has become possible to accurately identify the anatomical location of SNs inside or outside the extended pelvic lymph node dissection (ePLND) template, and subsequently this information can be used for surgical planning.

In parallel with the technical evolution of nuclear medicine-based imaging, there has been a shift towards robot-assisted laparoscopic procedures in urology, and in particular for prostate cancer. Unfortunately, this shift has resulted in a mismatch between the two disciplines. Moreover, in robotic surgery, the urologist is no longer present alongside the patient, limiting the control he/she has on the use of imaging technologies without robot assistance such as the gamma probe [9]. At the same time, the robot arms physically restrict access for larger devices such as portable gamma cameras. On the positive side, new-generation laparoscopes can be equipped with an integrated fluorescence imaging option [10–12]. Hence, integration of this technology in the robotic workflow currently seems to be more straightforward. Fluorescence guidance towards SNs and non-sentinel lymph nodes (LNs) has been achieved in a robotic setting through the use of an additional fluorescence laparoscope and via a robot-integrated fluorescence laparoscope [9– 11, 13]. Unfortunately, the fluorescent signal has very limited tissue penetration, meaning that more deeply lying SNs/LNs maybe missed when using fluorescence imaging alone [14]. Even worse, extensive surgery in the quest for a fluorescent signal may lead to an increase in surgical complications. In 2009, the hybrid tracer indocyanine green-<sup>99m</sup>Tc-nanocolloid (ICG-<sup>99m</sup>Tc-nanocolloid) was clinically introduced for SN biopsy. This tracer was designed to extend the European standard in nuclear medicine-based SN identification, <sup>99m</sup>Tc-nanocolloid, with intraoperative fluorescence guidance [10, 15–17]. With this development, the strengths of radioguided procedures (e.g. a high sensitivity and in-depth view of the SNs) are complemented by detailed real-time, but superficial, fluorescence guidance towards the pre-operatively identified SNs. In combination with the introduction of an additional fluorescence laparoscope, the hybrid concept has provided a significant step forward in connecting preoperative lymphatic mapping and real-time intraoperative fluorescence-based SN identification [9]. However, the

fact that the bedside assistant had to introduce and control the fluorescence laparoscope, rather than the operating urologist, was considered a limiting factor of this approach. We thus hypothesized that use of a robot-integrated fluorescence laparoscope could increase the level of control the operating urologist has, and could thus help increase the success rate in resecting preoperatively identified SNs via fluorescence guidance. To place these findings in perspective, the tumor-positive rate, sensitivity, false-negative rate and complication rate of SN biopsy using this approach was evaluated and compared to SN biopsy in a historical cohort [9].

## MATERIALS AND METHODS

### Patients

Between January 2014 and July 2015, 50 patients with a Briganti nomogram-based risk of >5% of LN metastases were included [18]. These patients were evaluated with the robot-integrated fluorescence laparoscope (standard settings). Between July 2015 and September 2015 another 5 patients were included for evaluation of the customized fluorescence imaging settings. All patients were scheduled for robot-assisted radical prostatectomy, ePLND and SN removal using the hybrid tracer, and provided written informed consent. The characteristics of the two groups of included patients are shown in Table 1.

### Preoperative SN mapping

Tracer preparation, injection and preoperative imaging (lymphoscintigraphy and SPECT/CT) were performed as previously described by KleinJan et al. [9].

Briefly, the hybrid tracer  $^{99m}\text{Tc}$ -nanocolloid was prepared by adding 2.0 mL pertechnetate (approximately 300 MBq) to a vial of nanocolloid (GE Healthcare, Eindhoven, the Netherlands). ICG (0.05 mL, 5.0 mg/mL; PULSION Medical, Feldkirchen, Germany) was then added to the vial of  $^{99m}\text{Tc}$ -nanocolloid. The total volume was subtracted from the volume of the vial and saline was added to reach a total volume of 2.0 mL in the syringe, after which the tracer was injected into the prostate under transrectal ultrasound guidance.

The injection was followed by preoperative lymphoscintigraphy (15 min and 2 h after injection) and SPECT/CT imaging directly after acquisition of the late lymphoscintigram. After imaging acquisition the nuclear medicine physician determined the number and location of the SNs.

	Group SN + ePLND	Group SN + ePLND Tunable Firefly settings	Total
No. patients	50	5	55
Age, median (IQR)	63 (58-68)	66 (62-68)	63 (59-68)
Preoperative PSA-level (ng/mL), median (IQR)	7.75 (5.44 -12.18)	7.9 (4.8 -23.35)	7.9 (5.46- 12)
Clinical T-stage			
- 1c (%)	6 (12%)	-	6 (11%)
- 2a (%)	5 (10%)	-	5 (9%)
- 2b (%)	9 (18%)	1 (20%)	10 (18%)
- 2c (%)	14 (28%)	1 (20%)	15 (27%)
- 3a (%)	12 (24%)	2 (40%)	14 (25%)
- 3b (%)	4 (8%)	1 (20%)	5 (9%)
Biopsy Gleason sum score			
- 6 (%)	3 (6%)	-	3 (5%)
- 7 (%)	30 (60%)	4 (80%)	34 (62%)
- 8 (%)	15 (30%)	1 (20%)	16 (29%)
- 9 (%)	2 (4%)	-	2 (4%)
Briganti score, median (IQR)			
	28 (21-53)	54 (20-68)	28 (21-50)
Clinical N-stage			
- N0 (%)	44 (88%)	5 (100%)	49 (89%)
- Nx (%)	6 (12%)	-	6 (11%)
Pathologic T-stage			
- 2a (%)	-	1 (20%)	1 (2%)
- 2b (%)	3 (6%)	-	3 (5%)
- 2c (%)	37 (74%)	2 (40%)	39 (71%)
- 3a (%)	4 (8%)	1 (20%)	5 (9%)
- 3b (%)	4 (8%)	1 (20%)	5 (9%)
- 4 (%)	1 (2%)	-	1 (2%)
- 4a (%)	1 (2%)	-	1 (2%)
Pathologic Gleason sum score			
- 6 (%)	6 (12%)	1 (20%)	7 (13%)
- 7 (%)	35 (70%)	2 (40%)	37 (67%)
- 8 (%)	7 (14%)	1 (20%)	8 (14%)
- 9 (%)	2 (4%)	1 (20%)	3 (54%)

**Table 1. Patient characteristics**

No. = number; SN = sentinel node; ePLND = extended pelvic lymph node dissection; IQR = Interquartile range, PSA = prostate specific antigen; ng = nanogram, ml = milliliter

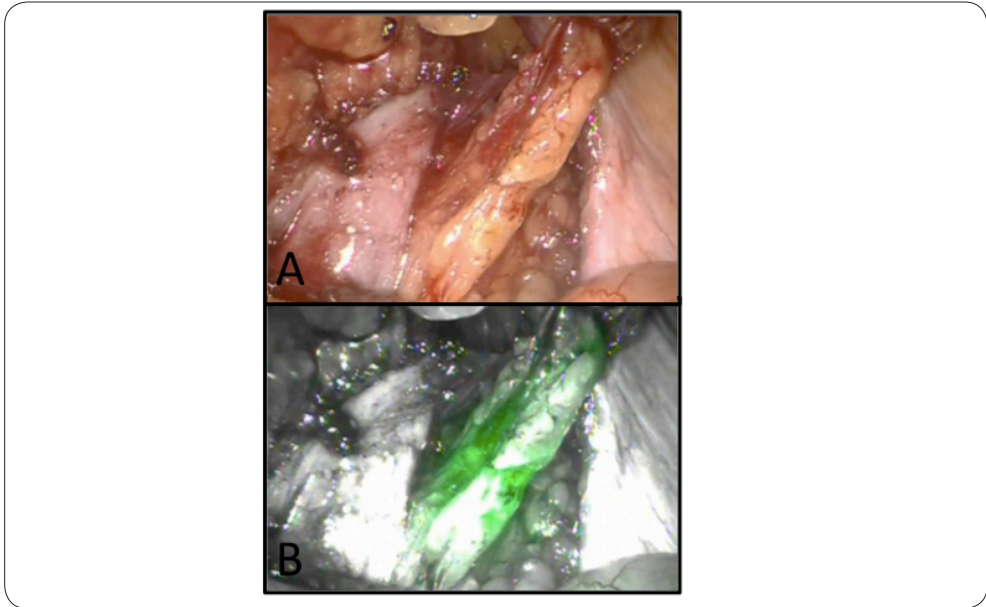


**Figure. 1 Fluorescence-based SN identification:**

a white light image; b fluorescence-based image

### **Surgical (imaging) tools**

For the surgical procedure a da Vinci Si system (Intuitive Surgical, Sunnyvale, CA, USA) with an integrated Firefly fluorescence laparoscope was used. Via the goggles of the master console, images obtained with the laparoscope are presented to the urologist. Using the controllers of the console the urologist is able to switch between the white light imaging mode and the fluorescence-imaging mode of the fluorescence laparoscope. In the initial 50 patients fluorescence imaging with the standard settings was evaluated.

After a software upgrade (P9 software update) of the da Vinci Si system, the urologist was able to manually adjust the fluorescence illuminator settings. In this second set-up, with which 5 patients were evaluated, the intensity of the white light background in the fluorescence image was varied from 30% (standard settings) to 15% and 0%. The visibility of the fluorescence signal within the SNs was evaluated at these three different settings.

### **Surgical procedure**

Prior to the start of the operation, the operating urologist viewed the SPECT/CT images using a DICOM viewer (PACS Vue Solutions; Carestream Health, Rochester, NY). The SNs identified on SPECT were again related to their anatomical context using the anatomical information provided by the low-dose CT scan. This information was used to help guide the positioning of the surgical tools and the fluorescence laparoscope for optimal SN localization and resection. Preoperatively identified SNs in a location with a high risk of surgical complications were left in situ. The remaining SNs, after initial preparation of the area of interest, were optically identified by switching between white light imaging and fluorescence imaging (Figure 1). After excision of the SN, the surgical bed was re-examined using a combination of white light and fluorescence imaging.

To simplify the surgical workflow, based on the results of our previous study[9], no laparoscopic gamma probe was used intraoperatively. However, *ex vivo* the gamma probe (Europrobe 2; Eurorad S.A., Eckbolsheim, France) was used to validate the radioactive signature in the excised SNs/LNs. To confirm the presence of fluorescence in the excised SNs, fluorescence imaging was performed *ex vivo* using a fluorescence camera for open surgery (PDE; Hamamatsu Photonics K.K., Hamamatsu, Japan).

The number and location of SNs identified preoperatively and intraoperatively were recorded together with their *in vivo* and *ex vivo* fluorescent and radioactive status.

Following SN excision, an ePLND was performed followed by the radical prostatectomy. The ePLND included dissection of LNs from the following areas: around the external iliac artery and vein, within the obturator fossa, and surrounding the internal iliac artery [19].

### **(Histo)pathological examination**

(Histo)pathological analysis of the SNs, additional LNs from the ePLND specimens and the prostate were performed as previously described[9].

### **Follow-up**

Complications occurring within 90 days of the operation were recorded using the Clavien-Dindo classification and were evaluated in the initial 50 patients [20]. In the last 5 patients evaluated follow-up was not sufficiently long for them to be included in the postoperative evaluation. The findings were compared to those reported in our previous study in which were ported on fluorescence guidance with out robotic integration [9].

### **Statistical analysis**

Statistical analysis was performed using SPSS Statistics, version 22 (SPSS Inc., Chicago, IL). A p -value <0.05 was considered significant. For continuous variables, the mean or median and interquartile ranges (IQR) are presented. For discrete variables, frequencies and percentages are reported. The Welch two-sample t -test was used to compare the preoperative Briganti scores, and the number of removed SNs and LNs in the patients in this study and in the patients in the previous study [9]. A Fisher's exact test was used to compare the tumor positivity rate (pN0 or pN1), and to evaluate differences in postoperative complications between the initial 50 patients included in this study and the patients in the previous study [9].

The false-negative rate was calculated on a per-patient basis using the following formula: false-negative rate = [false-negative patients/ (false-negative patients + true-positive patients)] x 100 %. The sensitivity of the SN biopsy procedure was also calculated on a per-patient basis using the following formula: [no. of true-positive patients/(no. of true-positive patients + no. of false-negative patients)] X 100 %.

## RESULTS

### Preoperative imaging

In 10 of the 55 patients (18.2%) only unilateral drainage was observed. In the overall group of 55 patients, 147 SNs were identified on the lymphoscintigrams. An additional 65 SNs were identified on SPECT/CT imaging, resulting in a total of 212 SNs (median 4 per patient, IQR 3 – 5) identified on preoperative imaging. Of these 212 preoperatively identified SNs, 55 (26%) were located outside the ePLND area. These results are specified for each patient group in Table 2 and in Figure 2.

### Intraoperative sentinel node identification

Of the 55 included patients, 54 were operated upon in a 1-day protocol with a median of 5.04h between tracer injection and the start of the operation (IQR 4.33 – 5.20h). One patient was operated 18.40 h after tracer injection. The preoperatively SPECT/CT images were analyzed in the operating theatre using an interactive DICOM viewer and provided a virtual starting point for placement of the fluorescence laparoscope in localizing the SNs via fluorescence guidance.

Of the 201 SNs identified in the initial 50 patients on preoperative imaging, 36 (17.9 %) were not pursued during the operation. The decision not to resect these SNs was made on the basis of its anatomical location or relationship to close structures, such as presacral and pararectal SNs located close to the rectum or SNs located behind vascular structures such as the internal iliac artery, external iliac artery or vessels in the para-aortal region (Figure 2c).

As a result of cluster formation, 19 extra SNs were surgically resected based on fluorescence identification. These clustered SNs were seen as one hotspot on SPECT, but the CT scan indicated multiple LNs at the location of the hotspot. A total of 148 SNs were removed using intraoperative fluorescence guidance (this was 80.4% of the 184 surgically resected SNs; Table 2). After removal, *ex vivo* gamma tracing confirmed excision of these SNs.

The 19.6% of SNs that could not be resected using fluorescence guidance were resected from the ePLND samples based on the anatomical information provided by the SPECT/CT images and *ex vivo* gamma tracing and fluorescence imaging. More detailed *ex vivo* analysis of the ePLND samples allowed fluorescence identification of 97.8% (180) of the 184 SNs resected and detection of the radioactive signal in 100% of the SNs.

	Group SN + ePLND (n= 50)	Group SN + ePLND Tunable Firefly settings (n=5)	Total (n=55)
<b>Preoperative SN detection</b>			
- Median no. detected SNs on lymphoscintigraphy / patient (IQR)	2.5 (1-4)	2 (1-3)	2 (1-4)
- Total no. SNs on lymphoscintigrams	137	10	147
- Median no. detected SNs on SPECT/ patient (IQR)	4 (3-5)	2 (1-3.5)	4 (3-5)
- Total no. SNs on SPECT/CT	201	11	212
<b>Intraoperative SN detection</b>			
- Total no. removed SNs	184	14	198
- Median no. removed SNs/ patient (IQR)	4 (2-5)	1 (1-5)	4 (2-5)
- No. not surgically resected SNs	36	0	36
- Additional no. surgically resected SNs (as a result of SN cluster formation)	19	3	22
<b>Tumor-positive rate</b>			
- No. patients pN1 (%)	14 (28)	0 (0)	14 (25)
<b>Pathological SN evaluation</b>			
- No. harvested SNs / patient, median (IQR)	4 (2-6)	1 (1-5)	4 (2-5)
- Total no. SNs	226	30	256
- Total no. tumor-positive SNs	17	0	17
<b>Pathological LN evaluation</b>			
- No. harvested LNs from ePLND specimen/patient, median (range)	10 (8-14)	12 (7 -22)	10 (8-15)
- Total no. LNs	582	69	651
- Total no. tumor-positive LNs (SNs + LNs)	41	0	41
<b>Pathological SN + LN evaluation (total)</b>			
- Total no. removed nodes per patient (SN + ePLND), median (IQR)	15.5 (12-20)	18 (12-28.5)	16 (12 -20)
- Total no. harvested SNs + LNs	807	99	906

**Table 2. Sentinel detection and pathological evaluation**

No. = number, SN = sentinel lymph node, LN = Lymph node, ePLND = extended pelvic lymph node dissection, IQR = interquartile range.

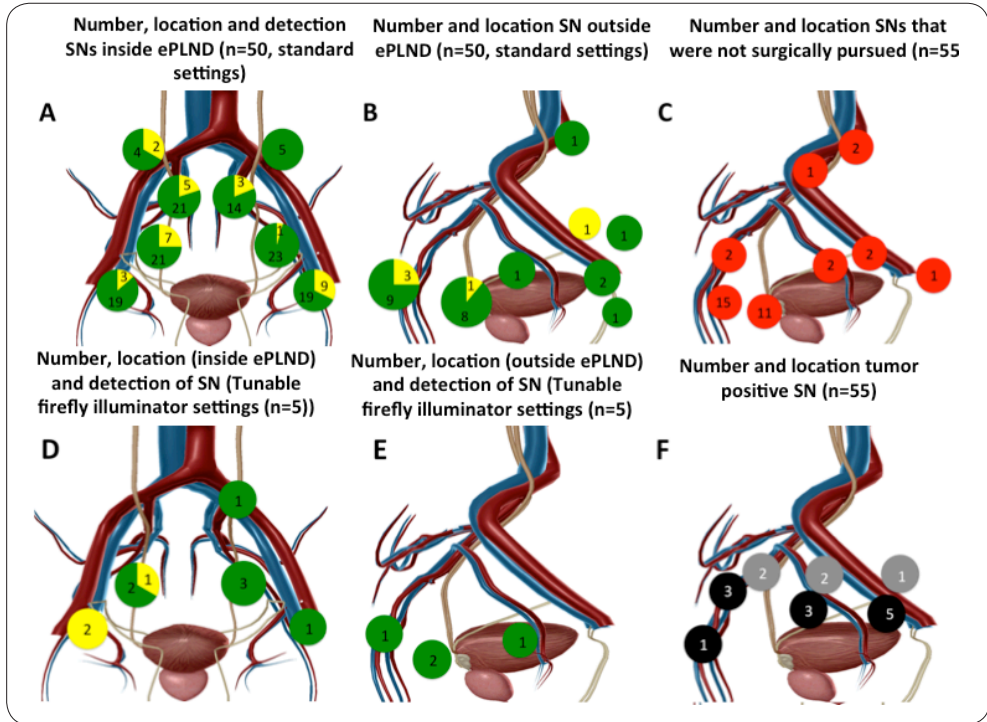


**Figure. 2 Locations of SNs and LNs detected intraoperatively.**

**A, B** SNs located inside and outside the ePLND area (green in vivo fluorescent SNs, yellow ex vivo identified SNs n= 50).

**C** SNs that could not be removed (red, n= 55).

**D,E** SNs located in the additionally included five patients inside and outside the ePLND area (green in vivo fluorescent SNs, yellow ex vivo identified SNs).

**F** Location of tumor-positive SNs (black right-sided SNs, grey left-sided SNs). The images were generated using Visible Bodysoftware (Argosy Publishing, Newton Upper Falls, MA)

In the five patients in whom the tunable fluorescence imaging settings were evaluated, as well as the 11 preoperatively identified SNs, 3 more SNs (part of a cluster of SNs) were removed under fluorescence guidance (Table 2). Of the 14 SNs, 11 (78.6%), 11 (78.6%) and 12 (85.7%) were visualized at 30%, 15% and 0% white light, respectively (*ex vivo*, 100% of the SNs were fluorescent and radioactive). The effect of the light settings on the fluorescence image quality is shown in Figure 3.

Because the fluorescence laparoscope is an integral part of the da Vinci Si system, the urologist maneuvered and placed the fluorescence laparoscope independently of the surgical assistant, a feature that had a positive influence on the surgical logistics.

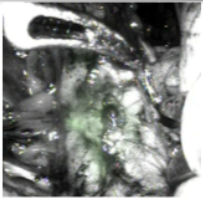
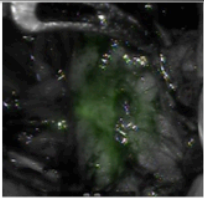
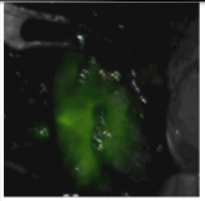
	30% intervention white light input	15% intervention white light input	0% intervention white light input
<b>Visualization of SN</b>			
<b>Number visualized SN</b>	11	11	12
<b>% visualized SN</b>	79	79	86

Figure. 3 Evaluation of adjustable fluorescence settings. SNs identified with various fluorescence settings

### **Pathological examination SNs and ePLND specimens**

At pathology, 256 nodes were extracted from the 198 SN specimens surgically excised from the 55 patients, (median 4 per patient, IQR 2–5). From the ePLND specimens a total of 651 LNs were removed, giving a median of 16 LNs per patient. The results are presented in more detail for each patient group in Table 2.

Histopathological examination revealed tumor-positive LNs in 25.4% of patients (14 of 55 patients, total 41 tumor-positive nodes). In 10 of these 14 pN1 patients (71.4%), the SNs were the only tumor-containing nodes. In 3 patients, tumor-positive LNs were also found next to the tumor-positive SNs. The result in one patient was false negative. In this patient the SN was tumor-negative but a metastasis was detected in a LN from the ePLND tissue specimen, and this LN was not fluorescent or radioactive during surgery. The false-negative rate in this study was therefore 7.1% (1/14). The sensitivity of SN biopsy in this cohort was good: the procedure correctly staged 13 of 14 node-positive patients (92.9%). In a previously reported group of patients with similar Briganti scores, we found a tumor-positive node rate of 20% (8/40 patients) [9]. Compared to the previous study, in the current study, significantly more LNs were removed per patient (median 16 vs. 12;  $p < 0.001$ ) and 5.4 % more node-positive patients were identified (14/55 patients; i.e. 25.4% vs. 20%;  $p = 0.6$ ). There was no significant difference in the a priori likelihood of LN metastasis ( $p = 0.3$ ).

### **Follow-up (complications)**

No significant differences were found in the postoperative complication rates between the patients in the current study and those in the previous study (Table 3) [9]. Changing and integrating the fluorescence laparoscope did not change the postoperative complication rate.

## DISCUSSION

Integrating molecular imaging and robotic surgery is an important step in the evolution that is taking place in the treatment of prostate cancer. In the current study, using a hybrid (radioactive and fluorescent) SN tracer, findings from nuclear medicine imaging were used to guide the surgical resection using a robot-integrated fluorescence laparoscope. In some patients, it was decided, based on the SPECT/CT information, that some of the preoperatively identified SNs were not eligible for surgical removal. In the remaining patients, the anatomical locations derived from the SPECT/CT images were used to position the fluorescence laparoscope or, when intraoperative fluorescence imaging did not provide accurate SN identification, to guide resection of the SNs.

Robotic integration of fluorescence imaging gives the urologist more control over the use and positioning of the laparoscope, thus increasing his/her autonomy [21,22]. To our surprise, using the standard fluorescence imaging settings of the robot-integrated fluorescence laparoscope, integration did not convert into an improved *in vivo* fluorescence-based SN visualization rate. In fact, the percentage found was lower than the rate we found previously in a setting where the bedside assistant was responsible for placement of an external fluorescence laparoscope [9]. This difference seems to be the result of differences in the camera technology used. However, it may also have been caused by the shorter time spent by the urologist in exploring the area of interest. The last point – saving surgical time to allow accurate fluorescence identification – seems to be inline with our previous finding [9]. Nevertheless, the fluorescence imaging miss-rate of 15 – 20% (in the 55 patients) means that with fluorescence guidance alone a large number of SNs would have been missed. Due to the hybrid nature of the tracer used, the radioactive signature could be used to compensate for this shortcoming and to identify the additional SNs. Rather than using cumbersome laparoscopic gamma tracing, which again has to be performed by the bedside assistant, we used a more time effective combination of *ex vivo* gamma tracing and SPECT/CT images to guide resection of the residual SNs. Next to the radioactive signatures, the fluorescent signatures we verified *ex vivo* considerably increased the fluorescence-based SN detection rate (>97 %). This finding emphasizes that the tissue attenuation encountered in the *in vivo* situation limits the success of the fluorescence guidance approach, rather than the presence of tracer in the SNs. It also indicates that the backup from SPECT/CT is of the utmost importance. In an ongoing randomized controlled study we are evaluating these aspects in more detail.

In the five patients, in whom the fluorescence settings could be adjusted, decreasing the percentage of white light, and thus decreasing the level of anatomical detail in the fluorescence image, helped improve the detection rate to 85.7 %. This improvement seems to contradict our previous findings. With a different fluorescence laparoscope, the introduction of white-light anatomical background information positively influenced the intraoperative fluorescence-based identification rate [9]. In this previous set-up we did not determine if the application of flexible white-light settings could improve fluorescence detection rates even further. The increased time used for the fluorescence detection at different light settings could also have played influenced the detection rate. Based on the current findings, an adjustable illuminator, wherein white light intensity can be tailored, may most flexibly accommodate the urologist's needs.

One may reason that increasing the proportion of tumor-positive LNs resected will increase the likelihood of the patient's recovery from the disease. In this sense, the 5.4 % greater rate of detection of tumor-positive LNs and the higher sensitivity than in our previous study (92.9% vs. 75.0%) [9] can be considered valuable. However, we cannot fully attribute this result to the surgical procedure. The tumor-positive LN detection rate may partly also be affected by the increased number of resected SNs and the pathological examination of the specimens. SNs have a higher chance of containing (micro) metastases and thus have a prognostic value [23] and as such receive more careful pathological evaluation including immunohistochemistry and cutting deeper levels than LNs out of a dissection template [24–27].

A crucial aspect of the clinical introduction of a new technology is the evaluation of the influence the technology will have on clinical outcome. For fluorescence guidance technologies such information is limited [14].

While one may reason that the SN biopsy procedure increases the chance of postoperative complications, the complication rate we observed was lower than in our previous study ( $p=0.4$ ) [9]. In both studies this result may in part be a consequence of using SPECT/CT planning to guide the procedure away from SNs located in areas that may be associated with postoperative complications.

The extensive introduction of new surgical technologies means that a need has been established for platforms that allow the integration of numerous imaging findings into the surgical workflow. In our view the da Vinci robot platform may act as such a linking

technology. For example, robotic surgical goggles have been used to introduce complementary intraoperative and preoperative imaging findings as well as virtual/augmented reality displays [12, 28]. Since in the current study it was not possible to interactively examine the DICOM SPECT/CT images in Tilepro® during the operation, the urologist had to leave the console to examine them on a separate DICOM viewing station. However, in another study we have already provided a proof-of-concept that directly linking SPECT/CT imaging information and fluorescence imaging during robot-assisted procedures may provide the next step in surgical guidance [29].

The hybrid tracer concept illustrated in this study and our previous prostate cancer-related studies [9,10,30] provide a valuable extension of routine SN identification. A similar hybrid concept holds promise for (tumor-) targeted tracers and may benefit from the set up we have applied for SN identification. One example of a target that holds promise for image-guided resection is prostate-specific membrane antigen (PSMA), which is already routinely used in PET/ CT-based diagnostics ( $^{68}\text{Ga}$ -PSMA-HBED-CC) and has been successfully used for radioguided resection ( $^{111}\text{In}$ -PSMA I&T)[31]. Theoretically, a hybrid PSMA derivative [32] would extend these efforts to accommodate (robot-integrated) hybrid surgical guidance towards the primary tumor margins, lymphatic metastases, and possibly even other distant metastases.

## CONCLUSION

Hybrid tracers help to integrate nuclear medicine and fluorescence-guided robotic surgery, but the use of a robot-integrated fluorescence laparoscope did not improve fluorescence-based SN identification. Hence, 3D preoperative imaging information from nuclear medicine remains crucial for (virtual) planning of complex surgical resections of multifocal lesions. Further technical refinement of robot-integrated guidance modalities in surgical procedures should improve the relationship between preoperative and intraoperative imaging findings.

## REFERENCES

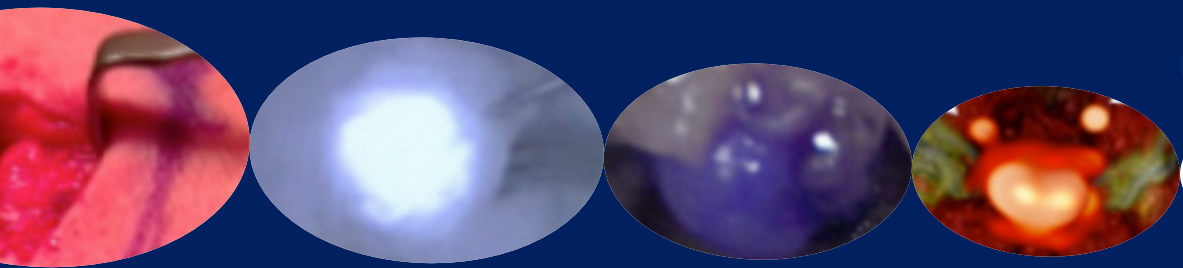
1. Vermeeren L, van der Ploeg IMC, Olmos RAV, Meinhardt W, Klop WMC, Kroon BBR, et al. SPECT/CT for preoperative sentinel node localization. *J Surg Oncol.* 2010;101(2): 184–90.
2. Zaknun JJ, Giammarile F, Olmos RAV, Vidal-Sicart S, Mariani G. Changing paradigms in radioguided surgery and intraoperative imaging: the GOSTT concept. *Eur J Nucl Med Mol Imaging.* 2012;39(1):1–3.
3. Mariani G, Erba P, Manca G, Villa G, Gipponi M, Boni G, et al. Radioguided sentinel lymph node biopsy in patients with malignant cutaneous melanoma: the nuclear medicine contribution. *J Surg Oncol.* 2004; 85(3):141–51.
4. Mariani G, Erba P, Villa G, Gipponi M, Manca G, Boni G, et al. Lymphoscintigraphic and intraoperative detection of the sentinel lymph node in breast cancer patients: the nuclear medicine perspective. *J Surg Oncol.* 2004; 85(3):112–22.
5. Van der Zee AGJ, Oonk MH, De Hullu JA, Ansink AC, Vergote I, Verheijen RH, et al. Sentinel node dissection is safe in the treatment of early-stage vulvar cancer. *J Clin Oncol.*2008;26(6):884–9.
6. Buckle T, Brouwer OR, Valdés Olmos RA, van der Poel HG, van Leeuwen FWB. Relationship between intraprostatic tracer deposits and sentinel lymph node mapping in prostate cancer patients. *J Nucl Med.* 2012;53(7):1026–33.
7. Holl G, Dorn R, Wengenmair H, Weckermann D, Sciuk J. Validation of sentinel lymph node dissection in prostate cancer: experience in more than 2,000 patients. *Eur J Nucl Med Mol Imaging.* 2009;36(9):1377–82.
8. Acar C, Kleinjan GH, van den Berg NS, Wit EM, van Leeuwen FW, van der Poel HG. Advances in sentinel node dissection in prostate cancer from a technical perspective. *Int J Urol.* 2015;22(10):898–909. doi:10.1111/iju.12863.
9. Kleinjan GH, van den Berg NS, Brouwer OR, de Jong J, Acar C, Wit EM, et al. Optimisation of fluorescence guidance during robot-assisted laparoscopic sentinel node biopsy for prostate cancer. *Eur Urol.*2014;66(6):991–8.
10. van der Poel HG, Buckle T, Brouwer OR, Valdés Olmos RA, van Leeuwen FWB. Intraoperative laparoscopic fluorescence guidance to the sentinel lymph node in prostate cancer patients: clinical proof of concept of an integrated functional imaging approach using a multimodal tracer. *Eur Urol.*2011;60(4):826–33.
11. Manny TB, Patel M, Hemal AK. Fluorescence-enhanced robotic radical prostatectomy using real-time lymphangiography and tissue marking with percutaneous injection of unconjugated indocyanine green: the initial clinical experience in 50 patients. *Eur Urol.* 2014;65(6):1162–8.
12. Volonté F, Buchs NC, Pugin F, Spaltenstein J, Schiltz B, Jung M, et al. Augmented reality to the rescue of the minimally invasive surgeon. The usefulness of the interposition of stereoscopic images in the Da Vinci™ robotic console. *Int J Med Robot.*2013;9(3):e34–8.
13. Jewell EL, Huang JJ, Abu-Rustum NR, Gardner GJ, Brown CL, Sonoda Y, et al. Detection of sentinel lymph nodes in minimally invasive surgery using indocyanine green and near-infrared fluorescence imaging for uterine and cervical malignancies. *Gynecol Oncol.* 2014;133(2):274–7.
14. van Leeuwen FW, Hardwick JC, van Erkel AR. Luminescence-based imaging approaches in the field of interventional molecular imaging. *Radiology.*2015;276(1):12–29.
15. van den Berg NS, Brouwer OR, Schaafsma BE, Mathéron HM, Klop WM, Balm AJ, et al. Multimodal surgical guidance during sentinel node biopsy for melanoma: combined gamma tracing and fluorescence imaging of the sentinel node through use of the hybrid tracer indocyanine green-(<sup>99m</sup>Tc)-nanocolloid. *Radiology.* 2015;275(2):521–9.
16. Brouwer OR, van den Berg NS, Mathéron HM, van der Poel HG, vanRhijn BW, Bex A, et al. A hybrid radioactive and fluorescent tracer for sentinel node biopsy in penile carcinoma as a potential replacement for blue dye. *Eur Urol.* 2014;65(3):600–9.
17. Mathéron HM, van den Berg NS, Brouwer OR, Kleinjan GH, van Driel WJ, Trum JW, et al. Multimodal surgical guidance towards the sentinel node in vulvar cancer. *Gynecol Oncol.* 2013;131(3): 720–5.
18. Briganti A, Chun FK-H, Salonia A, Zanni G, Scattoni V, Valiquette L, et al. Validation of a nomogram predicting the probability of lymph node invasion among patients undergoing radical prostatectomy and an extended pelvic lymphadenectomy. *Eur Urol.* 2006;49(6):1019–26;discussion 1026–7.
19. Heidenreich A, Bastian PJ, Bellmunt J, Bolla M, Joniau S, van der Kwast T, et al. EAU guidelines on prostate cancer. Part 1: screening, diagnosis, and local treatment with curative intent – update 2013. *Eur Urol.* 2014;65(1):124–37.
20. Clavien PA, Barkun J, de Oliveira ML, Vauthey JN, Dindo D, Schulick RD, et al. The Clavien-Dindo classification of surgical complications: five-year experience. *Ann Surg.*2009;250(2):187– 96.

21. Van Oosterom MN, Simon H, Laurent M, Welling MM, Van der Poel HG, Van den Berg NS, et al. Revolutionizing(robot-assisted) laparoscopic gamma tracing using a drop-in gamma probe technology. *Am J Nucl Med Mol Imaging*. 2015. In press.
22. Fuerst B, Sprung J, Pinto F, Frisch B, Wendler T, Simon H, et al. First robotic SPECT for minimally invasive sentinel lymph node mapping. *IEEE Trans Med Imaging*. 2015;PP(99):1. doi:10.1109/TMI.2015.2498125
23. Holtkamp LH, Wang S, Wilmott JS, Madore J, Vilain R, Thompson JF, et al. Detailed pathological examination of completion node dissection specimens and outcome in melanoma patients with minimal (<0.1 mm) sentinel lymph node metastases. *Ann Surg Oncol*. 2015;22(9):2972–7.
24. Gofrit ON, Zorn KC, Steinberg GD, Zagaja GP, Shalhav AL. The Will Rogers phenomenon in urological oncology. *J Urol*. 2008;179(1):28–33.
25. Staník M, Capák I, Macík D, Vašina J, LžicaDováE, Jarkovsk J, et al. Sentinel lymph node dissection combined with meticulous histology increases the detection rate of nodal metastases in prostate cancer. *Int Urol Nephrol*. 2014;46(8):1543–9.
26. Wawroschek F, Wagner T, Hamm M, Weckermann D, Vogt H, MärklB, et al. The influence of serial sections, immunohistochemistry, and extension of pelvic lymph node dissection on the lymph node status in clinically localized prostate cancer. *Eur Urol*. 2003;43(2):132–7.
27. Fukuda M, Egawa M, Imao T, Takashima H, Yokoyama K, Namiki M. Detection of sentinel node micrometastasis by step section and immunohistochemistry in patients with prostate cancer. *J Urol*. 2007;177(4):1313–7; discussion 1317.
28. Greco F, Cadeddu JA, Gill IS, Kaouk JH, Remzi M, Thompson RH, et al. Current perspectives in the use of molecular imaging to target surgical treatments for genitourinary cancers. *Eur Urol*. 2014;65(5): 947–64.
29. Brouwer OR, Buckle T, Bunschoten A, Kuil J, Vahrmeijer AL, Wendler T, et al. Image navigation as a means to expand the boundaries of fluorescence-guided surgery. *Phys Med Biol*. 2012;57(10): 3123–36.
30. van den Berg NS, Valdés-Olmos RA, van der Poel HG, van Leeuwen FWB. Sentinel lymph node biopsy for prostate cancer: a hybrid approach. *J Nucl Med*. 2013;54(4):493–6.
31. Maurer T, Weirich G, Schottelius M, Weineisen M, Frisch B, Okur A, et al. Prostate-specific membrane antigen-radioguided surgery for metastatic lymph nodes in prostate cancer. *Eur Urol*. 2015;68(3):530–4.
32. Banerjee SR, Pullambhatla M, Byun Y, Nimmagadda S, Foss CA, Green G, et al. Sequential SPECT and optical imaging of experimental models of prostate cancer with a dual modality inhibitor of the prostate-specific membrane antigen. *Angew Chem Int Ed Engl*. 2011;50(39):9167–70.

# Chapter 6



# Fluorescence guided surgery and tracer-dose, fact or fiction?



6

*Gijs H. KleinJan  
Anton Bunschoten  
Nynke S. van den Berg  
Renato A. Valdés Olmos  
W. Martin C. Klop  
Simon Horenblas  
Henk G. van der Poel  
Hans-Jürgen Wester  
Fijs W.B. van Leeuwen  
EJNMMI 2016;43(10):1857-1867.*

## ABSTRACT

### INTRODUCTION

Fluorescence guidance is an upcoming methodology to improve surgical accuracy. Challenging herein is the identification of the minimum dose at which the tracer can be detected with a clinical-grade fluorescence camera. Using a hybrid tracer such as indocyanine green (ICG)-<sup>99m</sup>Tc-nanocolloid, it has become possible to determine the accumulation of tracer and correlate this to intraoperative fluorescence-based identification rates. In this chapter, we determined the lower detection limit of tracer at which intraoperative fluorescence guidance was still feasible.

### METHODS

Size exclusion chromatography (SEC) provided a laboratory set-up to analyze the chemical content and to simulate the migratory behavior of ICG-nanocolloid in tissue. Tracer accumulation and intraoperative fluorescence detection findings were derived from a retrospective analysis of 20 head-and-neck melanoma patients, 40 penile and 20 prostate cancer patients scheduled for sentinel node (SN) biopsy using ICG-<sup>99m</sup>Tc-nanocolloid. In these patients, following tracer injection, single photon emission computed tomography fused with computed tomography (SPECT/CT) was used to identify the SN(s). The percentage injected dose (% ID), the amount of ICG (in nmol), and the concentration of ICG in the SNs (in  $\mu\text{M}$ ) was assessed for SNs detected on SPECT/CT and correlated with the intraoperative fluorescence imaging findings.

### RESULTS

SEC determined that in the hybrid tracer formulation, 41% (standard deviation: 12%) of ICG was present in nanocolloid-bound form. In the SNs detected using fluorescence guidance a median of 0.88% ID was present, compared to a median of 0.25% ID in the non-fluorescent SNs ( $p$ -value $<0.001$ ). The % ID values could be correlated to the amount ICG in a SN (range: 0.003–10.8 nmol) and the concentration of ICG in a SN (range: 0.006–64.6  $\mu\text{M}$ ).

### DISCUSSION

The ability to provide intraoperative fluorescence guidance is dependent on the amount and concentration of the fluorescent dye accumulated in the lesion(s) of interest. Our findings indicate that intraoperative fluorescence detection with ICG is possible above a  $\mu\text{M}$  concentration.

## INTRODUCTION

(Near-infrared) fluorescence guidance was introduced to improve the intraoperative identification of lesions and to guide resection of these lesions [1]. This technique has been extensively applied in Japan and provides a high spatial resolution (down to the sub-micrometer range when dedicated microscopes are used) [2]. Superficially in tissue, it offers an increased level of detail compared to the more traditional interventional molecular imaging approaches that are based on radioactive tracers (centimeter range resolution)[3]. Fluorescence guidance technologies are limited by the strong attenuation of the signal, meaning the technology loses value with increasing depth.

To allow fluorescence imaging during the operation, the fluorescent signal, which directly corresponds to the amount of accumulated tracer, has to exceed the detection limit of the imaging system used [4]. To make sure this limit is not an issue, fluorescent dyes are commonly administered to patients at high doses, for example indocyanine green (ICG; administered up to 25 mg) [5], fluorescein (administered up to 500 mg), or methylene blue (administered up to 10 mg; this compound comes with an FDA warning) [6]. When attached to a targeting moiety, the reported doses can still be considered high. Examples are 0.3 mg/kg folate-FITC [7], GE-137 up to 0.18 mg/kg [8], and cetuximab-CW800 (up to 62.5 mg/m<sup>2</sup>) [9]; in a man weighing 75 kg, 62.5 mg/m<sup>2</sup> corresponds to a total dose of approximately 125 mg (1.7 mg/kg). These latter groups of targeting compounds, therefore, will come at much higher production costs, especially when based on antibodies. The key question that needs to be addressed here is at what minimum dose can fluorescent dyes be used for surgical guidance? The answer to this question, in combination with knowing the binding efficiency of the fluorescence tracer to its target, helps to determine if future fluorescent probes can be applied in patients using much lower quantities.

The dose applied to a patient drives the ease of translation and the type of toxicity studies that are required. As a result of the (in-depth) detection sensitivity of nuclear medicine-based modalities, the relation between the administered radiotracer dose and e.g. tumor uptake and *in vivo* kinetics can be studied in detail. Moreover, because of their high specificity, resulting in efficient accumulation at the site of interest and providing high signal-to-background ratios, imaging can be realized in a microdosing regime. In microdosing studies <100 µg of a new drug or imaging agent can be used in a single patient [10], and extensive expensive toxicity studies can be circumvented. Yet, this is not applied for fluorescence tracers, where in the most first-in-human studies, trial-and-error or blood value evaluations have been used

for dose optimization [8]. The microdosing principle is, in part, also driven by economical aspects; the administered dose will directly relate to costs and thus is of importance for both business models and future reimbursement. For routine use of targeted fluorescence tracers in patients rather than first-in-human trials, it is, therefore, crucial to determine the lowest possible dose at which this technology can be applied.

Hybrid tracers, which contain both a radioactive and a fluorescent signature, may help to provide insight in the dose required for efficient intraoperative detection of a fluorescent signature. Based on the radioactive signal of such tracers, combined with nuclear imaging, a quantitative evaluation of the biodistribution can be made. This, in turn, can be directly related to the intraoperative fluorescence-based detection rate.

A number of hybrid tracers have been studied in humans [3], and of these ICG-<sup>99m</sup>Tc-nanocolloid has been most extensively used [11–13]. This tracer was introduced to complement preoperative sentinel node (SN) mapping and intraoperative radioactivity-based SN localization with intraoperative near-infrared fluorescence guidance [11–13]. Because of inter-patient variations in lymphatic drainage or differences in tissue composition, e.g. obesity, in some cases SNs do not contain tracer, or tracer-containing nodes cannot be detected intraoperatively, respectively. Nevertheless, the SNs defined at single photon emission computed tomography combined with computed tomography (SPECT/CT) display a radioactive and fluorescent signal after more accurate *ex vivo* evaluation [11–13]. We thus reasoned that via assessment of the radioactive signature of ICG-<sup>99m</sup>Tc-nanocolloid, it should be possible to determine the lower detection limit at which fluorescence guidance was still feasible intraoperatively. To adequately evaluate these aspects, malignancies with both superficial (head-and-neck melanoma, penile cancer; fluorescence camera for open surgery) and deep (prostate cancer; fluorescence laparoscope) lymphatic drainage were included.

## METHODS

### Preparation of the hybrid tracer

For penile cancer patients and head-and-neck melanoma patients, ICG-<sup>99m</sup>Tc-nanocolloid was prepared as previously described [12, 13]. In short, a vial of nanocolloid (GE Healthcare, Leiderdorp, the Netherlands) (0.5 mg human serum albumin (HSA)) was dissolved in 2 mL saline (0.9g/L NaCl) containing freshly eluted pertechnetate (1400 MBq) resulting in an HSA concentration of 3.76  $\mu$ M. A vial of ICG(25 mg) (Pulsion Medical Systems, Feldkirchen, Germany) was dissolved in 5 mL water for injection. 50  $\mu$ L of this ICG solution was added

to the  $^{99m}\text{Tc}$ -nanocolloid resulting in an ICG concentration of 161  $\mu\text{M}$ . From this vial approximately 90 MBq  $\pm 10\%$  was subtracted and supplemented to 0.4 mL with saline. This solution contained 0.49 nmol (32  $\mu\text{g}$ ) HSA and 20.8 nmol (16  $\mu\text{g}$ ) ICG.

For prostate cancer patients two different tracer formulations were evaluated [11]. The first group received the ICG- $^{99m}\text{Tc}$ -nanocolloid prepared according to an earlier used protocol. In this protocol a vial of nanocolloid (0.5 mg HSA) was dissolved in 1 mL saline containing freshly eluted pertechnetate (700 MBq) resulting in an HSA concentration of 7.52  $\mu\text{M}$ . A vial of ICG (25 mg) was dissolved in 5 mL water for injection. Of this ICG solution, 50  $\mu\text{L}$  was added to the  $^{99m}\text{Tc}$ -nanocolloid resulting in an ICG concentration of 323  $\mu\text{M}$ . From this vial approximately 250 MBq  $\pm 10\%$  (0.4 mL) was injected. This solution contained 3.01 nmol (200  $\mu\text{g}$ ) HSA and 129 nmol (100  $\mu\text{g}$ ) ICG.

The second group received ICG- $^{99m}\text{Tc}$ -nanocolloid prepared according to a new protocol. In this protocol a vial of nanocolloid (0.5 mg HSA) was dissolved in 2 mL saline containing freshly eluted pertechnetate (300 MBq) resulting in an HSA concentration of 3.76  $\mu\text{M}$ . A vial of ICG (25 mg) was dissolved in 5 mL water for injection. 50  $\mu\text{L}$  of this ICG solution was added to the  $^{99m}\text{Tc}$ -nanocolloid resulting in an ICG concentration of 161  $\mu\text{M}$ . The complete content of the prepared vial was injected. This solution contained 7.52 nmol (500  $\mu\text{g}$ ) HSA and 323 nmol (250  $\mu\text{g}$ ) ICG. All tracer preparations were performed under good manufacturing practice and under supervision of the institution's pharmacist.

### Size exclusion chromatography

Size exclusion chromatography (SEC) provided a laboratory set-up able to simulate the migratory behavior of ICG-nanocolloid in tissue. The small diameter pores in the stationary phase mimic the extracellular space in tissue.

ICG-nanocolloid was prepared as described above for the head-and-neck melanoma and penile cancer and the new formulation used in prostate cancer patients (161  $\mu\text{M}$  ICG), but without the radioactive pertechnetate addition. Samples of 450  $\mu\text{L}$  were extracted from the vial at 2, 4, 6, and 8 h after preparation. From each sample, 450  $\mu\text{L}$  was loaded onto a size exclusion column (52 mm x 9.6 mm) containing Sephadex G-50 fine (Sigma-Aldrich, St. Louis, Missouri, USA). Gravity was used to elute the column with saline.

Six fractions of 500  $\mu\text{L}$  were collected over approximately 20 min and diluted with 2  $\mu\text{M}$  HSA to obtain light absorption below 0.3 at 803 nm. Absorption of each fraction was measured with a Lambda Bio 20 UV-Vis spectrometer (Perkin Elmer, Waltham, MA, USA) and the fraction of the total ICG that co-eluted with nanocolloid in these six fractions was calculated [14].

## **Absorption**

To determine the presence of different stacked forms of ICG next to the fluorescent monomer form, UV-Vis absorption spectra were obtained of the different SEC fractions. Samples containing the clinical concentration of ICG (161  $\mu\text{M}$ ) were prepared by dissolving ICG in water for injection (5 mg/mL) and subsequent dilution of 50  $\mu\text{L}$  of this stock in 2 mL water for injection, saline, or in a vial of nanocolloid dissolved in 2 mL saline. UV-Vis absorption spectra were recorded in a 1 mm optical pathway quartz cuvette.

## **CLINICAL STUDY**

### **Patients**

This retrospective analysis evaluated the fluorescence detection of SNs in patients that underwent SN biopsy using the hybrid tracer ICG- $^{99\text{m}}\text{Tc}$ -nanocolloid: 20 patients with melanoma in the head-and-neck area, 40 patients with penile cancer, and another 20 patients with prostate cancer were included. From all patients written informed consent was obtained. The surgical procedures in melanoma patients and penile cancer patients were open procedures. The prostatectomies for prostate cancer were robot-assisted laparoscopic procedures. All procedures were performed between December 2010 and June 2013.

Given the intention to identify the lower detection levels for intraoperative fluorescence guidance, the selection of patients for this study was biased towards patients with intraoperative non-visualization; patients where fluorescence detection failed during surgery were selectively included.

### **Injection of the hybrid tracer and preoperative nuclear imaging**

Tracer injection and preoperative SN mapping for head-and-neck melanoma, penile cancer and prostate cancer have been described previously [11–13].

In all patient groups image acquisition was performed with a SPECT/CT dual-head gamma camera (SymbiaT; Siemens, Erlangen, Germany) equipped with parallel low energy high-resolution collimators. The following configurations were used during preoperative imaging: planar lymphoscintigraphy was acquired at source-to-collimator distances up to 15cm with an image acquisition time of 5min. Non-circular SPECT (256 x 256 matrix, 40 frames, 30 s/frame) was performed in combination with a low-dose CT (130kV, 40mAs, B30s kernel). Total acquisition time: approximately 14 min including the low-dose CT. The low-dose CT was based on 5 mm slices in penile cancer patients, and on 2 mm slices in head-and-neck melanoma and prostate cancer patients.

When the circumferential borders of the SNs could be clearly determined on low-dose CT, the volume of the SNs was determined. Diameters ( $a = 1/2 \times \text{length}$ ,  $b = 1/2 \times \text{width}$ ) of the SN were measured on the low-dose CT, in cms, and the volume was calculated according to the following formula:

$$V(\text{cm}^3) = \frac{4}{3}\pi \times (a) \times (b) \times (b).$$

### Image analysis

OsiriX medical imaging software (Pixmeo, Geneva, Switzerland) was used to measure total pixel values [15].

Measurements of the injection site and SNs were performed on the SPECT component of the SPECT/CT scan using a 3D region-growing tool with calculation of the pixel values. Besides the injection site, and the SN(s), the rest activity (higher-echelon nodes, spillage) was calculated. All calculated pixel values were combined resulting in the total pixel value on SPECT/CT.

Liver uptake as a result of shunting during the tracer administration was not taken into account because it could not be accurately determined in all patients; in the head-and-neck and penile cancer patients, the liver was not present in the field of view when performing lymphoscintigraphy and SPECT/CT imaging, and in the prostate cancer patients the liver was only partly present in the field of view.

Based on the measured total pixel values in the SPECT scan the percentage of drainage of the injected dose to an individual SN was calculated using the following formula:

$$\text{Drainage to SN (\%)} = \frac{\text{Total pixel value in an individual SN}}{\text{Total pixel value on SPECT}} \times 100$$

### Determination nodal ICG accumulation

The SNs were divided into four groups: nodes having received drainage of 0-1, 1-2, 2-3, and >3% of the total injected dose (ID). Based on the known ratio of ICG and  $^{99m}\text{Tc}$  (see above) the percentage of  $^{99m}\text{Tc}$  drainage determined on SPECT was used to calculate the amount of ICG that accumulated in the SN using the following formula:

$$\begin{aligned} & \text{ICG in SN (nmol)} \\ & = \text{Drainage to SN (\%)} \times \text{injected dose ICG (nmol)} \times \text{percentage of nanocolloid bound ICG (\%)} \end{aligned}$$

Here the injected dose of ICG was 20.8 nmol for the penile cancer and head-and-neck melanoma patients, 129 nmol for the old prostate preparation, and 323 nmol for the new prostate preparation. The percentage of ICG bound to nanocolloid after mixing the two was determined using SEC (see Results).

To determine the concentration of ICG in the SNs, the uptake of ICG in the SNs was divided by the volume of the SN (calculated as stated above) using the following formula:

$$[\text{ICG}] \text{ in SN (nM)} = \frac{\text{ICG in SN (nmol)}}{\text{Volume of SN (cm}^3\text{)}} \times 1000$$

### Fluorescence detection during surgical procedure

For open procedures (penile cancer, head-and-neck melanoma) the PhotoDynamicEye (Hamamatsu Photonics KK, Hamamatsu, Japan) was used as described previously [12,13]. SN biopsy combined with extended pelvic lymph node dissection and prostatectomy was performed robot-assisted (da Vinci S, Intuitive, Sunnyvale, CA, USA) in prostate cancer patients. For fluorescence detection in the laparoscopic robotic setting an additional fluorescence laparoscope (KARL STORZ GmbH & Co. KG, Tuttlingen, Germany) was used [11].

For localization of the SNs, intermittently the gamma probe and fluorescence camera were used. To limit the influence of tissue-based signal attenuation, fluorescence-based visibility of the SNs (yes/no) was assessed when they were maximally exposed by the surgeon. This yielded a portion of SNs that could be resected using intraoperative fluorescence guidance as well as a portion SNs that contained not enough signal to allow for intraoperative fluorescence detection.

### Statistical analysis

Statistical Package for the Social Sciences (SPSS, IBM, version 22) was used to calculate for continuous variables, the mean or median and interquartile range (IQR; 25–75 %) and range. For discrete variables, frequencies and percentages are reported. A Mann–Whitney U test was performed to compare the means of uptake (%ID) of fluorescent and non-fluorescent SNs and to compare the means of uptake (%ID) of tumor-negative and tumor-positive SNs. A comparison of the fluorescence detection rate between tumor-negative SNs and tumor-positive SNs was performed with a Fisher's exact test.

### Pathology

(Histo-)pathological evaluation of the SNs was performed as previously described [11–13]. The diameters of the excised SNs were not defined in the pathological specimens, merely the tumor status and size of metastases.

## RESULTS

### Size exclusion chromatography

Preparation of the hybrid tracer ICG-<sup>99m</sup>Tc-nanocolloid, resulted in an ICG to HSA ratio of approximately 43 to 1. ICG is well soluble in water, but poorly soluble in saline. This poor solubility in combination with the tendency of HSA to bind hydrophobic, aromatic, and fatty acid like compounds, led to the formation of a non-covalent complex between nanocolloid and ICG [16, 17]. When ICG-<sup>99m</sup>Tc-nanocolloid is injected in or around the primary tumor it ends up in the extra-cellular space, hence the marking of the injection site [18]. From there it will move, due to the increased interstitial pressure, through the spaces between the cells and through the extracellular matrix into the lymphatic ducts (Figure 1a). A phantom set-up for this process was provided by SEC chromatography; the columns used in SEC consist of small particles (with interstitial spaces) that allow gravity dependent flow wherein different sized compounds are eluted at different speeds. In this set up the large ICG-nanocolloid particles eluted first. 41 % (standard deviation: 12%) of ICG was present in this fraction, corresponding to 17 ICG molecules per HSA protein, which is in close agreement with previous findings [14]. The ICG-nanocolloid fractions remained stable for at least 8h after preparation. The SEC experiment also demonstrated that the residual but optically silent ICG fraction remained present on the column indicating a small size as well as poor solubility. Only when the column was washed extensively with demineralized water or a HAS solution did this fraction elute from the column. We assume similar behavior for the injected formulation at the site of injection.

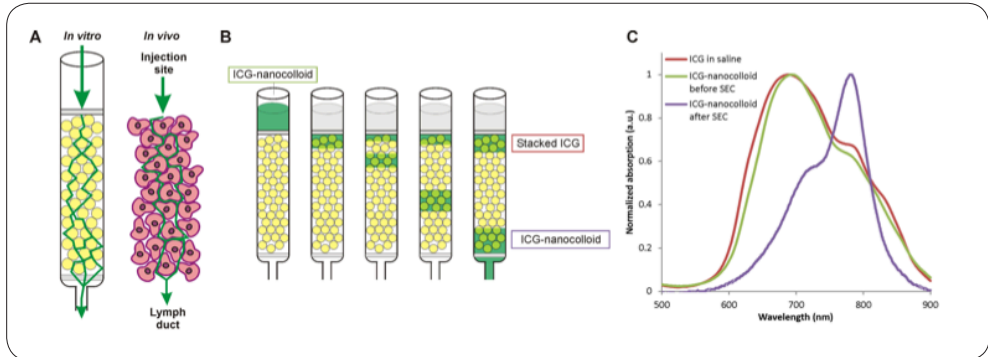


**Figure 1. Schematic overview of the size exclusion chromatography in an ICG-nanocolloid fraction and a fraction of stacked ICG that accumulates.**

Phantom set-up to mimic the *in vivo* drainage of the hybrid on the column experiments (b). Absorption spectra of ICG dissolved in saline, and of tracer (a). Size exclusion chromatography of the prepared hybrid tracer results ICG-nanocolloid before and after size exclusion chromatography (c)

### Spectral analysis

ICG diluted in saline (161  $\mu\text{M}$ ) without the presence of nanocolloid showed a strong and broad absorption peak around 685 nm which is associated with non-fluorescent (optically silent) H-stacking, J-stacking, and more elaborate stacking forms of ICG (Figure 1c) [19]. The non-separated ICG-nanocolloid formulation gave a similar absorption spectrum (Figure 1c), indicating that the solution contained a fair amount of stacked ICG. The ICG-nanocolloid fraction of the SEC purification, however, displayed an absorption peak correlating to the fluorescent monomer form of ICG (Figure 1b and c).

### Preoperative imaging

In our clinical dose-evaluation studies we focused on three patient groups, namely patients with head-and-neck melanoma (n=20; 60 SNs), penile cancer (n=40; 104 SNs) and prostate cancer (n= 20; 65 SNs). Figure 2 provides typical examples of the pre-and intraoperative imaging findings when using the hybrid tracer for SN biopsy [11–13].

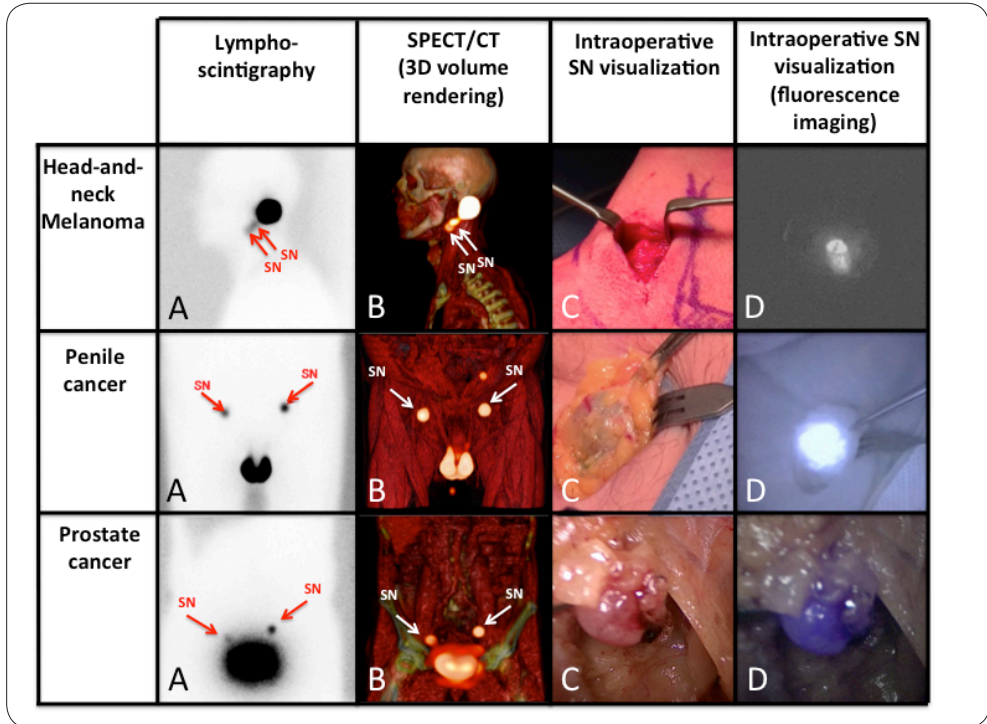


**Figure 2. Typical examples of the sentinel node biopsy procedure when using the hybrid approach**

In the first row ahead-and-neck melanoma case is illustrated, in the second row a penile cancer case is illustrated and in the third row a prostate cancer case is illustrated. From left to right a) lymphoscintigram with the location of the SN(s)(arrows); b) a 3D volume rendering of the SPECT/ CT (arrows); c) white light imaging of the SN in vivo; and d) in vivo fluorescence imaging of the SN. Fluorescence imaging with the PDE generates a black-and-white image, the fluorescence laparoscope shows the fluorescence signal in the SN in blue.

## **Intraoperative fluorescence guidance versus hybrid tracer uptake in the sentinel node(s)**

A total of 229 SNs were removed during surgery of which 203 SNs (88.6%) were identified intraoperatively via their fluorescence signature. The details for the three patient groups are further specified in Table 1. It must be noted, that in contrast to our previously published studies [11–13], based on the biased selection criteria, in this study we report a higher non-visualization rate during the operation. In the overall group, *ex vivo* analysis allowed visualization of 97.8% (224/229) of the SNs via fluorescence imaging. In some cases the small SNs with small amounts of tracer were embedded in fatty tissue also preventing their identification even *ex vivo*.

SNs were categorized with respect to the % ID uptake in the SN as defined on preoperative SPECT imaging: 0-1%, 1-2%, 2-3% and >3%; of the overall group, 57.2% of the SNs was categorized in the 0-1% group (Table 1). In the overall group, the median hybrid tracer uptake of a via fluorescence imaging identified SN was 0.88% ID (IQR 0.25-2.22% ID) which was significantly higher than the median hybrid tracer uptake in an SN that could not be detected *in vivo* using fluorescence imaging, which was 0.25% ID (IQR 0.13-0.73% ID) (Mann-Whitney U test, p-value <0.001). In the 0-1% ID drainage range intraoperative fluorescence guidance was least efficient (Table 1).

The open surgical procedures consisted of two groups. In the head-and-neck melanoma group, SNs that could be identified intraoperatively using fluorescence guidance showed a median hybrid tracer uptake of 0.33% ID (IQR 0.13-1.31% ID) (Table 2). The SNs that could not be identified intraoperatively using fluorescence guidance showed a median hybrid tracer uptake of 0.14% ID (IQR 0.12-0.44% ID). For the penile cancer patient group these values were 1.37% ID uptake per SN (IQR 0.63-2.86% ID) and 0.38% ID (IQR 0.13-0.94% ID), respectively (Table 2).

For the robot-assisted laparoscopic surgery application, in the first group (initial tracer preparation [11]), the SNs that could be identified with fluorescence imaging (9/10 SN) had a median uptake of 0.56% ID per SN (IQR 0.17-0.83% ID), only one SN could not be identified, giving a somewhat high % ID, with intraoperative fluorescence imaging (2.30% ID) (Table 2). In the second group (new tracer preparation), which received ICG-<sup>99m</sup>Tc-nanocolloid in a high dose formulation, the SNs identified with fluorescence imaging (n=47) had a median of 0.70% ID uptake (IQR 0.18-1.45% ID) versus 0.23% ID (IQR 0.09-0.60% ID) in the SNs that could not be identified with fluorescence imaging SN (n=8) (Table 2).

Percentage injected dose that drained to the SN	Estimated amount ICG (nmol)	Percentage successful surgical identification through fluorescence guidance (SN -based)	Distribution of SNs that were missed intraoperatively using fluorescence guidance
<b>H&amp;N melanoma patients (60 SN)</b>			
0 – 1% ID	0 – 0.085	80.0% (32/40)	89% (8/9)
1 – 2% ID	0.085 – 0.17	92.4% (12/13)	11% (1/9)
2 – 3% ID	0.17 – 0.255	100% (6/6)	0%
> 3% ID	> 0.255	100% (1/1)	0%
<b>Penile cancer patients (104 SN)</b>			
0 – 1% ID	0 – 0.085	85.1% (40/47)	88% (7/8)
1 – 2% ID	0.085 – 0.17	94.8% (18/19)	12% (1/8)
2 – 3% ID	0.17 – 0.255	100% (17/17)	0%
> 3% ID	> 0.255	100% (21/21)	0%
<b>Prostate cancer patients (10 SN; old preparation)</b>			
0 – 1% ID	0 – 0.53	100% (7/7)	0%
1 – 2% ID	0.53 – 1.06	100% (1/1)	0%
2 – 3% ID	1.06 – 1.59	0% (0/1)	100% (1/1)
> 3% ID	> 1.59	100% (1/1)	0%
<b>Prostate cancer patients (55 SN; new preparation)</b>			
0 – 1% ID	0 – 1.32	81.1% (30/37)	88% (7/8)
1 – 2% ID	1.32 – 2.65	88.9% (8/9)	12% (1/8)
2 – 3% ID	2.65 – 3.97	100% (2/2)	0%
> 3% ID	> 3.97	100% (7/7)	0%

**Table 1. Drainage % hybrid tracer in SNs related to the amount of ICG (nmol)**

<b>H&amp;N Melanoma</b>					
Fluorescent	SNs measured on low dose CT	Median % ID (IQR)	Median estimated nmol ICG per SN (IQR)	Median SN volume (cm <sup>3</sup> ) (IQR)	Median estimated concentration ICG in SN mM (IQR)
Yes	Yes (n = 33)	0.37 (0.13 – 1.67)	0.031 (0.011 – 0.142)	0.11 (0.03 – 0.23)	0.39 (0.15 – 0.91)
	No* (n = 18)	0.33 (0.15 – 1.10)	0.028 (0.012 – 0.094)	-	
No	Yes (n= 6)	0.23 (0.08 – 0.72)	0.020 (0.007 – 0.061)	0.03 (0.01 – 0.043)	1.32 (0.28 – 3.24)
	No* (n = 3)	0.14 (0.136)	0.012 (0.012)	-	
<b>Penile cancer</b>					
Yes	Yes (n= 90)	1.52 (0.70 – 2.90)	0.129 (0.060 – 0.247)	0.57 (0.36 – 1.12)	0.24 (0.08 – 0.48)
	No* (n= 6)	0.55 (0.20 – 1.07)	0.047 (0.017 – 0.910)		
No	Yes (n= 8)	0.38 (0.13 – 0.94)	0.032 (0.011 – 0.080)	0.64 (0.47 – 1.30)	0.08 (0.019 – 0.24)
	No* (n= 0)	-	-	-	
<b>Prostate old preparation</b>					
Yes	Yes (n= 5)	0.57 (0.44 – 2.10)	0.048 (0.037 – 0.179)	0.17 (0.08 – 0.86)	1.74 (1.01 – 4.52)
	No* (n= 4)	0.17 (0.07 – 0.87)	0.090 (0.037 – 0.46)	-	
No	Yes (n= 1)	2.30 (2.30)	1.22 (1.22)	0.24	5.16
	No* (n= 0)	-	-	-	
<b>Prostate new preparation</b>					
Yes	Yes (n= 36)	0.55 (0.14 – 1.34)	0.417 (0.185 – 1.769)	0.17 (0.09 – 0.32)	2.86 (1.27 – 15.62)
	No* (n= 11)	0.87 (0.63 – 3.15)	1.148 (0.832 – 4.158)	-	
No	Yes (n= 5)	0.29 (0.14 – 0.54)	0.383 (0.184 – 0.71)	0.14 (0.09 – 0.23)	2.44 (1.79 – 3.87)
	No* (n= 3)	0.08	0.106	-	

**Table 2. Percentage uptake in sentinel nodes related to the possibility of measurement of sentinel nodes on CT and to intraoperative fluorescence detection**

\* The inability to perform the required volumetric measurements in the low-dose CT depended mostly on the size of the SNs and the poor quality of the images. CT = computed tomography, ID = injected dose, IQR = interquartile range, SN = sentinel node, ICG = indocyanin green

It must be noted that the above-mentioned calculations are likely to overestimate the % ID in the SN and as such the amount of ICG present in the node. This is a direct consequence of the inability to measure the (3D) pixel values in the liver resulting in an underestimation of the total counts measured in the SPECT/CT images.

### **Volumes of the sentinel nodes**

The concentration of the hybrid tracer in a SN, and thus the concentration of ICG, was determined by relating the amount of ICG in a SN to the volume of that SN derived from the SPECT/CT images (Table 2). For the SNs located in the neck, the median size was 0.072 cm<sup>3</sup> (IQR 0.033–0.18 cm<sup>3</sup>). This value deviates from the 0.50 cm<sup>3</sup> and an IQR of 0.36–0.85 cm<sup>3</sup> that was previously reported [20]. A reason for this difference could be that the size of lymph nodes is very much dependent on the neck level where they are located [21]. In the group of penile cancer patients a median of 0.57 cm<sup>3</sup> (IQR 0.38–1.12 cm<sup>3</sup>) was found. In the prostate cancer group, the measured SNs (n=47) had a median volume of 0.17 cm<sup>3</sup> (IQR 0.09–0.27 cm<sup>3</sup>). The size of the nodes in the penile cancer group and prostate cancer groups were comparable with the sizes reported in previous literature of lymph nodes in the inguinal and pelvic area [22,23]. The SNs that could not be measured on CT, overall had a lower % ID uptake of tracer, suggesting they were small in size.

### **Amount of ICG in quantity and concentration in relation to intraoperative fluorescence-based detectability**

A clear relation was found between the detection rate of the SNs by fluorescence imaging and the hybrid tracer uptake (in % ID and amount of ICG; Figure 3a and b). However, when the detection rate was related to the ICG concentration, defined using low-dose CT-derived SN volumes, the relation was not clear (Figure 3c).

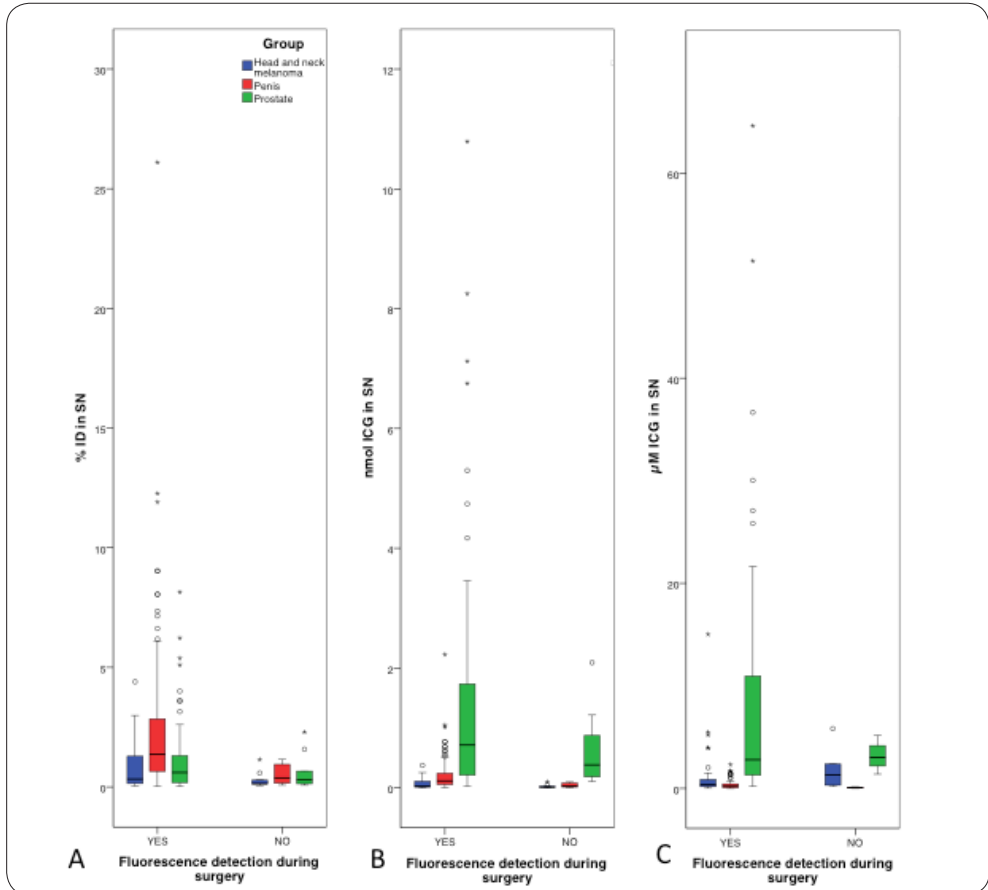
In head-and-neck melanoma, with the smallest SNs, the concentration of ICG in the SNs that were detected by fluorescence imaging was similar compared to the SNs that were not detected by fluorescence imaging (median 0.39 μM vs. 1.32 μM; Table 2 and Figure 3). In penile cancer patients the difference was more distinct, showing a higher ICG concentration in SNs that could be detected intraoperatively compared to those that could not be detected intraoperatively via fluorescence imaging (median 0.24 μM, vs. median 0.08 μM, respectively; Table 2 and Figure 3). In prostate cancer patients injected with the old and new tracer preparation, the median concentration of intraoperatively non-detectable SNs was 5.16 and 2.44 μM, versus 1.74 and 2.86 μM for the SNs that could be detected via fluorescence imaging, respectively (Table 2 and Figure 3). The lowest ICG concentration in

the SN of which intraoperative fluorescence detection was possible, was 0.006  $\mu\text{M}$ . This was observed in a penile cancer patient.

### **Pathology**

In the total group, 15 patients were tumor-positive (six head-and-neck patients, five penile cancer patients, and four prostate cancer patients) with a total of 24 tumor-positive SNs.

The %ID uptake of the tumor-positive SNs on SPECT was lower compared to the non-tumor positive SNs, with a median uptake 0.26% ID (IQR 0.13–1.04%) and median uptake 0.86% ID (IQR 0.24–2.08%), respectively (Mann–Whitney U test, p-value 0.036). This, however, did not influence the intraoperative fluorescence detection rate; 83.3% (20/24) versus 89.3% (183/205) for tumor-positive and tumor-negative SNs, respectively (Fisher's exact test, p-value 0.492).



## DISCUSSION

The dose at which fluorescent dyes can be identified during surgery is an important factor for future translation and application of tracers that enable fluorescence-guided surgery. The clinical use of the hybrid tracer ICG-<sup>99m</sup>Tc-nanocolloid provided a unique opportunity to correlate hybrid tracer uptake in SNs based on SPECT/CT imaging measurements (<sup>99m</sup>Tc-label) to the intraoperative fluorescence detection rate (ICG-label). From this analysis the lower detection limit of tracer at which fluorescence guidance was still feasible could be estimated. This limit was found to be at a  $\mu\text{M}$  concentration level (Table 2).

SEC experiments enabled us to relate the uptake of injected dose defined on SPECT to the amount of ICG that drained in the form of ICG-<sup>99m</sup>Tc-nanocolloid. One critical observation herein is that the portion of non-colloidal bound ICG fraction “stacked” in the formulation used, forming an optically silent dye deposit that could only dissolve slowly overtime and after extensive washing. In this and other clinical trials using ICG-<sup>99m</sup>Tc-nanocolloid (current experience in over 600 patients), however, we did not observe background signal coming from ‘free’ ICG, and *ex vivo* found a good correlation between the presence of radioactivity and fluorescence in the SNs [11–13]. We do want to point out that SEC experiments were used to simulate and approximate the behavior of ICG-nanocolloid in human tissue in its most basic form. This experiment does not represent the full complexity of the *in vivo* situation, e.g. tissue heterogeneity or the presence of competing proteins, but merely showed the difference in transport for the different components present in the tracer without such effects present. Nevertheless, there appears to be a good concurrence between the basic SEC findings and the findings observed in patients.

The % ID uptake of ICG-<sup>99m</sup>Tc-nanocolloid in the SNs, and the volume of the SNs, allowed us to directly relate the intraoperative fluorescence imaging-based identification of SNs to the amount and/or the concentration of ICG. From this we were able to determine the lower detection fluorescence limit at which ICG provided surgical guidance. In general, when a SN is covered by (fatty) tissue fluorescence-based detection is hindered significantly [1]. To minimize the influence of this important dimension in the analysis, the surgeons involved in this study always tried to remove the overlaying tissue, prior to analyzing the fluorescent content of the SN. Obviously, this does not exclude tissue attenuation by the node itself. When fluorescence could not be used to guide the surgeon during exploration, radioguidance was used to determine the exact location of the SN.

In our study groups the median hybrid tracer uptake in the SNs was 0.82% ID. For the SNs

visualized by fluorescence imaging, the median injected dose was slightly higher, namely 0.88% ID (IQR 0.25–2.22% ID). For the SNs that could not be intraoperatively identified using fluorescence guidance, the median was found 0.25% ID (IQR 0.13–0.73% ID) ( $p$ -value $<0.001$ ). In a sub-analysis comparing the uptake %ID in tumor-negative and tumor-positive SNs, the latter showed lower uptake ( $p$ -value 0.036), but this did not influence fluorescence imaging-based detection *in vivo*. These findings are in line with previous reports showing tracer uptake in SNs containing macrometastases ( $\leq 14$  mm)[13].

The tracer administration could not be accurately determined in all patients. In a prospective trial this shortcoming maybe compensated by using a calibrated external reference  $^{99m}\text{Tc}$ -source in the same field of view as the SNs. In this study the measured volume on the low-dose CT was used to calculate the volumes of the SNs. A more accurate calculation of the nodal volumes could be realized using, e.g. diagnostic CT or more advanced image processing/segmentation [24]. Alternatively, the weight and volume of the individual resected SNs could be defined at pathology. Unfortunately, both do not (yet) seem to be feasible in clinical routine.

The findings of the current study underline that there is a clear relation between the amount of ICG in the SNs and their detectability via fluorescence imaging *in vivo*. Hence, efficiency of tracer drainage identified using preoperative imaging may be predictive for the success of fluorescence-guided surgery; fluorescence examination of the surgical field should be more meticulous when the drainage is relatively low. We thus argue that the ability to assess the tracer-binding efficacy prior to surgery is a critical component in planning such interventions. It will help prevent timely and unnecessary surgical explorations towards fluorescent signals that can or cannot be detected during the operation [25].

To verify if a microdosing principle is within reach for fluorescence-based surgical guidance, one should estimate which part of the injected dosage can accumulate in the targeted lesions. A recent study of Herrmann et al. described that for the tumor-targeted tracer  $^{68}\text{Ga}$ -pentixafor, up to reached the targeted lesions [26]. If we use as representative uptake for a high affinity tracer, this would mean that intravenous administration of 100 mg [10] of a targeted tracer with a molecular weight of 3.3 kDa could yield a concentration of 0.09  $\mu\text{M}$  in a lesion of 1  $\text{cm}^3$ . In this study ICG in SNs was detected in a concentration range of 0.006–64.61  $\mu\text{M}$  with a median volume of  $<1$   $\text{cm}^3$ . Combined this suggests it is legitimate to assume that a well-designed and high-affinity receptor-targeted fluorescent tracer can be applied in a microdosing principle similar to what is standard for radiotracers.

The assumption that optical imaging can be effective at lower tracer doses is also in line with recent clinical reports that indicate *in vivo* Cerenkov imaging is feasible using standard PET-tracer formulations [27, 28]. Given the constant technical improvements that are being made in camera systems [11], one may assume that the sensitivity of fluorescence guidance will even improve further in the future. The same will be true if the signal intensity of the fluorescent dyes can be improved.

## **CONCLUSION**

For the first time we estimated the minimum amount of ICG in SNs ( $>0.003\text{nmol}$  or  $>0.006\ \mu\text{M}$  level) necessary to achieve a fluorescent signal suitable for intraoperative guidance. In addition our results suggest that ICG and perhaps other fluorescent-tracers can be applied on the basis of the microdosing concept.

## REFERENCES

1. Polom K, Murawa D, Rho Y-S, Nowaczyk P, Hünerbein M, Murawa P. Current trends and emerging future of indocyanine green usage in surgery and oncology: a literature review. *Cancer*. 2011;117(21):4812–22.
2. ICG Fluorescence Imaging and Navigation Surgery - Mitsuo Kusano, Norihiro Kokudo, Masakazu Toi, Masaki Kaibori ISBN 978-4-431-55528-5
3. van Leeuwen FWB, Hardwick JCH, van Erkel AR. Luminescence-based imaging approaches in the field of interventional molecular imaging. *Radiology*. 2015;276(1):12–29.
4. Vermeeren L, Muller SH, Meinhardt W, Valdés Olmos RA. Optimizing the colloid particle concentration for improved preoperative and intraoperative image-guided detection of sentinel nodes in prostate cancer. *Eur J Nucl Med Mol Imaging*. 2010;37(7):1328–34.
5. Manny TB, Patel M, Hemal AK. Fluorescence-enhanced robotic radical prostatectomy using real-time lymphangiography and tissue marking with percutaneous injection of unconjugated indocyanine green: the initial clinical experience in 50 patients. *Eur Urol*. 2014;65(6):1162–8.
6. Patel HP, Chadwick DR, Harrison BJ, Balasubramanian SP. Systematic review of intravenous methylene blue in parathyroid surgery. *Br J Surg*. 2012;99(10):1345–51.
7. van Dam GM, Themelis G, Crane LMA, Harlaar NJ, Pleijhuis RG, Kelder W, et al. Intraoperative tumor-specific fluorescence imaging in ovarian cancer by folate receptor- $\alpha$  targeting: first in-human results. *Nat Med*. 2011;17(10):1315–9.
8. Burggraaf J, Kamerling IMC, Gordon PB, Schrier L, de Kam ML, Kales AJ, et al. Detection of colorectal polyps in humans using an intravenously administered fluorescent peptide targeted against c-Met. *Nat Med*. 2015;21(8):955–61.
9. de Boer E, Warram JM, Tucker MD, Hartman YE, Moore LS, de Jong JS, et al. In vivo fluorescence immunohistochemistry: localization of fluorescently labeled cetuximab in squamous cell carcinomas. *Sci Rep*. 2015;5:10169.
10. Tewari T, Mukherjee S. Microdosing :concept ,application and relevance. *Perspect Clin Res*. 2010;1(2):61–3.
11. KleinJan GH, van den Berg NS, Brouwer OR, de Jong J, Acar C, Wit EM, et al. Optimisation of fluorescence guidance during robot-assisted laparoscopic sentinel node biopsy for prostate cancer. *Eur Urol*. 2014;66(6):991–8.
12. van den Berg NS, Brouwer OR, Schaafsma BE, Mathéron HM, KlopWMC ,Balm AJM, et al. Multimodal surgical guidance during sentinel node biopsy for melanoma: combined gamma tracing and fluorescence imaging of the sentinel node through use of the Hybrid Tracer indocyanine green-(99m)Tc-nanocolloid. *Radiology*. 2015;275(2):521–9.
13. Brouwer OR, van den Berg NS, Mathéron HM, van der Poel HG, van Rhijn BW, Bex A, et al. A hybrid radioactive and fluorescent tracer for sentinel node biopsy in penile carcinoma as a potential replacement for blue dye. *Eur Urol*. 2014;65(3):600–9.
14. Bunschoten A, Buckle T, Kuil J, Luker GD, Luker KE, Nieweg OE, et al. Targeted non-covalent self-assembled nanoparticles based on human serum albumin. *Biomaterials*. 2012;33(3):867–75.
15. Brouwer OR, Valdés Olmos RA, Vermeeren L, Hoefnagel CA, Nieweg OE, Horenblas S. SPECT/CT and a portable gamma-camera for image-guided laparoscopic sentinel node biopsy in testicular cancer. *J Nucl Med*. 2011;52(4):551–4.
16. Moody ED, Viskari PJ, Colyer CL. Non-covalent labeling of human serum albumin with indocyanine green: a study by capillary electrophoresis with diode laser-induced fluorescence detection. *J Chromatogr B Biomed Sci Appl*. 1999;729(1–2):55–64.
17. van Leeuwen AC, Buckle T, Bendle G, Vermeeren L, Valdés Olmos R, van de Poel HG, et al. Tracer-cocktail injections for combined pre—and intraoperative multimodal imaging of lymph nodes in a spontaneous mouse prostate tumor model. *J Biomed Opt*. 2011;16(1):016004.
18. Uren RF, Howman-Giles R, Thompson JF. Patterns of lymphatic drainage from the skin in patients with melanoma. *J Nucl Med*. 2003;44(4):570–82.
19. Mishra A, Behera RK, Behera PK, Mishra BK, Behera GB. Cyanines during the 1990s: a review. *Chem Rev*. 2000;100(6):1973–2012.
20. Ying M, Pang BSF. Three-dimensional ultrasound measurement of cervical lymph node volume. *Br J Radiol*. 2009;82(980):617–25.
21. Alkureishi LWT, Ross GL, MacDonald DG, Shoaib T, Gray H, Robertson G, et al. Sentinel node in head and neck cancer: use of size criterion to upstage the no neck in head and neck squamous cell carcinoma. *Head Neck*. 2007;29(2):95–103.
22. Vinnicombe SJ, Norman AR, Nicolson V, Husband JE. Normal pelvic lymph nodes: evaluation with CT after bipedal lymphangiography. *Radiology*. 1995;194(2):349–55.

23. Grey AC, Carrington BM, Hulse PA, Swindell R, Yates W. Magnetic resonance appearance of normal inguinal nodes. *Clin Radiol.* 2000;55(2):124–30.
24. Krishnasetty V, Bonab AA, Fischman AJ, Halpern EF, Aquino SL. Comparison of standard-dose vs low-dose attenuation correction CT on image quality and positron emission tomographic attenuation correction. *J Am Coll Radiol.* 2008;5(4):579–84.
25. van Leeuwen FWB, Hruby S. Fluorescence guidance during radical prostatectomy. *Eur Urol.* 2014;65(6):1169–70.
26. Herrmann K, Lapa C, Wester H-J, Schottelius M, Schiepers C, Eberlein U, et al. Biodistribution and radiation dosimetry for the chemokine receptor CXCR4-targeting probe 68Ga-pentixafor. *J Nucl Med.* 2015;56(3):410–6.
27. Spinelli AE, Ferdeghini M, Cavedon C, Zivelonghi E, Calandrino R, Fenzi A, et al. First human Cerenkography. *J Biomed Opt.* 2013;18(2):20502.
28. Thorek DLJ, Riedl CC, Grimm J. Clinical Cerenkov luminescence imaging of (18)F-FDG. *J Nucl Med.* 2014;55(1):95–8.



# Part two

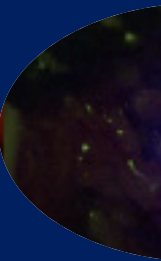
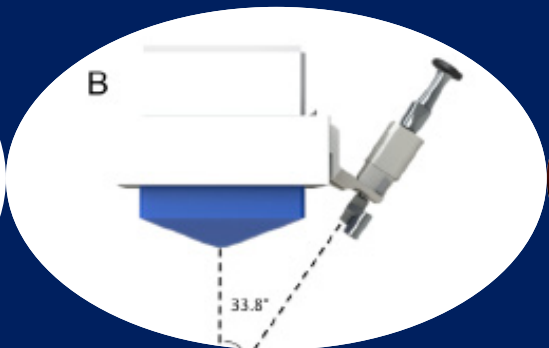
# New surgical modalities

7

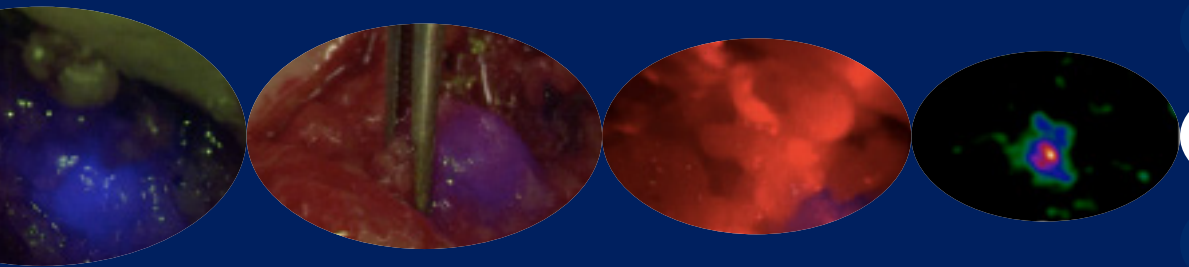
8

9

# Chapter 7



# Hybrid surgical guidance: Does hardware integration of gamma- and fluorescence- imaging modalities make sense?



7

*Gijs H. KleinJan  
Daan Hellingman  
Nynke S. van den Berg  
Matthias N. van Oosterom  
Kees Hendricksen  
Simon Horenblas  
Renato A Valdés Olmos  
Fijs WB van Leeuwen  
J Nucl Med. 2017;58(4):646-650.*

## ABSTRACT

### INTRODUCTION

The clinically applied hybrid tracer indocyanine green (ICG)-<sup>99m</sup>Tc-nanocolloid enables combined radio- and fluorescence image guidance during sentinel node (SN) biopsy procedures. In order to provide optimal surgical guidance this tracer requires the presence of both gamma and fluorescence modalities in the operating room. We reasoned that combination and/or integration of these modalities could further evolve the hybrid surgical guidance concept. To study the potential of this approach we clinically applied two set-ups that included the combination of gamma detection modalities and an open surgery fluorescence camera.

### METHODS

Clip-on brackets were designed and 3D-printed in sterilizable RC31. To attach the fluorescence camera (VITOM) to either 1) a gamma-ray detection probe (GP; VITOM-GP) or 2) a portable gamma camera (GC) (VITOM-GC). Both combined modalities were evaluated in respectively five and six patients with penile cancer during a SN biopsy procedure using ICG-<sup>99m</sup>Tc-nanocolloid. Intraoperatively, radio- and fluorescence guided SN detection rates were scored at working distances of 0, 10, 20, and 30 cm.

### RESULTS

Using the VITOM-GP combination 9 SNs were evaluated. Gamma tracing rates were shown to be 100, 88.9, 55.6 and 55.6 % at a respective working distance of 0, 10, 20 and 30 cm. Detection rates for the fluorescence imaging-based detection were found to be 100, 77.8 and 77.8 %, at respective working distances of 10, 20, and 30 cm. Using the VITOM-GC set-up, all 10 intraoperatively evaluated SNs could be visualized with the gamma camera independent of the working distance. Fluorescence detection rates were 90, 80 and 80% at 10, 20 and 30cm working distance. The integrated detection modalities were shown to work synergistically; overall the GC was most valuable for rough localization (10-30 cm range) of the SNs, the GP for providing convenient real-time acoustic feedback, while fluorescence guidance allowed detailed real-time SN visualization.

### CONCLUSION

The findings in this chapter suggest that full integration of a fluorescence camera with gamma detector (GP or GC) can be of value when a hybrid, radioactive and fluorescent, tracer is used.

## INTRODUCTION

The radioguided surgery technique has strongly evolved since its introduction in the early 1960's (1,2) whereby the sentinel node biopsy procedure can be considered the best-know example. Basically this technique uses a radiotracer to (specifically) label lesions that require surgical removal. In case of sentinel node (SN) biopsy, following the injection of a radiocolloid (often  $^{99m}\text{Tc}$ -nanocolloid) in or around the primary tumor, upon drainage of the radiocolloid through the lymphatic system the primary tumor draining lymph node(s), so-called sentinel nodes (SNs) can be identified [3]. Acoustic (and numerical) feedback generated by a gamma-ray detection probe (GP) can then be used to provide directional guidance during the intervention [4]. Alternatively, portable gamma-imaging modalities can be used to provide an intraoperative image of the nodal uptake [5,6]. Despite research oriented efforts commercially available portable gamma detection modalities do not yet allow depiction of detailed anatomical information [7,8].

To provide high resolution optical identification of the SNs, small dyes such as patent blue (V), fluorescein, and indocyanine green (ICG) have been used [9,10]. Unfortunately, when radiocolloids and fluorescent agents are used separately, superficial intraoperative optical findings (<1 cm) can deviate from the (in-depth) observations made using the radiocolloid [11]. Such shortcomings can be overcome using a hybrid tracer, for example indocyanine green (ICG)- $^{99m}\text{Tc}$ -nanocolloid, a tracer that contains both a radioisotope and an optical fluorescent dye. The clinical value of ICG- $^{99m}\text{Tc}$ -nanocolloid has already been extensively demonstrated by us [12–14] and others [11,15] whereby it was shown that using the hybrid tracer allows for direct translation of (in-depth) preoperative imaging findings into the operation theatre. The radiolabel of the hybrid tracer allows preoperative SN mapping in a similar fashion as the conventional radioguided approach [12], meaning it also provides directional information for the placement of the incisions. During the operation the combination of radio- and fluorescence guidance can be used to refine this even further by confirming the actual location and removal of the sentinel lymph nodes defined at preoperative imaging [12–14]. This combined approach significantly outperformed blue dye based sentinel node identification [12–14].

The increase in the combined clinical use of radio- and fluorescence-guidance methodologies, either using separate radioactive and fluorescent tracers or by using hybrid tracers has generated a need for multiple detection modalities in the operating room. This in turn has driven the development of integrated (or rather hybrid) navigation set-ups wherein the

fluorescence camera is positioned using single photon emission computed tomography (SPECT)-based findings [16,17]. To date only one true hybrid modality has been reported on in clinical use, namely a gamma-probe-based device that was extended with fiber based acoustic fluorescence tracing capabilities [18]. Based on this success one may wonder if it is also possible to accomplish the reverse in engineering by extending a known surgical fluorescence camera technology with the ability to detect gamma rays. To this end we combined a small-sized fluorescence camera (VITOM) [19,20] with a gamma probe (GP) and a portable gamma camera (GC). Using these two set-ups, we assessed the clinical logistics during the intervention and identified the engineering challenges that need to be resolved in order to make an optimal hybrid detection apparatus for clinical use.

## **METHODS**

### **Hardware**

Near infrared-fluorescence imaging was performed using a lightweight fluorescence camera (VITOM; KARL STORZ GmbH & Co. KG, Tuttlingen, Germany). This open surgery camera provides real-time on-screen fluorescence images (fluorescence signal in blue) with respect to the anatomy of the patient [20] and enables switching between the white light and the fluorescence imaging modus.

A hand-held GP (Europrobe 2, Eurorad, Eckbolsheim, France), providing both a numeric and an acoustic read-out, was used for intraoperative gamma tracing. A mobile GC (Sentinella; Oncovision, Valencia, Spain) was used for intraoperative gamma imaging (21). The latter is equipped with a hand-controlled laser pointer that enables marking of the focus point/ location of gamma imaging on the skin or in the wound.

### **Engineering of the clip-on devices**

To connect the VITOM to the GP or GC, custom clip-on brackets were designed using three-dimensional (3D) computer-aided engineering software (Solidworks; Dassault Systèmes, Vélizy-Villacoublay, France) and subsequently 3D printed (VDM Kunststofftechnik, Doetinchem, the Netherlands) in sterilizable RC31 (Envisiontec, Gladbeck, Germany) (Supplemental Figure 1).

The clip-on brackets were engineered in such a way that the focal points of gamma detection devices and the fluorescence camera were aligned (Figure 1 and Supplemental Figure 1). For

the fluorescence camera and gamma probe combination (VITOM-GP), the focal point was  $\approx 11$  cm, with an angle in alignment of both detection modalities of  $7.24^\circ$  (Figure 2A). For the fluorescence camera and gamma camera combination (VITOM-GC), the VITOM was placed under a  $33.8^\circ$  angle. The focal point was again localized at  $\approx 11$  cm (measured from the tip of the VITOM) and at 6.4 cm from the collimator of the GC (9.5 cm from the detector; Figure 1B).

## Patients

Eleven patients with cT1-cT3N0 penile cancer scheduled for SN biopsy and subsequent treatment of the primary tumor were prospectively included after obtaining written informed consent. Patient characteristics are shown in Table 1.

Followed procedures were in accordance with the ethical standards of the responsible committee on human experimentation (institutional and national) and with the Helsinki declaration of 1975, as revised in 2008. This study was approved by the Institutional Review Board of the Netherlands Cancer Institute – Antoni van Leeuwenhoek hospital (NKI-AVL, Amsterdam, The Netherlands).

## Injection procedure and preoperative imaging

Hybrid tracer injection and preoperative SN mapping were performed one day prior to surgery or on the morning of the day of surgery as previously described (13). In brief, four deposits of 0.1 mL hybrid tracer ICG- $^{99m}\text{Tc}$ -nanocolloid were injected per patient around the primary lesion. Dynamic (during the first ten minutes post injection) and static (at fifteen minutes and two hours post injection) planar lymphoscintigraphy was performed. Lymphoscintigrams at two hours post injection were followed by single photon emission computed tomography fused with computed tomography (SPECT/CT) imaging. The number and location of SNs was determined based on preoperative imaging and marked on the skin.

## System evaluation

The current study was performed by experienced surgical personnel that regularly uses intraoperative fluorescence- and gamma tracing modalities, even in combination with the hybrid tracer [13].

Prior to incision the ability of the VITOM-GP or the VITOM-GC to detect the SN transcutaneously, via fluorescence imaging [22] and gamma detection, was evaluated when the probe was placed in direct contact with the skin (0 cm; VITOM-GP only) and at the optimal focal point ( $\approx 11$  cm) of the VITOM. After tissue preparation and full exposition

of the SN, the sensitivity of fluorescence imaging and gamma detection (visual or acoustic (numeric)) of the VITOM-GP and VITOM-GC was evaluated at different working distances namely: 0 cm (VITOM-GP only), 10 cm ( $\approx$ VITOM focal plane), 20 cm and 30 cm (Figure 2). The efficiency of detection was scored and presented in percentage detected SNs relative to the total amount of SNs pursued (Table 1). The true value of a possible future hybrid device was evaluated in the focal plane as here both signals were detected synchronically in the same focal spot.

After SN excision, the wound bed was checked for the presence of residual radioactivity and fluorescence with either the VITOM-GC or VITOM-GP. The SNs that were removed without evaluation of the respective hybrid modality were located with intermittent use of the GP and fluorescence detection (VITOM).

## **Pathology**

Excised tissue specimens were processed as described previously [13].

## **RESULTS**

### **Preoperative imaging and pathology**

Details on the injected dose of the hybrid tracer, preoperative SN mapping, as well as pathology results are stated in Table 1.

### **Intraoperative evaluation of the VITOM-GP combination**

Preoperatively fourteen SNs were identified on SPECT/CT in the VITOM-GP patient group. For practical reasons in some patients the limited available time prevented us to evaluate all SNs using the VITOM-GP combination. Therefore only nine of these fourteen preoperatively identified SNs were included in the evaluation of the VITOM-GP combination.

Prior to placement of the incision the gamma detection rate was 100% in all cases. In contrast, via fluorescence detection none of the SNs could be detected transcutaneously (Figure 3C). Here it should be noted that the VITOM was unable to fully focus at this short distance (0 cm). Upon SN exposure, the detection rates in the focal plane ( $\approx$ 11 cm from the SN) were 88.9% for the gamma detection and 100% for fluorescence detection. At 20 and 30 cm working distance, gamma tracing identified 55.6% of the pursued SNs, while fluorescence imaging enabled detection of 88.9% of the SNs (Figure 2). At the larger

distances SN detection using the numeric/acoustic nature of the read-out of the GP was sometimes hindered by emissions coming from the nearby primary injection site.

The VITOM-GP combination was relatively small in size and could easily be handled with one hand. It also allowed real-time interpretation of both the gamma signal (acoustic/numeric) and fluorescence signal (on-screen, visual). When moving the device, the gamma tracing option provided directional feedback for the placement of the VITOM-GP. As a result of the angulation of the different modalities, dual imaging was only possible at the focal point ( $\approx 11$  cm). Beyond that distance placement of the two modalities had to be corrected horizontally to accommodate fluorescence detection (Figure 1).

### **Intraoperative evaluation of the VITOM-GC combination**

Again, for practical reasons only ten of the fifteen SNs identified using SPECT/CT were surgically pursued with the VITOM-GC combination. Prior to initiation of the surgical procedure the detection rate of the GC was 100%, irrespective of the evaluated working distance (10, 20, or 30 cm). Transcutaneous fluorescence-based SN detection was not possible. Upon SN exposure, the GC detection rate remained 100%. Fluorescence imaging provided a 90% detection rate at the focal plane, which dropped to 80% at 20 and 30 cm. When performing gamma imaging beyond 20 cm distance, the injection site also became visible. Other than with the GP (see above), here the GC signal could be used to aid in the orientation (Figure 2J and 2K).

The VITOM-GC combination was large and heavy, and required a retractable (external) supporting device for placement. This device was considered convenient as it enabled accurate camera placement for longer periods of time, while leaving the surgeons hands free to perform the resection under image guidance. The laser pointer on the GC could be used to highlight the area of interest during gamma imaging (acquisition times up to 30 sec). However, as the pointer interfered with the fluorescence findings, it had to be switched off before fluorescence imaging was initiated (Supplemental Figure 2E and 2F). Data interpretation in the focal plane was limited by the fact that both signals were visually displayed and the operating surgeon had to look at two screens to determine the relation between the two findings. Beyond the focal point the large angle between both modalities ( $33.8^\circ$ ) meant that the spatial displacement between fluorescence- and gamma imaging findings was even more critical in this set-up.

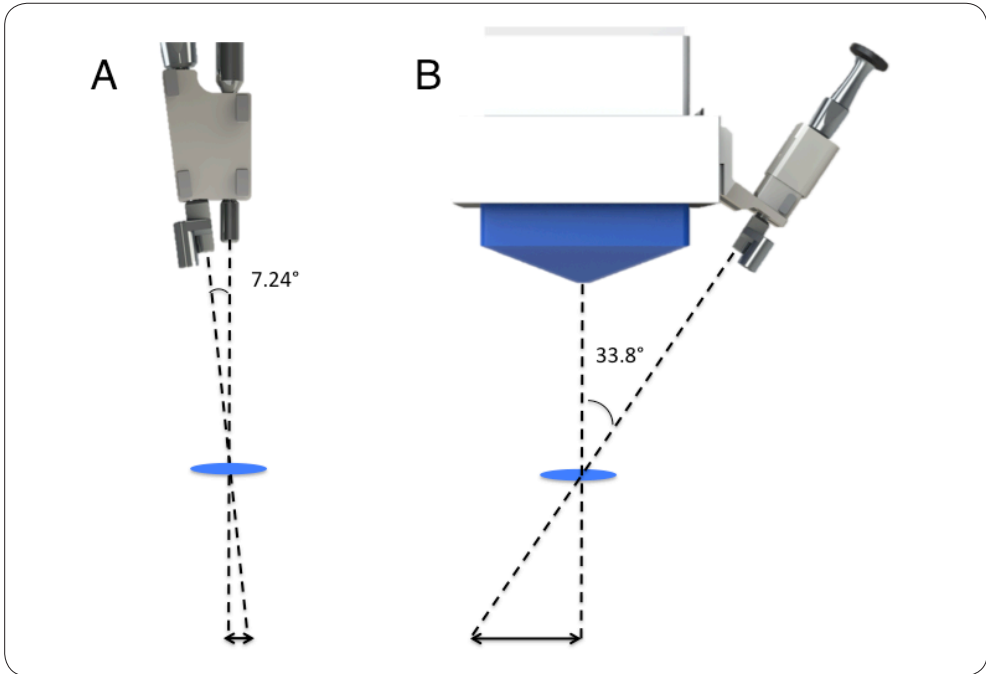


**Figure 1. Schematic overview of the VITOM-GP and VITOM-GC combination.**

**A:** The VITOM-GP combination.

**B:** The VITOM-GC combination. Because of the angle in alignment the devices had to be moved horizontally, to compensate for misalignment at distances beyond the focal plane.

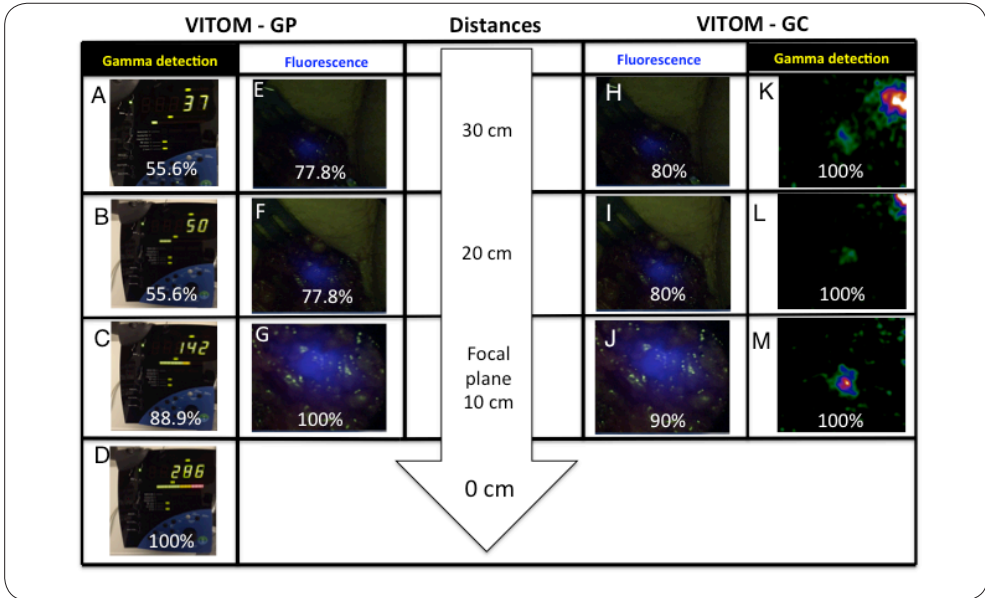
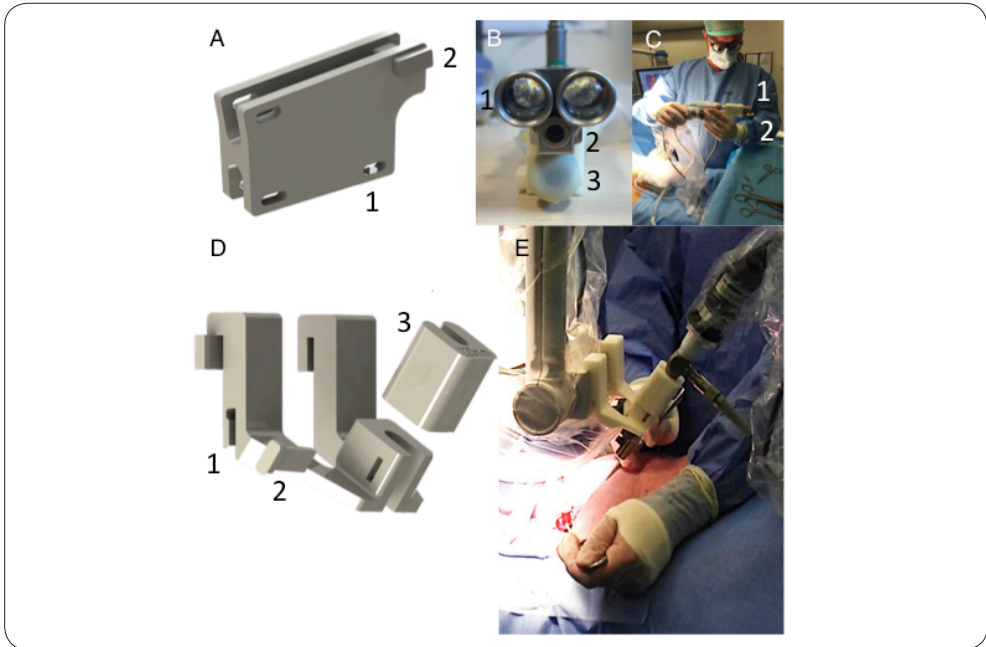


**Figure 2. Fluorescence imaging versus gamma detection.**

On the left side the SN detection rates (%) of the VITOM-GP combination are shown in relation to the four evaluated working distances (A-F). On the right, the SN detection rates (%) of the VITOM-GC are presented in relation to the three different evaluated working distances (G-L). GP = gamma probe; GC = gamma camera.



**SI Figure 1. Clip-on brackets developed to combine the VITOM to the GP or GC.**

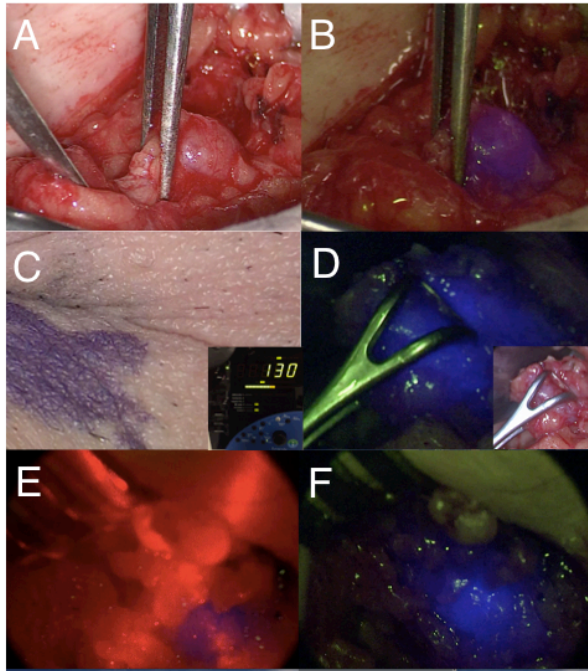
**A:** Clip-on bracket of the GP and VITOM (1) with VITOM securement (2).

**B:** VITOM-GP showing the light sources (1), the camera (2) and the gamma probe (3).

**C:** Intraoperative use of the VITOM-GP (1: GP, 2: VITOM).

**D:** 1.The clip-on bracket that allows secured coupling of the VITOM (2, 3) to the GC (1).

**E:** Intraoperative positioning of the VITOM-GC combination. GP = gamma probe; GC = gamma camera.



**SI Figure 2. Intraoperative fluorescence imaging of SNs.**

- A:** White light image of the area harboring the SN;
- B:** Fluorescence imaging of the area under A allowed optical confirmation of having localized the SN;
- C:** Fluorescence imaging of the same SN as in D, with intact skin. No fluorescence signal could be detected, while gamma detection was possible (picture in picture right under).
- D:** After tissue preparation, the borders of the fluorescent SNs were clearly shown (picture in picture: corresponding white light image);
- E:** The laser pointer of the portable gamma camera interfered with fluorescence imaging; SN detection was possible, although detection was not very efficient.
- F:** By switching off the laser pointer clear SN visualization via fluorescence imaging was possible.

## DISCUSSION

This study describes two hybrid imaging set-ups (VITOM-GP and VITOM-GC) and their potential to provide surgical guidance in combination with the hybrid tracer ICG-<sup>99m</sup>Tc-nanocolloid. In both set-ups the in-depth information of the gamma signal was used to determine the site of incision and provided directional guidance for positioning of the VITOM. When the SN was exposed fluorescence imaging could be used to visually detect the SNs with respect to the anatomical context. These findings clearly underline the strengths and weaknesses of the two individual imaging signatures. Moreover, the reported detection percentages show that the hybrid modality-based find rates are highly similar to those previously reported for the individual modalities [13]. The current prototype set-up was not optimized from an efficacy point of view and their use influenced operating room logistics and the operation time. Nevertheless, in future studies, it remains to be evaluated if the use of an optimized hybrid modality can result in reduced morbidity, operation time and postoperative infection rates.

From the findings of the current study we were able to derive a number of engineering challenges that have to be faced before imaging-based hybrid surgical guidance modalities will become efficient tools for routine use. The clip-on design was considered convenient as it efficiently combined two clinically available modalities, but still allowed for their individual use. Unfortunately, the angled alignment was not optimal for distances smaller or larger than the focal plane. In both combined devices the angle between the modalities dictated spatial placement in order to get the information from the SN for both modalities (Figure 1). Most likely future hybrid modalities will require both modalities to be placed perpendicular to each other and with an identical field of view. Though this will require full hardware integration. The findings of the current study also suggest that placement of both image guidance modalities on a stable, but retractable, arm could be of value.

In the current set up the optimal detection plane of the individual modalities was shown to differ for the VITOM (>11 cm), GP (0-10 cm) and GC (0-30 cm). Furthermore, intraoperative adaptation of the fluorescence focus was considered inconvenient. The concept of hybrid imaging hardware could only be accurately evaluated in the focal plane of the VITOM ( $\approx$ 11 cm). In future hybrid devices the focus of the two modalities should be matched, at least in a certain range. Possibly an autofocus option should also be included for the optical imaging. The difference in fluorescence detection between the VITOM-GP and VITOM-GP could partly be explained by the failure of fluorescence detection in a patient with a body mass index

over 40. Fatty tissue hampers the fluorescence signal detection and this risk increases in patients with obesity.

The largest and final hurdle to be tackled, however, will be the difference in detection sensitivity between the radioguidance and fluorescence modalities used. Although full integration is possible from an engineering point of view, its realization is not straightforward when combination of state-of-the-art detector sensitivity for both fluorescence and radioactivity is envisioned. Especially when considering that the fluorescence modality could benefit from higher fluorescence sensitivity at longer distances. This would require both a stronger excitation light-source and higher detection sensitivity. The white light option should remain included as this information created directional feedback and provided anatomical context. The difference in sensitivity between the GP and GC modalities influenced the acquisition time, collimation and field of view [2,6], all of which can be improved further.

Overall the VITOM-GP combination was preferred by the surgeons over the VITOM-GC combination. The reason for this was that the acoustic/numerical feedback provided by the GP provided information that could be processed simultaneously with the fluorescence imaging findings. Hereby two sensory organs, ears and eyes, work in conjunction, providing directional guidance for the placement of the fluorescence camera. In contrast, parallel display of the VITOM and GC findings relied on a single sensory organ, making it more difficult to process. Having the display of the two different imaging findings on two different screens was sometimes considered confusing. Hereby especially the lack of anatomical information in the GC images made it difficult to relate them to the fluorescence imaging findings. The value of the VITOM-GC combination could potentially increase when both imaging findings are integrated in a single (video screen) display, a technology that we previously successfully applied in a navigation set-up [23].

## CONCLUSION

In this study we demonstrated that combined radio- and fluorescence imaging modalities have the potential to make sense in the hybrid surgical guidance concept. The integrated detection modalities were shown to work synergistically; overall the GC was most valuable for rough localization (10-30cm range) of the SNs, the GP for providing convenient real-time acoustic feedback, while fluorescence guidance allowed detailed real-time SN visualization.

## REFERENCES

1. KleinJan GH, Bunschoten a., Brouwer OR, Berg NS, Valdés-Olmos R a., Leeuwen FWB. Multimodal imaging in radioguided surgery. *Clin Transl Imaging* [Internet]. 2013 Dec 4 [cited 2014 Feb 3];1(6):433–44.
2. Povoski SP, Neff RL, Mojzisek CM, O'Malley DM, Hinkle GH, Hall NC, et al. A comprehensive overview of radioguided surgery using gamma detection probe technology. *World J Surg Oncol* [Internet]. 2009 Jan [cited 2013 Feb 14];7:11.
3. Nieweg OE, Tanis PJ, Kroon BB. The definition of a sentinel node. *Ann Surg Oncol* . 2001 Jul;8(6):538–41.
4. Heller S, Zanzonico P. Nuclear probes and intraoperative gamma cameras. *Semin Nucl Med*. Elsevier Inc.; 2011;41(3):166–81.
5. Vermeeren L, Valdés Olmos RA, Klop WMC, Balm AJM, van den Brekel MWM. A portable gamma-camera for intraoperative detection of sentinel nodes in the head and neck region. *J Nucl Med*. 2010;51(5):700–3.
6. Tsuchimochi M, Hayama K. Intraoperative gamma cameras for radioguided surgery: technical characteristics, performance parameters, and clinical applications. *Phys Med*. 2013;29(2):126–38.
7. Hellingman D, Vidal-Sicart S, de Wit-van der Veen LJ, Paredes P, Valdés Olmos RA. A New Portable Hybrid Camera for Fused Optical and Scintigraphic Imaging: First Clinical Experiences. *Clin Nucl Med*. 2016 Jan;41(1):e39–43.
8. Lees JE, Bassford DJ, Blake OE, Blackshaw PE, Perkins AC. A Hybrid Camera for simultaneous imaging of gamma and optical photons. *J Instrum*. 2012;7(06):P06009–P06009.
9. Morton DL, Wen DR, Wong JH, Economou JS, Cagle LA, Storm FK, et al. Technical details of intraoperative lymphatic mapping for early stage melanoma. *Arch Surg*. 1992;127(4):392–399.
10. van Leeuwen FWB, Hardwick JCH, van Erkel AR. Luminescence-based Imaging Approaches in the Field of Interventional Molecular Imaging. *Radiology*. 2015;276(1):12–29.
11. Stoffels I, Leyh J, Pöppel T, Schadendorf D, Klode J. Evaluation of a radioactive and fluorescent hybrid tracer for sentinel lymph node biopsy in head and neck malignancies: prospective randomized clinical trial to compare ICG-(99m)Tc-nanocolloid hybrid tracer versus (99m)Tc-nanocolloid. *Eur J Nucl Med Mol Imaging* 2015;42(11):1631-1638
12. Brouwer OR, Buckle T, Vermeeren L, Klop WMC, Balm AJM, van der Poel HG, et al. Comparing the hybrid fluorescent-radioactive tracer indocyanine green-99mTc-nanocolloid with 99mTc-nanocolloid for sentinel node identification: a validation study using lymphoscintigraphy and SPECT/CT. *J Nucl Med*. 2012;53(7):1034–40.
13. Brouwer OR, van den Berg NS, Mathéron HM, van der Poel HG, van Rhijn BW, Bex A, et al. A hybrid radioactive and fluorescent tracer for sentinel node biopsy in penile carcinoma as a potential replacement for blue dye. *Eur Urol*. 2014;65(3):600–9.
14. KleinJan GH, van den Berg NS, Brouwer OR, de Jong J, Acar C, Wit EM, et al. Optimisation of Fluorescence Guidance During Robot-assisted Laparoscopic Sentinel Node Biopsy for Prostate Cancer. *Eur Urol*. 2014;66(6):991–8.
15. Christensen A, Juhl K, Charabi B, Mortensen J, Kiss K, Kjær A, et al. Feasibility of Real-Time Near-Infrared Fluorescence Tracer Imaging in Sentinel Node Biopsy for Oral Cavity Cancer Patients. *Ann Surg Oncol*. 2016;23(2):565–72.
16. Brouwer OR, Buckle T, Bunschoten A, Kuil J, Vahrmeijer AL, Wendler T, et al. Image navigation as a means to expand the boundaries of fluorescence-guided surgery. *Phys Med Biol*. 2012;57(10):3123–36.
17. KleinJan GH, van den Berg NS, van Oosterom MN, Wendler T, Miwa M, Bex A, et al. Towards (hybrid) navigation of a fluorescence camera in an open surgery setting. *J Nucl Med*. 2016;57(10):1650-1653.
18. van den Berg NS, Simon H, Kleinjan GH, Engelen T, Bunschoten A, Welling MM, et al. First-in-human evaluation of a hybrid modality that allows combined radio- and (near-infrared) fluorescence tracing during surgery. *Eur J Nucl Med Mol Imaging*. 2015;42(11):1639-47
19. Mamelak AN, Drazin D, Shirzadi A, Black KL, Berci G. Infratentorial supracerebellar resection of a pineal tumor using a high definition video endoscope (VITOM®). *J Clin Neurosci*. 2012;19(2):306–9.
20. Buda A, Dell'Anna T, Vecchione F, Verri D, Di Martino G, Milani R. Near-Infrared Sentinel Lymph Node Mapping With Indocyanine Green Using the VITOM II ICG Endoscope for Open Surgery for Gynecologic Malignancies. *J Minim Invasive Gynecol*. 2016;(4):628-32.
21. Sánchez F, Benlloch JM, Escat B, Pavón N, Porras E, Kadi-Hanifi D, et al. Design and tests of a portable mini gamma camera. *Med Phys*. 2004;31(6):1384–97.
22. van den Berg NS, Miwa M, KleinJan GH, Sato T, Maeda Y, van Akkooi ACJ, et al. (Near-Infrared) Fluorescence-Guided Surgery Under Ambient Light Conditions: A Next Step to Embedment of the Technology in Clinical Routine. *Ann Surg Oncol*. 2016;23(8):2586–2595.

23. KleinJan GH, Bunschoten A, van den Berg NS, Valdes Olmos RA, Klop WMC, Horenblas S, et al. Fluorescence guided surgery and tracer-dose, fact or fiction? *Eur J Nucl Med Mol Imaging*. 2016;43(10):1857-1867

# Chapter 8



# Toward (Hybrid) Navigation of a Fluorescence Camera in an Open Surgery Setting



*Gijs H. KleinJan  
Nynke S. van den Berg  
Matthias N. van Oosterom  
Thomas Wendler  
Mitsuharu Miwa  
Axel Bex  
Kees Hendricksen  
Simon Horenblas  
and Fijis W.B. van Leeuwen  
J Nucl Med. 2016;57(10):1650-1653.*

## **ABSTRACT**

### **INTRODUCTION**

With the introduction of the hybrid tracer indocyanine green (ICG)-<sup>99m</sup>Tc-nanocolloid, a direct relation between preoperative imaging and intraoperative fluorescence guidance was established. However, fluorescence guidance remains limited by its superficial nature. This study evaluated the feasibility of a nuclear medicine– based navigation concept that allowed intraoperative positioning of a fluorescence camera (FC) in the vicinity of preoperatively defined ICG-<sup>99m</sup>Tc-nanocolloid containing sentinel nodes (SNs).

### **METHODS**

Five patients with penile cancer scheduled for SN biopsy were injected with ICG-<sup>99m</sup>Tc-nanocolloid followed by preoperative SPECT/CT imaging. The navigation device was used to provide a real-time augmented reality overlay of the SPECT/CT images and video output of the FC. This overlay was then used for FC navigation.

### **RESULTS**

SPECT/CT identified 13 SNs in 9 groins. FC navigation was successful for all 12 intraoperatively evaluated SNs (average error, 8.8 mm; range, 0–20 mm).

### **CONCLUSION**

This study reveals the potential benefits of FC navigation during open surgery procedures.

## INTRODUCTION

Although interventional guidance can be provided using multiple modalities, because of its ability to provide detailed and real-time guidance, fluorescence imaging (FI) is receiving increasing interest. FI is highly effective in superficial applications at known locations but has a limited in-depth potential [1]. Radioguidance technologies on the other hand have been shown to have a great in-depth potential and even allow for preoperative confirmation of tracer uptake using, for example, SPECT combined with CT [2].

When separate approaches are used to provide pre- and intra-operative guidance, information may get lost between diagnostic imaging and the operation theater. Discrepancies in findings may subsequently result in over- or undertreatment of the patient. To solve these translational issues, and to enable a best-of-both-worlds scenario, a hybrid surgical guidance concept is advocated. This concept is based on integrating multiple complementary features that are of value for preoperative imaging (nuclear medicine) and intraoperative (fluorescence) image-guided surgery [3]. This can, in part, be realized using a hybrid tracer that contains 2 distinct signals, for example, the sentinel node (SN) tracer indocyanine green (ICG)-<sup>99m</sup>Tc-nanocolloid [1]. Recently, this hybrid concept was expanded beyond the field of tracer development to hardware-based integration of radioguidance and FI modalities [4,5].

Surgical navigation using 3-dimensional (3D) nuclear medicine findings has been used to provide directional movement to the lesion of interest, in the form of in-depth information. This technology was considered particularly valuable during SN biopsy procedures [6–8]. Apart from navigation of a g-probe, the navigation setup has also been used for laparoscope [4],  $\gamma$ -camera [7], and ultrasound probe [9] positioning. We thus reasoned it should be possible to also navigate a fluorescence camera (FC) in an open surgery setting [Figure 1]. For penile cancer SN biopsy, we have previously demonstrated that ICG-<sup>99m</sup>Tc-nanocolloid provides superior optical guidance toward SNs compared with blue dye [10]. However, in patients with increased fatty tissue surrounding the SNs, the limited tissue penetration of the fluorescent signal was not always sufficient to optically identify the SNs via fluorescence guidance [10]. Although the conventional radioguided approach was effective in identifying these SNs, these modalities provided no depth information to the target. By integrating navigation into the procedure, we made an attempt to overcome these shortcomings for penile cancer patients who were to undergo a SN biopsy procedure.

## METHODS

### Patients

Five patients with cT1–2N0Mx penile cancer [11] scheduled for SN biopsy and subsequent treatment of the primary tumor were prospectively included. All included groins were clinically node-negative [10].

The institutional review board of The Netherlands Cancer Institute–Antoni van Leeuwenhoek approved this study, and all subjects signed a written informed consent form. Procedures followed were in accordance with the ethical standards of the responsible committee on human experimentation (institutional and national) and with the Helsinki Declaration of 1975, as revised in 2008.

### Histopathology

The hybrid tracer is formed by mixing  $^{99m}\text{Tc}$ -nanocolloid with a small amount of ICG. Briefly, 2 mL of pertechnetate (1,400 MBq) in saline was added to a commercial vial of nanocolloid (containing 0.5 mg of albumin colloid [GE Healthcare]). After incubation at room temperature (30 min) and removal of any excess reactive elements, to the  $^{99m}\text{Tc}$ -nanocolloid solution (pH 6–7) 0.25 mg of ICG was added to form ICG- $^{99m}\text{Tc}$ -nanocolloid [12, 13].

For the SN biopsy procedure of penile cancer, the hybrid tracer injection procedure, preoperative SN mapping, and histopathologic tissue analysis have been previously described in detail by Brouwer et al. [10]. On average 96.7 MBq of ICG- $^{99m}\text{Tc}$ -nanocolloid was injected in 4 depots around the tumor (Supplemental Table 1 [supplemental materials are available at <http://jnm.snmjournals.org>]).

### Specifications of Navigation Device and FC (Software and Hardware)

#### Hardware and Reference Trackers.

As navigation device, the declipseSPECT (SurgicEye), in which DICOM files of the preoperatively acquired SPECT/CT datasets can be loaded, was used [4,8].

Preoperative images were acquired with a reference tracker containing three fiducials (hereafter referred to as  $\text{RT}_{\text{patient}}$ ) placed on the patient (Figure 1). In 4 patients, the patient reference tracker ( $\text{RT}_{\text{patient}}$ ) was placed on the pubic bone, whereas in 1 patient (patient 2) this was impossible because of the patient's obesity; here the tracker was placed on the superior anterior iliac bone.

The preoperative  $\text{RT}_{\text{patient}}$  location was marked (with ink), and during the operation a sterile  $\text{RT}_{\text{patient}}$  was placed on the same skin-marked location, allowing the navigation system to spatially merge the preoperative acquired SPECT/CT with the position of the patient in

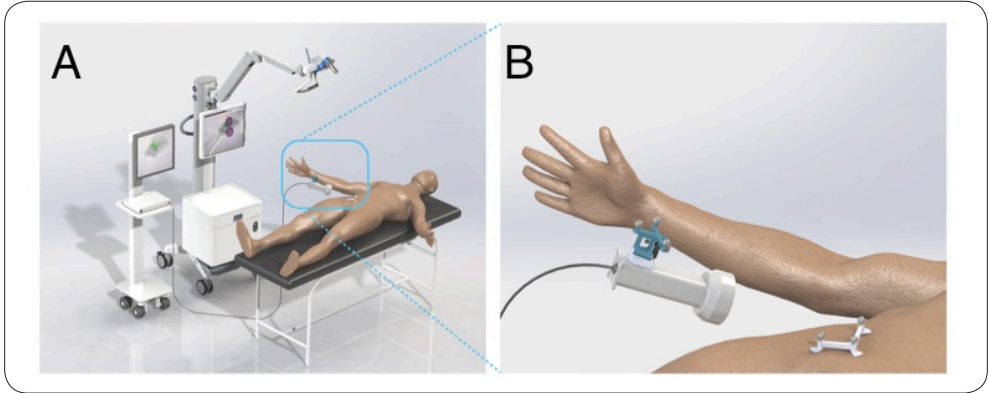


Figure 1. Fluorescence camera navigation

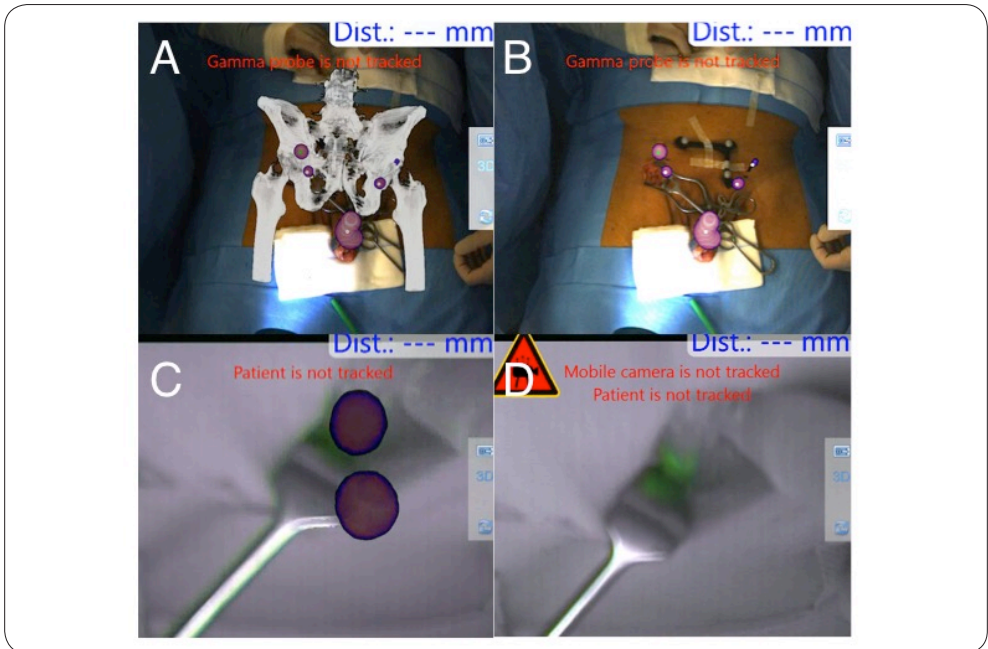


Figure 2. Navigation of the FC. Video signal of the overhead camera of navigation system allows projection of SPECT/CT

(A) or SPECT (B) onto the patient. Bony structures (low-dose CT) and SNs/injection site (SPECT) are shown.

(C) Overlay of the SPECT on near-infrared video signal of the FC showing 2 SNs.

(D) Fluorescence imaging optically visualized the SN and thus allowed confirmation of FC navigation accuracy.

the operating theater (registration). When fused with the real-time white light video-feed generated by the navigation device—embedded overhead camera, different on-screen mixed/augmented-reality views could be created. Intraoperative replacement of the sterile RT<sub>patient</sub> did not negatively affect the surgical workflow.

A second 3-fiducial reference tracker (hereafter referred to as RT<sub>fluorescence</sub>) was attached to the modified PhotoDynamicEye (m-PDE; Hamamatsu Photonics KK) FC to allow for its tracking by the navigation system (Figure 1). This FC has the ability to switch between white light and near-infrared FI mode and works under ambient light conditions [15]. For easy differentiation between the RT<sub>fluorescence</sub> and the RT<sub>patient</sub>, the trackers were geometrically differently shaped.

### **Incorporation of Imaging Information of FC into Navigation Device**

To import the video-feed of the FC into the navigation system, the Bayonet-Neill-Concelman connector (BNC) video output of the FC was taken and converted with a BNC to video graphics array converter (Ligawo), after which the signal was recorded in a Epiphan DVI2PCIe framegrabber (Epiphan Systems Inc.) that was integrated in the navigation device. Customized declipseSPECT 6.0 software (SurgicEye) was used to incorporate the external FC video-feed in both the calibration and the navigation workflow.

Calibration of the FC was performed in the following 2 steps. For intrinsic (e.g., focal length, principle point, lens distortions) and extrinsic camera parameters (translation and rotation with respect to the navigation device reference coordinate system), calibrations were performed using a tracked 7 · 8 checkerboard and an open source computer vision library for camera calibration based on the work as described by Zhang [14]. These calibrations were performed to allow the augmented projection of the preoperative SPECT/CT data in the FC video image. In the second step, calibration of the transformation between the camera lenses and the RT<sub>fluorescence</sub> on the FC was performed using a dedicated calibrator reference target. This calibration makes it possible to show the distance from the camera lenses relative to the designated navigation targets found in the SPECT imaging data, in this case the SNs.

To allow the FC to be tracked and navigated in the preoperative SPECT/CT images, a navigation display similar to the one generated for the conventional  $\gamma$ -probe was used [8]. Herein, an overlay of the 3D SPECT/CT images onto the patient was displayed in the video-feed of the FC. This same view also showed the distance from the tip of the FC to the designated targets (SNs).

Integration of the SPECT/CT images with the real-time fluorescence images of the FC could

be switched on and off at will. Moreover, because the FC allows for both white light and near-infrared FI, navigation could be performed in both imaging modes. When sudden movements were made with the FC during the navigation procedure, the SPECT/CT overlay followed with a slight lag (20–40 ms). This could be corrected easily by holding the FC still for a fraction of a second.

### **Surgical Procedure: Intraoperative Navigation to SNs**

Before incision, the FC was navigated in the preoperatively acquired SPECT/CT images toward the SNs in the groin. During this process, the distance between the FC and the center of the SN was provided. If the SN was not visible through the skin via FI, the  $\gamma$ -probe (Neoprobe; Johnson & Johnson Medical) was used to determine the site for incision.

After incision, alternating  $\gamma$ -tracing and FI allowed localization of the SNs in the groin. On localization of the SN, the FC was again navigated to determine the correlation between the acquired fluorescence image and the projected SPECT/CT image. The error of navigation (in the coronal plane) was determined by measuring the distance between the center of the radioactive hotspot and the center of the fluorescence hotspot as seen on-screen from the perspective of the FC.

### **Light Spectra Measurements**

Light spectra of the FC and the optical tracking device of the navigation device were measured using a Jobin Yvon VS140 linear array fiber spectrometer (Horiba) in the 300- to 1,200-nm range, with an integration time of 0.1 ms. The fiber was held at an approximate 2-m distance from the head of the device of which the light spectra were measured.

## RESULTS

### Preoperative SN Mapping

Preoperative imaging revealed bilateral drainage in 4 of the 5 included patients. In the remaining patient, only unilateral drainage was seen. With SPECT/CT imaging, 13 SNs, dispersed over 9 groins, were identified, of which 30.8% could already be visualized on the lymphoscintigrams acquired 15 min after injection of the hybrid tracer (Supplemental Table 1).

### Navigation

In the navigation setup, the overlay of the SPECT/CT images and the FC video-feed was displayed on-screen (Figs. 2 and 3).

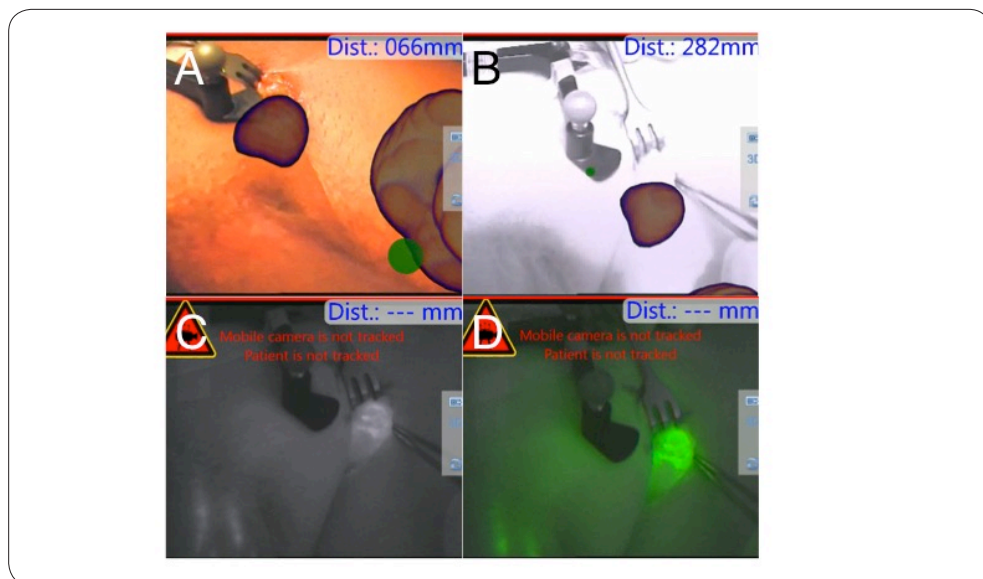


**Figure 3. Fluorescence imaging with integrated overlay.**

- (A)** Preoperative overlay of the SPECT onto the patient from the perspective of the FC (white light imaging mode) showing the primary injected tumor and, close to the reference tracker, the SN.
- (B)** Preoperative overlay of the SPECT onto the patient from the perspective of the FC (fluorescence imaging mode) illustrating the influence the flickering, caused by the tracking signal of the navigation device, has on the ability to visualize the fluorescence signal in the SN
- (C and D)**, in black-and-white or pseudocolored green, respectively).

Intraoperatively, 12 of the 13 SNs seen on preoperative imaging were navigated to with the FC (Supplemental Video 1) with an average navigation error of 8.8 6 9.1 mm (median, 7.5 mm; range, 0–20 mm). The 1 SN that was resected without using navigation was omitted because of logistical reasons.

Intraoperative repositioning of the RT<sub>patient</sub> directly resulted in a large navigation error (Supplemental Table 1, patients 3 and 4). In patient 4 only, we were able to correct this RT<sub>patient</sub> placement using the preoperative placed skin markings, thereby reducing the navigation error for the other SNs of this patient to 0 mm (Supplemental Table 1).

In 2 patients (patients 2 and 3), on localization of the SN we experienced that the hotspot in the preoperative images contained multiple (clustered) SNs, resulting in the intraoperative identification of 2 additional SNs. Overall, the navigation procedure was not found to be of influence on the length of the operation (average operation time, 91 min, including the primary tumor treatment).

### **Spectral Overlap Between Near-Infrared Camera and Fluorescence Emission of ICG**

Optical tracking by the navigation device occurred via reflection of pulsed near-infrared light (20 Hz) emitted by the tracking head of the declipseSPECT system. Following light reflection on the fiducials present on the RT<sub>patient</sub> and RT<sub>fluorescence</sub>, it can be selectively detected by the tracking head and used for position tracking. Unfortunately, the wavelength of this near-infrared light (800- to 900-nm range with a peak at 863 nm) overlapped with the emission spectrum of ICG (the only Food and Drug Administration clinically approved near-infrared fluorescent dye; peak, 810 nm). This meant that the tracking signal was also detected by the FC, causing a flickering interference when FI was performed in the near-infrared FI mode of the FC (Supplemental Figure 1). Yet, this did not hinder navigation of the FC in the white-light setting. This flickering could be blocked efficiently by manually covering the tracking light sources. However, it did mean that the in-depth navigation information was temporarily lost. When the FC remained at the exact same distance, FI could be performed to evaluate if the sentinel node was fluorescent.

The spectral overlap between the tracking device and the fluorescent emission of ICG did not prevent us from demonstrating the potential of the hybrid navigation concept (Supplemental Figure 1). However, for more routine use, the flickering issue needs to be solved. Here, the clinical availability of a spectrally different tracking light source or fluorescence tracer may provide outcome.

Because tracker placement appears to be a critical component for the navigation accuracy, much can be gained when this part of the procedure is improved. The RT<sub>patient</sub> used in this study had to be removed and replaced during the transfer from the Department of Nuclear Medicine to the operation theater. To overcome this shortcoming, one might use a different method of coregistration, for example, by using multiple small metal balls that are not susceptible to deformation or by implementing the concept of intraoperative freehandSPECT (6–8). FreehandSPECT may help to correct for errors caused by tissue deformation as a result of surgical manipulation.

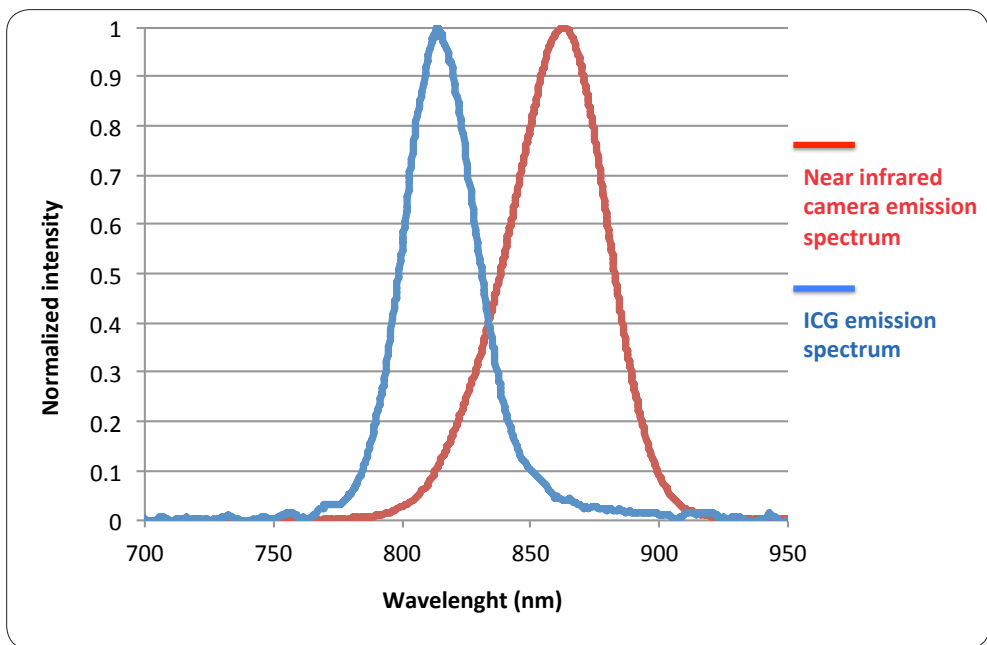


**Figure S11. Emission spectra of ICG and optical tracking device of the navigation system**

The emission spectrum of ICG (red curve) and optical tracking device of the navigation system (blue curve) partially overlap causing a flickering signal when imaging with the fluorescence camera in the fluorescence imaging modus.

Patient	Age	Tumor stage	Injected dose in Megabequerel	#SNs on early lymphoscintigrams		#SNs on late lymphoscintigrams		#SNs on SPECT/CT		Location tracker	Radioactive SNs		Location navigated SNs	Error location SN preoperative SPECT and location SN via fluorescence imaging	# Fluorescent SNs		# Groins	# Removed SNs	#SNs at Pathology		# Tumor-positive SNs	
				L	R	L	R	L	R		L	R			L	R			L	R	L	R
1	65	cT2	83.59	1	0	1	0	1	0	Pubic bone	L	R	Inguinal L	1 cm	1	-	1	1	3	0	0	-
2	54	cT2	74.8	0	0	1	1	1	1	RISA (L)	L	R	Inguinal L	1 cm	1	2	2	3	1	2	0	1
													Inguinal R	0 cm								
3	74	cT3	169.4	0	0	3	1	3	1	Pubic bone	L	R	Inguinal R	0 cm	4	1	2	5	4	1	0	0
													Inguinal L	0 cm								
													Inguinal L	2 cm								
4	71	cT2	80.4	1	2	1	2	1	2	Pubic bone	L	R	Inguinal L	2 cm	1	2	3	2	2	2	0	0
													Inguinal R	2 cm								
													Inguinal	2 cm								
5	67	cT0	75.1	0	0	1	2	1	2	Pubic bone	L	R	Inguinal R	0 cm	1	2	3	1	2	0	0	
													Inguinal R	0 cm								
													Inguinal L	0.5 cm								
Total				2	2	7	6	7	6		8	7			8	7	9	15	11	7	0	1

**Table S1 1.** = number; SN = sentinel node; SPECT/CT = single photon emission computed tomography combined with computed tomography; L = left; R = right; c = clinical, RISA

= Ramus Iliac Superior Anterior. One patient was treated within a 2-day protocol and therefore received a higher dose of Indocyanine green (ICG)<sub>99mTc</sub>-nanocolloid (169.4MBq). Preoperative imaging revealed bilateral drainage in four of the five included patients. In the remaining patient only unilateral drainage was seen. Pathological evaluation revealed that two more additional SNs could be retrieved from the 15 removed nodal samples. In one patient (patient 2), one tumor-positive lymph node was found after pathological evaluation.



## DISCUSSION

In this proof-of-concept study during open surgical SN biopsy procedures we demonstrated the feasibility of the hybrid navigator concept. This integrated approach provides an important step in the evolution of hybrid surgical guidance because it allows preoperative imaging information to be physically linked to FI in the intraoperative setting. Merging of modalities not only helps prevent a mismatch in findings, it also provides a step toward reducing space (e.g., in m2 they take up in the operation theater).

A fairly ideal evaluation setup was found in penile cancer patients as SNs were rather easy to locate because of their superficial location.

The main advantage of adding navigation in the hybrid surgical guidance concept was the improved directional feedback including depth estimation. As demonstrated in the current study, with the FC the accuracy of the navigation process could be confirmed or corrected. Similar to findings previously reported, the navigation error strongly depended on the accuracy with which we could replace the  $RT_{\text{patient}}$  during the surgical procedure [7,8].

By including patients who undergo SN biopsy procedures in other anatomies, for example, in the head and neck or axilla, the value of this technique can be further evaluated. Alternative to navigating toward an SN, one may also think of using this approach for hybrid tracer-based radioguided occult lesion localization (or for a seed-localization setup wherein hybrid marker seeds are applied) [16,17]. PET-based navigation in combination with intraoperative Cerenkov imaging could also provide an interesting extension [18].

## CONCLUSION

Navigation-based integration of preoperative 3D SPECT/CT information with real-time FI provides an interesting next step in the hybrid surgical guidance concept. If the technology evolves further, its implementation may be extended to other (hybrid) tracers and anatomies.

## REFERENCES

1. van Leeuwen FWB, Hardwick JCH, van Erkel AR. Luminescence-based imaging approaches in the field of interventional molecular imaging. *Radiology*. 2015; 276:12–29.
2. Maurer T, Weirich G, Schottelius M, et al. Prostate-specific membrane antigen- radioguided surgery for metastatic lymph nodes in prostate cancer. *Eur Urol*. 2015;68:530–534.
3. van den Berg NS, Valdés-Olmos R a, van der Poel HG, van Leeuwen FWB. Sentinel lymph node biopsy for prostate cancer: a hybrid approach. *J Nucl Med*. 2013;54:493–496.
4. Brouwer OR, Buckle T, Bunschoten A, et al. Image navigation as a means to expand the boundaries of fluorescence-guided surgery. *Phys Med Biol*. 2012;57:3123–3136.
5. van den Berg NS, Simon H, Kleinjan GH, et al. First-in-human evaluation of a hybrid modality that allows combined radio- and (near-infrared) fluorescence tracing during surgery. *Eur J Nucl Med Mol Imaging*. 2015;42:1639–1647.
6. Bluemel C, Schnelzer A, Okur A, et al. Freehand SPECT for image-guided sentinel lymph node biopsy in breast cancer. *Eur J Nucl Med Mol Imaging*. 2013;40:1656–1661.
7. Engelen T, Winkel BM, Rietbergen DD, et al. The next evolution in radioguided surgery: breast cancer related sentinel node localization using a freehandSPECT- mobile gamma camera combination. *Am J Nucl Med Mol Imaging*. 2015;5:233–245.
8. Brouwer OR, van den Berg NS, Mathéron HM, et al. Feasibility of intraoperative navigation to the sentinel node in the groin using preoperatively acquired single photon emission computerized tomography data: transferring functional imaging to the operating room. *J Urol*. 2014;192:1810–1816.
9. Freesmeyer M, Opfermann T, Winkens T. Hybrid integration of real-time US and freehand SPECT: proof of concept in patients with thyroid diseases. *Radiology*. 2014;271:856–861.
10. Brouwer OR, van den Berg NS, Mathéron HM, et al. A hybrid radioactive and fluorescent tracer for sentinel node biopsy in penile carcinoma as a potential replacement for blue dye. *Eur Urol*. 2014;65:600–609.
11. Sobin LH, Gospodarowicz MK, Wittekind C. *TNM Classification of Malignant Tumours*. 7th ed. Hoboken, NJ: Wiley-Blackwell. 2009.
12. KleinJan GH, Bunschoten A, van den Berg NS, et al. Fluorescence guided surgery and tracer-dose, fact or fiction? *Eur J Nucl Med Mol Imaging*. In press.
13. Bunschoten A, Buckle T, Kuil J, et al. Targeted non-covalent self-assembled nanoparticles based on human serum albumin. *Biomaterials*. 2012;33:867–875.
14. Zhang Z. A flexible new technique for camera calibration. *IEEE Trans Pattern Anal Mach Intell*. 2000;22:1330–1334.
15. van den Berg NS, Miwa M, Kleinjan GH, et al. (Near-infrared) fluorescence guided surgery under ambient light conditions, a next step to embedment of the technology in clinical routine. *Ann Surg Oncol*. In press.
16. van den Berg NS, Brouwer OR, Klop WMC, et al. Concomitant radio- and fluorescence-guided sentinel lymph node biopsy in squamous cell carcinoma of the oral cavity using ICG-99mTc-nanocolloid. *Eur J Nucl Med Mol Imaging*. 2012;39:1128–1136.
17. Buckle T, Chin PTK, van den Berg NS, et al. Tumor bracketing and safety margin estimation using multimodal marker seeds: a proof of concept. *J Biomed Opt*. 2010;15:056021.
18. Thorek DU, Riedl CC, Grimm J. Clinical Cerenkov luminescence imaging of 18F-FDG. *J Nucl Med*. 2014;55:95–98.

## SUPPLEMENTAL INFORMATION

### METHODS

#### Hybrid tracer preparation

The hybrid tracer is formed by mixing  $^{99m}\text{Tc}$ -nanocolloid with a small amount of indocyanine green (ICG). Briefly, two mL of pertechnetate (approximately 1400MBq) in saline was added to a commercial vial of nanocolloid (containing 0.5mg of albumin colloid (GE healthcare, Leiderdorp, the Netherlands). After incubation at room temperature (30min) and removal of any excess reactive elements, the  $^{99m}\text{Tc}$ -nanocolloid solution (pH 6–7) a 0.25mg ICG was added to form ICG- $^{99m}\text{Tc}$ -nanocolloid [1,2].

#### Hybrid tracer injection, preoperative sentinel node mapping and (histo)pathological analysis

For the sentinel node biopsy procedure of penile cancer the hybrid tracer injection procedure, preoperative sentinel node mapping, and (histo)pathological tissue analysis have been previously described by Brouwer et al. [3]. On average 96.7 MBq ICG- $^{99m}\text{Tc}$ -nanocolloid was injected in four depots around the tumor (Table SI 1).

#### Role of the reference trackers

Preoperative images were acquired with a reference tracker containing three fiducials (hereafter referred to as  $\text{RT}_{\text{patient}}$ ) placed on the patient (Figure 1 of the main manuscript). In four patients the patient reference tracker ( $\text{RT}_{\text{patient}}$ ) was replaced on the pubic bone, whereas in one patient (patient 2) this was impossible due to the patients' obesity; here the tracker was placed on the superior anterior iliac bone.

The preoperative  $\text{RT}_{\text{patient}}$  location was marked (with ink) and during the operation a sterile  $\text{RT}_{\text{patient}}$  was placed on the same skin-marked location. This allowed the navigation system to the system to spatially merge the preoperative acquired SPECT/CT with the position of the patient in the operating theatre (registration). When fused with the real-time white light video-feed generated by the navigation device embedded overhead camera, different on-screen mixed/augmented-reality views could be created. Intraoperative replacement of the sterile  $\text{RT}_{\text{patient}}$  did not negatively affect the surgical workflow.

A three fiducial reference tracker (hereafter referred to as  $\text{RT}_{\text{fluorescence}}$ ) was attached to a modified-PhotoDynamicEye (m-PDE; Hamamatsu Photonics KK, Hamamatsu, Japan) fluorescence camera (FC) to allow for its tracking by the navigation system (Figure 1 of the main manuscript). For easy differentiation between the  $\text{RT}_{\text{fluorescence}}$  and the  $\text{RT}_{\text{patient}}$  the

trackers were geometrically differently shaped. Incorporation of the imaging information of the fluorescence camera into the navigation device.

To import the video-feed of the FC into the navigation system, the Bayonet-Neill-Concelman connector (BNC) video output of the FC was taken and converted with a BNC to Video Graphics Array (VGA) converter (Ligawo, Leipzig, Germany), after which the signal was recorded in a Epiphan DV12PCIe framegrabber (Epiphan Systems Inc., Ottawa, Ontario, Canada) that was integrated in the navigation device (declipseSPECT; SurgicEye, Munich, Germany). Customized declipseSPECT 6.0 software (SurgicEye) was used to incorporate the external FC video-feed in both the calibration and navigation workflow.

Calibration of the FC was performed in two steps: 1) For intrinsic (e.g. focal length, principle point, lens distortions) and extrinsic camera parameters (translation and rotation with respect to the navigation device reference coordinate system) calibrations were performed using a tracked 7x8 checkerboard and an open source computer vision library for camera calibration based on the work as described by Zhang [4]. These calibrations were performed to allow the augmented projection of the preoperative SPECT/CT data in the FC video image; and 2) Calibration of the transformation between the camera lenses and the  $RT_{\text{fluorescence}}$  on the FC using a dedicated calibrator reference target. This calibration makes it possible to show the distance from the camera lenses relative to the designated navigation targets found in the SPECT imaging data, in this case the sentinel nodes (SNs).

Integration of the SPECT/CT images with the real-time fluorescence images of the m-PDE FC could be switched on and off at will. Moreover, because the m-PDE FC allows for both white light and near-infrared FI, navigation could be performed in both imaging modes. When sudden movements were made with the m-PDE FC during the navigation procedure, the SPECT/CT overlay followed with a slight lag (approximately 20-40 milliseconds). This could be corrected easily by holding the m-PDE FC still for a fraction of a second.

### Light spectra measurements

Light spectra of the fluorescence camera and the optical tracking device of the navigation device were measured using an Jobin Yvon VS140 linear array fiber spectrometer (Horiba, Kyoto, Japan) in the 300-1200 nm range with an integration time of 0.1 milliseconds. The fiber was held at an approximate 2 meter distance from the head of the device of which the light spectra was measured.

## RESULTS AND EXTENDED DISCUSSION

### Tracker placement in relation to the navigation accuracy

Since tracker placement appears to be a critical component for the navigation accuracy, much can be gained when this part of the procedure is improved. The  $RT_{\text{patient}}$  used in this study had to be removed and replaced during the transfer from the department of nuclear medicine to the operation theatre. To overcome this shortcoming, one can think of using a different way of co-registration, for example using multiple small metal balls that are not susceptible to deformation or by implementing the concept of intraoperative freehandSPECT [5–7]. FreehandSPECT may help to correct for errors caused by tissue deformation as a result of surgical manipulation.

### Spectral overlap between near infrared camera and fluorescence emission of ICG

Optical tracking by the navigation device occurred via reflection of pulsed near-infrared light (20 hertz (Hz)) emitted by the tracking head of the declipseSPECT system. Following light reflection on the fiducials present on the  $RT_{\text{patient}}$  and  $RT_{\text{fluorescence}}$  it can be selectively detected by the tracking head and used for position tracking. Unfortunately the wavelength of this near-infrared light (800-900 nm range with a peak at 863 nm overlapped with the emission spectrum of ICG (the only Food and Drug Administration (FDA) clinically approved near infrared fluorescent dye; peak around 810 nm). This meant that the tracking signal is also detected by the fluorescence camera causing “flickering” when performing FI in the near-infrared FI mode of the fluorescence camera (SI Figure1). Yet, this did not hinder navigation of the m-PDE in the white-light setting.

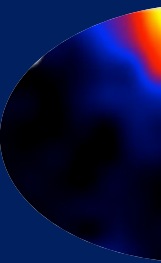
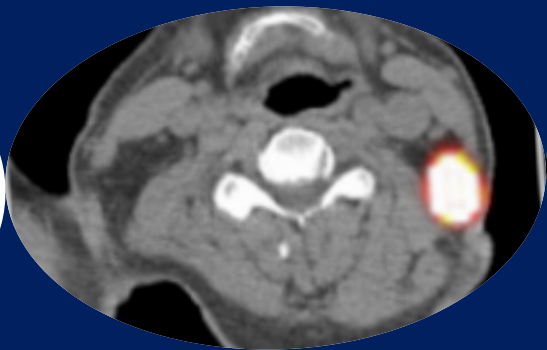
This flickering could be blocked efficiently by manually covering the tracking light sources. This, however, meant the in-depth navigation information was temporarily lost. When the fluorescence camera remained at the exact same distance, fluorescence imaging could be performed to evaluate if the sentinel node was fluorescent.

The spectral overlap between the tracking device and fluorescent emission of ICG did not prevent us from demonstrating the potential of the hybrid navigation concept (SI Figure 1). However, for more routine use the flickering-issue needs to be solved. Here the clinical availability of a spectrally different tracking light-source or fluorescence tracer may provide outcome.

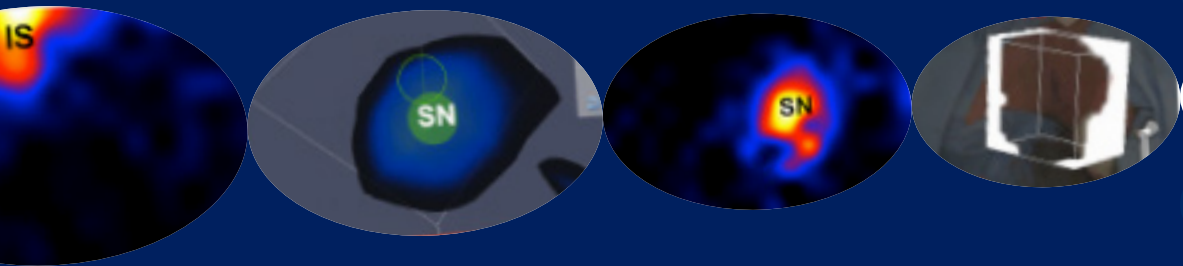
## REFERENCES

1. KleinJan GH, Bunschoten A, van den Berg NS, Valdes Olmos RA, Klop WMC, Horenblas S, et al. Fluorescence guided surgery and tracer-dose, fact or fiction? *Eur J Nucl Med Mol Imaging*. 2016;In press.
2. Bunschoten A, Buckle T, Kuil J, et al. Targeted non-covalent self-assembled nanoparticles based on human serum albumin. *Biomaterials*. 2012;33(3):867–875.
3. Brouwer OR, van den Berg NS, Mathéron HM, et al. A hybrid radioactive and fluorescent tracer for sentinel node biopsy in penile carcinoma as a potential replacement for blue dye. *Eur Urol* . 2014;65(3):600–609.
4. Zhang Z. A flexible new technique for camera calibration. *IEEE Trans Pattern Anal Mach Intell*. IEEE; 2000;22(11):1330–1334.
5. Bluemel C, Schnelzer A, Okur A, et al. Freehand SPECT for image-guided sentinel lymph node biopsy in breast cancer. *Eur J Nucl Med Mol Imaging*. 2013;40(11):1656–1661.
6. Engelen T, Winkel BM, Rietbergen DD, et al. The next evolution in radioguided surgery: breast cancer related sentinel node localization using a freehandSPECT-mobile gamma camera combination. *Am J Nucl Med Mol Imaging*. 2015;5(3):233–245.
7. Brouwer OR, van den Berg NS, Mathéron HM, et al. Feasibility of intraoperative navigation to the sentinel node in the groin using preoperatively acquired single photon emission computerized tomography data: transferring functional imaging to the operating room. *J Urol*. 2014;192(6):1810–1816.

# Chapter 9



**Extending the use of hand-held  
gamma camera technologies  
to generate intraoperative  
freehandSPECT images suitable for  
surgical navigation; a feasibility study  
in head-and-neck melanoma patients  
undergoing sentinel node biopsy**



## ABSTRACT

### INTRODUCTION

Intraoperative sentinel node (SN) identification in patients with head-and-neck malignancies can be challenging due to unexpected drainage patterns and the anatomical complexity. Here, intraoperative navigation-based guidance technologies may provide outcome. In this study gamma-camera-based freehandSPECT was evaluated in combination with the hybrid tracer ICG-<sup>99m</sup>Tc-nanocolloid.

### MATERIALS AND METHODS

Eight patients with melanoma located in the head-and-neck area were included. Indocyanine green (ICG)-<sup>99m</sup>Tc-nanocolloid was injected preoperatively, where after lymphoscintigraphy and SPECT/CT imaging were performed in order to define the location of the SN(s). FreehandSPECT scans were generated in the operation room using a portable gamma camera. For lesion localization during surgery freehandSPECT scans were projected in an augmented reality video-view that was used to spatially position a gamma-ray detection probe. Intraoperative fluorescence imaging was used to confirm the accuracy of the navigation-based approach and identify the exact location of the SNs.

### RESULTS

Preoperatively fifteen SNs were identified, of which fourteen were identified using freehandSPECT. Navigation towards these nodes using the freehandSPECT approach was successful in thirteen nodes. Fluorescence imaging provided optical confirmation of the navigation accuracy in all patients. In addition, fluorescence imaging allowed for the identification of (clustered) SNs that could not be identified based on navigation alone.

### CONCLUSION

The use of gamma camera-based freehandSPECT aids intraoperative lesion identification, and with that, supports the transition from pre- to intra-operative imaging via augmented reality display and directional guidance.

## INTRODUCTION

Over the past decades the sentinel node (SN) biopsy procedure for loco-regional lymph node (LN) staging in patients with (head-and-neck) melanoma has increasingly gained interest [1,2]. This procedure allows preoperative identification of the primary tumor draining LNs (so-called sentinel nodes (SNs)) using lymphoscintigraphy and single photon emission computed tomography combined with computed tomography (SPECT/CT) imaging [3]. This information can then be used to provide the base for a surgical roadmap.

Differences in patient placement during preoperative imaging and head and neck surgery complicates the direct translation of the pre-operative findings to the surgical field of view. Intraoperative guidance is therefore required in the form of a gamma-ray detection probe (referred to as gamma probe) [4,5] or portable/handheld gamma cameras that provide a superior sensitivity and high resolution [6,9]. Both techniques, however, lack in depth information; features that can be complemented through the use of superficial optical imaging/fluorescence guidance. Conversely, fluorescence imaging is limited by tissue induced signal attenuation, making the technology dependent on other in depth imaging technologies such as SPECT.

In order to provide placement of radioactive hot spots into anatomical context optical and gamma tracing modalities can be physically integrated [10–12]. Alternatively, navigation of surgical tools/modalities in a manner analogue to the use of global positioning systems (GPS) instead of an old-fashion paper road-map can be employed. Navigation was successfully introduced in radioguided surgery via the use of geometrically tracked gamma probe's that generate freehandSPECT scans that can be presented as augmented reality views [13–16]. Uniquely, these 3D data-sets also allow for surgical navigation by providing dynamic feedback with regard to the distance of the gamma probe to the lesion of interest e.g. SN's of head-and-neck malignancies [14,17,18]. Limiting factors in the practical application of this technology are the sensitivity and the time that is required to generate a freehandSPECT scan. Recently we presented that, in breast cancer, intraoperative use of a handheld gamma camera rather than a gamma probe for freehandSPECT acquisition could overcome these shortcomings [6]. Others have used this approach for SN biopsy in different malignancies and for the detection of parathyroid adenoma [19–21].

In the current clinical pilot study, the feasibility of the use of a handheld gamma camera for intraoperative freehandSPECT acquisition and subsequent navigation-guided surgery

was explored in patients with head-and-neck melanoma. Indocyanine green (ICG)-<sup>99m</sup>Tc-nanocolloid was used to help validate the accuracy of the navigation procedure, as this tracer can be detected using both freehandSPECT and high-resolution fluorescence imaging [22].

## **METHODS**

### **Patients**

Eight patients with histology-proven melanoma in the head-and-neck area whom were scheduled for wide re-excision of the melanoma scar and a SN biopsy procedure were included (for patient characteristics see Table 1). Clinically, the regional LNs of the patients were tumor-negative as defined by palpation, ultrasound and fine-needle aspiration cytology.

Prior to commencement of the study, approval from the institutional review board of The Netherlands Cancer Institute - Antoni van Leeuwenhoek was obtained and patients were only included after written informed consent was provided.

### **Preoperative procedure**

Preparation and injection of the hybrid tracer ICG-<sup>99m</sup>Tc-nanocolloid, as well as the applied preoperative imaging procedure have previously been described [22]. ICG-<sup>99m</sup>Tc-nanocolloid was injected intradermally in four deposits (0.1 mL/deposit) surrounding the melanoma scar. Lymphoscintigraphy (15 min and 2 h post-injection) and SPECT/CT imaging (2 h post-injection) were performed in order to determine the number and location of the SN-related hot spots. For SPECT/CT acquisition, the patient was placed in a supine position, with a straight neck. Preoperative findings are provided in Table 1.

	Preoperative findings				Intraoperative findings				Pathology				
	Age	Clinical T-stage	Tumor location	Administered dose (MBq)	# SNs on lymphoscintigrams	# SNs on SPECT/CT	Location SNs	Total # removed SNs	Fluorescent SNs	Radioactive SNs	Total # SNs	# Tumor-positive nodes	
								In vivo	Ex vivo	In vivo	Ex vivo		
1	60	T2a	Right cheek	82.0	0	4	Parotid gland (2x), level I (2x)	4	3	4	4	4	0
2	74	T2b	Left cheek	84.9	3	3	Parotid gland, level II, level V	4	4	4	4	4	0
3	67	-	Right eyelid	84.4	1	1	Parotid gland	1	1	1	1	1	0
4	52	T3b	Right cheek	78.2	1	1	Level V	1	1	1	1	1	0
5	59	T4b	Left occipital region	90.2	1	1	Level V	1	1	1	1	1	1
6	63	T3a	Right occipital region	101.4	0	1	Level II	3	3	3	3	4	0
7	66	T2a	Vertex	75.5	2	2	Level II (2x)	3	3	3	3	4	0
8	43	T3a	Left ear	90.1	2	2	Parotid gland, level II	3*	3	3	3	3	1
Average	60.5			85.8	1.25	1.9		2.5	2.4	2.5	2.5	2.5	3
Total					10	15		20	19	20	20	20	24

**Table 1. Patient characteristics, preoperative and intraoperative findings, and pathology**

MBq = mega Becquerel; SN = sentinel node; SPECT/CT = single photon emission computed tomography combined with computed tomography.

\* Additional SN near injection site found with transcutaneous fluorescence imaging (and confirmed using the gamma probe) which was not seen on preoperative imaging.

## Intraoperative procedure

### Reference tracker placement

Placement of reference trackers for acquiring freehandSPECT images and the set-up for navigation were carried out according to procedures described by Engelen et al. [6]. In short, after anesthetizing the patient and sterilizing the operation field, the neck of the patient was positioned in such a way that the surgeon had easy access to the SNs on one side of the neck. Thereafter a sterile reference tracker (referred to as  $RT_p$ ) was placed on the skull of the patient, followed by placement of a second reference tracker (referred to as  $RT_{hgc}$ ) onto the handheld gamma camera (ChrystalCam; Chrystal Photonics, Berlin, Germany). Finally, a third reference tracker (referred to as  $RT_{gp}$ ) was placed on the gamma probe (Chrystal probe; Chrystal Photonics).

To ensure continuous capture of all reference trackers in the field of view the navigation system, the optical tracking system was placed in direct line of site with the  $RT_p$ , above the head of the patient. Near-infrared optical tracking of the fiducials present on the  $RT_p$ , the  $RT_{hgc}$ , and the  $RT_{gp}$ , the navigation system (declipseSPECT; SurgicEye, Munich, Germany) was used to determine the position and orientation of the patient, the handheld gamma camera and the gamma probe, and to place these features in the same coordinate system [6,23]. The tip of the gamma probe (approx. 1 cm in diameter) was used for navigation, as this allowed easier identification of the SNs compared to the use of the bulkier hand-held gamma camera.

FreehandSPECT acquisition in the head-and-neck area using a handheld gamma camera

The 2D gamma-imaging mode of the handheld gamma camera was used to roughly localize the area harboring the SNs and to center the radioactive hotspot in the volume of interest (VOI; 12x12x12 cm) of the freehandSPECT. After defining the position of the VOI, the geometrically tracked handheld gamma camera was used to scan the VOI in different directions whereby the declipseSPECT device provided feedback on the radioactive counts collected. When >2500 counts were collected, the acquisition was stopped and the freehandSPECT image reconstructed. Subsequently, the "tracked" gamma probe was navigated by the surgeon until the intact skin was reached. The accuracy of this position was then evaluated by comparing the position of the "tracked" gamma probe with that of a second gamma probe that was placed based on acoustic guidance.

Sentinel node identification: Navigation, gamma probe- and fluorescence-guidance  
After incision, the SN was pursued using the conventional approach of combined gamma tracing (Neoprobe; Johnson & Johnson Medical, Amersfoort, the Netherlands) and fluorescence imaging (PhotoDynamic Eye (PDE); Hamamatsu Photonics K.K., Hamamatsu, Japan) in a manner similar as described previously [22]. When the SN was visible, the “tracked” gamma probe was navigated towards the SN using the freehandSPECT scan acquired prior to placement of the incision. The distance from the tip of the “tracked” gamma probe to the SN for each procedure, as reported by the navigation device, is provided in Table 2.

A post-excision freehandSPECT was generated after removal of the SNs to evaluate possible residual radioactivity present in the VOI. A mobile gamma camera (Sentinella; Oncovision, Valencia, Spain) was used to confirm removal of the preoperatively identified SNs [24]. The techniques used in this study and the type of information they provide during the surgical procedure are described in Table 3. Since the study entailed the evaluation of a new technology this resulted in the duplication of gamma-probe and -camera systems.

### **Pathology**

Excised SN specimens were formalin-fixed and the nodes present in the specimens counted before being bisected and paraffin-embedded. Tissue sections cut at 50-150 nm intervals were used for histopathological evaluation and evaluation of the presence of nodal metastasis [22].

	Acquisition time (s)	% VOI scanned	Reconstruction time (s)	# SNs on freehandsPECT/total # SNs preoperative imaging (%)	# SNs located with navigation/# SNs seen on freehandsPECT (%)	Error of navigation per SN (mm)	Note
1	85	66.3	31	3/4 (75)	3/3 (75)	7, 8, 4	SN in parotid gland not visible on freehandsPECT
2	100	78	n.n.	3/3 (100)	3/3 (100)	9, 9, 9	Level V cluster of 2
3	121	67.6	87	1/1 (100)	1/1 (100)	5	-
4	126	51.5	211	1/1 (100)	1/1 (100)	2	-
5	94	71	31	1/1 (100)	1/1 (100)	5	-
6	74	59	89	1/1 (100)	0/1 (0)	-	SN part of IS, navigation not possible; level II SN cluster of 3
7	132	82	135	2/2 (100)	2/2 (100)	0, 5	Level II cluster of 2
8	199	80.4	90	2/2 (100)	2/2 (100)	7, 5	-
Average	116.4	69.5	96.3			5.8	
Total				14/15 (93.3)	13/14 (92.9)		

**Table 2. Intraoperative freehandsPECT findings**

SN = sentinel node; SPECT/CT = single photon emission computed tomography; VOI = volume of interest; 3D = three-dimensional; n.n.

= not noted; IS = injection site

\* = this SN was not reported by the nuclear medicine physician, but was visible on freehandsPECT.

	2D information	3D information	Acoustic read-out	Numerical read-out	Visual read-out	Depth information	Anatomical detail
Neoprobe gamma probe <sup>a,†</sup>	-	-	+	+	-	-	-
Sentinella gamma camera <sup>a,†</sup>	+	-	+	+	+(gamma image)	-	-
PDE fluorescence camera <sup>a,†</sup>	+	-	-	-	+(fluorescence image)	+/-	+
(Chrysal) gamma camera combined with freehandSPECT (incl. navigation of Chrysal gamma probe and acoustic confirmation with the same probe) <sup>#</sup>	+	+	+	+	+(gamma image)	+	-
Fluorescence camera combined with freehandSPECT	+	+	+	+	+(gamma + fluorescence image)	+	+

**Table 3. Information provided by different intraoperative imaging modalities**

2D = two-dimensional; 3D = three-dimensional. <sup>†</sup> Technologies applied in this study. <sup>#</sup> Routine modality used for the procedures describe in the study.

## RESULTS

### Preoperative imaging procedure

With preoperative lymphoscintigraphy and SPECT/CT imaging a total of 15 SN-related hot spots were identified (Table 1). Interestingly, in one patient (patient 1) non-visualization occurred on early- and late lymphoscintigrams while with SPECT/CT four SN-related hot spots were identified (Table 1).

Direct translation of the preoperative SPECT/CT scans to the surgical setting was not always possible, due to the difference in patient positioning during the preoperative SPECT/CT scan and the intervention. Complexity of translation further increased when SN-related hot spots were identified in both sides of the neck, which required repositioning of the patient during surgery in order to expose both sides of the neck. These features complicated the surgeons ability to relate anatomical reference points in preoperative SPECT/CT to those in the intraoperative situation.

### Pre-incision imaging procedure

On average, freehandSPECT acquisition took a mere 116.4 seconds (range 74-199 seconds), in which an average of 69.5% of the VOI was scanned (range 51.5-82.0%). FreehandSPECT reconstruction time was on average 96.3 seconds (range 31-211 seconds; Table 2). As the patient was immobilized on the operation table, the acquired freehandSPECT scans were limited by the degree of freedom wherein the camera could be positioned over the lesion in order to generate a 3D image. Furthermore, the limited volume of interest of scanned (12x12x12 cm) resulted in the acquisition of multiple freehandSPECT in the first two patients.

Using preoperative SPECT/CT as a reference for identified SNs, intraoperatively obtained freehandSPECT images provided a 93% detection rate (14/15 SN-related hot spots visualized). When identified, the exact location of the SNs in the surgical set-up could be depicted as an augmented reality overlay. As demonstrated by a typical example in Figure 1, handheld gamma camera and freehandSPECT scans depicted the same features as the preoperatively acquired lymphoscintigrams and SPECT/CT images in 75% of patients (no complete conformity in patient 1 and 6).

In patient 1, four SN-related hot spots were preoperatively identified with SPECT/CT. In this patient, low tracer uptake in a SN located in the parotid gland prevented detection using freehandSPECT. In patient 6, a lower-activity SN-related hot spot near the high-

activity injection site was identified on preoperative SPECT/CT which could also not be identified using freehandSPECT. A cluster of SN-related hot spots in level II was identified on preoperative SPECT/CT in patient 7, which could be differentiated into three SN-related hot spots after examination of the freehandSPECT scan.

### **Post-incision imaging procedure**

Placement of the tracker on the rigid skull and outside the surgical field prevented the need for replacement during the surgical procedure and resulted in minimal deformations. The “tracked” gamma probe could be virtually navigated in seven patients (13 of the 14 SN-related hot spots (93%)) with a navigation inaccuracy of 5.8 mm in the numeric distance to the target (Table 2, Figures 1 and 2). It should be noted that this inaccuracy seemed to be influenced for a large part by the mere 3mm spatial resolution of the freehandSPECT images [25]. Inaccuracy induced by movement artifacts could be contributed to e.g. the incision process or retractors used. In all cases wherein the navigation procedure was slightly inaccurate identification of the SNs was enabled by a manual correction based on fluorescence imaging.

In cases wherein the navigation option could not be used, the combined use of the SPECT/CT images, gamma probe and fluorescence camera allowed identification of the SNs (Table 2). In patients 1 and 6, the superior spatial resolution of fluorescence imaging allowed localization of the SNs that were not detected by freehandSPECT. In patient 6, intraoperative fluorescence imaging revealed three SNs at the location of the hotspot that was identified on SPECT/CT. Post-SN-excision freehandSPECT and use of the alternative mobile gamma camera, confirmed accurate removal of the SNs in all patients.

### **Pathology**

Pathological evaluation of the biopsy specimens resulted in identification of a total of 24 nodes, of which two were tumor-positive (found in patient 5 and 8; Table 1). In patient 8, a tumor-positive SN was found in the parotid gland, while in patient 5 a tumor-positive node was located in the re-excision specimen of the melanoma scar. This last node was overshadowed by the high-activity of the injection site, which prevented identification on preoperative images and was therefore not explored during the operation.

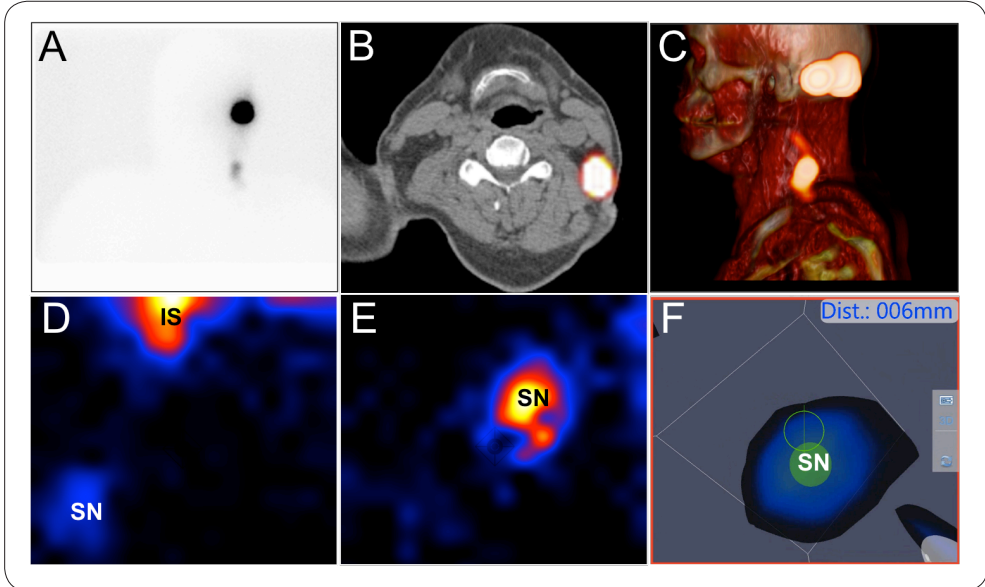


**Figure 1. Overview of the acquired images.**

- A.** Example of an anterior lymphoscintigram showing a clear sentinel node in the neck.
- B, C.** SPECT/CT imaging of the patient shown under A allowed to place the hotspot in its anatomical context with the sentinel node being located in level V. The fused SPECT/CT images provided the surgeon with an anatomical roadmap for planning of the surgical procedure.
- D.** 2D mobile gamma camera image acquired in the operation room showing a sentinel node (SN) and the injection site (IS).
- E.** Zoom-in of the image shown in D.
- F.** A freehandSPECT scan was acquired and subsequently the gamma probe was navigated, in augmented reality, to the sentinel node as seen in the freehandSPECT scan.

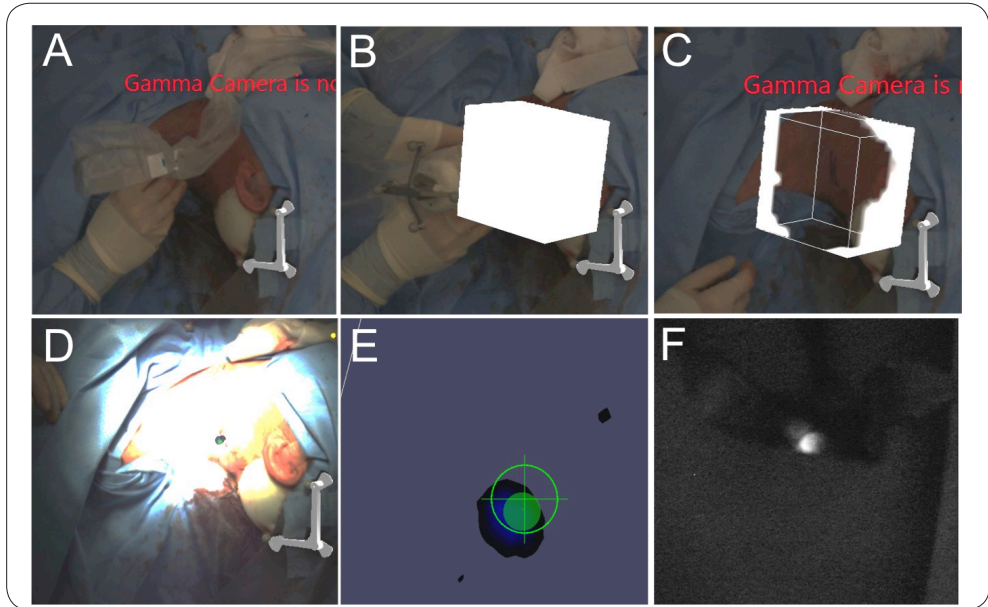


**Figure 2. Intraoperative navigation procedure.**

- A.** Pre-navigation overview.
- B, C** Intraoperative freehandSPECT acquisition.
- D.** Augmented reality following reconstruction of the acquired data, a 3D overlay is obtained.
- E.** Navigation of the gamma probe in 3D-virtual-reality.
- F.** Optical confirmation of sentinel node localization via fluorescence imaging.

## DISCUSSION

The results described in this study demonstrate that intraoperative freehandSPECT scans that are generated using a handheld gamma camera provide a 93% detection-rate of SNs that were preoperatively identified on SPECT/CT identified in the head-and-neck area. The use of the hybrid tracer ICG-<sup>99m</sup>Tc-nanocolloid allowed for the (high-resolution) detection of the remaining SNs using fluorescence imaging. During the surgical procedure, the freehandSPECT device helped to place the nuclear medicine findings within the anatomical context. In addition, the use of an augmented reality overlay also provided dynamic information with regard to the distance to the target.

Due to the common occurrence of so-called clustered nodes in the head and neck area [22], there continues to be a discrepancy between the SN-related hot spots identified at SPECT/CT and the actual number of SNs removed during surgery (38% increase in this particular study; 24 in Table 1 vs. 15 in Table 2)). Unfortunately, intraoperative use of freehandSPECT did not demonstrate the resolution and real-time confirmation that is required to solve this issue. Hence, resection of all SNs in one hot spot still demands the use of high-resolution and real-time feedback, as is provided by fluorescence imaging.

When using preoperative SPECT/CT scans for navigation purposes identical RTP placement in the pre- and intra-operative setting was required to limit the degree of deformations [26–29]. This practical limitation was now overcome by the use of intraoperatively generated freehandSPECT scans. Unfortunately, the relatively small volume of interest of the freehandSPECT (12x12x12 cm) resulted in the generation of multiple freehandSPECT scans in some patients. The disruption of the surgical workflow was minimized by the prior knowledge of the location wherein the SNs resided. Such disruption, however, remains common during the introduction of new technologies and can be contributed to the early stage development of the technology as well as the limited experience with the technology (learning curve). It may be envisioned that integration of the freehandSPECT and navigation options in the surgical workflow can be optimized further from a technical point of view. For example, prevention of duplication of modalities (See Table 3) would already save time. Based on the fact that surgeons used the depth estimation provided by the navigation set-up to estimate the risk of damage to delicate tissues, one may also reason that striking a balance between cure and surgery induced toxicity would warrant a slight prolongation of the surgical procedure.

Previously we demonstrated that preoperative SPECT/CT remains incremental in the SN identification process, even when fluorescence-based surgical guidance to the same target is available [22]. Given the revealed need for positional information during placement of the freehandSPECT VOI we see no reason to deviate from this view. This study, however, does illustrate how freehandSPECT imaging and the matching “GPS-like” navigation capabilities can help strengthen the connection between the findings of both modalities [30]. The use of the hybrid tracer (ICG-<sup>99m</sup>Tc-nanocolloid), a tracer that can be detected using both modalities [26], enabled complementary use of nuclear and fluorescent technologies. In the current study a gamma probe was used for navigation, but in the future other tools may be positioned using navigation, for example a fluorescence camera that displays a real-time augmented reality overlay of freehandSPECT data within the fluorescence images (see Table 3) [28]. In such an integrated image guided surgery approach the use of augmented reality displays, virtual navigation and fluorescence guidance can all be used in the same setting [31].

## CONCLUSION

Generation of an intraoperative freehandSPECT scan using the handheld gamma camera/navigation system allows for the identification of SNs in the head and neck area, with an accuracy that approaches that of conventional SPECT/CT. The augmented reality display and directional positioning options provided by the navigation system help refine lesion localization, compared to traditional radioguided surgery tools.

## REFERENCES

1. de Bree E, de Bree R. Implications of the MSLT-1 for sentinel lymph node biopsy in cutaneous head and neck melanoma. *Oral Oncol.* 2015;51(7):629-33.
2. de Rosa N, Lyman GH, Silbermins D, Valsecchi ME, Pruitt SK, Tyler DM, et al. Sentinel node biopsy for head and neck melanoma: a systematic review. *Otolaryngol Head Neck Surg.* 2011;145(3):375-82
3. Nieweg OE, Tanis PJ, Kroon BB. The definition of a sentinel node. *Ann Surg Oncol.* 2001;8(6):538-41.
4. Povoski SP, Neff RL, Mojzisik CM, O'Malley DM, Hinkle GH, Hall NC, et al. A comprehensive overview of radioguided surgery using gamma detection probe technology. *World J Surg Oncol.* 2009;27;7:11
5. Tsuchimochi M, Hayama K. Intraoperative gamma cameras for radioguided surgery: technical characteristics, performance parameters, and clinical applications. *Phys Med.* 2013;29(2):126-38.
6. Engelen T, Winkel BM, Rietbergen DD, KleinJan GH, Vidal-Sicart S, Olmos RAV, et al. The next evolution in radioguided surgery: breast cancer related sentinel node localization using a freehandSPECT-mobile gamma camera combination. *Am J Nucl Med Mol Imaging.* 2015;15;5(3):233-45.
7. Heller S, Zanzonico P. Nuclear probes and intraoperative gamma cameras. *Semin Nucl Med.* 2011;41(3):166-81.
8. Tsuchimochi M, Hayama K. Intraoperative gamma cameras for radioguided surgery: technical characteristics, performance parameters, and clinical applications. *Phys Med.* 2013;29(2):126-38.
9. Hellingman D, de Wit-van der Veen LJ, Klop WMC, Olmos RAV. Detecting near-the-injection-site sentinel nodes in head and neck melanomas with a high-resolution portable gamma camera. *Clin Nucl Med.* 2015;40(1):e11-6.
10. Hellingman D, Vidal-Sicart S, de Wit-van der Veen LJ, Paredes P, Valdés Olmos RA. A New Portable Hybrid Camera for Fused Optical and Scintigraphic Imaging: First Clinical Experiences. *Clin Nucl Med.* 2016;41(1):e39-43.
11. KleinJan GH, Hellingman D, van den Berg NS, van Oosterom MN, Hendricksen K, Horenblas S, et al. Hybrid Surgical Guidance: Does Hardware Integration of  $\gamma$ - and Fluorescence Imaging Modalities Make Sense? *J Nucl Med.* 2017;58(4):646-50.
12. Lees JE, Bassford DJ, Blake OE, Blackshaw PE, Perkins AC. A Hybrid Camera for simultaneous imaging of gamma and optical photons. *J Instrum.* 2012;7(6):P06009-P06009.
13. Bluemel C, Herrmann K, Kübler A, Buck AK, Geissinger E, Wild V, et al. Intraoperative 3-D imaging improves sentinel lymph node biopsy in oral cancer. *Eur J Nucl Med Mol Imaging.* 2014;41(12):2257-64.
14. Bluemel C, Herrmann K, Müller-Richter U, Lapa C, Higuchi T, Wild V, et al. Freehand SPECT-guided sentinel lymph node biopsy in early oral squamous cell carcinoma. *Head Neck.* 2014;36(11):E112-6.
15. Bluemel C, Schnelzer A, Okur A, Ehlerding A, Paepke S, Scheidhauer K, et al. Freehand SPECT for image-guided sentinel lymph node biopsy in breast cancer. *Eur J Nucl Med Mol Imaging.* 2013;40(11):1656-61.
16. Okur A, Ahmadi S-A, Bigdelou A, Wendler T, Navab N. MR in OR: First analysis of AR/VR visualization in 100 intraoperative Freehand SPECT acquisitions. 2011 10th IEEE Int Symp Mix Augment Real. *IEEE;* 2011 Oct;211-8.
17. de Bree R, Pouw B, Heuveling DA, Castelijns JA. Fusion of Freehand SPECT and Ultrasound to Perform Ultrasound-Guided Fine-Needle Aspiration Cytology of Sentinel Nodes in Head and Neck Cancer. *AJNR Am J Neuroradiol.* 2015;36(11):2153-8.
18. Heuveling DA, van Weert S, Karagozoglou KH, de Bree R. Evaluation of the use of freehand SPECT for sentinel node biopsy in early stage oral carcinoma. *Oral Oncol.* 2015;51(3):287-90.
19. Heuveling DA, Karagozoglou KH, van Schie A, van Weert S, van Lingen A, de Bree R. Sentinel node biopsy using 3D lymphatic mapping by freehand SPECT in early stage oral cancer: a new technique. *Clin Otolaryngol.* 2012;37(1):89-90.
20. Wendler T, Herrmann K, Schnelzer A, Lasser T, Traub J, Kutter O, et al. First demonstration of 3-D lymphatic mapping in breast cancer using freehand SPECT. *Eur J Nucl Med Mol Imaging.* 2010;37(8):1452-61.
21. Bluemel C, Kirchner P, Kajdi GW, Werner RA, Herrmann K. Localization of Parathyroid Adenoma With Real-Time Ultrasound: Freehand SPECT Fusion. *Clin Nucl Med.* 2016;41(3):e141-2.
22. van den Berg NS, Brouwer OR, Schaafsma BE, Mathéron HM, Klop WMC, Balm AJM, et al. Multimodal Surgical Guidance during Sentinel Node Biopsy for Melanoma: Combined Gamma Tracing and Fluorescence Imaging of the Sentinel Node through Use of the Hybrid Tracer Indocyanine Green-(99m)Tc-Nanocolloid. *Radiology.* 2015;275(2):521-9.

23. Waelkens P, van Oosterom MN, van den Berg NS, Navab N, van Leeuwen FW. Surgical Navigation: An Overview of the State-of-the-Art Clinical Applications. In: Herrmann K, Nieweg OE, Povoski SP, editors. Radioguided surgery. Springer International Publishing; 2016
24. Vermeeren L, Valdés Olmos RA, Klop WMC, Balm AJM, van den Brekel MWM. A portable gamma-camera for intraoperative detection of sentinel nodes in the head and neck region. *J Nucl Med*. 2010;51(5):700–3.
25. Bluemel C, Matthies P, Herrmann K, Povoski SP. 3D scintigraphic imaging and navigation in radioguided surgery: freehand SPECT technology and its clinical applications. *Expert Rev Med Devices*. 2016;13(4):339–51.
26. Brouwer OR, Buckle T, Bunschoten A, Kuil J, Vahrmeijer AL, Wendler T, et al. Image navigation as a means to expand the boundaries of fluorescence-guided surgery. *Phys Med Biol*. 2012;57(10):3123–36.
27. Brouwer OR, van den Berg NS, Mathéron HM, Wendler T, van der Poel HG, Horenblas S, et al. Feasibility of intraoperative navigation to the sentinel node in the groin using preoperatively acquired single photon emission computerized tomography data: transferring functional imaging to the operating room. *J Urol*. 2014;192(6):1810–6.
28. KleinJan GH, van den Berg NS, van Oosterom MN, Wendler T, Miwa M, Bex A, et al. Towards (hybrid) navigation of a fluorescence camera in an open surgery setting. *J Nucl Med*. 2016;57(10):1650-1653.
29. van den Berg NS, Engelen T, Brouwer OR, Mathéron HM, Valdés-Olmos RA, Nieweg OE, et al. A pilot study of SPECT/CT-based mixed-reality navigation towards the sentinel node in patients with melanoma or Merkel cell carcinoma of a lower extremity. *Nucl Med Commun*. 2016;37(8):812-7.
30. van den Berg NS, Valdés-Olmos R a, van der Poel HG, van Leeuwen FWB. Sentinel lymph node biopsy for prostate cancer: a hybrid approach. *J Nucl Med*. 2013;54(4):493–6.
31. van den Berg NS, Miwa M, Kleinjan GH, Sato T, Maeda Y, van Akkooij AC, et al. (Near-infrared) fluorescence guided surgery under ambient light conditions, a next step to embedment of the technology in clinical routine. *Ann Surg Oncol*. 2016 Aug;23(8):2586-95.

# Part three

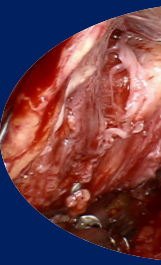
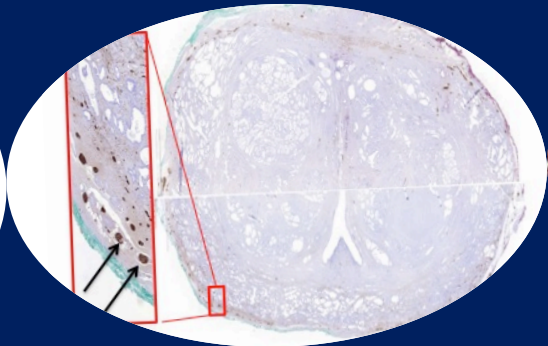
# Nerve sparing surgery

10

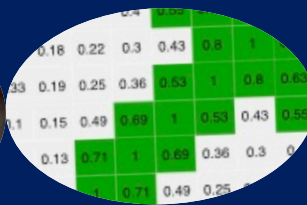
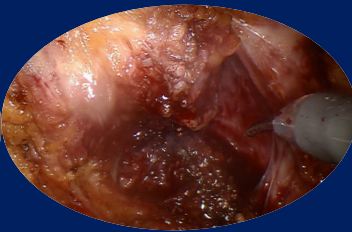
11

12

# Chapter 10



# A prediction model that relates intraoperative fascia preservation to erectile dysfunction in patients that underwent nerve-sparing prostatectomy



*Gijs H. KleinJan*

*Karolina Sikorska*

*Clarize M. Korne*

*Tessa Buckle*

*Corinne Tillier*

*Rosanne C.M. van der Roest*

*Jeroen J. de Jong*

*Fijs W.B. van Leeuwen*

*Henk G van der Poel*

*Submitted for publication*

## ABSTRACT

### INTRODUCTION

Robot assisted radical prostatectomy (RARP) is performed in patients with prostate cancer. Unfortunately, 10-46% of the men who underwent RARP suffer from limited erectile function (EF). The objective for this chapter was to relate fascia preservation (FP) to EF and use these relations to develop a prediction model.

### METHODS

To study the predictive value of a FP score for post-prostatectomy EF (following the international index erectile function (IIEF) score) a cohort of 1241 patients was examined. To increase the predictive value of the scoring system, the FP regions were related to postoperative IIEF, nerve distribution and co-morbidity factors. Finally, a prediction model for EF was developed based on the studied cohort.

### RESULTS

Patient, tumor and surgical characteristics were registered. FP score was explored using the Phi coefficient. A multivariable linear regression model was fitted to all locations, and the importance of each region was measured by the contribution to the R<sup>2</sup>. To predict the postoperative IIEF score a logit transformed postoperative IIEF was used as the dependent variable in the regression models. When corrected for the preoperative IIEF, the FP score was shown to be significant denominator for IIEF ( $p = 2.5 \times 10^{-15}$ ) with an R<sup>2</sup> of 35%. Variable selection performed using the Akaike information criterion led to a final prediction model for postoperative IIEF after nerve-preservation based on the FP score.

### CONCLUSION

Quantitative nerve-sparing FP scoring could be related to the EF and integrated into a multivariate prediction model, which includes with age, use of surgical clips, the Charlson Comorbidity Index Score (CCIS), and preoperative IIEF. The retrospective design of this study and relative inaccuracy of the IIEF were considered to be limiting factors.

## INTRODUCTION

Robot assisted radical prostatectomy (RARP) is frequently performed in patients with clinically localized prostate cancer. While use of a robot is said to enhance the surgical accuracy, 10-46% of the men who have undergone RARP still suffer from limited erectile function (EF) [1]. EF is thought to be directly influenced by damage induced to the periprostatic nerves that surround the prostate on the dorsolateral side (neurovascular bundle (NVB)) [1-3].

After Walsh et al.[4] identified the importance of the NVB for erectile function preservation, several nerve-preservation methods have been reported [1-3,5]. While it is not yet completely clear which nerves are most important for EF, the potential of extended nerve preservation is underlined by the fact that anatomical studies indicate that nerve structures extend into the entire circumference of the periprostatic fascia [3,4,6]. This realization has resulted - among others - in the development of the “veil of Aphrodite-approach”, using the so-called high anterior release to preserve as much periprostatic fascia as possible [7]. Other approaches are bi- or unilateral nerve sparing [8-10] or the intrafascial and interfascial nerve sparing technique [2,11]. The latter was further refined into the inverse five-grade scale, as described by Patel et al. [12]. A common denominator for the intrafascial and interfascial approaches is the separation of different layers within the fascia that surrounds the prostate [11].

Currently, nerve sparing is guided by the tumor spread and the urologists ability to dissect around the delicate nerves. While desirable, intraoperative distinction between the fascia layers is technically not always feasible. To circumvent this limitation, the fascia preservation (FP) score was developed and initially evaluated in 107 patients [13]. This procedure accounts for the full circular distribution of the periprostatic nerves via a 12-tier score (Figure 1A). As the resulting  $\pm 1\text{cm}$  wide fascia segments can be easily assessed and documented intraoperatively, this scoring system can be applied based on tumor location and extracapsular growth. This results in a quantitative score of preserved nerves that is in optimal balance with R0 tumor resections. With such a scoring mechanism the surgical procedure can be related with patient characteristics and postoperative EF preservation, providing the basis for a much desired prediction model for the surgical outcome. The latter would help preoperative assessment of the possible value of the complex and time consuming nerve preservation approaches. In addition, a prediction model will enable the patient and urologist to jointly realize fitting care by striking a more precise consensus in the balance that should be struck between radical tumor excision and the EF. Herein EF can be

considered as a measure of the patient's quality of life. In the present study the predictive value of FP score for post-prostatectomy EF was validated in an independent cohort of 1241 patients. To increase the predictive value of the scoring system the different FP regions were related to postoperative EF and nerve distribution as well as additional co-morbidity factors such as the Charlson Comorbidity Index Score (CCIS), alcohol use, smoking, use of clips, lymph node dissection (LND) and age. Finally, a prediction model for EF was developed based on the studied cohort.

## **METHODS**

### **Patients and International index of erectile function – Erectile Function 5 (IIEF)**

In this study 1241 patients who underwent RARP were included. The International index of erectile function – Erectile Function 5 (IIEF) was evaluated both pre- and postoperatively. Interventions were performed at the Netherlands Cancer Institute - Antoni van Leeuwenhoek hospital. A more detailed description of the inclusion criteria and the evaluation of the IIEF score is provided in the supplemental information (SI) section.

### **Surgical procedure**

Transperitoneal RARP procedures were performed as previously described by Menon et al. [14]. Fascia preservation was performed in an antegrade fashion, following bladder neck transection. The FP score was rated intraoperatively by assessing fascia preservation at twelve positions circumferentially (Fig 1A) using laparoscopic inspection of both the preserved fascia and the prostate surgical specimen [13]. More details considering the surgical procedure are provided in the SI.

### **Statistical Methods**

Patient, tumor and surgical characteristics describing the population are presented descriptively in the SI (Table S11). FP score-based patterns of the nerve sparing procedure were explored using the Phi coefficient, which is the equivalence of the Pearson correlation coefficient for binary data. A multivariable linear regression model was fitted to all locations and the importance of each of them was measured by the contribution to the R<sup>2</sup>, as described by Lindemann et al. [15].

To predict the postoperative IIEF score (range between 0 and 30) a logit transformed postoperative IIEF ( $\text{logit(IIEF)} = \log(\text{IIEF}/30 / (1 - \text{IIEF}/30))$ ) was used as the dependent variable in the regression models. The obtained logit transformed postoperative IIEF's were transformed back, realizing an interpretable value of the predicted IIEF. For exploratory

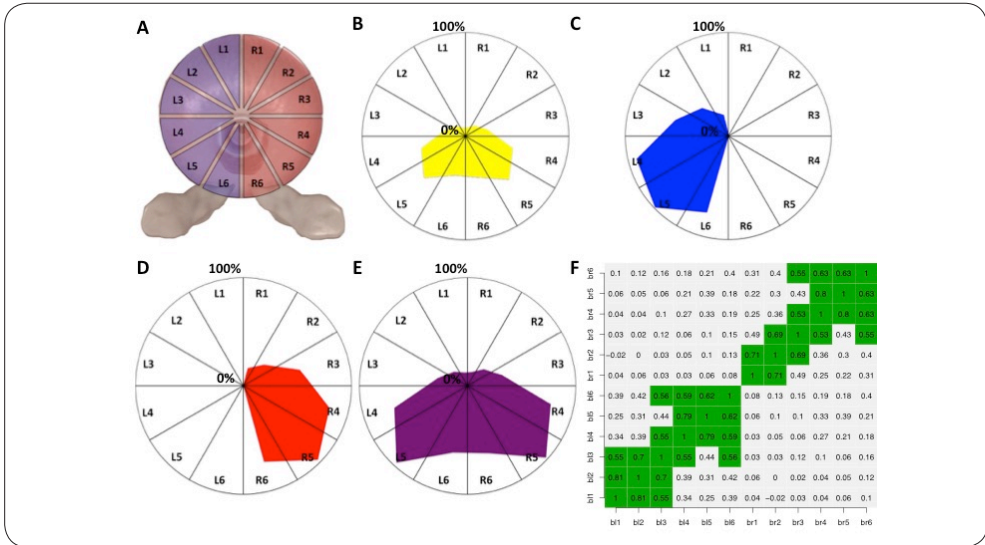


**Figure 1. Surgical sparing of FP regions (n =473):**

- A)** Schematic overview of the different FP locations (left in blue and right in red).
- B)** Illustration of the overall percentile distribution of the FP segments spared during surgery of the total group (FP 0 patients included, n = 1241; yellow). The pattern of FP segments spared in patients have been provided for **C)** patients that only received unilateral sparing on the left side (n= 208; blue), **D)** unilateral sparing on the right side (n =208; red), and **E)** for patients that received bilateral sparing (n = 538; purple).
- F)** Matrix-based correlation between the spared FP segments measured through Phi coefficient. Herein green presents a moderate or high correlation, while weak or no correlation is represented by uncolored sections.

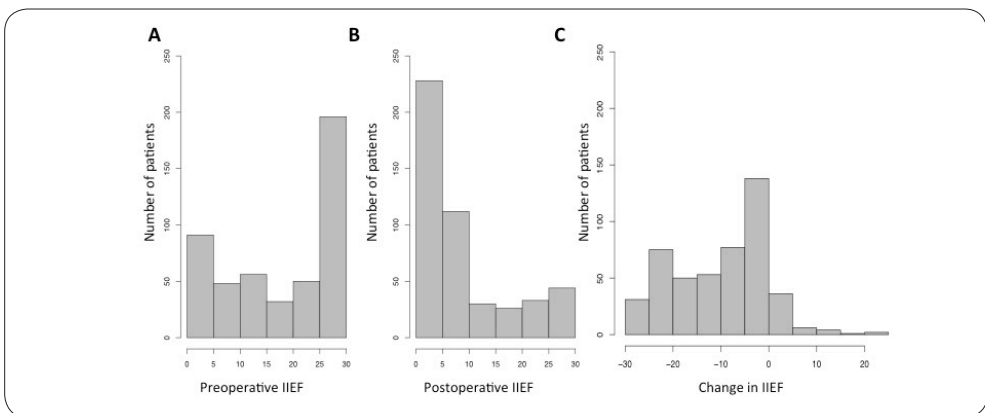


**Figure 2. Pre- and postoperative frequency histograms of IIEF and change in IIEF after 12 months (n = 473):**

- A)** preoperative IIEF scores; **B)** postoperative IIEF at 12 months; **C)** postoperative changes in IIEF.

purposes, univariable linear regression models were fitted for the individual predictors. The linearity assumption between the logit-transformed IIEF and continuous predictors was explored and, if necessary, the quadratic terms were entered. In the final multivariable model all predictors were entered, irrespective of their significance in the univariable models. Additionally, three interaction terms were added:  $IIEF_{\text{preoperative}} * FP \text{ score}$ ,  $IIEF_{\text{preoperative}} * \text{age}$  and  $FP \text{ score} * \text{age}$ . Variable selection was performed using the Akaike information criterion (AIC). Goodness of fit was evaluated using R2 and the accuracy was evaluated visually by plotting smoothed relationship between observed and predicted scores.

## RESULTS

### Nerve sparing surgery

The regions and frequencies wherein fascia was spared within the specific FP regions for the total group of 1241 patients are presented in Figure 1. The median FP score was 4 (Interquartile range IQR 0-6), and 17% of patients who underwent a RARP presented an  $FP \leq 6$ . In approximately a quarter of the patients (27%), fascia sparing was not applied (FP 0). In a mere 1% of the patients the total fascia was preserved during prostatectomy (FP 12). Intraoperatively, adjacent FP regions were often spared in combination, e.g. quadrants of the prostate circumference (Figure 1F). In the sub-population of patients that filled in the questionnaires postoperatively ( $n = 473$ ; 38% of the total number of patients included) a highly similar trend was observed (Figure S13A).

To obtain insight into the nerve distribution in the complete fascia, mid prostate stained sections of ten patients that did not receive nerve sparing surgery were analyzed (FP 0; Figure SI 1 the results were in line with previous literature (See SI for methods and results).

### Correlation of postoperative IIEF and FP score

The non-parametric correlation coefficient between the IIEF score at 12 months after RARP (postoperative IIEF; Figure 2 and Table SI2) and the total FP score was 0.5 (Figure 3B). When corrected for the preoperative IIEF, the FP score was shown to be significant denominator for IIEF ( $p = 2.5 * 10^{-15}$ ; Figure 3B) with an R2 of 35% (19.9% of variance explained by baseline IIEF and 15.60% of variance explained by FP). A linear regression model that included preoperative IIEF and 12 binary variables representing sparing of a particular location resulted in an R2 of 38% (adjusted R2 of 36%). Baseline IIEF contributed to 16% of variance, while the remaining 22% could be contributed to FP regions, with the highest contribution of L3, L5, L6, R3 and R4 (2.3, 3.5, 3.0, 2.6 and 2.2%, respectively).

No specific FP region could be identified as being most relevant for postoperative IIEF outcome (Figure 3C), but there seemed to be a positive influence of bilateral sparing (Figure S13). Comparison between bilateral and unilateral sparing revealed a mean drop in IIEF of 8.8 and 11.5, respectively (Mann Whitney U test  $p = 0.006$ ). For a more detailed description of exact uni- or bi-lateral FP score numbers and their influence on the IIEF, see the SI.

### Prediction model

Age, CCIS, smoking, alcohol intake, preoperative IIEF score, FP score, use of clips and lymph node dissection were considered potentially predictive for the postoperative IIEF (Table 1). Univariable linear regression showed that all covariates, apart from alcohol intake and smoking, were significantly associated with postoperative IIEF. The relationship between  $\text{logit(IIEF)}$  and preoperative IIEF was nonlinear, hence the added quadratic effect for this predictor. Variable selection done using the AIC led to the following prediction model:

$$y = \text{logit(IIEF)} = 1.95 - 0.0168 * \text{IIEF}_{\text{preoperative}} + 0.0017 * \text{IIEF}_{\text{preoperative}}^2 - 0.0671 * \text{age} + 0.0021 * \text{FP} + 0.3651 * \text{clips(=yes)} + 0.0078 * \text{IIEF}_{\text{preoperative}} * \text{FP}$$

Hereafter, the predicted postoperative IIEF can be calculated as  $30 * \exp(y) / (1 + \exp(y))$ . The  $R^2$  for this model was 43% (adjusted  $R^2 = 42\%$ ). Correlation between fitted and observed IIEF was 0.66. The accuracy of predictions is displayed in Figure 4F.

The interaction between preoperative IIEF and FP score is depicted in Figure 4A-C. The benefit of higher FP on the postoperative IIEF was shown to be larger with increasing baseline IIEF. The negative value of the coefficient for age illustrates the fact that with increasing age a decrease in the IIEF<sub>postoperative</sub> was seen. The use of clips improved the postoperative IIEF outcome (Figure 4E). Due to the separation of the pedicles wherein the NVB is located, the use of clips is directly related to nerve-sparing without diathermia, which is accompanied by a  $\approx 3$  point increase in postoperative IIEF.

After variable selection, the dissection explained 38% variation of the IIEF (adjusted  $R^2 = 37\%$ ), with a 5% decrease in the goodness of fit in  $R^2$  decreases when the FP information was omitted (Figure 4F).

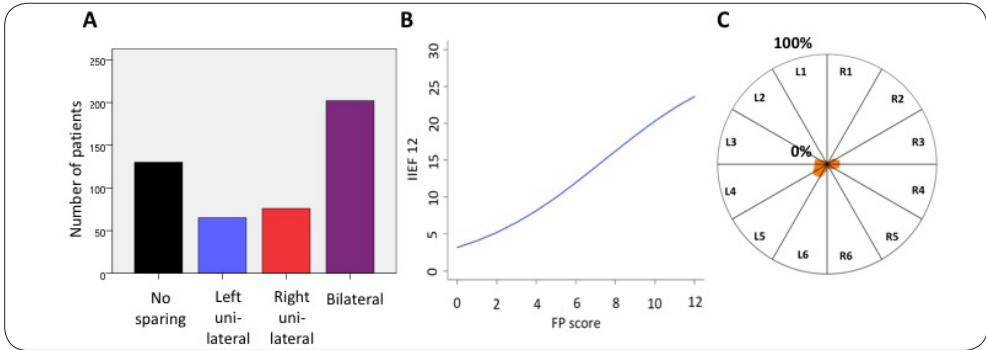


**Figure 3. Average IIEF score at 12 months in relation to FP:**

- A)** Frequency of nerve sparing based on laterality, **B)** The trend between the total FP score and IIEF at 12 months (blue line).  
**C)** The importance of individual FP segments (%) in relation to the postoperative IIEF as presented in (orange).

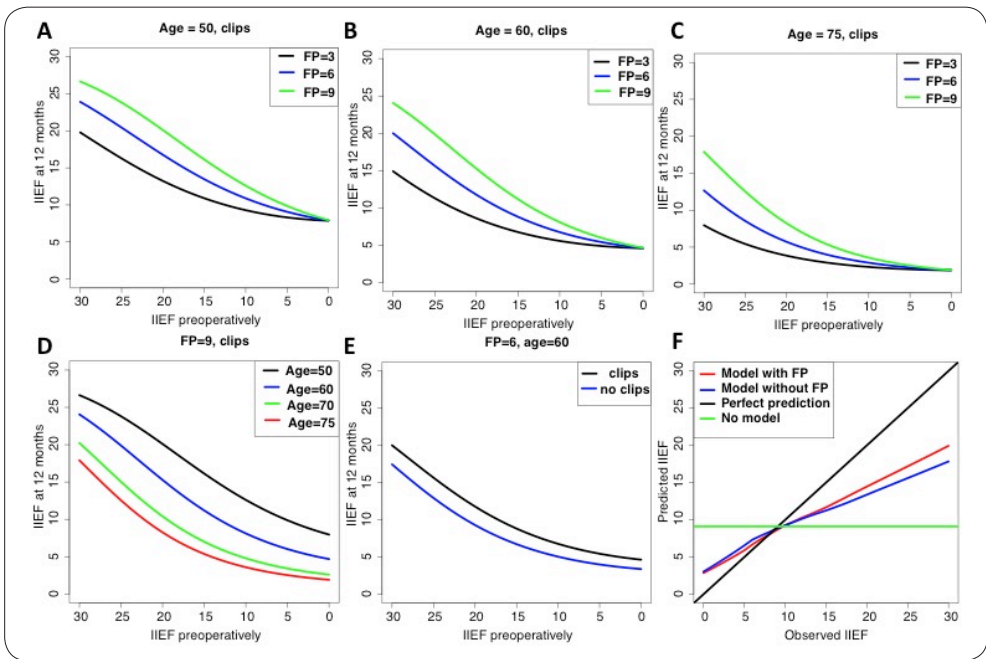


**Figure 4. Outcome in the current cohort as predicted by our prediction model.**

- A-C)** The influence of age (50, 60, and 70 years) in relation to FP score (FP = 3, 6, or 9). **D)** Comparison of the slopes of FP 9 curves for the age groups 50, 60, 70, and 75 years. **E)** Illustration of the influence of clip use. **F)** The relationship between actual and predicted IIEF based on the prediction score based on the prediction model was compared to use of no model for prediction (green line) and to the perfect prediction.

## DISCUSSION

In the multivariable analysis, the FP score obtained during RARP was shown to be an important variable for the prediction of EF recovery together with patient's age, preoperative IIEF score, CCSI and use of clips for nerve sparing. The successful generation of a prediction model provides an important first step towards empowering the urologist to, in the future, realize a more personalized (precision) management of the EF in relation to radical surgery.

Literature indicates that bilateral nerve sparing, irrespective to the quantity of nerves spared, is more favorable compared to unilateral sparing [16,17]. In our cohort bilateral sparing also yielded superior outcomes, irrespective of the amount of fascia spared. Based on the FP score, we were able to further assess the contribution of the different preserved FP segments. Underlined by previous studies, our immunohistochemical findings (Figure S11 and S12) indicate that nerves related to EF were located mainly in the NVB dorsolateral to the prostate [18]. In line with these results, segment number R4 and L4 both displayed the strongest correlation with postoperative EF. A possible explanation for this effect might be found in the high nerve density per mm<sup>2</sup> in these FP regions and the fact that these FP segments were among those most frequently conjointly preserved (FP 4-6). Nevertheless, sparing of the more anteriorly located fascia and nerves (FP segments R1-R2 and L1-L2; see Figure S11) did contribute to a further improvement of postoperative EF with an estimated benefit of 5-10% (Figure 4C). As supported in our immunohistochemical nerve analysis (S11), these observations are in line with the presence of nerve structures in these areas. This finding also supports earlier reports that indicate that nerves are present in the entire circumference of the prostate [5-7,19-21].

It is generally assumed that EF recovery after surgery is age dependent, hereby accounting for the negative impact of older age on EF outcome. Similar to our observations Mandel et al. [22] found a strong negative correlation between age and EF outcome after surgery [23]. A higher FP score was associated with improved EF outcome at all ages and the slope of postoperative IIEF score as a function of preoperative IIEF score was similar for all ages. This supports the argument that nerve preservation in older men could also be attempted and that although they often have diminished preoperative EF, fascia preservation at older age may still result in a relative improvement of outcome similar to that for younger men.

Kang et al. described an EF prediction model based on the intraoperative technique used, laterality (bilateral vs. unilateral), nerve sparing grading (NS 1-10), and age [24]. We found

that besides a patient' age, the FP score and use of clips instead of bipolar diathermia for prostate pedicle control were significant predictive factors in the nomogram. Kang et al. based their study on a EF cut-off value, a feature that is complicated given the variety cut-off values reported in literature [1,9,10,13,22,24,25]. We reasoned that a continuous score provides insight into the relative function loss and therefore better reflects the surgical impact in clinical practice where most men are able to assess their erectile function in a more continuous scale than as a dichotomous condition [24].

A limitation of the current study is its retrospective design. Ideally this nomogram, or a derivative, will in the future be used for virtual EF prediction and as such guide the surgical approach. To prove that indeed the nomogram can help to improve EF outcome, such a study will need to have a randomized setup. Prospectively, however, the nomogram can still be helpful during counseling. Moreover, in a postoperative setting there is less concern with the effects of data sampling: all data including the intraoperative FP score were prospectively obtained and documented in a standardized, ethically approved database. Hence, retrospective chart analysis with the associated limitations was not required. A second limitation of this study is the use of the IIEF score as outcome measure for EF, rather than an erection hardness test or other more physical assessments of EF [26]. Although earlier studies do support the use of questionnaires in EF assessment, it should be noted that originally the IIEF questionnaire was not designed for postoperative EF assessment. When validated in other populations the prediction model will provide patients and caregivers a qualitative estimation of EF outcome after RARP. Future studies should be initiated to validate the nomogram, as such, prospectively generated feedback can be provided to improve its accuracy further e.g. by including imaging variables such as fascia thickness or nerve density as assessed on preoperative MRI [27]. Additionally, in the near future intraoperative fluorescence imaging of nerves may help improve the accuracy of nerve preservation [28,29].

## CONCLUSION

In this study a quantitative nerve-sparing scoring technique during RARP was validated and integrated into a multivariate prediction model, which includes age, use of surgical clips, CCI, and preoperative EF. More anterior fascia preservation was correlated with better EF outcome and age was a strong independent predictor of EF outcome. In older men the relative benefit of more extensive fascia preservation was at least similar to younger men, despite a lower baseline IIEF score.

## REFERENCES

1. Ficarra V, Novara G, Ahlering TE, Costello A, Eastham JA, Graefen M, et al. Systematic review and meta-analysis of studies reporting potency rates after robot-assisted radical prostatectomy. *Eur Urol.* 2012;62(3):418–30.
2. Tewari AK, Srivastava A, Huang MW, Robinson BD, Shevchuk MM, Durand M, et al. Anatomical grades of nerve sparing: a risk-stratified approach to neural-hammock sparing during robot-assisted radical prostatectomy (RARP). *BJU Int.* 2011;108:984–92.
3. Tewari A, Srivastava A, Sooriakumaran P, Grover S, Dorsey P, Leung R. Technique of traction-free nerve-sparing robotic prostatectomy: delicate tissue handling by real-time penile oxygen monitoring. *Int J Impot Res.* 2012;24(1):11–9.
4. Walsh PC, Donker PJ. Impotence following radical prostatectomy: insight into etiology and prevention. *J Urol.* 1982;128(3):492–7.
5. Costello AJ, Brooks M, Cole OJ. Anatomical studies of the neurovascular bundle and cavernosal nerves. *BJU Int.* 2004;94(7):1071–6.
6. Kang SG, Schatloff O, Haidar AM, Samavedi S, Palmer KJ, Cheon J, et al. Does Surgeon Subjective Nerve Sparing Score Predict Recovery Time of Erectile Function Following Robot-Assisted Radical Prostatectomy? *J Sex Med.* 2015;12(6):1490–6.
7. Savera AT, Kaul S, Badani K, Stark AT, Shah NL, Menon M. Robotic Radical Prostatectomy with the “Veil of Aphrodite” Technique: Histologic Evidence of Enhanced Nerve Sparing. *Eur Urol.* 2006;49(6):1065–74.
8. Nielsen ME, Schaeffer EM, Marschke P, Walsh PC. High anterior release of the levator fascia improves sexual function following open radical retropubic prostatectomy. *J Urol.* 2008;180(6):2557–64.
9. Rossi MS, Moschini M, Bianchi M, Gandaglia G, Fossati N, Dell’Oglio P, et al. Erectile Function Recovery After Nerve-Sparing Radical Prostatectomy for Prostate Cancer: Is Back to Baseline Status Enough for Patient Satisfaction? *J Sex Med.* 2016;13(4):669–78.
10. Gallina A, Ferrari M, Suardi N, Capitanio U, Abdollah F, Tutolo M, et al. Erectile function outcome after bilateral nerve sparing radical prostatectomy: which patients may be left untreated? *J Sex Med.* 2012;9(3):903–8.
11. Cornu J-N, Phé V, Fournier G, Delmas V, Sèbe P. Fascia surrounding the prostate: clinical and anatomical basis of the nerve-sparing radical prostatectomy. *Surg Radiol Anat.* 2010;32(7):663–7.
12. Patel VR, Schatloff O, Chauhan S, Sivaraman A, Valero R, Coelho RF, et al. The role of the prostatic vasculature as a landmark for nerve sparing during robot-assisted radical prostatectomy. *Eur Urol.* 2012;61(3):571–6.
13. van der Poel HG, de Blok W. Role of extent of fascia preservation and erectile function after robot-assisted laparoscopic prostatectomy. *Urology [Internet].* 2009 Apr [cited 2014 Dec 30];73(4):816–21. Available from: <http://www.ncbi.nlm.nih.gov/pubmed/19195692>
14. Menon M, Hemal AK, VIP Team. Vattikuti Institute prostatectomy: a technique of robotic radical prostatectomy: experience in more than 1000 cases. *J Endourol.* 2004;18(7):611–9.
15. Lindeman RH, Merenda PF, Gold RZ. Introduction to bivariate and multivariate analysis. Scott, Foresman; 1980. 444 p.
16. Briganti A, Gallina A, Suardi N, Capitanio U, Tutolo M, Bianchi M, et al. Predicting Erectile Function Recovery after Bilateral Nerve Sparing Radical Prostatectomy: A Proposal of a Novel Preoperative Risk Stratification. *J Sex Med.* Elsevier; 2010;7(7):2521–31.
17. Rossi MS, Moschini M, Bianchi M, Gandaglia G, Fossati N, Dell’Oglio P, et al. Erectile Function Recovery After Nerve-Sparing Radical Prostatectomy for Prostate Cancer: Is Back to Baseline Status Enough for Patient Satisfaction? *J Sex Med.* 2016 ;13(4):669–78.
18. Rassweiler J, Wagner AA, Moazin M, Gözen AS, Teber D, Frede T, et al. Anatomic nerve-sparing laparoscopic radical prostatectomy: comparison of retrograde and antegrade techniques. *Urology.* 2006;68(3):587–91.
19. Stolzenburg J-U, Rabenalt R, Do M, Schwalenberg T, Winkler M, Dietel A, et al. Intrafascial nerve-sparing endoscopic extraperitoneal radical prostatectomy. *Eur Urol.* 2008;53(5):931–40.
20. Park YH, Jeong CW, Lee SE. A comprehensive review of neuroanatomy of the prostate. *Prostate Int.* 2013;1(4):139–45.
21. Walz J, Burnett AL, Costello AJ, Eastham JA, Graefen M, Guillionneau B, et al. A critical analysis of the current knowledge of surgical anatomy related to optimization of cancer control and preservation of continence and erection in candidates for radical prostatectomy. *Eur Urol.* 2010;57(2):179–92.
22. Mandel P, Graefen M, Michl U, Huland H, Tilki D. The effect of age on functional outcomes after radical prostatectomy. *Urol Oncol.* 2015;33(5):203.e11-203.e18.

23. Han M, Trock BJ, Partin AW, Humphreys EB, Bivalacqua TJ, Guzzo TJ, et al. The impact of preoperative erectile dysfunction on survival after radical prostatectomy. *BJU Int.* 2010;106(11):1612–7.
24. Kang SG, Schatloff O, Haidar AM, Samavedi S, Palmer KJ, Cheon J, et al. Does surgeon subjective nerve sparing score predict recovery time of erectile function following robot-assisted radical prostatectomy?. *J Sex Med.* 2015;6:1490–6.
25. Novara G, Ficarra V, D’Elia C, Secco S, De Gobbi A, Cavalleri S, et al. Preoperative criteria to select patients for bilateral nerve-sparing robotic-assisted radical prostatectomy. *J Sex Med.* 2010;7:839–45.
26. Miyake H, Miyazaki A, Yao A, Hinata N, Fujisawa M. Significance of erection hardness score as a diagnostic tool to assess erectile function recovery in Japanese men after robot-assisted radical prostatectomy. *J Robot Surg.* 2016;10(3):221–6.
27. Buckle T, KleinJan GH, Engelen T, van den Berg NS, DeRuiter MC, van der Heide U, et al. Diffusion-weighted-preparation (D-prep) MRI as a future extension of SPECT/CT based surgical planning for sentinel node procedures in the head and neck area? *Oral Oncol.* 2016;60:48–54.
28. Whitney M a, Crisp JL, Nguyen LT, Friedman B, Gross L a, Steinbach P, et al. Fluorescent peptides highlight peripheral nerves during surgery in mice. *Nat Biotechnol.* 2011;29(4):352-6.
29. KleinJan GH, Buckle T, van Willigen DM, van Oosterom MN, Spa SJ, Kloosterboer HE, et al. Fluorescent lectins for local in vivo visualization of peripheral nerves. *Molecules.* 2014;19(7):9876–92.

## SUPPLEMENTAL INFORMATION (SI)

### METHODS

#### Patients

1241 men whom underwent robot assisted radical prostatectomy (RARP) at the Netherlands Cancer Institute - Antoni van Leeuwenhoek Hospital (NKI-AvL) between September 2007 and November 2014 were included in this study (SI Table 2). Exclusion criteria included any prior local therapy (radiation, HIFU, cryoablation, TURP) or androgen ablation. Tumors were clinically and pathologically staged (TNM 2009, 7<sup>th</sup> edition) and graded according to Gleason sum score. Ethical approval for the execution of this study was provided by the institutional review board (IRB) of the NKI-AvL.

#### International index of erectile function – Erectile Function 5

All data recorded during treatment and follow-up was documented in the prospective database of the Department of urology of the NKI-AVL, which was approved by the IRB of the NKI-AVL. For evaluation of EF, patients were asked to fill out a self-administered erectile function evaluation tool (IIEF-EF5 later referred to as IIEF; Supplemental Information (SI), Table SI1) [1–4] prior to undergoing RARP (baseline IIEF) and at 12 months after the procedure (postoperative IIEF; recorded between nine and fifteen months).

As consensus on the optimal cut-off for ED based on IIEF score is lacking, a continuous read-out of the IIEF score (which provides better insight into the relative function loss (independent of IIEF scaling) during comparison of preoperative and postoperative IIEF) was used [1,2,4].

#### Comorbidity

Comorbidity was preoperatively scored using the CCIS [5] (Table SI1). For statistical analysis, the CCIS without age correction was divided into the following two groups, the group with score 0 and the group with CCIS >0 [5].

#### Surgical procedure

Fascia preservation was defined as the presence of a continuous fascia segment from base to apex without clinically visible interruptions after prostate removal. The extent of fascia sparing during RARP was then quantified as the FP score that ranged from 0-6 on both sides, with a total score between 0 and 12. Nerve preservation was attempted in patients who requested erectile function preservation, which had no evidence of extracapsular disease and a Gleason score of <7 ipsilaterally. Prostate pedicle vasculature dissection was performed

either using careful bipolar coagulation or by using 10mm titanium clips (Aesculap, Inc., Center Valley, USA).

LND was performed in patients with a nomogram estimated risk of nodal metastases exceeding 5% and was generally executed after prostate removal [6].

### **Immunohistochemistry**

Harvested tumor tissue was formalin-fixed and paraffin-embedded. Five  $\mu\text{m}$  sections were stained for general tissue characteristics (heamatoxylin and eosin; H&E) and the presence of nerves was evaluated through staining myelin.

### **Heamatoxylin and eosin staining**

For the H&E staining, deparaffinized and rehydrated tissue sections were incubated for 10 min with heamatoxylin, rinsed in tap water for 10 min, incubated in eosin (5 min) and extensively rinsed with MilliQ, dehydrated and mounted (Estellan; Merck Millipore, Amsterdam, The Netherlands).

### **Myelin staining**

For the myelin staining, tissue sections were deparaffinized and rehydrated after which an endogenous peroxidase inhibition step in 0.3% H<sub>2</sub>O/PBS was performed. After rinsing (PBS, PBS, PBS/0.05% Tween), sections were incubated overnight with a polyclonal-rabbit-anti-S100 antibody (1:4000; cat no. Z0311; Dako, Heverlee, Belgium). The next day, sections were rinsed (PBS, PBS, PBS/0.05% Tween), incubated with a secondary goat-anti-rabbit-biotin antibody (1:200; cat no. BA-1000; Vector Laboratories Inc., Burlingame, CA, USA) and normal goat serum (1:66; cat no. S-1000; Vector Laboratories Inc., Burlingame, CA, USA) for 1 h, rinsed again (PBS, PBS, PBS/0.05% Tween), and incubated for 1 h with ABC-reagents (Vector Laboratories Inc., Burlingame, CA, US) rinsed (PBS, PBS, PBS/Tris maleate), developed with 3,3'-diamobenzidine tetrahydrochloride (Sigma-Aldrich, Zwijndrecht, the Netherlands) and slightly counterstained with hematoxylin after which they were dehydrated and mounted (Estellan).

## SI Tables

Table S1. Patient characteristics of responders with IIEF questionnaire results

Total (number)	1241
Number of patients that did not fill in the queries	252
Number of patients that filled in the preoperative queries	989
Number of patients that filled in the postoperative queries	566
Number of patients that filled in both the pre- and post operative queries (only these patients were used for further analysis)	473
BMI, median (IQR) (kg/m <sup>2</sup> )	25.98 (24.24 – 27.78)
Age, median (IQR) (years)	63 (59 – 67)
PSA-level (ng/mL), median (IQR)	8 (5.8 – 12.0)
Preoperative International Index of Erectile Function (IIEF-EF) score, median (IQR)	21 (8 – 29)
Clinical T-stage	
- cT1 (%)	128 (27%)
- cT2 (%)	272 (58%)
- cT3 (%)	70 (15%)
Missing %	3 (0%)
Biopsy Gleason sum score	
- 4-6 (%)	242 (51%)
- 7 (%)	174 (37%)
- 8-10 (%)	57 (11%)
Clinical N-stage	
- cN0 (%)	201 (43%)
- cN1 (%)	9 (2%)
- cNx (%)	263 (56%)
Pathological T-stage	
- pT0 (%)	3 (1%)
- pT2 (%)	351 (74%)
- pT3 (%)	108 (23%)
- pT4 (%)	11 (2%)
Pathological Gleason sum score	
- 0 (0%)	1 (0%)
- 5-6 (%)	156 (33%)
- 7 (%)	255 (54%)
- 8-10 (%)	60 (12%)
Pathological N-stage	
- pN0 (%)	206 (44%)
- pN1 (%)	38 (8%)
- pNx (%)	229 (48%)
Tumor side	
Left (%)	31 (7%)
Left + Right (%)	401 (85%)
Right (%)	38 (8%)
Missing (%)	3 (1%)
Charlson comorbidity index score (CCIS)	
0 (%)	383 (81%)
+1 (%)	90 (19%)
Smoker	
Yes (%)	409 (88%)
No (%)	57 (12%)
Alcohol use	
None (%)	85 (18%)
<8 (%)	139 (30%)
8-14 (%)	122 (26%)
>14 (%)	121 (26%)
Intraoperative techniques	
FP (median, IQR)	4 (0 -6)
Clips yes	
Clips no	390 (83%)
Lymph node dissection	
No lymph node dissection	227 (48%)

		Points IIEF score					
		0	1	2	3	4	5
1. How often were you able to get an erection during sexual activity	No sexual activity		Almost never or never	A few times (much less than half the time)	Sometimes (about half the time)	Most times (much more than half the time)	Almost always or always
Percentage preoperative and postoperative	16.1%	24.5%	5.0%	11.4%	6.7%	11.6%	49%
			37.6%	8.4%	8.7%	8.0%	12.7%
2. When you had erections with sexual stimulation, how often were your erections hard enough for penetration?	No sexual activity		Almost never or never	A few times (much less than half the time)	Sometimes (about half the time)	Most times (much more than half the time)	Almost always or always
Percentage preoperative and postoperative	17.7%	27.7%	10.1%	7.8%	7.2%	8.9%	48.4%
			42.7%	7.2%	5.9%	5.7%	10.7%
3. When you attempted intercourse, how often were you able to penetrate (enter) your partner?	Did not attempt intercourse		Almost never or never	A few times (much less than half the time)	Sometimes (about half the time)	Most times (much more than half the time)	Almost always or always
Percentage preoperative and postoperative	28.5%	38.5%	8.2%	8.0%	4.6%	7.8%	42.7%
			34.3%	5.7%	5.7%	5.1%	10.8%
4. During sexual intercourse, how often were you able to maintain your erection after you had penetrated (entered) your partner?	Did not attempt intercourse		Almost never or never	A few times (much less than half the time)	Sometimes (about half the time)	Most times (much more than half the time)	Almost always or always
Percentage preoperative and postoperative	31.9%	43.6%	5.7%	7.6%	6.1%	10.5%	39.1%
			30.9%	6.1%	4.4%	5.5%	9.5%
5. During sexual intercourse, how difficult was it to maintain your erection to completion of intercourse?	Did not attempt intercourse		Extremely difficult	Very difficult	Difficult	Slightly difficult	Not difficult
Percentage preoperative and postoperative	31.7%	54.1%	4.4%	2.7%	7.0%	12.7%	41.4%
			17.7%	4.9%	5.3%	7.4%	10.5%
15. How do you rate your confidence that you could get and keep an erection?			Very low	Low	Moderate	High	Very high
Percentage preoperative and postoperative	1.3%	0.8%	11.2%	10.1%	23.9%	41.1%	21.3%
			48.8%	17.5%	16.5%	12.1%	4.2%

**Table S2 IIEF score (preoperative and 12 months after prostatectomy)**

Note: Questions in this questionnaire are not necessarily related to erectile dysfunction, but could also be related to the patients drive for sexual activity e.g. "Did not attempt intercourse" or "No sexual activity".

## RESULTS

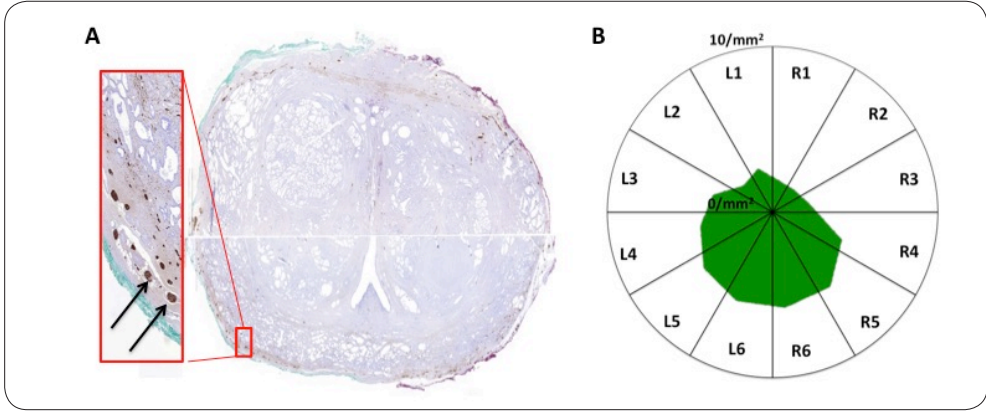
### Pre- and postoperative IIEF outcome

The patient characteristics of the cohort with follow-up ( $n = 473$ ) are presented in Table S11. The median preoperative IIEF was 19 (Figure 2A), while the median postoperative IIEF (twelve months post surgery) was 6 (IQR 3-9; Figure 2A &B). Concurrently, the vast majority of the patients reported lower IIEF scores after prostatectomy (Figure 2C), indicating surgery-induced side effects. Unexplainably, in some cases increases in IIEF were also reported. We consider this as a reflection of the subjective nature of erectile dysfunction.

### Comparison of unilateral and bilateral sparing

In some patients only the lower FP regions were spared ( $n = 140$  unilateral and  $n = 99$  bilateral). In the patients where the upper/higher FP regions R1 – R3 and L1 – L3 were spared ( $n = 70$  for unilateral and  $n = 104$  for bilateral sparing) this generally coincided with sparing of the lower regions ( $n = 343$ ; 72.5%). Not all patients received bilateral sparing (Figure S12D;  $n = 141$ ), unilateral sparing was performed on both the left ( $n = 76$ ; Figure S12B) and right side ( $n = 65$ ; Figure S12C). Even when these groups were split the focus on the lower FP regions remained dominant, whereby sparing of the FP 4 and 5 regions was most prevalent.

To illustrate the effect of unilateral vs. bilateral nerve sparing regarding the mean drop in IIEF after prostatectomy, we compared the unilateral approach with the same FP and bilateral sparing for every FP score up to 6. For a total score of FP 2 with unilateral sparing there was a mean drop in IIEF after prostatectomy of 13 compared to 7.4 in IIEF with bilateral sparing (Mann Whitney U test,  $p$ -value = 0.051). In the patients with total FP of 3 the mean drop in IIEF for unilateral sparing was 14.3 and for bilateral 9.4 (Mann Whitney U,  $p$ -value 0.208). In the patients with total FP of 4, unilateral sparing resulted in a mean drop in IIEF of 11.8 after prostatectomy and for bilateral sparing a drop of 10.9 was seen (Mann Whitney U,  $p$ -value 0.579). In patients with a total FP score of 5 the mean drop in IIEF was lower for the unilateral group as compared to the bilateral group (9.9 vs. 10.9 respectively,  $p$ -value 0.794). In the total FP 6 group bilateral sparing resulted in a non-significant lower drop in IIEF when unilateral sparing was applied compared to bilateral sparing (6.5 vs. 9.7 respectively;  $p$ -value 0.320).



**Pathological analysis of the nerve spread over the FP regions**

**Figure S11. Pathological evaluation of the nerve distribution in different FP-regions of the prostate (n = 10).**

- A)** Representative pathological image of the whole prostate (right) revealing nerves in the fascia (zoom-in of left showing stained nerves as indicated by the arrow).
- B)** Spider plot presenting the number of nerves per mm<sup>2</sup> per FP-region (average of ten patients that did not receive nerve-sparing). The individual values are provided in Figure S12.

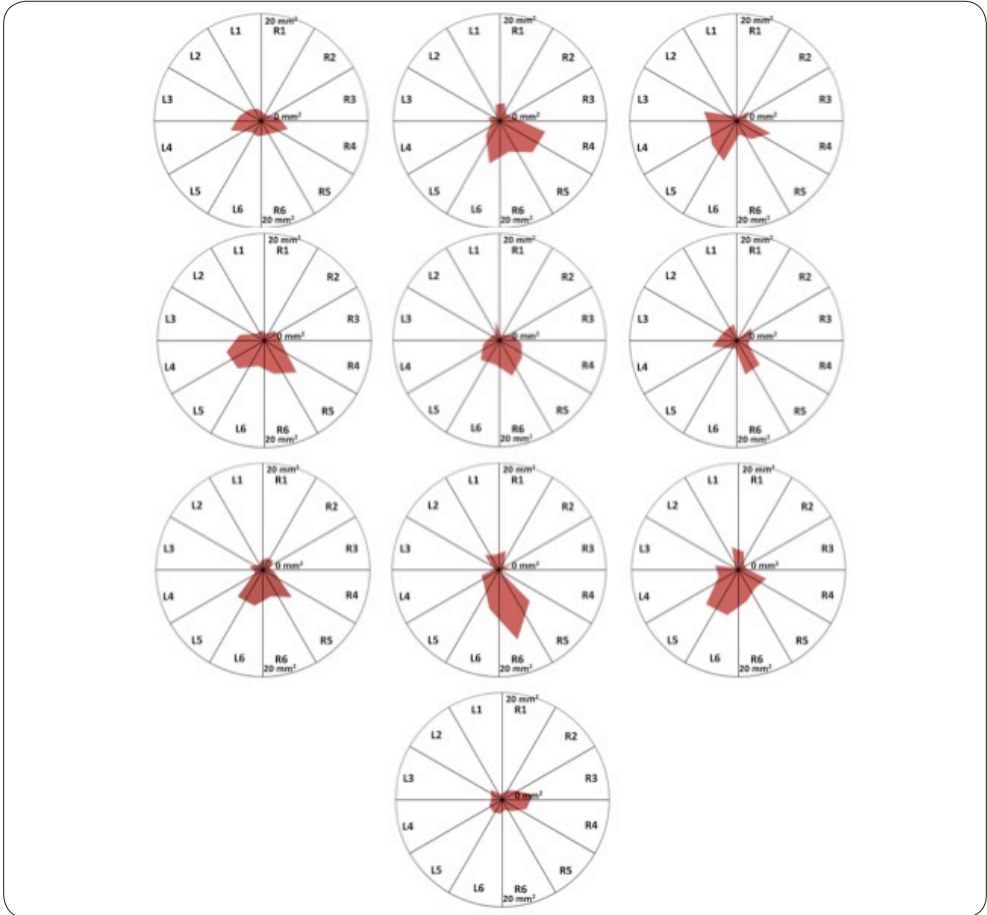


**Figure S12. Variation in nerve distributions per PF region in ten individual FP0 prostate samples.**

Nerve distribution calculated in nerves per  $\text{mm}^2$  per evaluated patient with a FP 0 score. In general the number of nerves was highest in the lower located quadrants.

### Immunohistochemical staining

Quantitative assessment of immunohistochemical staining of myelin containing nerves (Figure S11A) revealed the average number of nerves in the individual FP regions and the overall distribution of these nerves. In line with literature [7, 8], the highest density of nerves was found in the lower FP regions L3-L6 and R3-R6 (Figure S12B). It should, however, be noted that the variance observed between the individual patients was large, underlining the need for personalized resection methods (Figure S13).

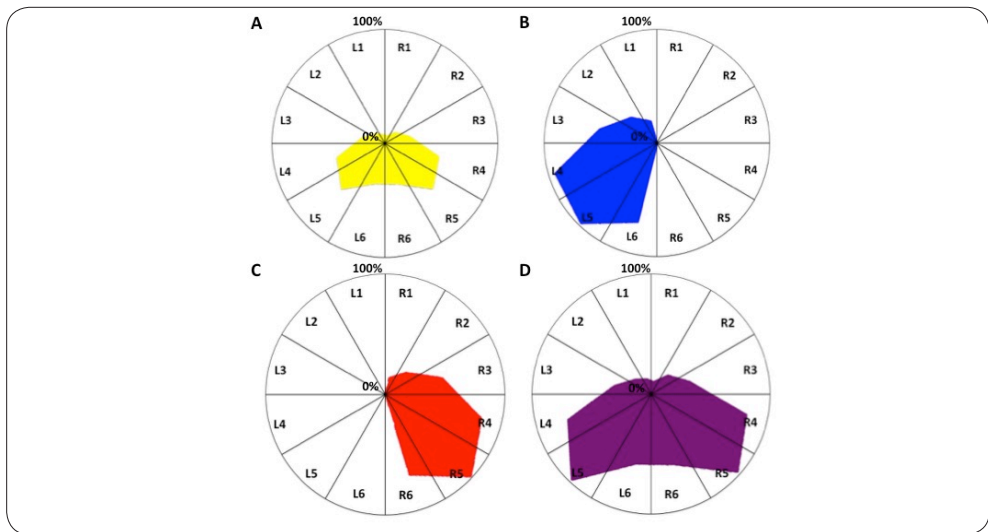


**Figure S3. Surgical sparing of FP regions (n=473)**

**A)** Overall percentile distribution of the FP regions spared during surgery of the total group (FP 0 patients included; n = 473; yellow).

**B)** Pattern of saving in patients that only received unilateral sparing on the left side (n= 65; blue),

**C)** on the right side (n =76; red), and **D)** after bilateral sparing (n = 202; purple).

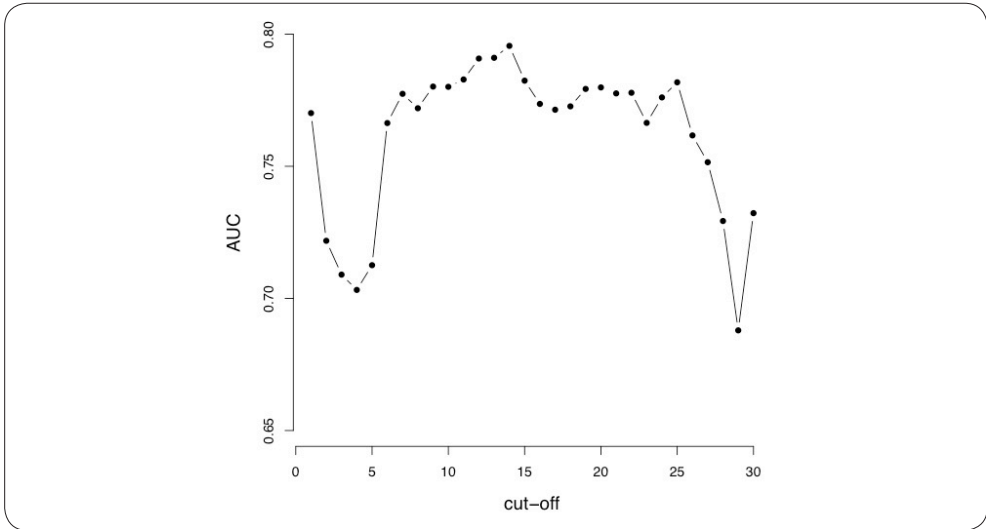


**Figure S4. Relationship between the IIEF cut-off classifying patients into ED and no ED versus AUC for the model predicting ED with FP score.**

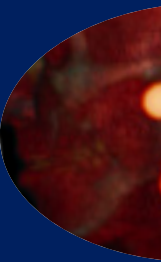
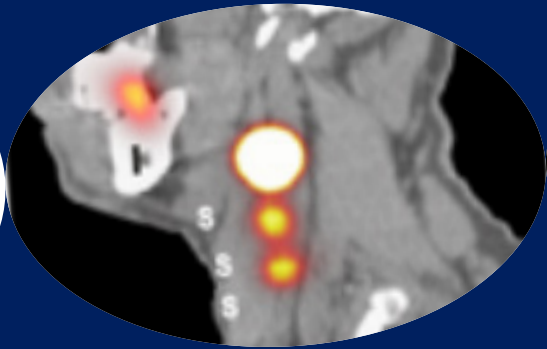
In previous studies different cut-off values were used for IIEF score-based evaluation of ED. [3] However, placement of the cut-off value can directly influence the classification of patients into ED and no ED and the predictive value of the total FP score (Figure S14). The highest area under the curve (AUC) was estimated when ED was defined as IIEF<14.

## REFERENCES

1. Rossi MS, Moschini M, Bianchi M, Gandaglia G, Fossati N, Dell'Oglio P, et al. Erectile Function Recovery After Nerve-Sparing Radical Prostatectomy for Prostate Cancer: Is Back to Baseline Status Enough for Patient Satisfaction? *J Sex Med.* 2016;13(4):669–78.
2. Gallina A, Ferrari M, Suardi N, Capitanio U, Abdollah F, Tutolo M, et al. Erectile function outcome after bilateral nerve sparing radical prostatectomy: which patients may be left untreated? *J Sex Med.* 2012 Mar;9(3):903–8.
3. van der Poel HG, de Blok W. Role of extent of fascia preservation and erectile function after robot-assisted laparoscopic prostatectomy. *Urology.* 2009;73(4):816–21.
4. Mandel P, Graefen M, Michl U, Huland H, Tilki D. The effect of age on functional outcomes after radical prostatectomy. *Urol Oncol Semin Orig Investig.* 2015;33(5):203.e11-203.e18.
5. Albertsen PC, Fryback DG, Storer BE, Kolon TF, Fine J. The impact of co-morbidity on life expectancy among men with localized prostate cancer. *J Urol.* 1996;156(1):127–32.
6. Heidenreich A, Bastian PJ, Bellmunt J, Bolla M, Joniau S, van der Kwast T, et al. EAU guidelines on prostate cancer. part 1: screening, diagnosis, and local treatment with curative intent-update 2013. *Eur Urol.* 2014 Jan;65(1):124–37.
7. Walsh PC, Donker PJ. Impotence following radical prostatectomy: insight into etiology and prevention. *J Urol.* 1982;128(3):492–7.
8. Walz J, Burnett AL, Costello AJ, Eastham JA, Graefen M, Guillonneau B, et al. A critical analysis of the current knowledge of surgical anatomy related to optimization of cancer control and preservation of continence and erection in candidates for radical prostatectomy. *Eur Urol.* 2010;57(2):179–92.

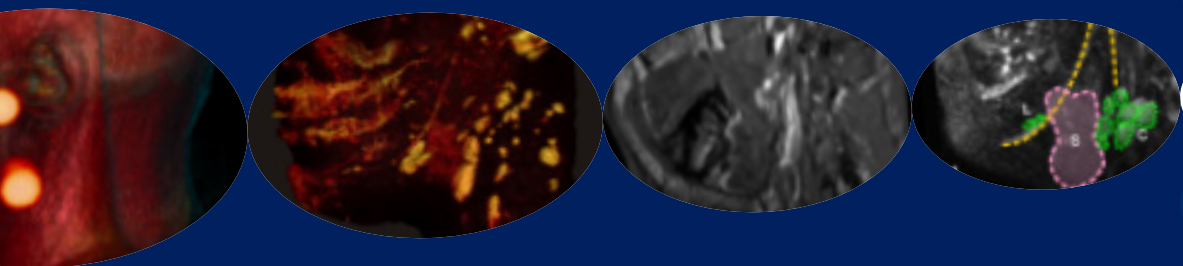


# Chapter 11



# Diffusion-weighted-preparation (D-prep) MRI as a future extension of SPECT/CT based surgical planning for sentinel node procedures in the head-and-neck area?

*Tessa Buckle  
Gijs H. KleinJan  
Thijs Engelen  
Nynke S. van den Berg  
Marco C. DeRuiter  
Ulke van der Heide  
Renato A. Valdés Olmos  
Andrew Webb  
Marc A. van Buchem  
Alfons J. Balm  
Fijs WB van Leeuwen  
Oral Oncol. 2016;60:48-54*



## **ABSTRACT**

### **INTRODUCTION**

Even when guided by SPECT/CT-based surgical planning of nodal resections in the head-and-neck area is challenging due to the many critical anatomical structures present within the surgical field. In this chapter the potential of a (SPECT)/MRI-based surgical planning method was explored. Hereby MRI increases the identification of SNs within clustered lymph nodes (LNs) and vital structures located adjacent to the SN (such as cranial nerve branches).

### **METHODS**

SPECT/CT and pathology reports from 100 head-and-neck melanoma and 40 oral cavity cancer patients were retrospectively assessed for SN locations in levels I-V and degree of nodal clustering. A diffusion-weighted-preparation magnetic resonance neurography (MRN) sequence was used in eight healthy volunteers to detect LNs and peripheral nerves.

### **RESULTS**

In 15% of patients clustered nodes were retrospectively shown to be present at the location where the SN was identified on SPECT/CT (level IIA: 37.2%, level IIB: 21.6% and level III: 15.5%). With MRN, improved LN delineation enabled discrimination of individual LNs within a cluster. Uniquely, this MRI technology also provided insight in LN distribution ( $23.2 \pm 4$  LNs per subject) and size (range 21-372 mm<sup>3</sup>), and enabled non-invasive assessment of anatomical variances in the location of the LNs and facial nerves.

### **CONCLUSION**

Diffusion-weighted-preparation MRN enabled improved delineation of LNs and their surrounding delicate anatomical structures in the areas that most often harbor SNs in the head-and-neck. A combined SPECT/MRI approach is envisioned for future surgical planning of complex SN resections in this region.

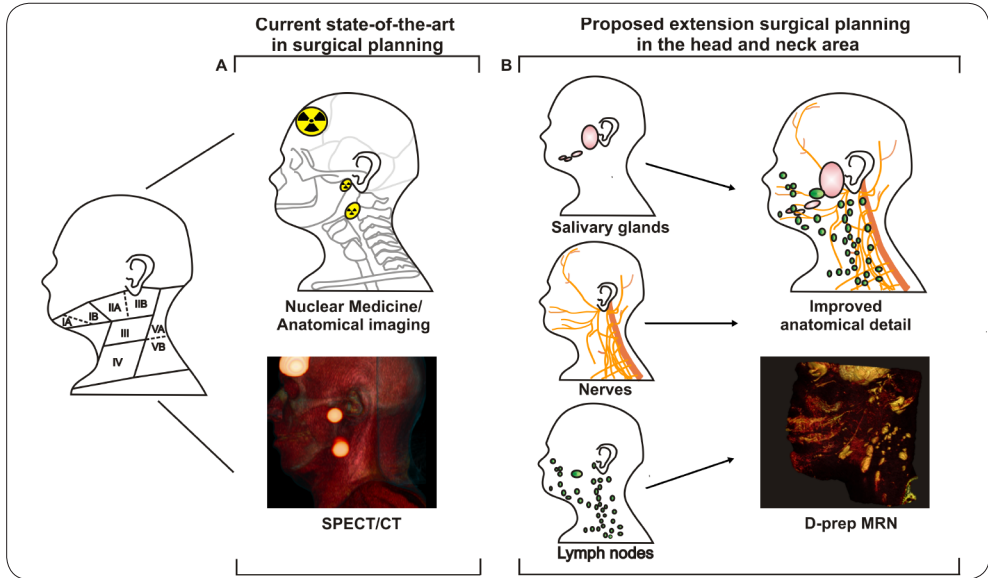
## INTRODUCTION

Sentinel node (SN) biopsy procedures are a common example of an approach routinely performed using image guidance [1-2]. In a state-of-the-art setting pre-operative single photon computed tomography combined with computed tomography (SPECT/CT) images is used to define the number and location of the SNs (using the nuclear component) and their general location (using the CT component; Scheme 1A). However, even with careful preoperative planning, in general 3-10% of patients that undergo lymph node (LN) biopsy in the neck show iatrogenic nerve damage-related side effects (e.g. persistent pain in neck and shoulder area) and long-term postoperative side-effects such as sensory disturbance are even more common (65%) [3].

Previous evaluation of SN biopsy procedures performed in the head-and-neck region revealed that in 8-19% of patients clustered nodes (clusters are defined as two or more nodes that lie in direct proximity/contact to each other) provide a challenge during surgery. Due to the relatively poor spatial resolution and limited anatomical soft-tissue contrast of SPECT/CT, identification of the true SN within a cluster of LNs can be considered challenging. This often results in the requirement to expand surgical exploration based on intraoperative nodal findings and can increase the chance of surgical side-effects when performed in the vicinity of vital structures in the neck. In the case of incomplete SN resection, meaning not all the positive nodes within such a cluster are removed, this may provide false-negative results [4-7].

Diagnostic CT (170 mA, 120 kV) has a much higher resolution than the routinely used low-dose CT (40mA, 130 kV) and its use could thereby inherently result in improved SPECT/CT-based delineation and discrimination of LNs. However, in our clinic, the corresponding high-dose radiation exposure is considered undesirable for the diagnostic SN biopsy procedure. Magnetic resonance (MR) imaging (MRI) is already part of the standard diagnostic work-up in head-and-neck cancer and has the possibility to provide a no-ionizing dose, high-resolution alternative to CT [8]. This is especially interesting when one considers that, depending on the imaging sequence used, MRI can provide unique types of soft-tissue contrast [9, 10]. For example, diffusion-weighted preparation (D-prep) MR neurography (MRN), which integrates a T2-weighted (spin-echo) preparation module, with diffusion weighted imaging and fat suppression can be used to identify nerve structures [11].

By combining the preoperative need for nodal cluster identification and peripheral nerve visualization it was reasoned that the implementation of MRI (T1 and D-prep MRN) into the planning of SN biopsy procedures could help improve the anatomical information provided



**Scheme 1. Virtual surgical planning for SN biopsies procedures the head-and-neck area.**

A) SPECT/CT provides the ability to localize SNs within their density-based anatomical context (neck level I-V), B) A proposed extension of the virtual planning concept using diffusion-weighted-preparation (D-prep) MRN to accurately delineate LNs and define their position relative to delicate anatomical structures such as peripheral nerves.

by SPECT/CT (Scheme 1B). To study the possible value of such an approach, first SPECT/CT results, surgical findings and pathology reports from 140 patients that underwent an SN biopsy procedure for head-and-neck or oral cavity malignancies were retrospectively assessed. This information was used to assess which area of the neck would benefit most from more detailed imaging evaluation. As clinical evaluation would require adaptation of the current clinical routine, the potential of D-prep MRN in the detection of peripheral nerves but also LNs and their distribution was first assessed in a pilot feasibility study in eight healthy volunteers. Together these findings allow for speculation on the value of D-prep MRN for future SN biopsy procedures.

## **MATERIAL AND METHODS**

### **Patients and volunteers**

Pre- and intraoperative imaging results and pathology reports from 100 head-and-neck melanoma and 40 oral cavity cancer patients who underwent SN biopsy between 2011-2014 using the hybrid tracer indocyanine green-<sup>99m</sup>Tc-nanocolloid were assessed in retrospect. Patients included in this database were, in part, previously included in other clinical studies focused on image-guided removal of the SNs [5,13-15].

Eight healthy volunteers were prospectively included after obtaining written informed consent. The study was approved by the Scientific Committee of the Department of Radiology at the LUMC and all procedures were performed in accordance with the ethical standards of the institutional research committee and with the 1964 Helsinki declaration and its later amendments or comparable ethical standards.

### **SN biopsy procedure**

Tracer injection and preoperative SN mapping was performed as previously described [4, 12]. In brief, a total of 0.4 mL hybrid tracer was injected surrounding the primary tumor lesion or the melanoma scar. Thereafter lymphoscintigraphy and SPECT and CT (40 mAs, 130 kV, 2 mm slices) imaging was performed. After reconstruction, SPECT and CT images were fused using Osirix Medical imaging software (Pixmeo, Geneva, Switzerland) and 3D volume-rendered SPECT/CT images (Osirix) were generated. The nuclear medicine physician determined the number and location of SNs based on the preoperative imaging dataset. The SN was defined as a LN receiving direct drainage from the primary tumor site [6]. The SN location was indicated on SPECT/CT according to the American Joint Committee on Cancer

AJCC)-Union for International Cancer Control (UICC) TNM staging system which distinguishes seven lymph node levels in each side of the neck [13].

Intraoperatively SNs were identified at the neck levels indicated by SPECT/CT using a combination of gamma imaging, gamma tracing and fluorescence imaging [4,12]. Histopathology was performed to determine whether or not the excised nodes contained (micro-) metastasis.

### **SN biopsy database analysis**

A nodal cluster was defined as a hotspot identified on SPECT that contained several components or a diffuse pattern on CT. Clustered LNs were identified via retrospective analysis of the CT images i) when intraoperative SN identification via fluorescence imaging or gamma tracing/imaging revealed multiple nodes at the same location, [4] and ii) when during pathological evaluation excised specimen multiple nodes were identified by the pathologist.

The percentage of nodal clusters, and the incidence of SN identification per level (I-V), and the percentage of tumor-positive SNs were calculated using the following equations:

Eq. 1) Percentage of nodal clusters per level:  $((\text{number of clusters per level})/(\text{total number of CT-identified clusters level I-V})) * 100\%$ ;

Eq. 2) Percentage incidence of SNs per neck level:  $((\text{number of SNs per level})/(\text{total number of excised SNs level I-V})) * 100\%$ ;

Eq. 3) Percentage of tumor-positive SNs:  $((\text{number of SNs with metastasis})/(\text{total number of excised SNs level I-V})) * 100\%$ .

### **MRI in healthy volunteers**

D-prep MRN was performed on a Philips 3T Ingenia MRI system in eight healthy volunteers using a slightly altered version of the D-Prep MRN sequence described by Yoneyama et al [11], with a spin-echo module (TE: 52 ms) and a spatially adiabatic inversion recovery (SPAIR)-based fat suppression (voxel size: 1.09x1.09x0.899 mm) using an eight-channel receive only head coil. Scanning time was approximately five minutes for a field of view (FOV) that comprised level I-V and two-to-three minutes for a FOV that comprised the submandibular region (level I-III). Sagittal images were acquired for both different sequences. Evaluation of

the location of the different levels within the D-prep MRN images was performed using side-by-side comparison with anatomical reference images of the same field of view (acquired using a standard clinical T1-3D turbo spin echo (TSE) sequence).

### **MR image analysis**

Maximum intensity projection (MIP) images (max 10 slices) and overlays of both MR images were made using Osirix Medical imaging software (Pixmeo).

For assessment of the anatomical variances that can influence the risk of nerve damage during the SN biopsy procedure the diameter and location of the facial nerves were determined. On top the diameter and width of the LNs were measured. Finally the range in distance between the nerves and LNs located within level I-V and the nerves or LNs in relation to the submandibular salivary gland were determined. All measurements were performed using the measuring tool in the Osirix Medical imaging software package (Pixmeo).

To determine the (smallest) nerve diameter that could be visualized, three different measurements along the course of the nerves were taken. Here it must be noted that sections with a diameter of <0.7 mm could not be accurately assessed and were therefore not taken into account. To provide a quantitative measure for the risk of nerve damage during nodal dissection the distance between facial nerves, the closest LN and the submandibular salivary gland was measured (in triplicate). In all measurements the reproducibility between observers was determined by calculating the average and standard deviation (SD) for each measurement.

The distribution of the LNs over level I-V was evaluated by determining the number and size of LNs located in each level. Volumetric assessment of the size of the LNs and nodal clusters was conducted as previously described using the Cavalieri principle [14]. As such for assessment of ellipsoid shapes the following equation was used:

Eq. 4) LN volume:  $(3/4\pi) \times (1/2a) \times (1/2b) \times (1/2c)$ .

Here a and b represent the measured width (short axis) of the LN or cluster and c represents the diameter of the LN (long axis).

## RESULTS

Retrospective assessment of cluster incidence and location within level I-V based on preoperative SPECT/CT imaging

Retrospective assessment of SPECT/CT scans, intraoperative imaging data and pathology results, which contained level I-V of the 140 included patients (Scheme 1), revealed that in 15% of patients more than one LN was found at the location of the hotspot that was identified as the SN on SPECT/CT (Figure 1 for nodal cluster distribution and Figure SI1D for an overview of SN localization). Re-assessment of the preoperatively obtained low-dose CT images resulted in the identification of some of the LN clusters (53; Figure 1A), but did not allow for in the identification of the exact number of SN within these LN clusters. For additional information on preoperative identification of SNs using SPECT/CT imaging (Figure SI1 shows a typical example), and surgical and pathological findings, see the supporting information (SI) section. Combined these findings suggest that the highest number of SN clusters and tumor-positive SNs are encountered in level II (Figure 1).

### **MRI-based evaluation of LN distribution in level I-V**

MRI-based efforts on improving the preoperative imaging for the planning of minimally-invasive surgery were first also focused on level I-V. The D-prep MRN sequence used was originally designed for nerve visualization, based on the diffusion properties the nerve. As the diffusion properties of LNs are thought to be comparable to those of nerves, it is therefore not surprising that the use of this sequence also allowed visualization of LNs; LNs within level I-V of the healthy volunteers studied could be clearly delineated (Figure 2; scan time approximately five minutes). Not only were individual LNs visualized, discrimination could also be made between LNs located in clusters of three to five nodes (Figure 2).

Comparison of the images obtained in the eight different volunteers revealed a clear intra-volunteer variation in the distribution and number of LNs over the levels (see Figure 2, LNs highlighted in green) (as demonstrated in Scheme 1). On average  $2 \pm 3$  LNs were identified within level I-V (range: 1-11 LNs per level). An average number of nine, six and five LNs were detected per subject in level IIA, IIB and III respectively. Only a small number of nodes were detected in level I, IV or V (average of 1-4 nodes per level). For differences in sizes between individual LNs and LN clusters, see SI.

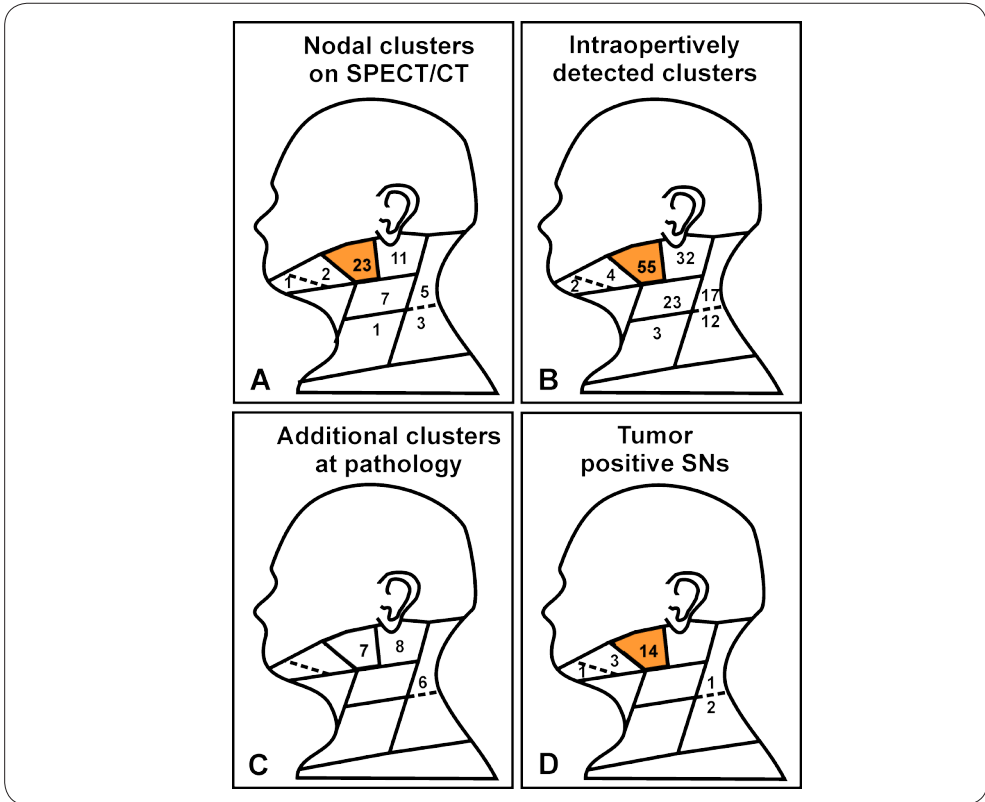


**Figure 1. Incidence and location of LN clusters and metastases.**

**A)** Amount of nodal clusters detected in level I-V (See Scheme 1) using preoperative SPECT/CT imaging:

**B)** Intraoperatively identified nodal clusters;

**C)** Additional nodal clusters identified at pathology;

**D)** Pathologically identified metastases. In orange, the level with the highest incidence of clustered nodes or nodal metastasis. Also see the supporting information for additional information on preoperative identification of SNs using SPECT/CT imaging and surgical and pathological findings.

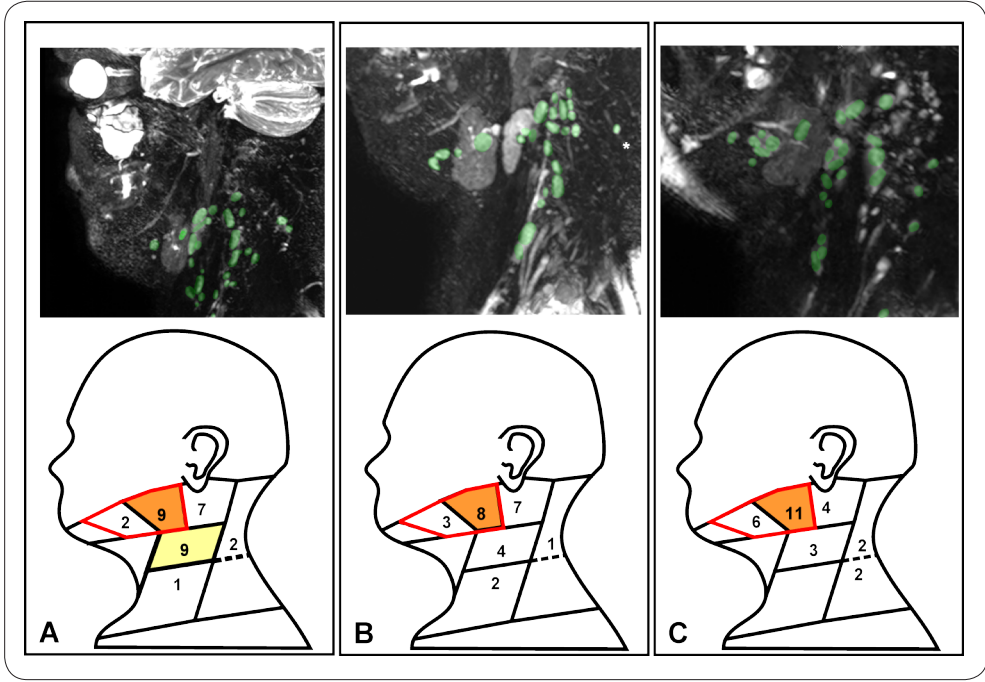


**Figure 2. Variation in LN distribution within level I-V.**

MRN images of the distribution of LNs in three different subjects (A-C) with stratification of LNs (highlighted in green) in level I-V (MIP of one side of the neck; scan time approximately five minutes). The level with the highest amount of visualized LNs is highlighted in orange, or in case of detection of the same amount of LNs in two different levels, in orange and yellow. Levels where the smallest LNs were found are traced in red.

MR-based imaging of the nerves in the submandibular region (including level II) As both the highest number of SNs (Figure 1) and LNs (Figure 2) were shown to be located in level II further efforts on the improvement of the detail of preoperative imaging were focused on the submandibular region, which intricate anatomy includes level II (Figure 3A; FOV traced in red). Images of this FOV obtained with standard T1 3D TSE imaging (Figure 3; i) and D-prep MRN (Figure 3; ii en iii) resulted in the visualization of different anatomical features. Standard T1 3D TSE-based imaging did not result in clear LN delineation, but provided clear visualization of the blood vessels (Figure 3; i). With the D-prep MRN sequence these blood flow-related signals were suppressed. Combined with fat suppression, this resulted in visualization of nerve structures (Figure 3; ii).

### Anatomical variances

To determine if it was possible to provide a measure for the chance of damage to delicate peripheral nerves during the resection of LNs in the head-and-neck area, distances between the LNs and the nearby nerves were recorded (Table 2). The highlighted representation of the structures visualized using D-prep MRN shown in Figure 3iii demonstrate the close relation between the location of the visualized LNs (in green), nerves (in yellow) and the submandibular salivary gland (in pink). An example of how close this relationship can be, is demonstrated in Figure 3B, which shows a cluster of three nodes that are located between and in close proximity to a facial nerve and the submandibular salivary gland.

Overall the distance between the node located closest to the nerve and the nerve itself ranged from 0.9 mm to 6.2 mm. The measured distances varied strongly between subjects. For example, the distance measured in the subject depicted in Figure 3B ( $1.8 \pm 0.80$  mm) was three times smaller than the distance measured in the subject depicted in Figure 3C ( $6.2 \pm 0.1$  mm). In the subject depicted in Figure 3Ciii one LN (L) was found to be located directly on top of the nerve, while in the subject depicted in Figure 3Diii a individual node as well as a cluster of nodes was found to be directly overlaying the nerve (Table 1). In such cases resection without inducement of nerve damage may be complex. For additional observations on structures of interest (Table 1) and anatomical variances, e.g. between the position of the facial nerve and the submandibular salivary gland, see SI.

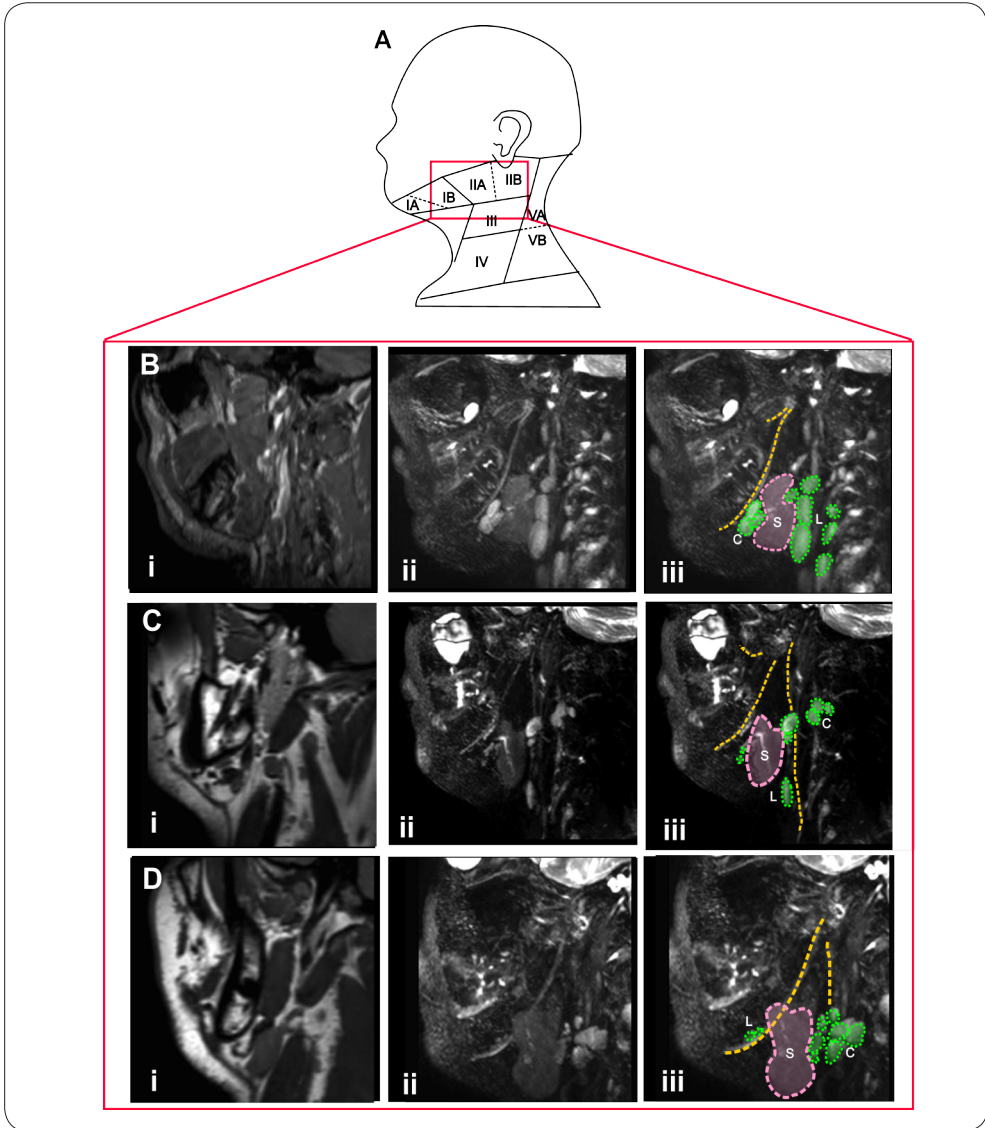


**Figure 3. MR-based imaging of the submandibular region.**

A) Schematic representation of the FOV, which includes level II (in red). B-D) MR images of different healthy volunteers obtained with i) standard T1-3D TSE (single slice) and ii) D-prep MRN (MIP, 10 slices. Scan time two-three minutes). iii) D-Prep MRN images of the same subject wherein visualized structures are traced and highlighted. Here LNs are depicted in green, nerves in yellow and the submandibular salivary gland in pink. Individual LNs = L, LN clusters = C and the submandibular salivary gland = S.

- Structures of interest	- Number of subjects in which structure is identified	- Range in distance between structures (mm)
- LN/ nerves	- 8/8	
- LN adjacent to nerve	- 8/8	- 0.9 – 6.2
- LN on top of nerve	- 1/8	- n.d.*
- Nerve alongside salivary gland	- 3/8	- 3.4 – 4.0
- Nerve adjacent to salivary gland	- 4/8	- 0.1 – 0.4

**Table 1. Relation between visualized structures.**

n.d. = not determined, \* = distance between structures too small to measure.

## DISCUSSION

Results from the current study demonstrate the potential D-prep MRN can have for further refinement of SPECT/CT-based planning of the SN biopsy procedure in the head-and-neck area. The next step will obviously be to initiate a clinical trial in which D-prep MRN is included in the diagnostic work-up of patients with head-and-neck malignancies that will have to undergo a SN biopsy procedure; such an approach will allow evaluation of the true value of D-prep MRN as well as SPECT and low-dose CT imaging for the SN biopsy procedure within the same patient. We envision that using such a hybrid SPECT/MRI-based approach (Scheme 1), the D-prep MRN findings could potentially provide a more detailed preoperative anatomical atlas with regard to the lymphatic and peripheral nerve anatomy. This feature may in the future help reduce procedure-associated morbidity in the form of nerve damage

Retrospective analysis of patients with head-and-neck malignancies who underwent a SN biopsy procedure indicated that nodal clusters and tumor-positive SNs were most abundantly present in the areas with the most intricate anatomy. This region includes the submandibular region (level IIA and IIB; Scheme 1 and Figures 1-3). Unfortunately more traditional (low-dose) CT-based anatomical reference data failed to detect clustered SNs prior to surgery in up to 15% of cases, which is in agreement with previous studies.[5-8] Furthermore this technique could also not provide feedback regarding the location of the SNs relative to other delicate anatomical structures (e.g. nerves). Based on their similar diffusion properties, the newly introduced D-prep MRN technology allowed clear delineation of LNs and clustered LNs (Figure 2), as well as peripheral nerves (Figure 3). Such visualization may help surgeons to assess variations in both the lymphatic and peripheral nerve anatomy of patients prior to surgery, and adapt their approach accordingly. With a scan time of only a couple of minutes, inclusion of D-prep MRN into the current MRI exam could be rather straight-forward. Further extension of the FOV for D-prep MRN would obviously take longer, but could possibly also enable visualization of other possibly critical structures located in or near level I-V (e.g. the auricular nerve). By also including contrast-enhanced MRI or 3D-time-of-flight (TOF)-based MRI approaches in the MRI protocol, the level of detail in the anatomical atlas could even be increased via the visualization of blood vessels [15, 16]. This can be especially valuable during the resection of cervical SNs in level II, where damage to the accessory nerve is the most significant intraoperative complication [17-19]. Here excision of SNs is hampered by anatomical variances in the course of the accessory nerve (see Figure 3), but also in the location of the nerve as this courses either anteriorly or posteriorly to the internal jugular vein (which occurs in 56% and 44% of patients respectively) [17,20,21].

The concept of preoperative surgical planning is expanding rapidly as it is being combined with (intraoperative) image-guided surgery technologies based on radioactivity-based imaging, fluorescence imaging, and/or a combination thereof [12]. Moreover, navigation technologies, in which surgical tools are navigated in preoperative imaging information [22,23], seems to provide a promising field as it can act as a personalized anatomical atlas. Combined, this refined approach may help to improve intraoperative SN excision, and as such help to reduce the false-negative rates. Although the SN-based application provides a good proof-of-concept application for new surgical guidance technologies, improved visualization of the important anatomical structures present in the surgical field and subsequently, improved surgical planning is certainly not limited to these procedures, or applications in the head-and-neck area for that matter. In our view an obvious extended application of the D-prep MRN technology lies within the virtual planning of oncological surgery where it can complement tumor delineation techniques using radiotracers. This can be particularly valuable in hybrid set-ups such as SPECT/MRI and/or positron emission tomography (PET)/MRI. One may, for example, reason that overlays of <sup>18</sup>F-FDG PET and D-Prep MRN images would enable assessment of the location of critical anatomical structures in relation to the location of the primary tumor. As such these combined images may help to improve the preoperative assessment of the potential nerve damage induced during tumor resection. Alternatively, application of this approach may also be found in high-precision radiation therapy with intensity-modulated radiation therapy (IMRT), volumetric arc therapy (VMAT) or proton beam therapy. As delineation of target volumes and organs at risk are a major source of uncertainty, and MRI and PET/CT are already increasingly used for this purpose [25]. By including dose constraints to the nerves, sparing may be achieved, reducing treatment-related side effects.

## CONCLUSION

The potential of D-prep MRN to provide accurate personalized delineation of LNs and their surrounding delicate anatomies, suggests that that this imaging method may provide a valuable extension of nuclear medicine-based treatment planning technologies. Such a technological evolution is well in line with the ongoing efforts wherein findings at nuclear medicine are linked to state-of-the-art radiological imaging.

## REFERENCES

1. Mariani G, Erba P, Manca G, Villa G, Gipponi M, Boni G, et al. Radioguided sentinel lymph node biopsy in patients with malignant cutaneous melanoma: the nuclear medicine contribution. *J Surg Oncol.* 2004;85:141-51.
2. Mariani G, Erba P, Villa G, Gipponi M, Manca G, Boni G, et al. Lymphoscintigraphic and intraoperative detection of the sentinel lymph node in breast cancer patients: the nuclear medicine perspective. *J Surg Oncol.* 2004;85:112-22.
3. Park SH, Esquenazi Y, Kline DG, Kim DH. Surgical outcomes of 156 spinal accessory nerve injuries caused by lymph node biopsy procedures. *J Neurosurg Spine.* 2015;23:518-25.
4. van den Berg NS, Brouwer OR, Schaafsma BE, Matheron HM, Klop WM, Balm AJ, et al. Multimodal Surgical Guidance during Sentinel Node Biopsy for Melanoma: Combined Gamma Tracing and Fluorescence Imaging of the Sentinel Node through Use of the Hybrid Tracer Indocyanine Green-(99m)Tc-Nanocolloid. *Radiology.* 2015;275:521-9.
5. Veenstra HJ, Klop WM, Speijers MJ, Lohuis PJ, Nieweg OE, Hoekstra HJ, et al. Lymphatic drainage patterns from melanomas at the shoulder or upper trunk to cervical lymph nodes and implications for the extent of neck dissection. *Ann Surg Oncol.* 2012;19:3906-12.
6. Veenstra HJ, Vermeeren L, Olmos RA, Nieweg OE. The additional value of lymphatic mapping with routine SPECT/CT in unselected patients with clinically localized melanoma. *Ann Surg Oncol.* 2012;19:1018-23.
7. Klop WM, Veenstra HJ, Vermeeren L, Nieweg OE, Balm AJ, Lohuis PJ. Assessment of lymphatic drainage patterns and implications for the extent of neck dissection in head and neck melanoma patients. *J Surg Oncol.* 2011;103:756-60.
8. Abraham J. Imaging for head and neck cancer. *Surg Oncol Clin N Am.* 2015;24:455-71.
9. Partovi S, Kohan A, Rubbert C, Vercher-Conejero JL, Gaeta C, Yuh R, et al. Clinical oncologic applications of PET/MRI: a new horizon. *Am J Nucl Med Mol Imaging.* 2014;4:202-12.
10. Queiroz MA, Huellner MW. PET/MR in cancers of the head and neck. *Semin Nucl Med.* 2015;45:248-65.
11. Yoneyama M, Takahara T, Kwee TC, Nakamura M, Tabuchi T. Rapid high resolution MR neurography with a diffusion-weighted pre-pulse. *Magn Reson Med Sci.* 2013;12:111-9.
12. van den Berg NS, Brouwer OR, Klop WM, Karakullukcu B, Zuur CL, Tan IB, et al. Concomitant radio- and fluorescence-guided sentinel lymph node biopsy in squamous cell carcinoma of the oral cavity using ICG-(99m)Tc-nanocolloid. *Eur J Nucl Med Mol Imaging.* 2012;39:1128-36.
13. Edge SB, Compton CC. The American Joint Committee on Cancer: the 7th edition of the AJCC cancer staging manual and the future of TNM. *Ann Surg Oncol.* 2010;17:1471-4.
14. Buckle T, van Berg NS, Kuil J, Bunschoten A, Oldenburg J, Borowsky AD, et al. Non-invasive longitudinal imaging of tumor progression using an (111)indium labeled CXCR4 peptide antagonist. *Am J Nucl Med Mol Imaging.* 2012;2:99-109.
15. Fellner FA, Fellner C, Wutke R, Lang W, Laub G, Schmidt M, et al. Fluoroscopically triggered contrast-enhanced 3D MR DSA and 3D time-of-flight turbo MRA of the carotid arteries: first clinical experiences in correlation with ultrasound, x-ray angiography, and endarterectomy findings. *Magn Reson Imaging.* 2000;18:575-85.
16. van den Berg R, Verbist BM, Mertens BJ, van der Mey AG, van Buchem MA. Head and neck paragangliomas: improved tumor detection using contrast-enhanced 3D time-of-flight MR angiography as compared with fat-suppressed MR imaging techniques. *AJNR Am J Neuroradiol.* 2004;25:863-70.
17. Cooper JS, Mukherji SK, Toledano AY, Beldon C, Schmalfluss IM, Amdur R, et al. An evaluation of the variability of tumor-shape definition derived by experienced observers from CT images of supraglottic carcinomas (ACRIN protocol 6658). *Int J Radiat Oncol Biol Phys.* 2007;67:972-5.
18. Nason RW, Abdulrauf BM, Stranc MF. The anatomy of the accessory nerve and cervical lymph node biopsy. *Am J Surg.* 2000;180:241-3.
19. Lloyd S. Accessory nerve: anatomy and surgical identification. *J Laryngol Otol.* 2007;121:1118-25.
20. Lanisnik B, Zargi M, Rodi Z. Electrophysiologic analysis of injury to cranial nerve XI during neck dissection. *Head Neck.* 2015. doi:10.1002/hed.24002.21.
21. Kim DH, Cho YJ, Tiel RL, Kline DG. Surgical outcomes of 111 spinal accessory nerve injuries. *Neurosurgery.* 2003;53:1106-12; discussion 2-3.
22. Brouwer OR, Buckle T, Bunschoten A, Kuil J, Vahrmeijer AL, Wendler T, et al. Image navigation as a means to expand the boundaries of fluorescence-guided surgery. *Phys Med Biol.* 2012;57:3123-36.

23. Zaknun JJ, Giammarile F, Olmos RA, Vidal-Sicart S, Mariani G. Changing paradigms in radioguided surgery and intraoperative imaging: the GOSTT concept. *Eur J Nucl Med Mol Imaging*. 2012 Jan;39(1):1-3.
24. Bhatnagar P, Subesinghe M, Patel C, Prestwich R, Scarsbrook AF. Functional imaging for radiation treatment planning, response assessment, and adaptive therapy in head and neck cancer. *Radiographics*. 2013;33:1909-29.
25. Saito T, Ishikawa H, Ohnishi K, Aihara T, Mizumoto M, Fukumitsu N, et al. Proton beam therapy for locally advanced and unresectable (T4bN0M0) squamous cell carcinoma of the ethmoid sinus: A report of seven cases and a literature review. *Oncol Lett*. 2015;10:201-5.

## SUPPORTING INFORMATION

### RESULTS

#### **Preoperative identification of SNs using SPECT/CT imaging**

A typical example of a SPECT/CT image is provided in Figure S11. The overlay of CT and SPECT images shown in Figure S11B, and the 3D volume rendering of these SPECT/CT images (Figure S11C) enable distinction between the injection site (I) and the SNs (S). Retrospective assessment of SPECT/CT scans of the 140 included patients revealed that of the total number of preoperatively identified SNs ( $n=345$ ; Figure S11D), 79.9% were located in level IB, II and III (283 nodes). Within these three levels, level IIA clearly showed the highest SN incidence (Figure S11D, highlighted in orange); the number of SNs that were located in level IIA was (over) two-fold higher (120 nodes, 33.8%) than the number of SNs located in level IB (60 nodes, 16.9%), level IIB (53 nodes, 14.9%) or level III (50 nodes, 14.1%).

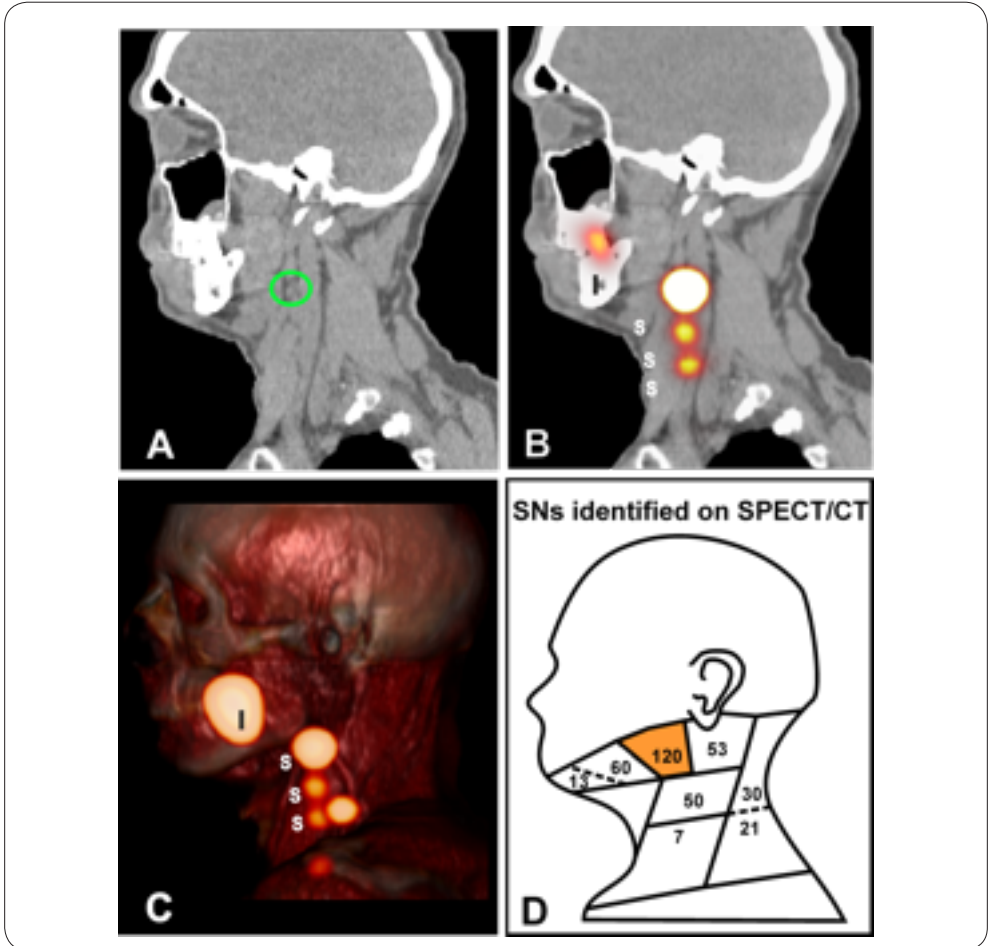


**Figure S11. Preoperative identification of SNs using SPECT/CT imaging.**

Preoperative images of a typical patient showing A) a representative CT image with a LN cluster encircled in green, B) a fused SPECT and CT image; and C) a 3D volume rendered SPECT/CT image in which the injection site (I) and identified SNs (S) have been denoted. D) The total number of SNs identified on SPECT/CT in the database containing 140 patients with head-and-neck malignancies, specified per level. The level with the highest number of identified SNs (level IIA) is highlighted in orange.

### **Surgical and pathological findings**

In 15% of patients more than one LN was found at the location of the hotspot that was identified as the SN on SPECT/CT. Intraoperatively, 148 nodal clusters were identified, using radioguidance and/or fluorescence imaging (Figure 1). Pathological analysis revealed 21 additional nodal clusters (Figure 1).

The number of SNs excised during surgery was highest in level IIA (37%). At pathology level IIA was also shown to be the level that showed the highest incidence SN metastases was found (42.6%; overall 11.7% of SNs identified in this level contained metastases; Figure 1).

### **Size lymph nodes and lymph node clusters**

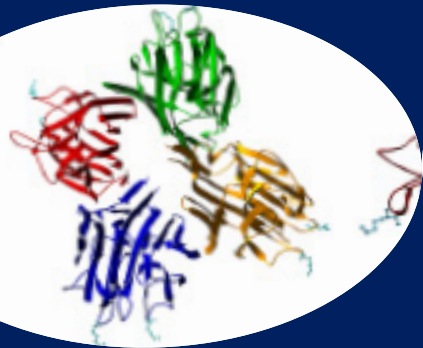
Besides defining differences in the lymphatic anatomy (Figure 2), a broad range in LN size could be derived from the MRN images. The mean size of the individual LNs was  $100 \pm 97$  mm<sup>3</sup>, ranging from small LNs of 21 mm<sup>3</sup> in size to large LNs of 372 mm<sup>3</sup>. LN clusters containing up to five nodes measured up to 1233 mm<sup>3</sup>. The size of the LNs was also related to the level in which they were located (See Scheme 1 for an overview of the different levels), with the largest LNs identified in level II and III, and the smallest in level IB and IIA (Figure 2; traced in red).

### **Visualization of nerves and anatomical variances between the position of facial nerves and the submandibular salivary gland**

When focusing on the position of facial nerves (Figure 3, in yellow; measured diameter:  $1.7 - 1.9 \pm 0.1$  mm)) and its marginal mandibular branch another distinct variation was observed. In all subjects the course of the nerves relative to other structures present in the FOV, such as the submandibular salivary gland (S), was also shown to vary. In three subjects the nerve was clearly located alongside to the salivary gland (Figure 3C; distance:  $3.6 \pm 0.4$ ), while in four others it was located exactly adjacent to the salivary gland (example shown in Figure 3B; distance:  $2.3 \pm 1.4$ ). In a different volunteer yet another pattern was seen (Figure 3D). The smallest nerve that could be accurately detected was  $<0.7$  mm in diameter. Visualization of the nerves seemed to be related to the angulation of the FOV along the position of the jawbone (planning of the sequence was based on the survey images obtained at the start of the imaging session and the T1-3D TSE reference images). The submandibular salivary gland was detected in all subjects (Table 1).



# Chapter 12



# Fluorescent lectins for local *in vivo* visualization of peripheral nerves

*Gijs H KleinJan*

*Tessa Buckle*

*Danny M. van Willigen*

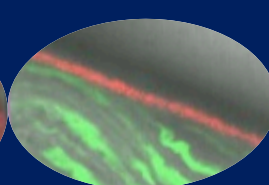
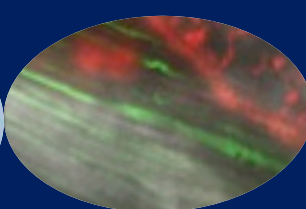
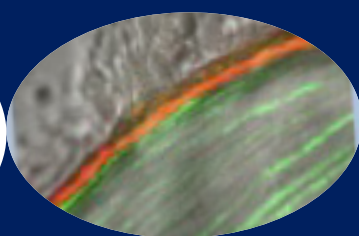
*Matthias N. van Oosterom*

*Silvia J. Spa*

*Harmen E. Kloosterboer*

*and Fijs W.B. van Leeuwen*

*Molecules. 2014;19(7):9876-9892*



## ABSTRACT

### INTRODUCTION

Damage to peripheral nerves caused during a surgical intervention often results in function loss. Fluorescence imaging has the potential to improve intraoperative identification and preservation of these structures. However, only very few nerve targeting agents are available. This study describes the *in vivo* nerve staining capabilities of locally administered fluorescent lectin-analogues.

### METHODS

For the purpose of this study, WGA, PNA, PHA-L and LEL were functionalized with Cy5 (  $\lambda_{\text{ex}}$  max 640 nm;  $\lambda_{\text{em}}$  max 680 nm). Transfer of these imaging agents along the sciatic nerve was evaluated in Thy1-YFP mice (n = 12) after intramuscular injection. Migration from the injection site was assessed *in vivo* using a laboratory fluorescence scanner and *ex vivo* via fluorescence confocal microscopy.

### RESULTS

All four lectins showed retrograde movement and staining of the epineurium with a signal-to-muscle ratio of around two. On average, the longest transfer distance was obtained with WGA-Cy5 (0.95 cm).

### CONCLUSION

Since WGA also gave minimal uptake in the lymphatic system, this lectin type had the highest potential to be used as a migration-based nerve imaging agent.

## INTRODUCTION

Damage to the peripheral nervous system (PNS) is a surprisingly common complication after surgery (e.g. prostatectomy, colorectal surgery and the removal of head and neck tumors) [1–5]. Many peripheral nerves are encountered within the surgical field and their intraoperative identification is often difficult. Unfortunately, trauma to these nerves can lead to chronic function loss and, as such, can negatively influence the quality of life of patients [6,7].

In recent years intraoperative fluorescence imaging was introduced to increase contrast between a target lesion and the surrounding anatomy. Fluorescent dyes such as fluorescein and indocyanine green (ICG) are routinely used in the evaluation of perfusion and optical detection of cancerous lesions [8]. During sentinel lymph node biopsies the addition of fluorescence, incorporated in a hybrid imaging agent, was shown to improve optical detection after local administration of a tracer [9,10].

In the preclinical setting fluorescence has been used to image (peripheral) nerves. Unfortunately, fluorescent dyes alone have not yet shown the required specificity for nervous tissue necessary for their application in the clinic [11]. To increase specificity, a targeting moiety can be introduced that selectively binds to cells expressing a specific biomarker. This approach has already been applied frequently in cancer imaging [12,13]. Compounds that stain the entire nervous system have been described in literature, e.g. FAM-NP 41 [14]. Unfortunately, intravenous administration may also increase the chance of systemic toxicity. Since the latter is a great concern, we reasoned that, in analogy to the clinically applied sentinel node procedure [9,10], local tracer administration could provide an alternative means to highlight nerves while reducing the (systemic) dose [15]. Following a local administration, only the nerves in the anatomy that is being surgically interrogated will be stained.

Lectins are a group of proteins, with size varying between 4–10 nm, which have shown promise as imaging agents [16–19]. Previously, these proteins have been used for (trans synaptic) axonal tracing in *ex vivo* histological research to identify neuronal pathways; labeling occurred with horseradish peroxidase (HRP)[16,18,20,21]. Lectins are able to bind to specific sugar groups (oligosaccharides), leading to affinity for proteoglycans (PGs) present on the extracellular matrix of peripheral nervous tissue [22]. These PGs consist of a protein core to which one or more glycan chains are attached [23], creating five distinct PGs; chondroitin sulfate proteoglycan (CSPG), heparan sulfate proteoglycan (HSPG), keratan sulfate

proteoglycan (KSPG), dermatan sulfate proteoglycan (DSPG) and hyaluronan proteoglycan (HP) [24,25]. For examples of different lectins and their corresponding accessory sugar moieties and PGs, see Table 1.

Reasoning that a local administration of lectins may also provide in vivo migration along peripheral nerves, in this study Cy5-labeled lectin derivatives were evaluated for their value in vivo. Performance of the lectins was scored by: (i) measuring the transfer distance of the lectins along the course of the nerve, (ii) determining the fluorescence signal measured in the nerve to the signal in the surrounding tissue (signal-to-background-ratio; SBR) and (iii) evaluating the binding mode after *ex vivo* incubation of nerve tissue.

Lectin	Sugar Moiety	PG	Molecular Weight (KD)
Triticum Vulgaris (Wheat germ agglutinin; WGA);	$\beta$ -D-GlcNAc, Neu5Ac	HSPG, KSPG, HP	36
Arachis Hypogaea (Peanut lectin; PNA)	Gal $\beta$ (1-3)GalNAc	CSPG, DSPG	110
Phaseolus Vulgaris Leucoagglutinin (Red kidney bean; PHA-L)	Antennary branched $\beta$ (1-6) GlcNAc	HSPG, KSPG, HP	120
Lycopersicon Esculentum (Tomato lectin; LEL)	[GlcNAc $\beta$ (1-4)] <sub>2-4</sub>	HSPG, KSPG, HP	71

**Table 1. Lectins and their corresponding binding sugar moiety/proteoglycan [22,26-28].**

## RESULTS AND DISCUSSION

### Labeling Efficacy

To study the value of lectins for *in vivo* visualization of nerves following a local tracer administration, the four different lectins used in this study (Table 1) had to be labeled with a fluorescent dye. We chose the far-red dye Cy5 based on its previous use in preclinical and clinical studies on fluorescence guided surgery [13,29]. To ensure optimal comparison between the lectins, all four were labeled via an identical labeling protocol (Figure 1A). The reaction between Cy5-OSu and the free lysine groups available on the lectins (Figure 1B,C lysine groups in blue), resulted in a successful fluorescent labeling with corresponding labeling ratios (Figure 2). Via absorption spectroscopy the average Cy5/lectin ratio was determined to be  $1.38 \pm 0.24$ , meaning that, at least one fluorophore was attached to the protein scaffold. Slight differences in labeling efficiency (Figure 2) can presumably be explained by the amount of available lysines on the lectins and their spatial conformation within the protein structure. As depicted in Figure 1, WGA has four available lysines per subunit, namely LYS33, LYS88, LYS134 and LYS149, whereas PHA-L and PNA have only 2, respectively LYS129/LYS215 and LYS77/LYS112.

By increasing the ratio of fluorophores per lectins, the fluorescence signal in the stained nerve, and the resulting SBR, could potentially increase. The fluorescence signal will, however, not only be limited by the number of available binding sites on the molecule, but also by the quenching effect that will occur when these dyes are being placed within 10 nm of each other [30]. The maximum distances between available lysines were measured using the crystal structures (Figure 2) and Swissprot software. Here we found that, in the case of WGA, no more than one fluorophore per lectin is desired, as the maximum lysine-to-lysine distance is approximately 7.3 nm. For PNA and PHA-L, the maximum distance between the lysines is approximately 8.4 and 9.7 nm. As such, an average of 1.5 fluorophores per lectin is considered the optimal labeling ratio.

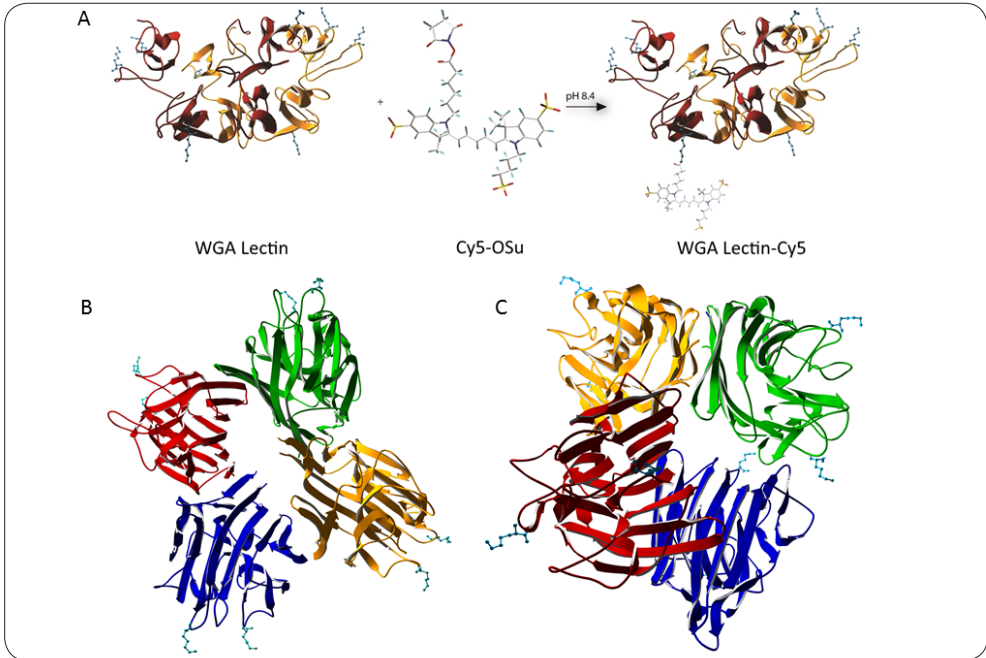


**Figure 1. Crystal structures and method of labeling.**

(A) WGA, consisting of two subunits, with four readily available lysines per subunit, covalently attached to sulphonated Cy5-OSu. (B) PHA-L, consisting of four subunits, with two readily available lysines per subunit. (C) PNA, consisting of four subunits forming a tetrahedral structure, with two readily available lysines per subunit. To the best of our knowledge, the crystal structure for LEL (tomato lectin) is unknown.

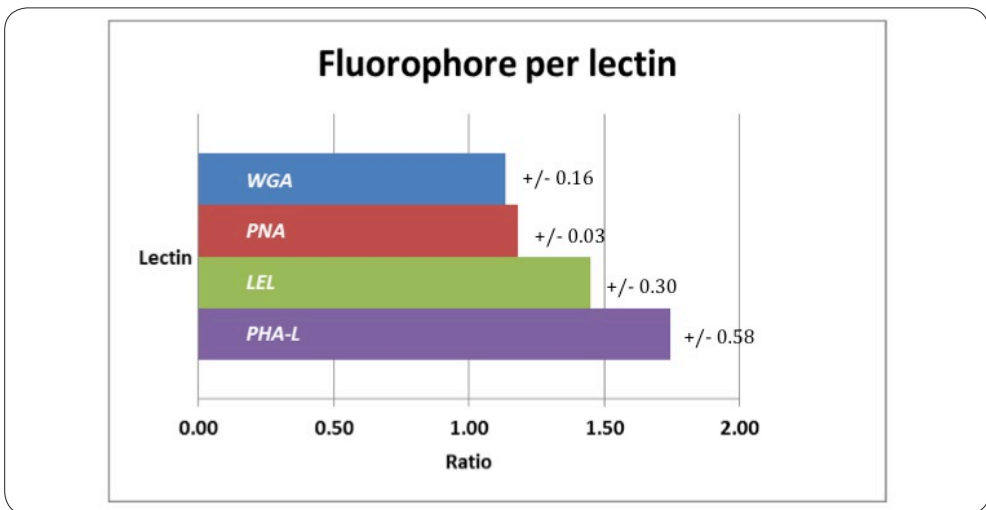


**Figure 2. Cy5/Lectin labeling ratio per lectin.**

### ***In vivo* Migration**

Good visualization of a nerve following local administration of a fluorescently labeled lectin requires migration of the imaging agent along the course of the nerve. Staining of the nerve will commence at the site of injection and continue along the length of the migration (Figure 3A). This process was studied *in vivo* using transgenic THY-1 YFP mice in which the nerves themselves are fluorescent in the 520–550 nm region, thereby providing an internal reference for the migration path (Figure 3B; nerve in green). An intramuscular injection was aimed at the distal part of the sciatic nerve in the hind leg (Figure 3A). From this location, the lectin-analogues were allowed to migrate for 24 h. After this period, consecutive imaging at Cy5 settings (ex 633 nm, em 650–700 nm) was performed before and after dissection of the muscle tissue that surrounds the sciatic nerve (Figure 3C,D).

As the images in Figure 3 demonstrate, the background signal emitted by the injection site was so intense that initial removal of this tissue was required to enable detection of fluorescence in the nerve (Figure 3E). No fluorescence was observed in the control nerve in the opposite leg (Figure 3, red arrow). Clinically the drawback of an intense signal at the injection site is also encountered during e.g. sentinel lymph node biopsy, a procedure that relies on the local injection of a radiocolloid and/or fluorescent dye that subsequently migrates through the lymphatic system [31]. In this application, the signal from the injection site sometimes overshines lymph nodes located in close proximity [32]. Here, technical solutions such as changes in the imaging equipment and imaging software have been successfully applied to circumvent this problem [33,34].

Analysis in the different animals revealed that all four lectins migrated along the nerve, but slight differences in the efficiency could still be recorded (Table 2, Figure 4). To do this, the maximal retrograde transfer length determined from the normalized curves produced by MATLAB, was set at the point where the (average) signal in the nerve was equal to the signal in the unstained control.

The value of the lectins as nerve visualizing imaging agents will increase with an increasing migration distance. For all four lectins-analogues, the normalized curves show a fast decrease in signal intensity along the nerve (Figure 4). Although not significant ( $p$ -value = 0.659), WGA gave the best migration properties (0.95 cm; Figure 4A) compared to PHA-L (0.81 cm; Figure 4C), and PNA and LEL (both 0.72 cm; Figure 4B,D). Local identification of peripheral nerves may help surgeons to navigate around the complex (nerve) anatomy in the head-and-neck area; numerous (small) nerves are located within a surgical field of  $2 \times 2$  cm [35]. One may question the value of a “mere 1 cm migration” along the nerve within this field of view.

However, during our clinical studies in the field of fluorescence guided sentinel node biopsy we already found that fluorescence may provide surgical guidance towards sentinel nodes located within 1 cm of the injection site [36]. In our view this suggests that the compound described here may already provide value. Chemical modification of these imaging agents (e.g. functionalization, solubility) may increase the migration along the nerves, which will further broaden the application of this approach.

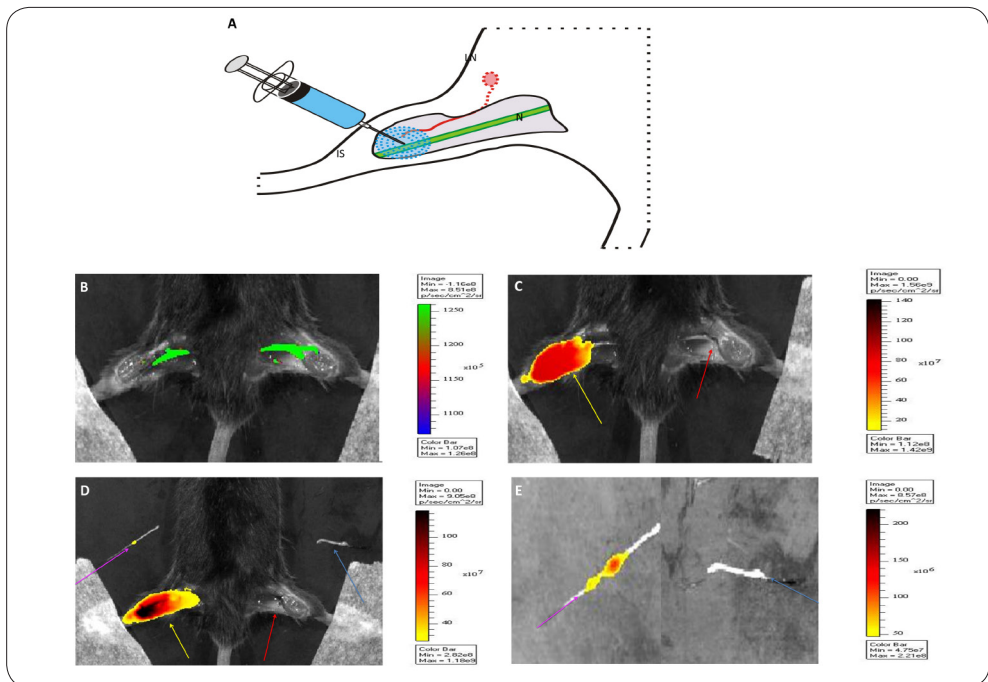


**Figure 3. In vivo distribution of locally injected lectins (A) Schematic representation of the local injection of Cy5-lectins and the corresponding migration path.**

The injection site (IS) and sciatic nerve (N) are depicted in blue and green respectively. The lymphatic tract leading from the IS to the lymph node (LN) is shown in red. (B) Illustration of the YFP signal in the nerves (green) which served as control for the localization of the nerves. Representative images of the injection site before (C) and after (D) removal of the nerve, and excised nerves (E). In each of these pictures, yellow arrows -the injection site; purple arrows -fluorescence signal from injection site and nerve, red arrows -the control side nerve and light blue arrows -the control nerve.

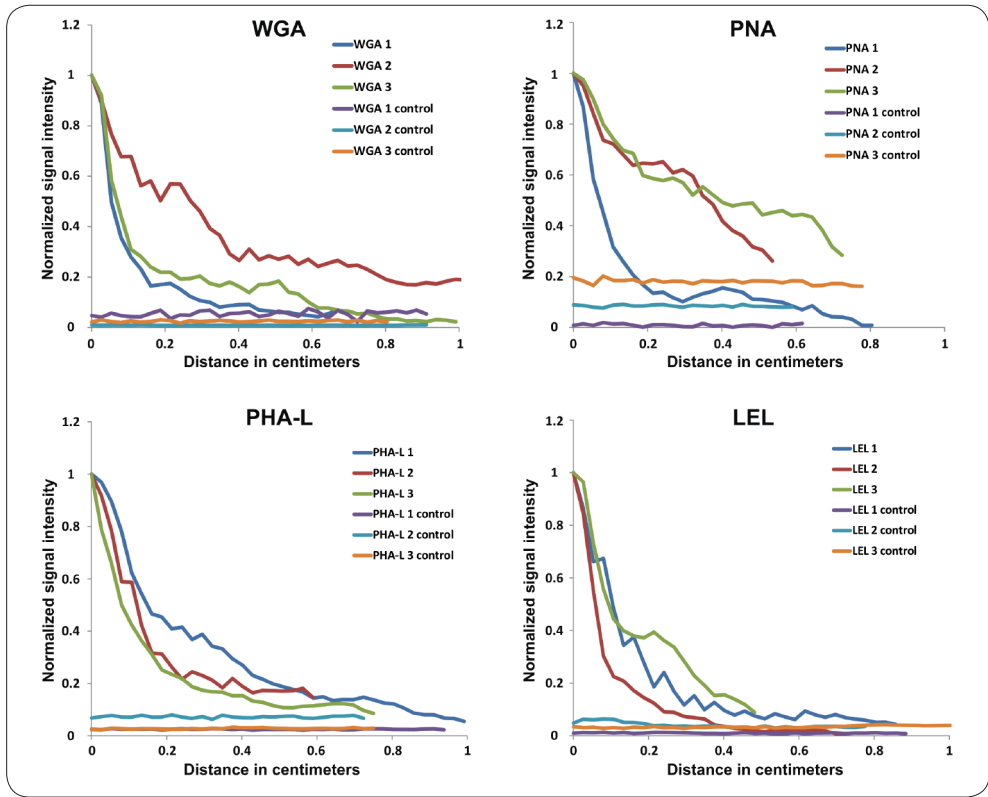


**Figure 4. Migration curves.** Normalized curves of (A) WGA, (B) PNA, (C) PHA-L and (D) LEL show the migration of the lectins along the individual nerves. On the y-axis the normalized intensity signal is depicted, on the x-axis the migration distance (cm).

## Signal Intensity

*In vivo* visualization efficacy depends on the intensity of the fluorescence signal emitted by the nerve-bound lectins and the difference between the signal in the nerve and the surrounding tissue.

The degree of visibility of the individual nerves was determined by calculating the SBR in the lectin-stained nerve compared to the control nerve (SBR control; Table 2). The SBR of Cy5 labeled WGA and LEL was shown to be 1.1 to 2.8-fold higher than the ratio found for PNA and PHA-L. The SBR between the signal in the nerve and the signal in the control muscle tissue (SBR muscle; Table 2) reveals how well a stained nerve can be potentially detected when surrounded by non-stained tissue. With WGA a ratio of 1.86 was obtained while with LEL and PHA-L SBR values of 1.26 and 1.12 were found respectively (Table 2). Based on the assumption that a SBR of approximately 2 is desirable for efficient *in vivo* visualization [37], it can be concluded that WGA would be the most effective imaging agent in this setting.

	WGA	PNA	PHA-L	LEL
Average migration distance (cm) (SD)	0.95 (0.20)	0.72 (0.13)	0.81 (0.20)	0.72 (0.20)
SBR nerve <sub>control</sub> (Average + SD)	2.08 (1.11)	1.72 (0.32)	1.86 (0.70)	4.88 (2.48)
SBR nerve <sub>muscle</sub> (Average + SD)	1.86 (1.00)	1.42 (0.12)	1.12 (0.13)	1.26 (0.46)
SBR <sub>ipsilateral lymph node</sub> (Average + SD)	0.61 (0.26)	0.70 (0.06)	3.73 (1.36)	1.11 (0.87)
SBR <sub>contralateral lymph node</sub> (Average + SD)	0.45 (0.42)	0.55 (0.17)	0.79 (0.33)	0.86 (0.62)

**Table 2. Migration distance and signal to background ratios.**

SD = Standard deviation; cm = centimeters; SBR = signal to background ratio.

### Alternative Drainage Routes

After local injection, edema is created at the site of injection. As a result, part of the injected volume may be transported through the lymphatic system to the lymph nodes (Figure 3A). Since in this experiment the aim was to achieve maximal selective staining of the nerves, such distribution via the lymphatics was unwanted. To determine the degree of lymphatic clearance through the lymphatic system, the SBR between the fluorescence signal in the nerve and inguinal lymph nodes (LN) was calculated (signal nerve/signal LN; Table 2). The SBR between the fluorescence signal in the ipsilateral lymph node and the injection site was shown to be higher for LEL and PHA-L, compared to WGA and PNA. Similar results were obtained when comparing the fluorescence signal in the injection site and the contralateral inguinal lymph node. Although the lymphatic drainage makes lectins like PHA-L (SBR = 3.73) candidates for sentinel node imaging, the lower degree of lymphatic clearance of WGA and PNA makes these two compounds more suitable for nerve specific staining.

### Evaluation of Binding Mode

Staining of a nerve by fluorescent-labeled lectins is influenced by the availability and accessibility of PGs (See Table 1). Peripheral nerves, such as the sciatic nerve, are surrounded by a dense layer of connective tissue. This layer, the epineurium, encloses multiple nerve fascicles as well as fatty tissue and blood vessels. Smaller branches of these blood vessels penetrate into the perineurium, a protective sheath serving as blood-nerve barrier that surrounds the different fascicles. Within these fascicles, nerve fibers are bundled together. Each fiber is again surrounded by its own protective layer (the endoneurium; a thin layer of connective tissue) that encloses individual axons (Figure 5) [4,38].

To assess the binding mode of the individual lectins after local *in vivo* injection, the nerves were analyzed *ex vivo* using fluorescence confocal microscopy. This experiment demonstrated that in all cases, after intramuscular injection, a Cy5 signal could be detected at the location of the epineurium throughout the course of the nerve. The epineurium, which consists out of collagen type 1 (connective tissue), expresses the sugar moieties targeted by the different lectins (Table 1) [39,40].

For all lectins, the intensity of the staining was the highest at the distal side of the nerve (also representing the injection site, Figure 6A). While fluorescence could still be detected in the middle part (Figure 6B) and the proximal part of the nerve (Figure 6C), the intensity of the signal decreased at longer migration distances. The latter is in agreement with the findings shown in Figure 4, which illustrates a gradual decrease in signal along the course of the nerve.

To determine if the migration process influences the binding of the lectin-analogues, nerves were also stained *ex vivo*. To this end, excised nerves were placed in a solution containing (one of) the Cy5-labeled lectins. By doing so, exposure to the imaging agent may not be limited to the epineurium. This, however, resulted in a highly similar staining pattern compared to which is observed after *in vivo* incubation (Figure 7); Staining of the epineurium and not of other structures within the nerve (e.g. the axons) was observed. As staining of the epineurium will not affect the signal conduction within the nerve and the neurons itself, this feature can be considered favorable for *in vivo* use. This may also provide an advantage over neuronal tracing using neurotoxins [15].

Previous studies have shown that CSPG and HSPG are present on the endoneurium, epineurium and perineurium (Figure 5) of the peripheral nerves [41,42]. WGA the best binding lectin in this study was shown to have the highest affinity for HSPG, KSPG and HP [23–25,43]. However, the lectins PHA-L and LEL share its affinity for HSPG (see Table 1). For that reason, something other than the affinity for HSPG seems to drive the difference in migration. Most likely, the size of the lectin is a determining factor during the migration, where smaller molecules show increased migration speed. As shown in Table 1 and Figure 1, WGA is the smallest of the lectins evaluated; it only consists out of two subunits, while PHA-L and PNA consist out of four subunits (structure of LEL is unknown, see above).

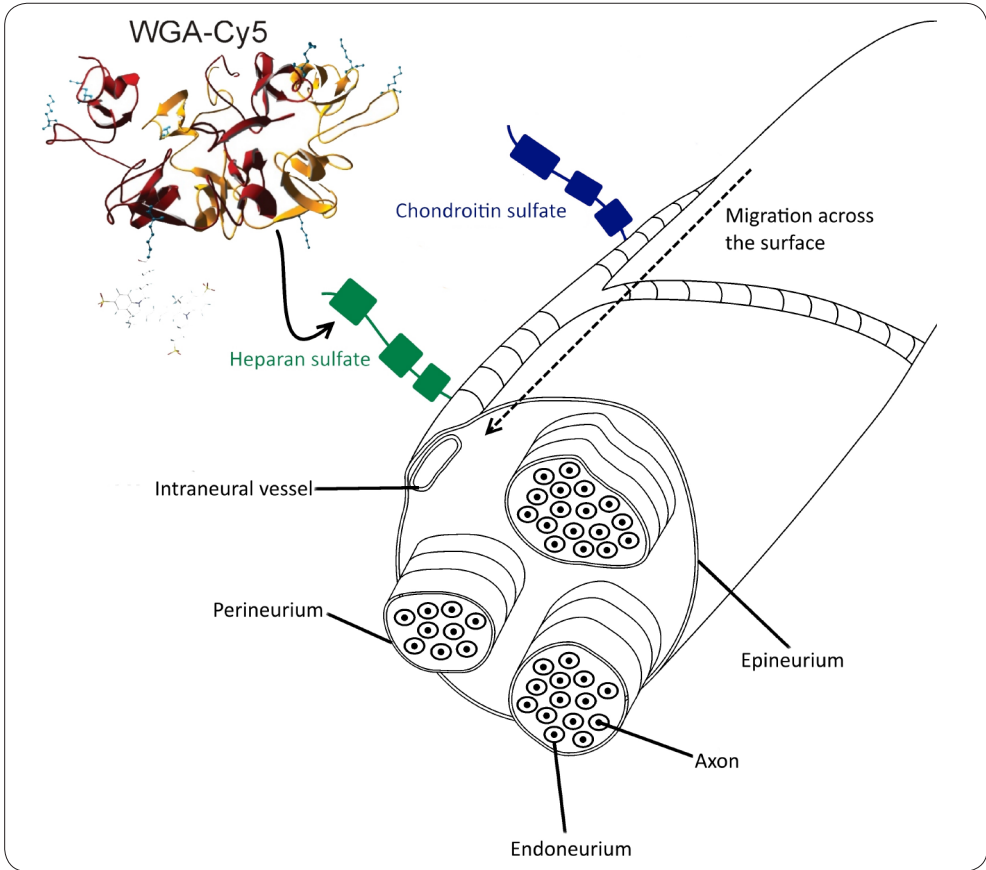


**Figure 5.** Schematic overview peripheral nerve wherein Cy5/ WGA lectin binds to PG's located on the epineurium and extracellular matrix.

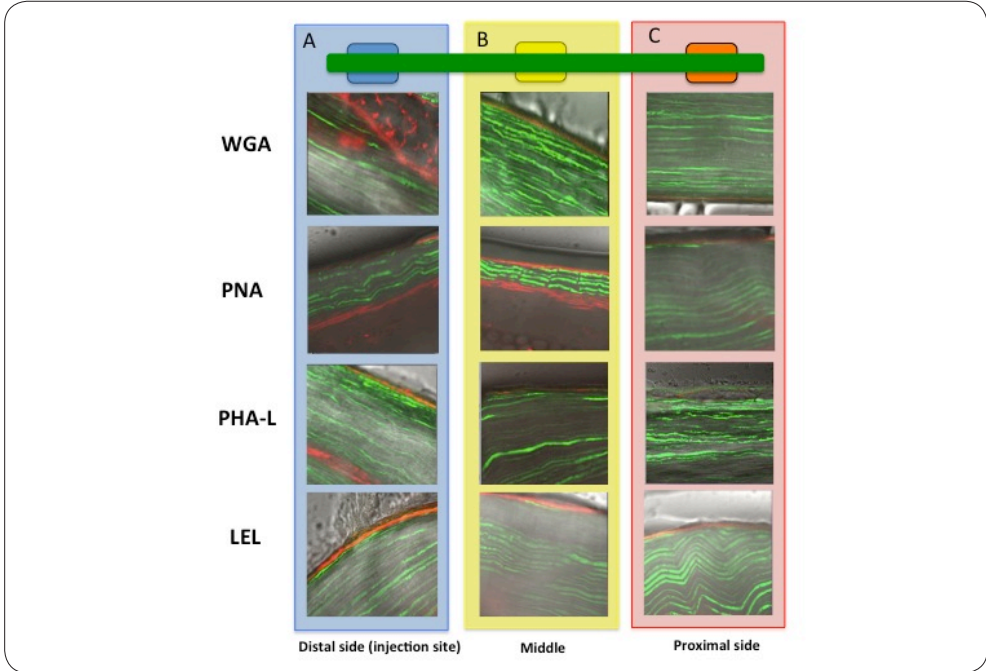


**Figure 6. Binding mode after in vivo local administration.**

The fluorescence signal in nerves from Thy-1 YFP mice (YFP in green and Cy5 in red) was traced from (A) the injection site to (B) the middle and (C) the proximal side of the nerve. In all cases, staining of the epineurium was observed with a decrease in signal when the distance from the injection site increased.

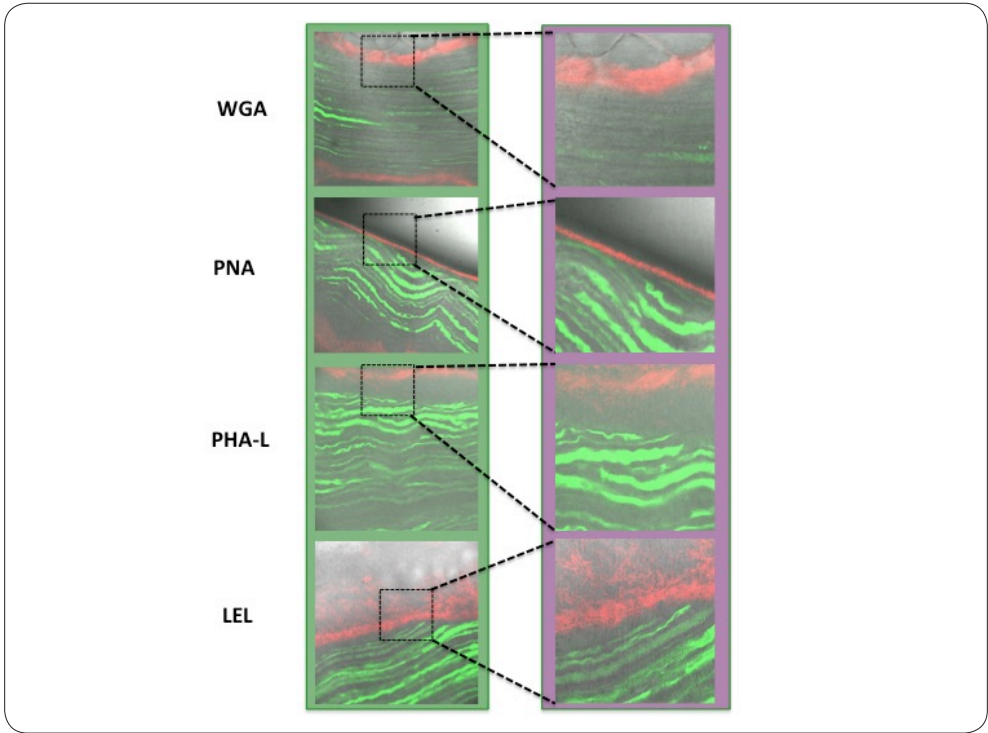


**Figure 7. Ex vivo incubation.**

Ex vivo incubation confirmed the in vivo localization of staining. (YFP in green and Cy5 in red)

## EXPERIMENTAL SECTION

### Experimental Equipment

The fluorescent dye Cy5 was purified with an HPLC 1525 Pump and 2489 UV/vis detector (Waters, Etten-Leur, The Netherlands), using a Reprosil-Pur 120 C18-AQ 10  $\mu\text{m}$  column (Dr. Maisch GmbH, Ammerbuch-Entringen, Germany) using a 60 min gradient of H<sub>2</sub>O/MeCN (0.1% TFA) 95:5 – 5:95. Reaction mixtures were filtered using 10K Amicon Ultra-0.5 mL Centrifugal Filters (Merck Millipore, Billerica, MA, USA). Centrifugation was performed with an Eppendorf 5415D centrifuge (Eppendorf Nederland B.V., Nijmegen, The Netherlands). Absorption was measured with a Nanodrop ND-1000 spectrophotometer (Thermo Scientific, Wilmington, DE, USA). Protein figures were made using SwissProt PDB viewer and Adobe Illustrator CS6 (Adobe Systems Inc., San Jose, CA, USA). The WGA, PNA, PHA-L lectins were purchased from Sigma Aldrich (St. Louis, MO, USA). The LEL lectin was purchased from Vector Laboratories Inc. (Burlingame, CA, USA).

An IVIS Spectrum animal fluorescence scanner (Perkin Elmer, Waltham, MA, USA) was used for evaluation of *in vivo* migration. The acquired IVIS data was analyzed with Living Imaging Acquisition and Analysis software. Furthermore, for analysis of migration and intensity signals in the nerves, the raw IVIS data was analyzed with MATLAB software (Mathworks Inc., Torrance, CA, USA). An SP5 Confocal Microscope (Leica Microscopes B.V., Rijswijk, The Netherlands) was used for fluorescence confocal microscopy. Nerve tissue was placed on glass bottom dishes ( $\varnothing$  35 mm dish, No. 1.5,  $\varnothing$  14 mm glass surface, MatTek, Ashland, MA, USA) prior to imaging. Confocal images were acquired with Leica LAS AF software. Statistical analysis was performed with SPSS Statistics data analysis (Version 20, SPSS Inc., Chicago, IL, US).

### Synthesis of Sulphonated Cy5-OSu

Sulphonated Cy5 was synthesized according to previously described methods [44]. The OSu activation was performed in DMSO (800  $\mu\text{L}$ ), using HSPyU (5 eq) and DIPEA (10 eq). After completion of the reaction, water (0.1% TFA) was added (3.2 mL) and the mixture was purified by RP-HPLC. The collected fractions were lyophilized and a dark blue solid (Sulphonated Cy5-OSu) was obtained (28.1 mg, 46%). MS MALDI-TOF Calculated: m/z 860.0, found: m/z 862.8. Of this dark blue solid a stock solution was prepared (0.97 mM in DMSO).

### General Conjugation Procedure

WGA (Figure 1A), PHA-L (Figure 1B) and PNA (Figure 1C), and LEL were each dissolved in 200  $\mu$ L of 0.1 M phosphate buffer pH 8.4 and Cy5-OSu stock solution was added. The aim was to achieve a labeling ratio of 1–1.5 fluorophores per lectin. The necessary equivalents of dye per lectin were calculated using Equation (1) and the labeling ratios that were determined by a test-conjugation (Table 3). The test-conjugation was performed to determine how many equivalents of fluorophore were necessary to achieve the optimal labeling ratio. As a starting point, 5 equivalents of fluorophore were used and the ratios were calculated according to Equations (2-4). The obtained ratios were inserted in formula 1 and the appropriate amounts of equivalents calculated. Note: the compounds obtained during the test-conjugations were not used for further experiments. The reaction was repeated with the calculated equivalents of fluorophore (Table 4) and the reaction mixture was gently stirred at room temperature for 2 hours. Hereafter, the mixture was transferred to a 10KD cut-off filter (Amicon) and centrifuged at 14.000 G. Saline (400  $\mu$ L) was added and the mixture was again centrifuged, this was repeated until the filtrate was colorless. Subsequently, the residue (blue liquid) was collected.

Equation (1): Calculation of needed equivalents of fluorophore

$$\text{Equivalents dye/lectin} = \left( \frac{\text{Desired labeling ratio}}{\text{Labeling ratio from test conjugation}} \right) \times 5 \text{ equivalents}$$

Equation (2): Fluorophore concentration

$$\text{Concentration fluorophore} = \left( \frac{\text{Measured absorption}}{250\,000 \times 0.1} \right) \times 100$$

	WGA	PNA	PHA-L	LEL
Labeling ratio from test-conjugation	1.08	1.25	0.75	1.48
Amount of lectin (nmol)	27.8	9.1	4.2	14.1
Amount of fluorophore (nmol)	191.8	54.6	35.3	70.5
Equivalents of dye/lectin	6.9	6.0	9.9	5.0

**Table 3. Amounts used for final conjugation.**

	WGA	PNA	PHA-L	LEL
Measured absorption	0.068	0.019	0.008	0.028
Fluorophore concentration (nmol/μL)	0.272	0.076	0.032	0.112
Total sample volume (μL)	139	139	128	150
Total amount of fluorophore (nmol)	37.81	10.56	4.10	16.80
Total amount of lectin (nmol)	27.80	9.10	4.15	14.10

**Table 4. Calculation data.**

Equation (3): Amount of fluorophore

$$\text{Total amount of fluorophore} = \text{Concentration fluorophore} \times \text{Total sample volume}$$

Equation (4): Labeling ratio

$$\text{Labeling ratio} = \frac{\text{Total amount of fluorophore}}{\text{Total amount of lectin}}$$

### Labeling Ratio Analysis

The samples were diluted 100× and 2 μL of each sample was used for the absorption spectroscopy measurement (Nanodrop). The labeling ratio was calculated according to the following equations, using and/or generating the data in Table 3.

### *In vivo* Distribution

To study the *in vivo* distribution of the lectins, Thy1-YFP mice were used (n = 12). In these genetically modified mice, neurons are fluorescently labeled with YFP. The YFP signal can be used as an internal control regarding the location of (peripheral) nerves. Per animal, 20

$\mu\text{L}$  (32  $\mu\text{M}$  lectin-Cy5) was injected in the thigh muscle and the injection was aimed for the sciatic nerve (Figure 1A). All animals tolerated the lectin injections without evidence for systemic toxicity; this is in concordance with previous literature where lectins were injected in the fore limb [17]. Animal experiments were conducted according to Dutch law and after approval was obtained from the institutional animal ethics committee.

Twenty-four hours after injection, the animal was sacrificed, whereafter fluorescence imaging with IVIS was performed to visualize the distribution of the lectins throughout the sciatic nerve. The contralateral side was taken as a negative control. Fluorescence images were acquired with Cy5 filter settings ( $\lambda$  ex max, 640 nm;  $\lambda$  em max, 680 nm), while the YFP signal was measured at  $\lambda$  ex max, 465 nm and  $\lambda$  em max, 520 nm. To depict the staining sites and locations, the nerves in mice were imaged three times with the IVIS, first with intact skin, second with the skin removed and last with the muscle structures surrounding the nerve removed. Both the injection site nerve and the control nerve were collected from the mice for *ex vivo* imaging. The fluorescence signal in the inguinal lymph nodes was analyzed to study the migration of the lectins through the lymphatic system (Figure 3A). Both the ipsilateral and the contralateral inguinal lymph nodes were removed for analysis.

The measured intensities (photons/s/cm<sup>2</sup>/sr) were quantified by Living Imaging Acquisition and Analysis software. The total flux (photons/s/cm<sup>2</sup>/sr) in the nerves was measured by drawing a region of interest around both nerves. The signal to background ratios were measured by: a) dividing the signal of the injection site nerve by the control nerve and b) dividing the signal of the injection site nerve by the signal in the surrounding muscle tissue on the contralateral side.

MATLAB software was used to generate a signal profile along the sciatic nerve (injection site and control), based on the raw IVIS data. A virtual pixel-wide line was drawn along the *ex vivo* sciatic nerve to measure the signal intensity. The counts measured and generated by the software were converted into a normalized curve for all the experiments. The maximum of these curves was determined as the site of injection and the normalization was done by setting the peak corresponding to the Cy5 fluorescent signal along the injection nerve, at  $y = 1$ . From punctum maximum ( $y = 1$ ), the length of the curve over the x-axis was measured in pixels, and thereafter converted into centimeters. A signal (curve) higher than the control nerve signal was designated as fluorescent signal in the nerve (Figure 4). With this technique, the migration of the x-axis in number of pixels (0.0268 cm per pixel) was calculated. The average migration distance of all lectins were compared using a Kruskal Wallis test, a p-value of  $< 0.05$  is accepted as statistical significance.

### ***Ex vivo* Incubation and Fluorescence Confocal Microscopy**

The location of the signal was analyzed using fluorescence confocal imaging. Nerves were assessed after local injection and the control nerves were used for *ex vivo* incubation (1 h) experiments. For analysis with confocal microscopy, the nerves were washed with PBS after the incubation and placed on glass bottom dishes, which were mounted on the confocal microscope. YFP was excited with a 488 nm laser and emission was detected between 520 nm and 550 nm. Cy5 was excited with a 633 nm laser and emission was detected between 650 nm and 700 nm. The location of the lectin was assessed with the Cy5 signal in/on the nerve.

### **CONCLUSION**

Fluorescent lectins were shown to be potential candidates for *in vivo* visualization of the peripheral nerves. Using local administration, WGA was shown to have the best properties of the four different lectins tested. Since all four lectins only showed staining in the nerve epineurium, the chance of inducing systemic toxic side effects after administration of these agents will be limited.

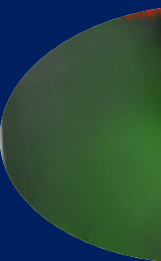
## REFERENCES

1. Mauroy, B.; Demondion, X.; Drizenko, A.; Gouillet, E.; Bonnal, J.L.; Biserte, J.; Abbou, C. The inferior hypogastric plexus (pelvic plexus): Its importance in neural preservation techniques. *Surg. Radiol. Anat.* 2003, 25, 6–15.
2. Stelzner, S.; Holm, T.; Moran, B.J.; Heald, R.J.; Witzigmann, H.; Zorenkov, D.; Wedel, T. Deep pelvic anatomy revisited for a description of crucial steps in extralevator abdominoperineal excision for rectal cancer. *Dis. Colon. Rectum.* 2011, 54, 947–957.
3. Tewari, A.K.; Srivastava, A.; Huang, M.W.; Robinson, B.D.; Shevchuk, M.M.; Durand, M.; Sooriakumaran P.; Grover S.; Yadav R.; Mishra N.; Mohan S.; Brooks D.C.; Shaikh N.; Khanna A.; Leung R. Anatomical grades of nerve sparing: A risk-stratified approach to neural-hammock sparing during robot-assisted radical prostatectomy (RARP). *BJU Int.* 2011, 108, 984–992.
4. Pfister, B.J.; Gordon, T.; Loverde, J.R.; Kochar, A.S.; Mackinnon, S.E.; Cullen, D.K. Biomedical engineering strategies for peripheral nerve repair: Surgical applications, state of the art, and future challenges. *Crit. Rev. Biomed. Eng.* 2011, 39, 81–124.
5. Myssiorek, D. Recurrent laryngeal nerve paralysis: Anatomy and etiology. *Otolaryngol. Clin. North. Am.* 2004, 37, 25–44.
6. Wei, J.T.; Dunn, R.L.; Marcovich, R.; Montie, J.E.; Sanda, M.G. Prospective assessment of patient reported urinary continence after radical prostatectomy. *J. Urol.* 2000, 164, 744–748.
7. Guntinas-Lichius, O. The facial nerve in the presence of a head and neck neoplasm: Assessment and outcome after surgical management. *Curr. Opin. Otolaryngol. Head Neck Surg.* 2004, 12, 133–141.
8. Polom, K.; Murawa, D.; Rho, Y.S.; Nowaczyk, P.; Hünerbein, M.; Murawa, P. Current trends and emerging future of indocyanine green usage in surgery and oncology: A literature review. *Cancer* 2011, 117, 4812–4822.
9. Van der Poel, H.G.; Buckle, T.; Brouwer, O.R.; Valdés Olmos, R.A.; van Leeuwen, F.W.B. Intraoperative laparoscopic fluorescence guidance to the sentinel lymph node in prostate cancer patients: Clinical proof of concept of an integrated functional imaging approach using a multimodal tracer. *Eur. Urol.* 2011, 60, 826–833.
10. Brouwer, O.R.; van den Berg, N.S.; Mathéron, H.M.; van der Poel, H.G.; van Rhijn, B.W.; Bex, A.; van Tinteren H.; Valdés Olmos R.A.; van Leeuwen F.W.; Horenblas S. A hybrid radioactive and fluorescent tracer for sentinel node biopsy in penile carcinoma as a potential replacement for blue dye. *Eur. Urol.* 2014, 65, 600–609.
11. Gibbs-Strauss, S.L.; Nasr, K.A.; Fish, K.M.; Khullar, O.; Ashitate, Y.; Siclovan, T.M.; Johnson B.F.; Barnhardt N.E.; Tan Hehir C.A.; Frangioni J.V. Nerve-highlighting fluorescent contrast agents for image-guided surgery. *Mol. Imaging.* 2011, 10, 91–101.
12. Kuil, J.; Buckle, T.; Oldenburg, J.; Yuan, H.; Borowsky, A.D.; Josephson, L.; van Leeuwen F.W. Hybrid peptide dendrimers for imaging of chemokine receptor 4 (CXCR4) expression. *Mol. Pharm.* 2011, 8, 2444–2532
13. Bunschoten, A.; Buckle, T.; Visser, N.L.; Kuil, J.; Yuan, H.; Josephson, L.; Vahrmeijer A.L.; van Leeuwen F.W. Multimodal interventional molecular imaging of tumor margins and distant metastases by targeting  $\alpha$  v  $\beta$  3 integrin. *Chembiochem* 2012, 13, 1039–1045.
14. Whitney, M.A.; Crisp, J.L.; Nguyen, L.T.; Friedman, B.; Gross, L.A.; Steinbach, P.; Tsien R.Y.; Nguyen Q.T. Fluorescent peptides highlight peripheral nerves during surgery in mice. *Nat. Biotechnol.* 2011, 29, 352–356.
15. Schellingerhout, D.; le Roux, L.G.; Bredow, S.; Gelovani, J.G. Fluorescence imaging of fast retrograde axonal transport in living animals. *Mol. Imaging.* 2009, 8, 319–329.
16. Streit, W.J.; Schulte, B.A.; Balentine, D.J.; Spicer, S.S. Histochemical localization of galactose-containing glycoconjugates in sensory neurons and their processes in the central and peripheral nervous system of the rat. *J. Histochem. Cytochem.* 1985, 33, 1042–1052.
17. Borges, L.F.; Sidman, R.L. Axonal transport of lectins in the peripheral nervous system. *J. Neurosci.* 1982, 2, 647–653.
18. Zhou, C.J.; Kawabuchi, M.; He, J.W.; Kuraoka, A.; Hirata, K.; Wang, S.; Nada O. Changes in the distribution of peanut agglutinin (PNA) binding molecules during muscle reinnervation following nerve crush injury. *Arch. Histol. Cytol.* 1999, 62, 261–272.
19. Gerfen, C.R.; Sawchenko, P.E. An anterograde neuroanatomical tracing method that shows the detailed morphology of neurons, their axons and terminals: Immunohistochemical localization of an axonally transported plant lectin, Phaseolus vulgaris leucoagglutinin (PHA-L). *Brain Res.* 1984, 290, 219–238.
20. Roth, J.; Binder, M.; Gerhard, U.J. Conjugation of lectins with fluorochromes: An approach to histochemical double labeling of carbohydrate components. *Histochemistry* 1978, 56, 265–273.

21. Shehab, S.A.S.; Hughes, D.I. Simultaneous identification of unmyelinated and myelinated primary somatic afferents by co-injection of isolectin B4 and Cholera toxin subunit B into the sciatic nerve of the rat. *J. Neurosci. Methods* 2011, 198, 213–221.
22. Mislovicová, D.; Gemeiner, P.; Kozarova, A.; Kožár, T.; Lectinomics, I. Relevance of exogenous plant lectins in biomedical diagnostics. *Biologia* 2009, 64, 1–19.
23. Ruoslahti, E. Structure and biology of proteoglycans. *Ann. Rev. Cell. Biol.* 1988, 4, 229–255.
24. Scott, J.E. Proteoglycan-fibrillar collagen interactions. *Biochem. J.* 1988, 252, 313–323.
25. Reitsma, S.; Slaaf, D.W.; Vink, H.; van Zandvoort, M.A.J.M.; Oude Egbrink, M.G.A. The endothelial glycocalyx: Composition, functions, and visualization. *Pflugers Arch. Eur. J. Physiol.* 2007, 454, 345–359.
26. Schwefel, D.; Maierhofer, C.; Beck, J.G.; Seeberger, S.; Diederichs, K.; Moller, H.M.; Welte, W.; Wittman, V. Structural basis of multivalent binding to wheat germ agglutinin. *J. Am. Chem. Soc.* 2010, 132, 8704–8719.
27. Natchiar, S.K.; Srinivas, O.; Mitra, N.; Suroliá, A.; Jayaraman, N.; Vijayan, M. Structural studies on peanut lectin complexed with disaccharides involving different linkages: Further insights into the structure and interactions of the lectin. *Acta Crystallogr. Sect. D: Biol. Crystallogr.* 2006, 62, 1413–1421.
28. Hamelryck, T.W.; Dao-Thi, M.H.; Poortmans, F.; Chrispeels, M.J.; Wyns, L.; Loris, R. The crystallographic structure of phytohemagglutinin-L. *J. Biol. Chem.* 1996, 271, 20479–20485.
29. Burggraaf, J.; Kamerling I.M.C.; Gordon P.B.; Schrier L.; De Kam M.L.; Kales A. J.; Bendixsen r.; Indrevoll B.; Bjerke R.M.; Moestue S. A.; Yazdanfar S.; Langers A.M.J.; Swaerd-Nordmo M.; Torheim G.; Warren M.V.; Morreau H.; Dalsgaard G.T.; Voorneveld P.W.; Buckle T.; van Leeuwen F.W.B.; Ødegårdstuen L.L.; Healey A.; Hardwick J.C.H. Detection of colorectal neoplasia in vivo in humans using an intravenously administered fluorescent peptide targeted against c-Met and fluorescent colonoscopy; a proof of concept study. *Nature Med.* 2014; accepted for publishing
30. Stryer, L. Fluorescence energy transfer as a spectroscopic ruler. *Annu. Rev. Biochem.* 1978, 47, 819–846.
31. Nieweg, O.E.; Tanis, P.J.; Kroon, B.B. The definition of a sentinel node. *Ann. Surg. Oncol.* 2001, 8, 538–541.
32. KleinJan, G.H.; Bunschoten, A.; Brouwer, O.R.; Berg, N.S.; Valdés-Olmos, R.A.; Leeuwen, F.W.B. Multimodal imaging in radioguided surgery. *Clin. Transl. Imaging.* 2013, 1, 433–444.
33. Stoffels, I.; Poeppel, T.; Boy, C.; Mueller, S.; Wichmann, F.; Dissemond, J.; Schadendorf D.; Rosenbaum-Krumme S.; Klode J. Radio-guided surgery: Advantages of a new portable  $\gamma$ -camera (Sentinella) for intraoperative real time imaging and detection of sentinel lymph nodes in cutaneous malignancies. *J. Eur. Acad. Dermatol. Venereol.* 2012, 26, 308–313.
34. Vermeeren, L.; Valdés Olmos, R.A.; Meinhardt, W.; Horenblas, S. Intraoperative imaging for sentinel node identification in prostate carcinoma: Its use in combination with other techniques. *J. Nucl. Med.* 2011, 52, 741–744.
35. Brouwer, O.R.; Klop, W.M.C.; Buckle, T.; Vermeeren, L.; van den Brekel, M.W.M.; Balm, A.J.M.; Nieweg O.E.; Valdés Olmos R.A.; van Leeuwen F.W. Feasibility of sentinel node biopsy in head and neck melanoma using a hybrid radioactive and fluorescent tracer. *Ann. Surg. Oncol.* 2012, 19, 1988–1994.
36. Van den Berg, N.S.; Brouwer, O.R.; Klop, W.M.; Karakullukcu, B.; Zuur, C.L.; Tan, I.B.; Balm A.J.; van den Brekel M.W.; Valdés Olmos R.A.; van Leeuwen F.W. Concomitant radio-and fluorescence-guided sentinel lymph node biopsy in squamous cell carcinoma of the oral cavity using ICG-(99m)Tc-nanocolloid. *Eur. J. Nucl. Med. Mol. Imaging.* 2012, 39, 1128–1136.
37. Buckle, T.; Chin, P.T.K.; van den Berg, N.S.; Loo, C.E.; Koops, W.; Gilhuijs, K.G.A.; van Leeuwen F.W. Tumor bracketing and safety margin estimation using multimodal marker seeds: A proof of concept. *J. Biomed. Opt.* 2010, 15, 056021.
38. Maravilla, K.R.; Bowen, B.C. Imaging of the peripheral nervous system: Evaluation of peripheral neuropathy and plexopathy. *AJNR Am. J. Neuroradiol.* 1998, 19, 1011–1023.
39. Kostrominova, T.Y. Application of WGA lectin staining for visualization of the connective tissue in skeletal muscle, bone, and ligament/tendon studies. *Microsc. Res. Tech.* 2011, 74, 18–22.
40. Kaemmer, D.; Bozkurt, A.; Otto, J.; Junge, K.; Klink, C.; Weis, J.; Sellhaus B.; O'Dey D.M.; Pallua N.; Jansen M.; Schumpelick V.; Klinge U. Evaluation of tissue components in the peripheral nervous system using Sirius red staining and immunohistochemistry: A comparative study (human, pig, rat). *J. Neurosci. Methods* 2010, 190, 112–116.
41. Aquino, D.A.; Margolis, R.U.; Margolis, R.K. Immunocytochemical localization of a chondroitin sulfate proteoglycan in nervous tissue. I. Adult brain, retina, and peripheral nerve. *J. Cell. Biol.* 1984, 99, 1117–1129.
42. Carey, D.J.; Stahl, R.C.; Asundi, V.K.; Tucker, B. Processing and subcellular distribution of the Schwann cell lipid-anchored heparan sulfate proteoglycan and identification as glypican. *Exp. Cell. Res.* 1993, 208, 10–18.

43. Hoedt-Schmidt, S.; McClure, J.; Jasani, M.K.; Kalbhen, D.A. Immunohistochemical localization of articular cartilage proteoglycan and link protein in situ using monoclonal antibodies and lectin-binding methods. *Histochemistry* 1993, 99, 391–403.
44. Mujumdar, R.B.; Ernst, L.A.; Mujumdar, S.R.; Lewis, C.J.; Waggoner, A.S. Cyanine dye labeling reagents: Sulfoindocyanine succinimidyl esters. *Bioconjug Chem.* 1993, 4, 105–111.

# Chapter 13



# Future perspectives

1

2

3

4

5

6

7

8

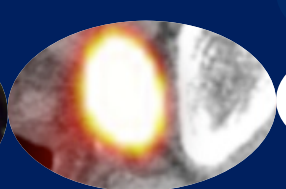
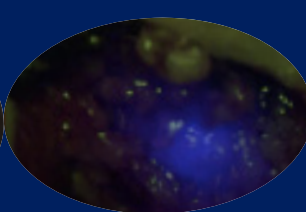
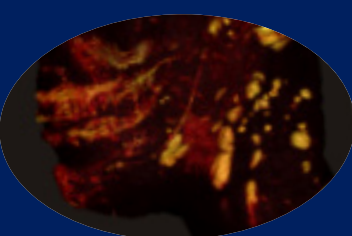
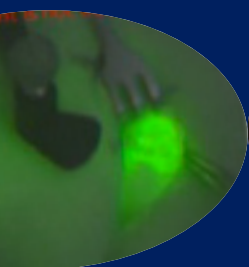
9

10

11

12

**13**



## SUMMARY

The studies described in this thesis illustrate the value of surgical guidance techniques and their further refinement.

In **part one** the focus is placed on intraoperative identification of lesions (in this case sentinel nodes) that need to be resected. Here the benefits of the hybrid surgical guidance concept, which combines radio- and fluorescence-guidance, are illustrated.

The review presented in **chapter 2** discusses the most common radioguided surgery approaches. The possibilities of different, clinically used radioactive tracers and their potential hybrid (radioactive and fluorescent) derivatives are reported on. Furthermore, the various imaging devices designed for radioactivity-based detection are briefly reviewed in the context of generating hybrid-imaging modalities.

In **chapter 3** the results of the clinical use of the hybrid tracer ICG-<sup>99</sup>mTc-nanocolloid in 501 procedures performed for different malignancies (skin malignancies (n= 191), vulva cancer (n= 21), penile cancer (n=192), oral cavity (n=51) and prostate cancer (n=40)) are discussed on. In this population 1643 SNs were identified based on the combination of gamma tracing (>98%) and fluorescence (>95%) optical detection. Intraoperative SN detection rates using fluorescence guidance proved to be superior to those of blue dye detection (22-78%). Follow-up revealed that use of the hybrid tracer did not negatively influence the false negative rates and outcome values. This study proved that with the use of ICG-<sup>99</sup>mTc-nanocolloid the radio- and optical guidance during SN biopsy procedure has become universal for different malignancies and anatomical locations.

In **chapter 4** is demonstrated how an increase in sensitivity and the introduction of anatomical context helped to improve the fluorescence detection of a clinically applied fluorescence laparoscope. This concept was studied in three patient groups of prostate cancer patients scheduled for sentinel biopsy using ICG-<sup>99</sup>mTc-nanocolloid. In the first group of prostate cancer patients (n=11) scheduled for SN biopsy the standard used concentration of ICG-<sup>99</sup>mTc-nanocolloid was used in combination with a standard used fluorescence laparoscope. In the second group (n=13) the concentration and volume of ICG-<sup>99</sup>mTc-nanocolloid were optimized and in the third group (n=16) an improved fluorescence laparoscope was introduced. Mean fluorescence-based SN identification improved from 63.7% (group 1) to 85.2% and 93.5% for groups 2 and 3, respectively (p=0.012).

Chapter 5 describes a study in 55 prostate cancer patients (Briganti nomogram-based risk >5 % on LN metastases) wherein the robot-integrated Firefly fluorescence laparoscope was used to provide guidance during robot-assisted radical prostatectomy, SN biopsy and extended pelvic lymph node dissection. Intraoperative fluorescence imaging using standard fluorescence settings visualized 80.4% (148/184SNs; 50 patients; *ex vivo* 97.8%); SPECT/CT images provided guidance towards the residual SNs. By integrating the fluorescence laparoscope directly into the robotic surgical system a direct link between the preoperative nuclear SPECT imaging information and intraoperative fluorescence detection of SNs was realized.

**Chapter 6** evaluated what the relation is between the amount of hybrid tracer (ICG-<sup>99m</sup>Tc-nanocolloid) that had collected in sentinel nodes and their intraoperative identification rates using fluorescence guidance. Intraoperative fluorescence detection findings were derived from a retrospective analysis of 20 head-and-neck melanoma patients, 40 penile and 20 prostate cancer patients scheduled for SN biopsy using ICG-<sup>99m</sup>Tc-nanocolloid. The % of migrated hybrid tracer could be correlated directly to the amount of ICG (range: 0.003–10.8 nmol) and the concentration of ICG (range: 0.006–64.6 μM) in a SN. The study indicates that intraoperative fluorescence detection with ICG is possible when higher than a 0.006 μM concentration.

Part two describes the use of surgical modalities that are used in the hybrid surgical concept. In **chapter 7** the value of a hybrid detection modalities that intergrade radio- and fluorescence imaging functions were assessed in a total of eleven penile cancer patients scheduled for SN biopsy. Two different hybrid detection modalities were created by combining a gamma –ray detection probe (GP) or a gamma camera (GC) with a fluorescence exoscope that allows fluorescence imaging in an open surgery setting. Both combined modalities were evaluated in respectively five and six penile cancer patients during SN biopsy procedures using ICG-<sup>99m</sup>Tc-nanocolloid. To assess the sensitivity of the individual modalities in this set-up, intraoperatively, radio- and fluorescence guided SN detection rates were scored at working distances of 0, 10, 20, and 30 cm. These comparisons indicated that the detection modalities work synergistically; overall the GC was most valuable for rough localization (10–30 cm range) of the SNs, the GP for providing convenient real-time acoustic feedback, while fluorescence guidance allowed detailed real-time SN visualization.

**Chapter 8** describes the feasibility, in five penile cancer patients injected with ICG-<sup>99m</sup>Tc-nanocolloid, of a nuclear medicine–based navigation concept that allowed intraoperative positioning of a fluorescence camera based on preoperative SPECT/CT images. The navigation device was used to provide a real-time augmented reality overlay of the SPECT/CT images and video output of the fluorescence camera. Navigation was successful for all 12 intraoperatively evaluated SNs (average error, 8.8 mm; range, 0–20 mm). These results are promising for future surgical application, where localization of lesions could be rather complicated, e.g. of SNs located in the pelvic area.

In **chapter 9**, in eight patients with melanoma located in the head and neck area, SNs were located based on freehandSPECT navigation. Using this approach 87% of SNs could be navigated to based on the freehandSPECT generated 3D image and could be resected under fluorescence guidance. Fluorescence imaging allowed for the identification of the SNs, which could not be identified using navigation. In addition fluorescence imaging provided optical confirmation of the navigation accuracy in all patients. The use of gamma camera based freehandSPECT helped to enhance intraoperative imaging and therewith strengthens the hybrid surgical guidance concept.

In part three the influence of nerve preservation on postoperative functional outcome is assessed and preoperative and intraoperative imaging techniques for nerve visualization are evaluated. An intraoperative score quantifying the nerve preservation during robot-assisted prostatectomy (the fascia preservation (FP) score) was used to improve and predict the postoperative erectile function in patients with prostate cancer. To improve the visualization of peripheral nerves before and during surgery, two possible techniques were evaluated, D-Prep MRI (preoperative) and fluorescence imaging (intraoperative), respectively

In **chapter 10** anatomy based nerve containing fascia preservation during robot-assisted radical prostatectomy is evaluated in 1241 prostate cancer patients and related to an international index of erectile function (IIEF) score. Based on age, preoperative IIEF score, Charlson comorbidity score index (CCSI), use of clips and the degree of nerve sparing, it was possible to predict the postoperative erectile function after RARP using a dedicated prediction model.

In an attempt to generate a personalized anatomical roadmap that depicts the location of delicate nerves, a D-Prep MRI sequence was applied in the head and neck area (6 volunteers; **Chapter 11**). The technology clearly detected anatomical variations and allowed for the visualization of peripheral nerves > 0.7 mm in diameter. Uniquely, this MRI sequence also provided enhanced insight in the lymphatic anatomy, such as the number of lymph nodes in the surgical field ( $23.2 \pm 4$ ), the sizes of these lymph nodes (range 21-372 mm<sup>3</sup>) and distances of lymph nodes to delicate anatomies.

Reasoning that fluorescence imaging could prevent damage to nerve structures by allowing intraoperative identification; in chapter 12 the *in vivo* nerve staining capabilities of locally administered fluorescent lectin-based tracers is described. To allow for fluorescence imaging, WGA, PNA, PHA-L and LEL were functionalized with Cy5. Transfer of these imaging tracers along the sciatic nerve was evaluated in transgenic Thy1-YFP mice (n = 12; in this model the nerves are YFP-fluorescent for reference). On average, this approach allowed for identification of nerves up to 1 cm from the administration site. Although the technique is promising, this technology is far from generating an impact in the clinical setting.

In conclusion, the techniques described in the above mentioned chapters could help to improve the clinical outcome after surgery for patients treated with different malignancies. These techniques could create an optimal balance in tumour or lymph node resection and the sparing of delicate structures in the surrounding anatomical area. Although the techniques are already feasible, their value in the clinical routine have to be proven in additional clinical studies evaluating the postoperative outcome.

## OUTLOOK AND FUTURE PERSPECTIVES

The surgical guidance techniques reported in this thesis were used in the first place to improve the pre- and intraoperative detection of the targeted lesion. However, it has been proposed that true optimization of surgical guidance requires that a balance is struck between complete resection of (potentially) malignant tissues and sparing of surrounding structures such as nerves. Fluorescence guidance during surgery could help to improve the intraoperative visual detection of the targeted lesions but could also allow navigation around structures that need to be spared. Such an approach could, for example, help to improve the erectile function and as such result in an improved quality of life in prostate cancer patients. A combination of acoustic, optical and directional guidance could be implied for all surgical fields to improve the surgical precision during operations. A logical extension of these techniques can be found in means to enhance the ability to provide feedback on different features. For example, in the near future multicolor fluorescence could be used to identify the targeted lesions and at the same time distinguish structures that need to be spared. To initiate this concept, in a preclinical (pigs) pilot study we evaluated whether it was technically feasible to intraoperatively distinguish sentinel nodes related to the prostate to those lymph nodes draining from the hind legs. Here two different dyes with complementary excitation and emission spectra were used, allowing for simultaneous visualization of the two independent features (prostate vs. leg, Figure 1).

Although intraoperative information based on (multicolor) fluorescence helped illuminate important details during the surgical resection, this technique is not able to integrate non-invasive preoperative planning information as is available from modalities like CT, MRI and or fuse modalities like SPECT/CT and PET/MRI. Such integration may be realized using navigation technologies. Ideally, the in depth three dimensional imaging information is presented as augmented reality overlay on the patient during the surgical procedure. This provides a roadmap in which surgical tools and modalities can be accurately positioned. Combined we envision that the above techniques could facilitate further improvements in the accuracy of surgery.

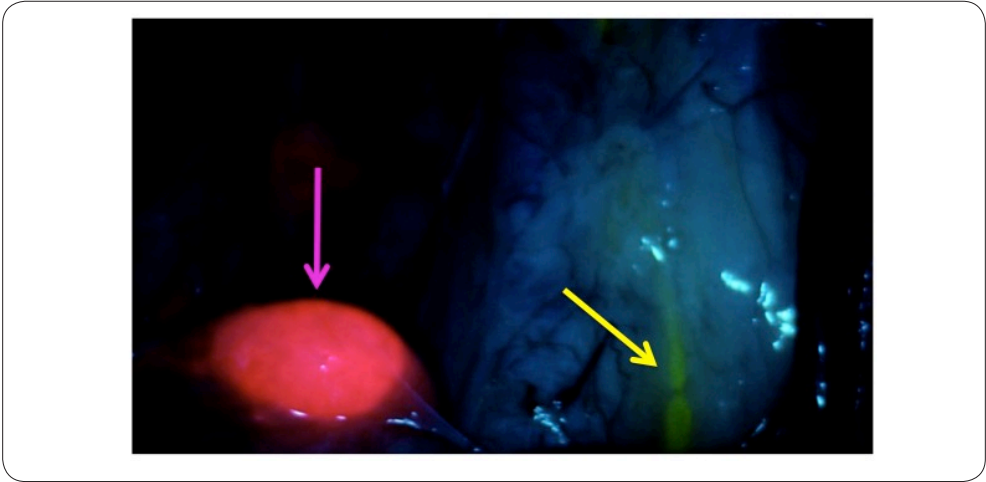


**Figure 1. Multicolor lymph node identification**

In pink an ICG positive SN directly related to the prostate. In yellow a lymph duct running from the leg.

## SAMENVATTING

De studies beschreven in het proefschrift illustreren de waarde van radio- en fluorescentie geleide chirurgische technieken die helpen om laesies te lokaliseren.

In **deel één** ligt de nadruk met name op de intra-operatieve identificatie van laesies (in dit geval schildwachtklieren), die chirurgisch worden verwijderd. Hierin worden de voordelen van de hybride chirurgische benadering, waarin radio- en fluorescentie-geleide chirurgie worden gecombineerd, beschreven.

Het review gepresenteerd in **hoofdstuk 2** beschrijft de meest gangbare radiogeleide chirurgische benaderingen. Hier worden verschillende radioactieve tracers besproken en de mogelijke hybride (radioactieve en fluorescente) varianten daarvan benoemd. Verder worden verschillende beeldvorming-apparaten beschreven die gebruikt worden tijdens radiogeleide chirurgie en die mogelijk een rol kunnen spelen voor het genereren van hybride beeldvormingsmodaliteiten.

In **hoofdstuk 3** worden de resultaten van het gebruik van de hybride tracer (ICG-<sup>99m</sup>Tc-nanocolloid) in 501 procedures voor verschillende soorten kanker beschreven (huidkanker (n=191), vulva kanker (n=21), penis kanker (n=192), mondholte kanker (n=51) en prostaat kanker (n=40)) beschreven. In deze populatie zijn 1643 schildwachtklieren geïdentificeerd aan de hand van gecombineerde gamma detectie (>98%) en fluorescentie (>95%) optische detectie. Intra-operatieve detectie aan de hand van fluorescentie bleek superieur vergeleken met de intra-operatieve detectie met behulp intra-operatief toegediende blauwe kleurstof (22-78%).

In de follow-up van de patiënten zagen we dat het gebruik van de hybride tracer geen negatieve invloed had op het aantal fout-negatieve procedures en andere postoperatieve uitkomsten. Deze studie bevestigde dat, met het gebruik van de hybride tracer, de radio- en optische chirurgische begeleiding tijdens de schildwachtklier procedure op universele wijze kan worden toegepast bij verschillende soorten kanker en op verschillende anatomische locaties.

**Hoofdstuk 4** laat zien dat er door een toename in sensitiviteit en de introductie van anatomische context ook de fluorescentie detectie kan worden verbeterd bij fluorescentielaparoscopie. Dit concept werd onderzocht in drie groepen prostaatkankerpatiënten die een schildwachtklier procedure ondergingen. In de eerste groep patiënten (n=11) die voor

een schildwachtklierprocedure waren gepland, werd de standaard concentratie van ICG-<sup>99m</sup>Tc-nanocolloid gebruikt in combinatie met de standaard fluorescentielaparoscoop. In de tweede groep (n=13) werd de geoptimaliseerde concentratie en het volume van ICG-<sup>99m</sup>Tc-nanocolloid toegepast en, in de derde groep (n=16), werd daarnaast een verbeterde fluorescentielaparoscoop geïntroduceerd. De gemiddelde fluorescentie-gebaseerde schildwachtklieridentificatie nam van 63.7% (in groep 1) naar 85.2% (groep 2) toe tot 93.5% (groep 3; p=0.012).

**Hoofdstuk 5** beschrijft een studie van 55 prostaatkankerpatiënten (met een risico op lymfkliermetastasen >5 % gebaseerd op het Briganti nomogram), waarin de robot-geïntegreerde Firefly fluorescentielaparoscoop was gebruikt tijdens robot-geassisteerde radicale prostatectomie. Intra-operatieve fluorescentiebeeldvorming met de standaard gebruikte instelling maakte het mogelijk om 80.4% van de schildwachtklieren aan de hand van fluorescentie te visualiseren (148/184 in 50 patiënten); de *ex vivo* fluorescentie detectie was 97.8%. Preoperatieve SPECT/CT maakt het mogelijk om schildwachtklieren te lokaliseren terwijl het niet mogelijk bleek om *in vivo* fluorescente signaal te detecteren. Door integratie van de beeldvorming van fluorescentielaparoscoop in de robotische operatietechniek, werd er een directe synergie tussen de SPECT/CT beeldvorming en de intra-operatieve fluorescentie beeldvorming gecreëerd en zo werd de beeldgeleide interventie versterkt.

**Hoofdstuk 6** evalueert de relatie tussen de hoeveelheid hybride tracer (ICG-<sup>99m</sup>Tc-nanocolloid) die in de schildwachtklier terecht komt en de intra-operatieve detecteerbaarheid van het fluorescente signaal. Dit werd geëvalueerd bij 20 patiënten met een melanoom gelokaliseerd in het hoofd-hals gebied, bij 40 peniskankerpatiënten en bij 20 prostaatkankerpatiënten. Deze 80 patiënten ondergingen allen een schildwachtklierprocedure ondergingen waarbij gebruik werd gemaakt van de hybride tracer ICG-<sup>99m</sup>Tc-nanocolloid.

Het percentage van de gemigreerde hybride tracer kon direct worden gecorreleerd aan de hoeveelheid van de fluorescente kleurstof indocyanine groen (ICG) (range: 0.003–10.8 nmol) en de concentratie van ICG (range: 0.006–64.6 µM) in een schildwachtklier. Deze studie laat zien dat fluorescentiedetectie met ICG mogelijk is vanaf een concentratie van 0.006 µM.

**Deel twee** beschrijft het gebruik van de chirurgische modaliteiten die worden gebruikt tijdens het hybride chirurgische geleiding concept. In **hoofdstuk 7** wordt de waarde van hybride detectie modaliteiten, waarin zowel radio- als fluorescentiedetectie mogelijkheden

geïntegreerd zijn, geëvalueerd in 11 peniskankerpatiënten waarin een schildwachtklier procedure word toegepast.

Twee verschillende hybride detectiemodaliteiten waren ontworpen door een gamma detectie probe en een mobiele gammacamera te combineren met een exoscoop die fluorescentiedetectie mogelijk maakt tijdens een open chirurgie setting. Beide gecombineerde apparaten werden geëvalueerd tijdens de schildwachtklierprocedure waarin ICG-<sup>99m</sup>Tc-nanocolloid werd gebruikt, respectievelijk in vijf en zes peniskankerpatiënten. Om de gevoeligheid van de individuele detectiemodaliteiten te evalueren werden intra-operatief de radio- en fluorescentiegeleide schildwachtklierdetectie percentages gescoord op werkafstanden van 0, 10, 20 en 30 cm. Deze vergelijkingen lieten zien dat de verschillende detectiemodaliteiten elkaar aanvullen. Over het algemeen was de mobiele gammacamera het meest waardevol in de geteste werkafstanden (10-30cm). Voor de gammaprobe gold, dat deze het meest van waarde was voor de ruwe lokalisatie van de schildwachtklier, terwijl de fluorescentie er voor zorgde dat er tegelijkertijd ook gedetailleerde informatie van de schildwachtklier en omringende anatomie werd verkregen.

**Hoofdstuk 8** beschrijft de mogelijkheid van intra-operatieve positionering door het gebruik van een op nucleair geneeskundig gebaseerde beeldvorming gestuurde navigatie. In deze studie werden vijf peniskankerpatiënten, met schildwachtklieren in de lies, geïnccludeerd. Het navigatieapparaat werd gebruikt om een augmented reality overlap van de SPECT/CT met het beeld van de fluorescentiecamera te realiseren en zo de pre- en intra-operatieve beelden te integreren. Navigatie was succesvol in voor alle twaalf intra-operatief geëvalueerde schildwachtklieren (gemiddelde error: 8,8 mm; range: 0-20mm). De resultaten van deze studie zijn veelbelovend voor toekomstige toegepaste chirurgische applicaties, waar de lokalisatie van laesies lastig kan zijn, bijvoorbeeld bij schildwachtklieren in het kleine-bekkengebied.

In **hoofdstuk 9** werden bij acht patiënten met een melanoom in het hoofd-halsgebied schildwachtklieren gelokaliseerd op basis van een freehandSPECT gebaseerde navigatietechniek. Met deze techniek kon er naar 87% van de schildwachtklieren worden genavigeerd in een 3-dimensionele afbeelding en konden deze vervolgens worden verwijderd onder fluorescentie geleiding. Tevens hielp de fluorescentiebeeldvorming bij de confirmatie van de nauwkeurigheid van de lokalisatie van de freehandSPECT gebaseerde navigatie van de schildwachtklieren. Het gebruik van de gammacamera gebaseerde freehandSPECT

verbeterde de intra-operatieve beeldvorming en hielp daarmee het hybride chirurgische concept te verbeteren.

In **deel drie** is de invloed van intra-operatieve zenuwsparing op de functionele uitkomst geëvalueerd en tevens zijn pre- en intra-operatieve beeldvorming technieken voor zenuwvisualisatie geëvalueerd. Een intraoperatieve score voor kwantificatie van de zenuwpreservatie (fascia preservatie - FP) van toepassing tijdens robot-geassisteerde prostatectomie is gebruikt om de postoperatieve erectiele disfunctie te voorspellen in patiënten met prostaatkanker. Om de visualisatie van perifere zenuwen te verbeteren werden twee mogelijke technieken onderzocht, namelijk D-Prep MRI (preoperatief) en fluorescentie (intraoperatief).

In **hoofdstuk 10** werd de fascia preservatie (FP) score die tijdens robot-geassisteerde prostatectomie wordt gebruikt als indirecte maat van zenuwsparing geëvalueerd in 1241 prostaatkankerpatiënten. De FP score werd gerelateerd aan de postoperatieve international index of erectile function (IIEF) score. Gebaseerd op leeftijd, preoperatieve IIEF score, Charlson comorbidity score index (CCSI), het gebruik van introperatieve clips en de hoeveelheid zenuwsparing (FP score), werd het mogelijk om de postoperatieve erectiele functie na robot-geassisteerde prostatectomie te voorspellen aan de hand van een predictiemodel.

In **hoofdstuk 11** is getracht een gepersonaliseerd anatomische landkaart van de lokalisatie van perifere zenuwen in het hoofd hals gebied te genereren. Een D-Prep magnetic resonance imaging (MRI) sequentie werd gebruikt bij zes vrijwilligers om in het hoofd-halsgebied zenuwen te visualiseren. De technologie liet duidelijk de anatomische variaties zien tussen de verschillende proefpersonen en het was daarbij mogelijk om perifere zenuwen met een diameter van  $>0,7$  mm te visualiseren. Deze MRI sequentie heeft daarnaast nog een unieke eigenschap, namelijk dat zij ook inzicht geeft in de anatomie van het lymfesysteem, zoals het aantal lymfeklieren in het chirurgische gebied ( $23.2 \pm 4$ ), de afmeting van de lymfeklieren (range 21-372 mm<sup>3</sup>) en de afstand van de lymfklieren ten opzichte van belangrijke anatomische structuren.

Vanuit de redenering dat fluorescentie zenuw schade kan voorkomen door het verbeteren van de intra-operatieve identificatie van de zenuwen, is in **hoofdstuk 12** de *in vivo* zenuwkleuring mogelijkheid van lokaal toegediende fluorescent-gelabelde lectine- gebaseerde tracers beschreven. Om fluorescentie beeldvorming mogelijk te maken werden de verschillende

lectinen WGA, PNA, PHA-L en LEL gelabeld met de nabij infrarode fluorescente kleurstof Cy5. De migratie van de lectinen langs de nerves ischiadicus werd geëvalueerd in transgene Thy1-YFP mice (n =12, deze muis modellen hebben YFP-fluorescente zenuwen die werden gebruikt als referentie kader). De gemiddelde afstand vanaf de injectie plaats waarmee de fluorescente lectines de zenuw hielpen te identificeren was 1 cm. Hoewel deze techniek veelbelovend lijkt, is deze techniek nog niet zover dat zij gebruikt kan worden in de klinische setting.

De technieken beschreven in de bovengenoemde hoofdstukken zouden van waarde kunnen zijn bij het verbeteren van de klinische uitkomsten van patiënten met verschillende soorten maligniteiten die worden behandeld met een chirurgische ingreep. Deze technieken kunnen een optimale balans creëren tussen tumor of lymfeklierresectie en het sparen van belangrijke anatomische structuren. Hoewel deze technieken in studieverband al beschikbaar zijn moet de waarde van het gebruik in de klinische routine nogmaals worden bevestigd in toekomstige studies die de postoperatieve uitkomsten van de patiënten evalueren.

## VOORUITZICHTEN EN TOEKOMSTIG PERSPECTIEF

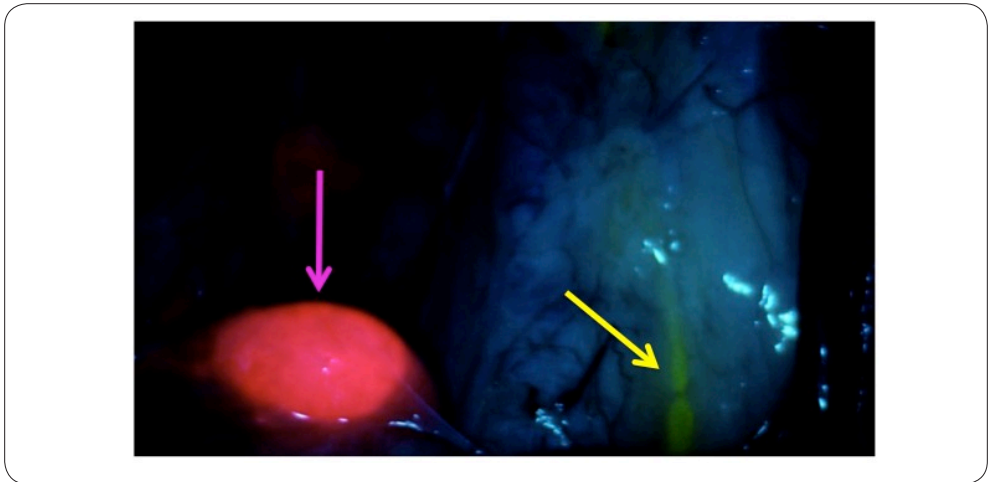
De chirurgische begeleiding technieken beschreven in deze thesis werden in eerste instantie gebruikt voor de pre- en intra-operatieve detectie van specifieke laesies. Bij de optimalisatie van een chirurgische techniek moet rekening worden gehouden met de balans tussen een complete resectie van (potentieel) maligne weefsel en het sparen van omliggend weefsel, zoals bijvoorbeeld zenuwen. Het gebruik van fluorescentie tijdens een chirurgische ingreep kan de intra-operatieve visualisaties van laesies verbeteren, tevens kan het de chirurg helpen te navigeren rondom andere belangrijke structuren om aldus deze te sparen. In prostaatkankerpatiënten kunnen de beschreven chirurgische benaderingen bijvoorbeeld de postoperatieve erectiele functie helpen verbeteren en daarmee ook de kwaliteit van leven van deze patiënten.

Een combinatie van akoestische, optische en directionele navigatie begeleiding kan toegepast worden in alle chirurgische disciplines om de chirurgische precisie tijdens operaties te verbeteren. Een logische uitbreiding van deze technieken kan worden gevonden in het verbeteren van terugkoppeling van verschillende functies en technieken. In de nabije toekomst zou het gebruik van multikleurenfluorescentie specifieke laesies kunnen identificeren en tegelijkertijd ook onderscheid kunnen maken in de anatomische structuren die moeten worden gespaard. Om dit concept toe te passen is er in preklinische pilot study geëvalueerd of deze multikleurenfluorescentie techniek technisch haalbaar was tijdens een chirurgische ingreep. In deze studie is gekeken of het intraoperatief mogelijk was om schildwachtklieren gerelateerd aan de prostaat te onderscheiden van lymfeklieren die draineren vanuit het bovenbeen. Hier werden twee verschillende kleurstoffen gebruikt met complementaire excitatie en emissiespectra, die ervoor zorgden dat het mogelijk werd om de twee onafhankelijke kleuren tegelijkertijd te visualiseren (lymfedrainage van prostaat versus lymfedrainage van het been, Figuur 1).

Hoewel de intra-operatieve informatie gebaseerd op de (multikleuren)fluorescentie ervoor zorgt dat belangrijke details tijdens een chirurgische operatie zichtbaar worden, is het met deze techniek nog niet mogelijk om non-invasieve preoperatieve informatie zoals CT, MRI en/of gefuseerde technieken SPECT/CT en PET/MRI tijdens de operatie te integreren.

De integratie van verschillende technieken kan bewerkstelligd worden door het gebruik van navigatietechnieken. In een ideale setting wordt de 3-dimensionale informatie gebruikt als een augmented reality overlay op de patiënt tijdens de chirurgische procedure. De

augmented reality overlay kan dan gebruikt worden als een digitale landkaart om de chirurgische instrumenten met nauwkeurigheid te plaatsen. Gecombineerd zouden de bovenstaande beschreven technieken verbeteringen in nauwkeurigheid van de chirurgische techniek bewerkstellingen.



**Figuur 1. Multikleuren lymfeklieridentificatie**

In het roze een schildwachtklier, direct gerelateerd aan de prostaat, met indocyanine groen geïdentificeerd en in geel een lymfebaan die draineert vanuit het been.



## RESUME

Gijs KleinJan was born in Apeldoorn, the Netherlands on July 17th 1985. Since 2003 Gijs studied Medicine at the University of Amsterdam. During his clerkships, he performed a research internship at the department of Orthopedic Surgery at the hospital Onze Lieve Vrouwe Gasthuis (OLVG) in Amsterdam. After graduating from medical school in 2011, Gijs started his medical career as a physician at the surgical ward the Netherlands Cancer Institute – Antoni van Leeuwenhoek Hospital (NKI-AvL). During this time he got acquainted with the image guided surgery trial of the group (the group was previously housed at the NKI-AvL).

In October 2012, he started his PhD at the Interventional Molecular imaging Laboratory (IMI-Lab), of the Radiology department at Leiden University Medical Center. His primary goal was to develop new approaches to improve the imaging of malignant lesions, (tumor) positive lymph nodes and nerves, both pre-operative and during surgery. To obtain clinical insight in the field of image guided surgery he worked on the clinical validation of a hybrid (radioactive and fluorescent) concept for surgical operations in various malignancies. These clinical trials run at the NKI-AvL and are conducted in close collaboration with the departments of Urology, Nuclear Medicine , and (Head&Neck) Surgery of the NKI-AvL.

After his time at the IMI-lab Gijs “re-started” his clinical career as a physician at the department of Urology at the Canisius Wilhelmina Ziekenhuis (CWZ), Nijmegen, the Netherlands. In September 2017 Gijs was accepted for the training to become a urologist. He started the residency in general surgery in January 2018 at the Flevoziekenhuis, Almere, the Netherlands. In 2020 Gijs will start his residency in Urology at the Leiden University Medical Center.

## PUBLICATIONS

1. van Oosterom MN, Meershoek P, **KleinJan GH**, Hendricksen K, Navab N, van de Velde CJH, van der Poel HG, van Leeuwen FWB. Navigation of fluorescence cameras during soft-tissue surgery - is it possible to use a single navigation setup for various open and laparoscopic urological surgery applications? *J Urol*. 2017. pii: S0022-5347(17)77965-7.
2. **KleinJan GH**, Karakullukçu B, Klop WMC, Engelen T, van den Berg NS, van Leeuwen FWB. Introducing navigation during melanoma-related sentinel lymph node procedures in the head-and-neck region. *EJNMMI Res*. 2017; 17;7(1):65.
3. Van Willigen DM, van den Berg NS, Buckle T, **KleinJan GH**, Hardwick JC, Van der Poel HG, van Leeuwen FWB. Multispectral fluorescence guided surgery; a feasibility study in a phantom using a clinical-grade laparoscopic camera system. *Am J Nucl Med Mol Imaging*. 2017;15;7(3):138-147
4. Grivas N, Wit E, **KleinJan GH**, Kuusk T, Donswijk M, Van Leeuwen FWB, Van der Poel HG. The impact of adding sentinel node biopsy to extended pelvic lymph node dissection on the biochemical recurrence of prostate cancer patients treated with robot-assisted radical prostatectomy. *JNM 2017* accepted for publication
5. Grivas N, Wit E, Pos F, de Jong J, Vegt E, Bex A, Hendricksen K, Horenblas S, **KleinJan GH**, van Rhijn B, Van der Poel HG Sentinel node dissection to select clinically node-negative prostate cancer patients for pelvic radiotherapy: impact on biochemical recurrence and systemic progression. *Int J Radiat Oncol Biol Phys*. 2017;1;97(2):347-354.
6. Van der Poel HG, Meershoek P, **Grivas N, KleinJan G**, van Leeuwen FW, Horenblas S. Sentinel node biopsy and lymphatic mapping in penile and prostate cancer. *Urologe A*. 2017;56(1):13-17.
7. **KleinJan GH**, Hellingman D, van den Berg NS, van Oosterom MN, Hendricksen K, Horenblas S, Valdes Olmos RA, van Leeuwen FWB Hybrid surgical guidance: Does hardware integration of gamma- and fluorescence- imaging modalities make sense? *J Nucl Med*. 2017;58(4):646-650.
8. Van Oosterom MN, Engelen MA, van den Berg NS, **KleinJan GH**, Van der Poel HG, Wendler T, Van der Velde CJH, Navab N, van Leeuwen FWB. Navigation of a robot-integrated fluorescence laparoscope in preoperative SPECT/CT and intraoperative freehand SPECT imaging data - a phantom study. *J Biomed Opt*. 2016;1;21(8):86008..
9. Van den Berg NS, Buckle T, **KleinJan GH**, Van der Poel HG, van Leeuwen FWB. Multispectral fluorescence imaging during robot-assisted laparoscopic sentinel node biopsy, a first step towards a fluorescence-based anatomical roadmap. *Eur Urol*. 2016;23. pii: S0302-2838(16)30282-2.

10. Buckle T, **KleinJan GH**, Engelen T, van den Berg NS, DeRuiter MC, van der Heide U, Valdes Olmos RA, Webb A, van Buchem MA, Balm AJ, van Leeuwen FW., Diffusion-weighted-preparation (D-prep) MRI as a future extension of SPECT/CT based surgical planning for sentinel node procedures in the head-and-neck area? *Oral Oncol.* 2016;60:48-54.
11. **KleinJan GH**, van den Berg NS, van Oosterom MN, Wendler T, Miwa M, Bex A, Hendricksen K, Horenblas S, van Leeuwen FWB. Towards (Hybrid) navigation of a fluorescence camera in an open surgery setting. *J Nucl Med.* 2016;57(10):1650-1653.
12. **KleinJan GH**, Brouwer OR, Mathéron HM, Rietbergen DDD, Valdés-Olmos RA, Wouters MW, van den Berg NS, van Leeuwen FWB. Hybrid radioguided occult lesion localization (hROLL) of 18F-FDG-avid metastases using the hybrid tracer indocyanine green-99mTc-nanocolloid. *Rev Esp Med Nucl Imagen Mol.* 2016 ;35(5):292-7
13. Van den Berg NS, Miwa M, **KleinJan GH**, Sato T, Maeda Y, van Akkooi AC, Horenblas S, Karakullukcu B, van Leeuwen FW (Near-Infrared) Fluorescence-Guided Surgery Under Ambient Light Conditions: A Next Step to Embedment of the Technology in Clinical Routine. *Ann Surg Oncol.* 2016. *Ann Surg Oncol.* 2016;23(8):2586-95
14. **KleinJan GH**, Bunschoten A, Van den Berg NS, Olmos RA, Klop WM, Horenblas S, Van der Poel HG, Wester HJ, van Leeuwen FW. Fluorescence guided surgery and tracer-dose, fact or fiction? *Eur J Nucl Med Mol Imaging.* 2016. *Eur J Nucl Med Mol Imaging.* 2016 Sep;43(10):1857-67.
15. **KleinJan GH**, Van den Berg NS, de Jong J, Wit EM, Thygessen H, Vegt E, Van der Poel HG, Van Leeuwen FW. Multimodal hybrid imaging agents for sentinel node mapping as a means to (re)connect nuclear medicine to advances made in robot-assisted surgery. *Eur J Nucl Med Mol Imaging.* 2016;43(7):1278-87
16. Van den Berg NS, Simon H, **KleinJan GH**, Engelen T, Bunschoten A, Welling MN, Tijink BM, Horenblas S, Chambron J, van Leeuwen FWB. First-in-human evaluation of a hybrid modality that allows combined radio- and (near-infrared) fluorescence tracing during surgery. *Eur J Nucl Med Mol Imaging.* 2015;42(11):1639-47.
17. Acar C\*, **KleinJan GH\***, van den Berg NS, Wit EM, van Leeuwen FWB, van der Poel HG. The advances in sentinel node dissection in prostate cancer: from a technical perspective. *Int J Urology.* 2015. (\* equal first author)
18. Engelen T, Winkel BM, Rietbergen DD, **KleinJan GH**, Vidal-Sicart S, Olmos RA, van den Berg NS, van Leeuwen FW. The next evolution in radioguided surgery: breast cancer related sentinel node localization using a freehandSPECT-mobile gamma camera combination. *Am J Nucl Med Mol Imaging.* 2015;15;5(3):233-45 2015.

19. Engelen T, **KleinJan GH**, van Leeuwen FWB en van den Berg NS. Virtual-reality in de operatiekamer: Kan intra-operatieve navigatie op basis van preoperatieve (nucleaire) beeldvorming worden gebruikt om de chirurgische opsporing van laesies te verbeteren? Medisch Contact. Februari 2015
20. van der Poel HG, van den Berg NS, **KleinJan GH**, van Leeuwen FW. Reply from Authors re: Francesco Montorsi, Giorgio Gandaglia. Sentinel Node Biopsy for Prostate Cancer: A Useless Surgical Exercise? Removing Nodes that Count Rather than Counting Nodes that Don't. Eur Urol. 2014 Dec;66(6):1000-1.
21. Chícharo de Freitas JR, **KleinJan GH**, van der Poel HG, van den Berg NS, Vegt E, Stokkel MP, Valdés Olmos RA. Utility of SPECT/CT scan for anatomical localization of pararectal and presacral sentinel nodes in prostate cancer. Rev Esp Med Nucl Imagen Mol. 2014 Oct 23
22. **KleinJan GH\***, van den Berg NS\*, Brouwer OR, de Jong J, Acar C, Wit EM, Vegt E, van der Noort V, Valdés Olmos RA, van Leeuwen FW, van der Poel HG. "Optimisation of fluorescence guidance during robot-assisted laparoscopic sentinel node biopsy for prostate cancer". Eur Urol. 2014. DOI: 10.1016/j.eururo.2014.04.014. (Highlighted in Nature Reviews Urology, 2014; \* equal first author)
23. **KleinJan GH**, Buckle T, van Willigen DM, van Oosterom MN, Spa SJ, Kloosterboer HE, van Leeuwen FW. "Fluorescent lectins for local *in vivo* visualization of peripheral nerves". Molecules. 2014 Jul 8;19(7):9876-92.
24. van den Berg NS, Buckle T, **KleinJan GH**, Klop WMC, Horenblas S, van der Poel HG, Valdés Olmos RA, van Leeuwen FWB. "Hybrid tracers for sentinel node biopsy". Q J Nucl Med Mol Imaging. 2014;58(2):193-206.
25. **KleinJan GH**, Bunschoten A, Brouwer OR, van den Berg NS, Valdés-Olmos RA, van Leeuwen FWB. "Multimodal imaging in radioguided surgery". Clinical and Translational Imaging. 2013;1:433-444.
26. Mathéron HM, van den Berg NS, Brouwer OR, **KleinJan GH**, van Driel WJ, Trum JH, Vegt E Kenter G, van Leeuwen FWB, Valdés Olmos RA. "Multimodal surgical guidance towards the sentinel node in vulvar cancer". Gynecol Oncol. 2013;131(3):720-5.
27. van der Linde JA, van Kampen DA, Terwee CB, Dijkman LM, **KleinJan G**, Willems WJ. "Long-term results after arthroscopic shoulder stabilization using suture anchors: an 8- to 10-year follow-up". Am J Sports Med. 2011; 39(11):2396-403.

## DANKWOORD

Allereerst Prof. dr. Mark van Buchem, dank voor het optreden als promotor. Daarbij mag ik natuurlijk Elmi van Beelen niet vergeten, dank voor het helpen regelen van de laatste loodjes.

Dan mijn co-promotores dr. Fijs van Leeuwen en dr. Renato Valdés Olmos.

Fijs bedankt voor het optreden als drijver en inspirator voor het doen van dit onderzoek en de uiteindelijk productie van dit boekje. Ik bewonder je passie en inzet voor dit onderzoek, soms is de nodige rust en ontspanning ook wel eens verstandig en goed voor jouw (en andermans) hart. Nogmaals dank.

Renato, oftewel mister Mediator, bedankt voor alle momenten waarop ik bij jou terecht kon om advies in te winnen. Jouw sociale input en humor heeft er mede voor gezorgd dat ik de energie weer kon vinden om dit boekje tot een goed einde te brengen. Daarbij wil ik natuurlijk ook jouw Marianne bedanken, want achter elke sterke man....

Commissieleden: prof. dr. Tanke, prof. dr. Balm, prof. dr. Marion de Jong, dr. Van Erkel, bedankt voor jullie tijd, input en kritische noot.

Nynke van den Berg, wat heb jij hard gewerkt in de tijd dat we samen bij het IMI-lab hebben gezeten. Mede dankzij jou hebben we in een redelijk rap tempo een hoop artikelen geproduceerd. Ik hoop dat je het goed gaat in de States en pak daar natuurlijk ook je verdiende vrije momenten.

Dan wil ik natuurlijk alle (ex) collega's van het IMI-lab bedanken, toch bijzonder om te zien dat onder de leiding van Fijs een kruisbestuiving en (soms lastige) samenwerking is ontstaan van chemici, technenuten, biologen en (ook die) artsen, die zo veel wetenschappelijke output levert. Tessa, Steffen, Danny, Mick, Pip, Sylvia, Anton, Mark, Thijs, Oscar en Matthias bedankt voor jullie tips en hulp bij het (lab) werk.

Verder wil ik de directe onderzoek collega's op de nucleaire geneeskunde van het AVL bedanken: Daan, Bas, Jacob en Suzanna bedankt voor het zij aan zij zwoegen in een veel te klein kantoortje.

Veel dank gaat er uit naar alle OK-assistenten op de operatie kamers van het AVL, met name voor de nodige tijd die ik kreeg om alweer “onderzoekjes/testjes” uit te voeren. Rob van Meinetten dank voor het altijd soepeltjes en humorvol meedenken waar de experimenten konden plaats vinden. Micha bedankt dat de camera’s, trackers etc. altijd op tijd steriel waren.

Dr. van der Poel, mr. Robot, Henk ik wil je bedanken voor de rust en tijd die jij me voornamelijk in het begin van mijn onderzoeksperiode hebt gegeven. Met het maken van de nodige lijstjes wist je voor mij structuur te scheppen in de wereld die onderzoek heet. Zo hielp je me met de nodige humor de realiteit onder ogen te zien. Mede dankzij jouw kennis en kunde heb ik me verder verdiept in de urologie.

Prof. Simon Horenblas bedankt voor alle oefenpresentaties en oefensollicitaties. Jouw humor werkt altijd relativerend.

Esther Wit, het laatste jaar van mijn promotie traject heb ik met veel plezier meegelopen tijdens de donderdagmiddag poli op het OBC. Natuurlijk wil ik je ook bedanken voor de samenwerking binnen het onderzoek.

Verder wil ik alle urologen en verpleegkundig specialisten van het urologie team van het AVL bedanken voor jullie tijd, het includeren patiënten en coördineren van de nodige onderzoeken. Kees, Bas, Axel, Jolanda, Eva, Corinne en Erik bedankt.

Daarnaast gaat er dank uit naar de hoofd-hals chirurgen van het AVL. Met jullie heb ik de nodige tijd op OK gependeed op zoek naar dat ene laatste schildwachtkliertje. Martin, Baris, prof. Balm, prof. Van den Brekel, Dr. Zuur en Pim bedankt.

Dan gaat er ook nog dank uit naar de afdeling nucleaire geneeskunde. Ik wil alle nucleair geneeskundigen en natuurlijk alle MNW-ers die mij, waar nodig, hebben geholpen, bedanken.

Bob dank voor het helpen met de lay-out van dit prachtige boekje.

(Ex) collega promovendi uit het AVL: Lotte, Rosa, Rosa, Bas, Noortje, Sarah, Elies, Sharon en Laura bedankt en succes gewenst in jullie verdere carrière.

Verder wil ik alle collega's van de urologie uit het CWZ bedanken voor het warm bad waarin ik ben gestapt en de tijd en ruimte die me is geboden binnen om klinisch werk weer op te pakken, na een lange periode van onderzoek.

(Schoon)familie en vrienden dank voor alle gezelligheid. Samen met jullie hoop ik het glas te heffen op mijn promotie en natuurlijk op de mooie momenten die daarna nog volgen.

Mijn paranimfen Yves en Jur:

Yves, ik vind het nog altijd bijzonder om met jou bevriend te zijn. Als ik een mindere dag heb, denk ik terug aan alle reizen en avonturen die we hebben meegemaakt. Jeanette, Yves kan zich geen betere vriendin en moeder van zijn kinderen wensen. Gelukkig ben jij een baken van rust en breng je veel gezelligheid, "helaas" vorm je daarnaast ook de nodige handrem voor Yves.

Jurriaan, de ADT avonden gesponsord door G&G zijn altijd legendarisch. De kracht zit hem gelukkig in herhaling.

Ans en Henny niemand kan zich zulke gezellige en lieve schoonouders bedenken, bij jullie is het altijd feest. Ik kan jullie niet genoeg bedanken voor het optreden als opvanghuis voor radeloos verloren schoonzoons.

Margot, mijn (schwager) zus, bedankt voor al je humor en tegengas.

Michiel en Hans, mijn broers, bij jullie heb ik weinig woorden nodig. Als we op reis/ op stap gaan maken we altijd weer iets bijzonders mee, wat vervolgens niet aan anderen uit te leggen is. Ik hoop dit nog veel met jullie te blijven doen.

Ge(r)t en Vonsje, ik wil jullie bedanken voor alle materiele steun, maar natuurlijk voor alle liefde en zorg (soms in overvloed) die jullie me in mijn leven hebben gegeven. Ik hou van jullie.

Anke ik hou van jou.

